Strain and Stress: Derivation, Implementation, and Application to Organic Crystals

im Fachbereich Physik der Freien Universität Berlin
eingereichte Dissertation

zur Erlangung des akademischen Grades eines
Doktors der Naturwissenschaften

vorgelegt von
Franz Knuth

Berlin 2015

Erstgutachter: Prof. Dr. Matthias Scheffler
Zweitgutachter: Prof. Dr. Felix von Oppen

Tag der Disputation: 11.11.2015

Abstract

Organic semiconductors form an active and promising field of research since they can be used to develop and construct highly efficient and flexible (opto)electronic devices with tailored structural and electronic properties, e.g., band gaps and conductivities. Typically, these properties do not only depend on the chemical composition but also on the growth conditions, e.g., on the strain or pressure applied during fabrication. However, little is yet known about these dependencies since a systematic assessment of these effects is challenging for experiment and theory alike. To shed light on these aspects, we have developed and implemented techniques to study the pressure dependence of the geometry and of the electronic structure of organic semiconductors with the help of density-functional theory.

Nowadays, isolated molecules (< 100 atoms) can be described with high accuracy by quantum chemistry methods. Applying these techniques to molecular crystals, i.e., periodic lattices of such molecules, is to date computationally extremely challenging. Therefore, density-functional theory is still the workhorse electronic-structure tool to investigate these systems – in spite of its deficiencies. In this thesis, we critically discuss to which extent they can be cured by van der Waals corrections and hybrid functionals, which include a portion of Hartree-Fock exchange.

To investigate the pressure dependencies, the stress tensor defined as the total energy derivative with respect to the strain tensor is required. In this thesis, the analytical strain derivatives have been derived and implemented in the electronic-structure code FHI-aims including the terms that stem from van der Waals corrections and Hartree-Fock exchange. The excellent accuracy and performance of our implementation is demonstrated by extensive benchmark calculations for a wide range of inorganic and organic crystals.

In particular, we discuss the prototypical organic semiconductors anthracene and polyacetylene, which are built from molecules and polymer chains, respectively. To capture their weakly bonded nature, van der Waals corrections are required, and for polyacetylene, hybrid functionals are critical for the correct description of the equilibrium geometry. We find that the interactions between the molecules or chains of the organic crystals significantly influence the electronic band structure and lead to band splitting. Under hydrostatic pressure, both crystals are strongly compressed, which increases these interactions, thereby modifying the band structure.

Eventually, the electrical band conductivity of both organic semiconductors is investigated with the Boltzmann transport equation in the constant relaxation time approximation to clarify to which extent the discussed changes in geometry and electronic structure can affect macroscopic properties. We calculate the pressure-dependent trend of the charge carrier concentration and band conductivity for intrinsic and doped systems and point out the dominant transport directions. It is discussed how the behavior of the conductivity can be attributed to the changes in the band structure. Comparison with experiments shows that our calculations yield consistent results.

Kurzfassung

Organische Halbleiter bilden ein lebhaftes und vielversprechendes Forschungsgebiet, da sie zur Entwicklung und zum Bau hoch effizienter und biegsamer (opto)elektronischer Geräte mit maßgeschneiderten strukturellen und elektronischen Eigenschaften, z.B. Bandlücken und Leitfähigkeiten, eingesetzt werden können. Diese Eigenschaften hängen typischerweise nicht nur von der chemischen Zusammensetzung ab sondern auch von den Wachstumsbedingungen, z.B. von Verformungen oder Druck während der Fertigung. Über diese Abhängigkeiten is bisher jedoch wenig bekannt, weil ein systematischer Zugang zu diesen Effekten für Experiment und Theorie herausfordernd ist. Um diese Aspekte zu beleuchten, haben wir Methoden entwickelt und implementiert, um die Druckabhängigkeit der Geometrie und Elektronenstruktur von organischen Halbleitern mit Hilfe der Dichtefunktionaltheorie zu untersuchen.

Heutzutage können Moleküle (< 100 Atome) mit hoher Genauigkeit mit quantenchemischen Methoden beschrieben werden. Diese Methoden auf Molekülkristalle, also periodische Gitter solcher Moleküle, anzuwenden, ist bislang äußerst herausfordernd. Deshalb ist die Dichtefunktionaltheorie noch immer die gängige Elektronenstrukturmethode, um diese Systeme zu untersuchen – trotz ihrer Defizite. Im Rahmen dieser Dissertation diskutieren wir kritisch, in welchem Maße diese behoben werden können durch Van-der-Waals-Korrekturen und Hybridfunktionale, die anteilig Hartree-Fock-Austausch beinhalten.

Um die Druckabhängigkeiten zu untersuchen, wird der Spannungstensor benötigt, welcher als die Ableitung der totalen Energie nach dem Verformungstensor definiert ist. Die analytischen Ableitungen nach der Verformung sind im Rahmen dieser Dissertation im Elektronenstrukturcode FHI-aims implementiert worden und beinhalten die Beiträge der Van-der-Waals-Korrekturen und des Hartree-Fock-Austauschs. Die exzellente Genauigkeit und Effizienz unserer Implementierung wird durch umfangreiche Benchmark-Rechnungen für ein breites Spektrum an anorganischen und organischen Kristallen demonstriert.

Insbesondere behandeln wir die prototypischen organischen Halbleiter Anthracen und Polyacetylen, die aus Molekülen bzw. Polymerketten aufgebaut sind. Um ihre schwach gebundene Natur zu erfassen, werden Van-der-Waals-Korrekturen benötigt und für Polyacetylen sind Hybridfunktionale entscheidend für die korrekte Beschreibung der Grundzustandsgeometrie. Wir zeigen, dass die Wechselwirkungen zwischen den Molekülen oder Ketten der organischen Kristalle die elektronische Bandstruktur signifikant beeinflussen und zu einer Bandaufspaltung führen. Unter hydrostatischem Druck werden beide Kristalle stark komprimiert, was diese Wechselwirkungen erhöht und dabei die Bandstruktur modifiziert.

Schließlich wird die elektrische Bandleitfähigkeit beider organischer Kristalle mit der Boltzmann-Transportgleichung in der konstanten Relaxationszeitnäherung untersucht, um zu klären, in welchem Maße die behandelten Geometrie- und Elektronenstrukturveränderungen makroskopische Eigenschaften beeinflussen können. Wir berechnen den druckabhängigen Verlauf der Ladungsträgerkonzentration und der Bandleitfähigkeit für intrinsische und dotierte Systeme und zeigen die dominanten Transportrichtungen auf. Es wird besprochen, wie das Verhalten der Leitfähigkeit auf die Veränderungen in der Bandstruktur zurückgeführt werden kann. Vergleiche mit Experimenten zeigen, dass unsere Berechnungen konsistente Ergebnisse liefern.

Contents

Part II: Derivation and implementation of stress tensor

Part III: Application to organic crystals

Acronyms

AM	Armiento and Mattsson
BLA	bond length alternation
BLYP	Becke, Lee, Yang, and Parr
CBM	conduction band minimum
DFA	density-functional approximation
DFT	density-functional theory
DOS	density of states
FHI-aims	Fritz Haber Institute *ab initio* molecular simulations
GGA	generalized gradient approximation
HF	Hartree-Fock
HK	Hohenberg-Kohn
HSE	Heyd, Scuseria, and Ernzerhof
KS	Kohn-Sham
LDA	local-density approximation
LR	long range
MP	multipole
PBE	Perdew, Burke, and Ernzerhof
RI	resolution of identity
SCF	self-consistent field
SR	short range
TPA	*trans*-polyacetylene
TS	Tkatchenko-Scheffler
VBM	valence band maximum
vdW	van der Waals

Notation

$\alpha, \beta, \ldots$	Greek indices denote Cartesian components
A	matrix with lattice vectors as columns
$\boldsymbol{a}_i$	lattice vector i
α	real-valued parameter in interval $[0,1]$ determining the amount of added Hartree-Fock exchange to hybrid exchange-correlation functionals
c_{ij}	coefficients for basis set expansion
E_c	correlation energy
E_el	electronic energy
E_es	total (electrons and nuclei) electrostatic energy
E_ext	interaction energy of external potential and electron density
E_H	Hartree energy
E_KS	Kohn-Sham total energy
$E_\mathrm{nuc\text{-}nuc}$	nuclear-nuclear interaction energy
E_tot	total ground state energy
E_vdW	van der Waals energy
E_x	exchange energy
E_xc	exchange-correlation energy
ϵ_c	correlation energy per electron
ϵ_i	Kohn-Sham (single-particle) eigenvalue
ϵ_x	exchange energy per electron
ϵ_xc	exchange-correlation energy per electron
ε	strain tensor
f_i	occupation number
$\hat{H}$	Hamilton operator
$\hat{H}_\mathrm{el}$	electronic Hamilton operator

$\hat{h}_{\mathrm{KS}}$	Kohn-Sham Hamilton operator
N_{el}	number of electrons in system
N_{nuc}	number of nuclei in system
n	electron density
Φ_i	Kohn-Sham orbital
φ_i	basis function
Ψ	many-body wave function of electrons and nuclei
ψ_{el}	many-body wave function of electrons
ψ_{nuc}	many-body wave function of nuclei
$\boldsymbol{R}_I$	position vector of nucleus I
σ	stress tensor
ς	electrical conductivity tensor
T	temperature
T_{s}	kinetic energy of non-interacting electron system
τ	relaxation time from Boltzmann transport equation
V	volume of unit cell
v_{es}	total (electrons and nuclei) electrostatic potential
v_{ext}	external potential
v_{H}	Hartree potential
v_{xc}	exchange-correlation potential
Z_I	charge of nuclei I

1 Introduction

The synthesis and optimization of semiconducting organic crystals, i.e., bulk materials built from periodically repeated organic compounds, has paved the route towards organic electronics and photonics. They allow the development and construction of highly efficient, flexible, easy-to-process, and low-cost (opto)electronic devices such as organic light-emitting diodes, organic photovoltaic cells, and organic field-effect transistors [For04, Hei11, Pod13]. Most prominently, these materials have been used in recent years to construct curved displays in consumer electronics, e.g., mobile phones and televisions. For these kinds of applications, there are two classes of organic semiconductors that are relevant: crystals made up from π-conjugated polymers and crystals composed of small organic molecules, which themselves contain conjugated π electrons [For04]. In both classes, the π electrons are the key for the electronic behavior of the organic crystals and thus, determine the semiconducting or even metallic behavior.

Historically, anthracene became a prototype for an organic photoconductor and led to an emerging interest in organic semiconductors made up from molecules [Kar01a]. In turn, this led to the development of high-quality molecular crystals with high charge carrier mobilities. As an example, the mobility in single crystal rubrene can reach values in the order of $10^{-3}\,\mathrm{m}^2/(\mathrm{Vs})$ [Pod13]. For comparison, single crystal silicon has mobilities only one order of magnitude larger ($10^{-2}\,\mathrm{m}^2/(\mathrm{Vs})$ [Pod13]). Also, light-emitting diodes made from organic molecules were realized in the late 1980s [Tan87].

In 1977, it was discovered that doped polyacetylene, a conjugated polymer, shows a high electrical conductivity comparable to metals [Chi77, Shi77]. For these findings, the 2000 Nobel Prize in Chemistry was awarded jointly to Alan J. Heeger, Alan G. MacDiarmid, and Hideki Shirakawa "for the discovery and development of conductive polymers" [Nob00, Hee01, Mac01, Shi01]. In highly oriented polyacetylene, electrical conductivities in the order of $10^5\,(\Omega\mathrm{m})^{-1}$ can be achieved [Väk93]. For comparison, metals typically have a conductivity in the order of 10^6 to $10^7\,(\Omega\mathrm{m})^{-1}$ [Tip08]. This discovery sparked the interest in this field and led to the development of light-emitting diodes based on conjugated polymers in the late 1980s [Bur90].

As it is the case for inorganic semiconductors, all these transport properties depend on the structural and electronic properties of organic semiconductors, e.g., band gaps and conductivities, which in turn depend on the growth conditions during fabrica-

tion [Hei11]. Hence, strain, stress, and pressure employed during crystal growth will affect the performance of materials and devices. For instance, Kim *et al.* [Kim07] showed that the performance of organic light-emitting diodes can be notably improved by applying external pressure while processing the organic layers of the device. Along these lines, is was demonstrated by Giri *et al.* [Gir11] that the charge carrier mobility in TIPS-pentacene can be doubled by applying shear forces to the organic film during growth. This procedure led to strained crystals with reduced stacking distance between the molecules. For most organic crystals, however, the pressure dependence of their electronic properties is still unknown due to the associated experimental difficulties in the fabrication and characterization under these thermodynamic conditions – in spite of the fact that such strain effects can be of utmost importance in curved or flexible devices. The creation of high-quality organic crystals is very challenging and measuring transport properties under exactly determined pressures is no easy task. Therefore, the development of a microscopic theory and of atomistic models to understand the underlying electronic effects is desirable.

However, a theoretical investigation of these effects in organic crystals is challenging as well: High-level quantum chemistry methods are indeed able to describe isolated organic molecules (< 100 atoms) with high accuracy, but their excruciating computational cost (scaling $\mathcal{O}(N^4 - N^7)$ with number of atoms N) prevents their application for periodic systems of molecules, i.e. organic crystals. Therefore, other electronic-structure methods are typically used for such investigations, most prominently density-functional theory with (semi-)local exchange-correlation functionals. This method is a computationally extremely efficient *ab initio* tool to compute the ground state electron density and energy of molecules and solids. However, this comes at a price: The involved approximations fail under certain circumstances, which is particularly critical for organic molecules. On the one hand, long-range, non-local van der Waals interactions are known to play a decisive role in organic crystals but are not at all accounted for in the typical (semi-)local functionals used to describe the exchange-correlation in density-functional theory. On the other hand, also the local self-interaction error of such (semi-)local functionals can cause severe artifacts especially in π-conjugated systems and thus result in fundamentally different geometries and electronic structures. Hence, the approximations of the exchange-correlation need to be critically evaluated and checked with higher-level methods and experiments. Last but not least, the influence of these effects on strain, stress, and pressure need to to be accounted for as well to achieve a reliable microscopic description.

This thesis addresses exactly these issues with the final goal to theoretically study and predict the pressure dependence of the electronic structure and the electronic transport properties of organic semiconductors and to lay the founding for a microscopic understanding of the pressure dependence in the properties of organic crystals. For this purpose, we employ density-functional theory in the Born-Oppenheimer approximation and critically discuss the accuracy of the employed exchange-correlation approximations.

The description of solids under stress and pressure requires the stress tensor; a quantity that is not easily accessible in the framework of density-functional theory and is defined as the total energy derivative with respect to the strain tensor[1].

In order to achieve our goal, we have derived and implemented the analytical strain derivatives of the total energy in the numeric, atom-centered orbitals based all-electron electronic-structure code FHI-aims [Blu09]. For the analytical derivation of these derivatives, every contribution to the total energy that changes under strain has to be considered: Since the atomic positions and lattice vectors of the crystal change under strain, many contributions are affected. Therefore, strain derivatives of the kinetic, electrostatic, and the exchange-correlation energy expressions used in density-functional theory are required. Our derivation and implementation includes the strain derivatives of popular approximations to the exchange-correlation energy, namely local-density approximation, generalized gradient approximation, and hybrid functionals, which incorporate a portion of Hartree-Fock exchange. Special care has to be taken if integrals are involved whose boundaries are the unit cell of the crystal. Since the unit cell changes under strain, a so-called Jacobi term occurs. Other non-trivial contributions arise because the electronic-structure code FHI-aims uses atom-centered basis functions, which move under strain. Also, the strain derivatives of van der Waals corrections, which are of pivotal importance for organic crystals, are accounted for. We critically evaluate the accuracy and efficiency of our implementation by performing extensive benchmark calculations for a wide range of inorganic and organic crystals. Additionally, the consistency for various numerical settings is checked and tests for the optimization of unit cells under pressure are performed.

We then employ our implementation to study organic crystals under hydrostatic pressure – exemplary for the two prototypical organic semiconductors anthracene and polyacetylene. In this context, it is crucial to choose an appropriate approximation for the exchange-correlation functional since the geometric and electronic structure of these materials can be critically affected by this approximation – even fundamentally as in the case of polyacetylene: The local-density approximation and generalized gradient approximation wrongly predict a metallic ground state of pure crystalline polyacetylene. In contrast, hybrid functionals yield the correct semiconducting ground state. Also, it is important to incorporate van der Waals interactions in density-functional theory calculations since the weak bonding between the molecular constituents of organic crystals typically stems from these interactions [For04]. For instance, this can be achieved by explicitly adding the long-range $1/R^6$ tail of the van der Waals energy [Tka09].

Under pressure, crystalline anthracene and polyacetylene are compressed, which increases both the intermolecular and interchain interactions. These interactions strongly influence the electronic band structure of the crystals in a non-trivial fashion. In particular, the dispersion (band width) increases dramatically under pressure, which in turn

[1] The strain tensor measures the elastic deformation of a crystal relative to a reference state (see Chapter 5).

reduces the direct and indirect gaps and thus determines the respective thermodynamic properties.

With respect to macroscopic transport properties, it is essential to note that there are several possible mechanisms of charge carrier transport in organic semiconductors, for instance pure electronic hopping, coupled electron-phonon transport (e.g. polarons), or electronic band transport as in traditional inorganic semiconductors. However, no simple *a priori* distinction between these mechanisms can be made in most cases since all mechanisms are active in most organic crystals and dominate over another in different limits. Hopping, for instance, is typically important for higher temperatures (e.g. $T > 100\,\mathrm{K}$ in rubrene and pentacene [Pod13]). Conversely, band transport has been experimentally shown to dominate for highly ordered organic crystals at low temperatures [Sch78, War85, Kar03, Pod13]. Nevertheless, this thesis solely focuses on band transport as one of the possible limits of transport behavior in organic crystals. Still, it allows qualitative insight to which extent changes in the geometric and electronic structure under pressure affect macroscopic equilibrium (charge carrier concentration) and non-equilibrium properties (electrical band conductivity). For anthracene and polyacetylene, we find that changes in band transport due to pressure are predominantly driven by the respective band gap reduction, which enhances the charge carrier concentration exponentially in the intrinsic case. Accordingly, we identify dominant transport directions for intrinsic and doped semiconducting crystals and trace back the behavior of their electrical conductivity under hydrostatic pressure to the changes in the electronic band structure.

Overall, the concepts and methods developed in this thesis are hoped to substantially contribute to our ability to predict and design the electronic and transport properties of organic semiconductors, much beyond the prototypical example systems considered here. These methods may additionally serve as a solid basis to incorporate additional effects that are not yet covered, such as hopping-type transport, electron-phonon coupling, or the impact of defects, all of which play a critical role in the design and manufacture of real organic electronic devices.

The structure of this thesis is as follows: Chapter 2 explains the basic principles of density-functional theory and Chapter 3 discusses the basic concepts on how electronic-structure calculations are performed by the electronic-structure code FHI-aims. Chapter 4 briefly summarizes how we calculate electrical band conductivities using the Boltzmann transport equation in the constant relaxation time approximation. The listing of all relevant total energy contributions in Chapter 3 is the cornerstone for our implementation of the stress tensor discussed in Chapter 5. A full derivation of the analytical strain derivatives is given including a description on how the stress tensor is used to optimize the unit cell of crystal structures under pressure. Chapter 6 is dedicated to the validation of our implementation by extensive benchmark calculations. The organic crystals anthracene and polyacetylene are studied in Chapters 7 and 8, respectively. Their ground state properties (geometry, electronic band structure) are investigated

as well as their behavior under hydrostatic pressure. These investigations include the behavior of macroscopic properties (intrinsic charge carrier concentration and electrical band conductivity) under pressure. Lastly, a summary and an outlook are presented in Chapter 9.

Part I

Theoretical background

2 The many-electron problem and approximations to it

Our goal is to accurately and efficiently compute and predict the properties of materials in an *ab initio* manner by calculating the electronic structure of materials from first principles. This chapter will present the underlying theoretical framework employed in this thesis. This framework includes the fundamental Hamiltonian, the Born-Oppenheimer approximation, the Hohenberg-Kohn theorems, which are the foundation of density-functional theory, and eventually, the Kohn-Sham equations. Furthermore, approximations to the exchange and correlation energy are discussed, which are needed to solve the Kohn-Sham equations in practice. In order to keep the notation concise, explicit spin indices are omitted and atomic units are used (see App. A).

Molecules and materials are a collection of interacting atoms. They can be described as a set of N_{el} electrons and N_{nuc} atomic nuclei, which interact via electrostatic forces. The Hamiltonian of such a system is given by [Mar04, Koh06]

$$\hat{H} = \hat{T}_{\text{el}} + \hat{T}_{\text{nuc}} + \hat{V}_{\text{el-el}} + \hat{V}_{\text{el-nuc}} + \hat{V}_{\text{nuc-nuc}}. \tag{2.1}$$

The individual terms are the kinetic energy operator of the electrons

$$\hat{T}_{\text{el}} = -\frac{1}{2}\sum_{i}^{N_{\text{el}}} \Delta_i, \tag{2.2}$$

the kinetic energy operator of the nuclei

$$\hat{T}_{\text{nuc}} = -\frac{1}{2}\sum_{I}^{N_{\text{nuc}}} \frac{\Delta_I}{M_I}, \tag{2.3}$$

the electron-electron interaction

$$\hat{V}_{\text{el-el}} = \frac{1}{2}\sum_{i}^{N_{\text{el}}}\sum_{j\neq i}^{N_{\text{el}}} \frac{1}{|\boldsymbol{r}_i - \boldsymbol{r}_j|}, \tag{2.4}$$

the electron-nuclear interaction

$$\hat{V}_{\text{el-nuc}} = -\sum_{i}^{N_{\text{el}}}\sum_{I}^{N_{\text{nuc}}} \frac{Z_I}{|\boldsymbol{r}_i - \boldsymbol{R}_I|}, \tag{2.5}$$

and the nuclear-nuclear interaction

$$\hat{V}_{\text{nuc-nuc}} = \frac{1}{2}\sum_{I}^{N_{\text{nuc}}}\sum_{J\neq I}^{N_{\text{nuc}}}\frac{Z_I Z_J}{|\boldsymbol{R}_I - \boldsymbol{R}_J|}. \tag{2.6}$$

The position vectors of electrons and nuclei are denoted by $\boldsymbol{r}_i$ and $\boldsymbol{R}_I$, respectively. The charge of the nuclei Z_I is given in units of the elementary charge and the mass of the nuclei M_I in units of the electron mass. The Laplacian is denoted by Δ. The energy spectrum of the system is then determined by the stationary Schrödinger equation

$$\hat{H}\Psi = E\Psi, \tag{2.7}$$

in which Ψ is the full many-body wave function of the combined electrons-nuclei system and E its energy.

In order to reduce the complexity of the problem, the so-called Born-Oppenheimer approximation is applied. The mass ratio between an electron and a proton is less than 0.1 %. Therefore, it is often assumed that the electrons instantaneously adapt to any movement of the nuclei and thus, adiabatically occupy the respective electronic ground state. This allows a separation of the full many-body wave function Ψ into an electronic and a nuclear part, $\Psi = \psi_{\text{el}}\psi_{\text{nuc}}$. Hence, the Born-Oppenheimer approximation allows to decouple the dynamics of electrons and nuclei and leads to the fundamental equation of electronic-structure theory,

$$\hat{H}_{\text{el}}\psi_{\text{el}} = E_{\text{el}}\psi_{\text{el}}, \tag{2.8}$$

with the electronic Hamiltonian

$$\hat{H}_{\text{el}} = \hat{T}_{\text{el}} + \hat{V}_{\text{el-el}} + \hat{V}_{\text{el-nuc}} + \hat{V}_{\text{nuc-nuc}} \tag{2.9}$$

and the energy of the electronic system E_{el}. Here, the positions of the nuclei enter the equation only parametrically. The corresponding Schrödinger equation for the nuclei is

$$\left[-\frac{1}{2}\sum_{I}^{N_{\text{nuc}}}\frac{\Delta_I}{M_I} + E_{\text{el}}\Big(\{\boldsymbol{R}_I\}\Big)\right]\psi_{\text{nuc}} = E_{\text{nuc}}\psi_{\text{nuc}}, \tag{2.10}$$

and E_{nuc} is the energy of the nuclear system. Accordingly, the solution of Eq. (2.8) for different sets of nuclear positions $\{\boldsymbol{R}_I\}$ provides the potential energy surface on which the nuclei move.

2.1 Density-functional theory and Hohenberg-Kohn theorems

Solving the many-body electronic Schrödinger equation (2.8) requires to determine the N_{el}-electron wave function, which depends on $3N_{\text{el}}$ coordinates. The intriguing

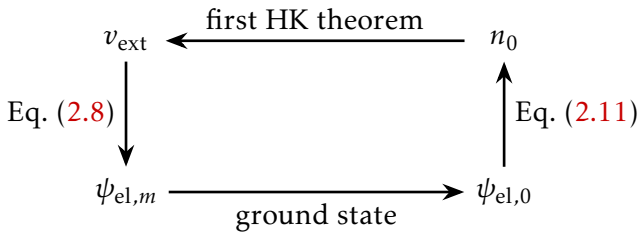

Figure 2.1: Schematic representation of the first Hohenberg-Kohn theorem. Starting from the top left, the external potential v_{ext} fully determines the Hamiltonian $\hat{H}_{\text{el}}$ in Eq. (2.8). The set of electronic many-body wave functions $\psi_{\text{el},m}$ is then obtained by solving the Schrödinger equation. Choosing the ground state wave function yields the ground state density n_0 via Eq. (2.11). At last, the circle is completed by the first HK theorem. It states that the external potential v_{ext} is determined up to a constant by the ground state density n_0.

principles of density-functional theory (DFT) allow to simplify this problem by showing that any ground state property of a system of interacting particles is a functional of the electron ground state density n_0. Thus, it is possible to obtain the ground state energy via a variational principle using only the electron density n, i.e., the probability to find an electron at a given point $\boldsymbol{r}$,

$$n(\boldsymbol{r}) = N_{\text{el}} \int\cdots\int \mathrm{d}\boldsymbol{r}_2 \ldots \mathrm{d}\boldsymbol{r}_{N_{\text{el}}} |\psi_{\text{el}}(\boldsymbol{r}, \boldsymbol{r}_2, \ldots, \boldsymbol{r}_{N_{\text{el}}})|^2. \tag{2.11}$$

This reduces the complexity of the problem considerably since the density depends only on three spatial coordinates and not on $3N_{\text{el}}$ coordinates as the many-body wave function. The fundamental basis of DFT are the two Hohenberg-Kohn (HK) theorems [Hoh64, Mar04].

First Hohenberg-Kohn theorem: *For any system of interacting particles in an external potential v_{ext}, the potential v_{ext} is determined up to a constant by the ground state density n_0.*

The external potential v_{ext} can be any interaction between the system and its surroundings. In our case, it is the interaction between the electrons and nuclei. Together with the external potential, the Hamiltonian describing the system is fully determined up to a constant energy shift. Thus, all ground state properties are determined by the ground state density. Figure 2.1 shows a schematic representation of the first HK theorem.

Second Hohenberg-Kohn theorem: *A universal functional for the energy $E[n]$ in terms of the electron density n can be defined, valid for any external potential v_{ext}. For any particular potential v_{ext}, the exact ground state energy of the system is the global minimum value of this functional, and the density that minimizes the functional is the exact ground state density n_0.*

In the HK scheme, a universal functional means that it does not depend on the external potential, but only on the electron density (and the form of the internal interactions).

Formally, the energy functional is defined as

$$E_{\mathrm{HK}}[n] = F_{\mathrm{HK}}[n] + \int \mathrm{d}\boldsymbol{r}\, v_{\mathrm{ext}}(\boldsymbol{r}) n(\boldsymbol{r}) \tag{2.12}$$

with the HK functional

$$F_{\mathrm{HK}}[n] = T_{\mathrm{el}}[n] + E_{\text{el-el}}[n], \tag{2.13}$$

which includes all internal energies of the interacting system, namely the kinetic energy of the electrons T_{el} and the electron-electron interaction energy $E_{\text{el-el}}$. One important remark is that the HK theorems are only valid for v-representable densities, i.e., densities that are derived from electronic ground states $\psi_{\mathrm{el},0}$ that are solutions of the many-body electronic Schrödinger equation (2.8).

The HK theorems state that the energy of a system is a universal functional of the electron ground state density. However, this statement itself is not helpful in solving the many-electron problem because it does not provide a recipe on how this universal functional can be constructed. In the next section, such a recipe will be presented.

2.2 Kohn-Sham equations

The pioneering work of Kohn[1] and Sham provides a recipe on how to actually calculate the ground state energy. Without their contribution, DFT would not be such a helpful and successful theory in the field of electronic-structure calculations. The main idea of Kohn and Sham was to replace the interacting many-electron system with an auxiliary system that gives the same electron density – and thus the same ground state energy – but is easier to solve. For this purpose, they have used a non-interacting system, which has several advantageous properties.

Auxiliary non-interacting system

For the auxiliary system, the following holds: There is a system of non-interacting electrons embedded in an auxiliary potential v_{aux} whose ground state density is the same as the one of the interacting system, see Fig. 2.2. The Hamiltonian $\hat{H}_{\mathrm{aux}}$ of this system is a sum of single particle Hamiltonians,

$$\hat{H}_{\mathrm{aux}} = \sum_{i}^{N_{\mathrm{el}}} \hat{h}_{\mathrm{aux},i} = \sum_{i}^{N_{\mathrm{el}}} \left[-\frac{\Delta}{2} + \hat{v}_{\mathrm{aux}}(\boldsymbol{r}_i) \right]. \tag{2.14}$$

[1] Walter Kohn was awarded with one half of the 1998 Nobel Prize in Chemistry "for his development of the density-functional theory". The other half was awarded to John A. Pople "for his development of computational methods in quantum chemistry" [Nob98, Koh99, Pop99].

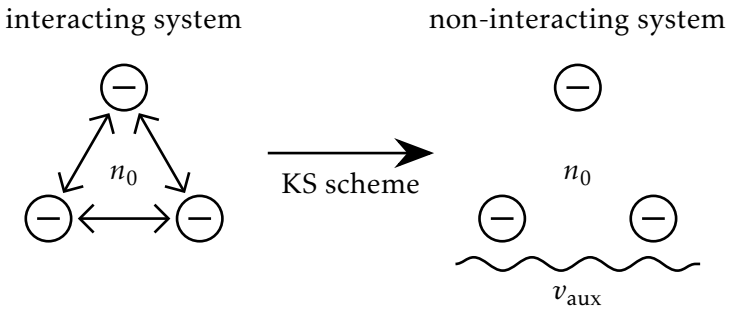

Figure 2.2: Sketch of the main idea of the Kohn-Sham scheme. The system of interacting electrons is replaced by an auxiliary system of non-interacting electrons embedded in an auxiliary potential v_{aux}. The ground state electron density n_0 is the same for both systems.

The single particle orbitals[2] Φ_i are the eigenfunctions of the single particle Hamiltonian $\hat{h}_{\mathrm{aux}}$ with eigenvalues ϵ_i. Hence, the ground state wave function $\psi_{\mathrm{aux},0}$ of the Hamiltonian $\hat{H}_{\mathrm{aux}}$ is the single Slater determinant of N_{el} orbitals Φ_i corresponding to the N_{el} lowest eigenvalues ϵ_i. The Slater determinant is defined as

$$\psi_{\mathrm{aux}}(\boldsymbol{r}_1,\boldsymbol{r}_2,\ldots,\boldsymbol{r}_{N_{\mathrm{el}}}) = \frac{1}{\sqrt{N_{\mathrm{el}}!}}\begin{vmatrix} \Phi_1(\boldsymbol{r}_1) & \Phi_2(\boldsymbol{r}_1) & \cdots & \Phi_{N_{\mathrm{el}}}(\boldsymbol{r}_1) \\ \Phi_1(\boldsymbol{r}_2) & \Phi_2(\boldsymbol{r}_2) & \cdots & \Phi_{N_{\mathrm{el}}}(\boldsymbol{r}_2) \\ \vdots & \vdots & \ddots & \vdots \\ \Phi_1(\boldsymbol{r}_{N_{\mathrm{el}}}) & \Phi_2(\boldsymbol{r}_{N_{\mathrm{el}}}) & \cdots & \Phi_{N_{\mathrm{el}}}(\boldsymbol{r}_{N_{\mathrm{el}}}) \end{vmatrix}, \tag{2.15}$$

which yields a fully antisymmetric wave function under exchange of two electrons and thereby obeys the Pauli principle.

For orthonormalized orbitals, $\langle\Phi_i|\Phi_j\rangle = \delta_{ij}$, the electron density (Eq. (2.11)) of such a wave function is

$$n(\boldsymbol{r}) = \sum_i f_i|\Phi_i(\boldsymbol{r})|^2. \tag{2.16}$$

Here, the usual bra-ket notation was used for the inner product in Hilbert space, which corresponds to an integral in real space,

$$\langle\Phi_i|\hat{O}|\Phi_j\rangle = \int \mathrm{d}\boldsymbol{r}\,\Phi_i^*(\boldsymbol{r})\hat{O}\Phi_j(\boldsymbol{r}), \tag{2.17}$$

$\hat{O}$ being an arbitrary operator. The occupation numbers f_i determine how many electrons are located in orbital Φ_i. In the electronic ground state, they are one for the orbitals that correspond to the N_{el} lowest eigenvalues ϵ_i and zero otherwise so that the kinetic energy

[2] The term orbital is used here instead of wave function because the Φ_i are one-electron functions.

of the non-interacting system T_s is given by

$$T_s = -\frac{1}{2}\sum_i f_i \langle \Phi_i | \Delta | \Phi_i \rangle. \tag{2.18}$$

In classical electrostatics, the Coulomb interaction between the electron density n and itself is given by the Hartree energy[3]

$$E_H = \frac{1}{2}\iint \mathrm{d}\boldsymbol{r}\,\mathrm{d}\tilde{\boldsymbol{r}}\,\frac{n(\boldsymbol{r})n(\tilde{\boldsymbol{r}})}{|\boldsymbol{r}-\tilde{\boldsymbol{r}}|}. \tag{2.19}$$

Mapping of Kohn-Sham

The HK theorems state that the ground state energy of the above described non-interacting auxiliary system is equal to the ground state energy of the interacting system, if they have the same ground state density. Accordingly, the Kohn-Sham (KS) approach provides a mapping between the fully interacting system and an auxiliary non-interacting system with exactly the same ground state density. Although there is no general proof that such a system of non-interacting particles always exists, this assumption seems to be justified in many cases in practice [Mar04].

In the KS approach, the HK energy functional (Eq. (2.12)) of the interacting system is rewritten in the following way:

$$\begin{aligned} E_{KS}[n] &= T_s[n] + E_H[n] + \int \mathrm{d}\boldsymbol{r}\, v_{ext}(\boldsymbol{r})n(\boldsymbol{r}) + \underbrace{\Big(T_{el}[n] - T_s[n]\Big) + \Big(E_{el\text{-}el}[n] - E_H[n]\Big)}_{} \\ &= T_s[n] + E_H[n] + \int \mathrm{d}\boldsymbol{r}\, v_{ext}(\boldsymbol{r})n(\boldsymbol{r}) + \qquad\qquad E_{xc}[n]. \end{aligned} \tag{2.20}$$

Formally, the kinetic energy T_s as given in Eq. (2.18) is indeed a functional of the electron density n since the single particle orbitals Φ_i are functionals of the density as well. However, no explicit and exact expression for the kinetic energy T_s in terms of the density is known. Therefore, T_s must be explicitly expressed in terms of the orbitals, which removes some of the elegance of the HK theorems. All energy contributions that are not accounted for by T_s and E_H in Eq. (2.20) are subsumed in the exchange-correlation functional E_{xc}. The first parenthesis denotes the difference between the kinetic energy of the interacting and of the non-interacting system. This difference is non-zero due to the correlation of interacting electrons. The second parenthesis is the energy contribution of the electron-electron interaction due to the quantum nature of the electrons. Accordingly, all complex interactions of the many-electron system are condensed into the exchange-correlation functional E_{xc}.

[3] Treating the electron-electron interactions fully quantum mechanically gives rise to the non-classical exchange term.

Finding the ground state electron density

In order to find the solution for the ground state electron density, the KS energy functional in Eq. (2.20) has to be minimized with respect to the electron density n. Because the kinetic energy of the non-interacting system T_s is only explicitly known in terms of the single particle orbitals Φ_i, the minimization has to be done with respect to the orbitals. Minimizing with respect to the orbitals is equivalent to minimizing with respect to the density since varying the orbitals over the space of continuous functions covers all allowed densities for the KS energy functional E_KS [Par89]. The single particle orbitals are constrained to be orthonormalized, $\langle\Phi_i|\Phi_j\rangle = \delta_{ij}$, and this constraint is equivalent to the conservation of numbers of electrons under consideration of Eq. (2.16) since

$$\int \mathrm{d}\boldsymbol{r}\, n(\boldsymbol{r}) = \sum_i f_i \int \mathrm{d}\boldsymbol{r}\, |\Phi_i(\boldsymbol{r})|^2 = \sum_i^{N_\mathrm{el}} 1 = N_\mathrm{el}. \tag{2.21}$$

Using the Lagrange multipliers ϵ_i, the Lagrange function L corresponding to this optimization problem is given by

$$L[\{\Phi_i\}] = E_\mathrm{KS}[\{\Phi_i\}] - \sum_i f_i \epsilon_i \Big(\langle\Phi_i|\Phi_i\rangle - 1\Big). \tag{2.22}$$

The KS energy E_KS is also a functional of the single particle orbitals Φ_i since the electron density n and orbitals are linked via Eq. (2.16). This means that the total ground state energy E_tot of the system, i.e., a system of interacting electrons coupled electrostatically to interacting nuclei, is

$$E_\mathrm{tot} = \min_{\{\Phi_i\}} \left[E_\mathrm{KS}[\{\Phi_i\}] - \sum_i f_i \epsilon_i \Big(\langle\Phi_i|\Phi_i\rangle - 1\Big) \right] + E_\text{nuc-nuc} \tag{2.23}$$

with the nuclear-nuclear interaction energy

$$E_\text{nuc-nuc} = \frac{1}{2} \sum_I^{N_\mathrm{nuc}} \sum_{J\neq I}^{N_\mathrm{nuc}} \frac{Z_I Z_J}{|\boldsymbol{R}_I - \boldsymbol{R}_J|}. \tag{2.24}$$

The set of single particle orbitals Φ_i that minimizes the Lagrange function L can be obtained by taking the functional derivative with respect to the orbitals and setting it to zero,

$$\frac{\delta L}{\delta \Phi_i^*} = \frac{\delta T_\mathrm{s}}{\delta \Phi_i^*} + \left[\frac{\delta E_\mathrm{ext}}{\delta n} + \frac{\delta E_\mathrm{H}}{\delta n} + \frac{\delta E_\mathrm{xc}}{\delta n} \right] \frac{\delta n}{\delta \Phi_i^*} - \epsilon_i \Phi_i = 0 \tag{2.25}$$

with $E_\mathrm{ext} = \int \mathrm{d}\boldsymbol{r}\, v_\mathrm{ext}(\boldsymbol{r}) n(\boldsymbol{r})$. The chain rule was used to reintroduce the functional derivative with respect to the electron density n. Evaluating the individual derivatives yields the KS equations [Koh65]

$$\hat{h}_\mathrm{KS} \Phi_i = \epsilon_i \Phi_i \tag{2.26}$$

with the KS Hamiltonian

$$\hat{h}_{\mathrm{KS}} = -\frac{\Delta}{2} + \hat{v}_{\mathrm{ext}} + \hat{v}_{\mathrm{H}} + \hat{v}_{\mathrm{xc}}, \tag{2.27}$$

the external potential (interaction with nuclei)

$$\hat{v}_{\mathrm{ext}} = -\sum_{I}^{N_{\mathrm{nuc}}} \frac{Z_I}{|\boldsymbol{r} - \boldsymbol{R}_I|}, \tag{2.28}$$

the Hartree potential

$$\hat{v}_{\mathrm{H}} = \int \mathrm{d}\tilde{\boldsymbol{r}}\, \frac{n(\tilde{\boldsymbol{r}})}{|\boldsymbol{r} - \tilde{\boldsymbol{r}}|}, \tag{2.29}$$

and the exchange-correlation potential

$$\hat{v}_{\mathrm{xc}} = \frac{\delta E_{\mathrm{xc}}[n]}{\delta n}. \tag{2.30}$$

In the context of the KS formalism, the Φ_i are called KS orbitals and the ϵ_i KS eigenvalues. The ground state density is then given in terms of the KS orbitals by Eq. (2.16). By comparing Eq. (2.14) with Eq. (2.27), it can be seen that the auxiliary potential v_{aux} of the auxiliary system is given by $v_{\mathrm{aux}} = v_{\mathrm{ext}} + v_{\mathrm{H}} + v_{\mathrm{xc}}$. It is important to note that the KS equations are exact within the Born-Oppenheimer approximation. The only formal constraint is that such an auxiliary system has to exist as explained above.

Two obstacles remain that complicate the solving of the KS equations in practice. Firstly, the Hartree potential v_{H} and the exchange-correlation potential v_{xc} depend on the electron density n (Eqs. (2.29) and (2.30)), which in turn depends on the KS orbitals Φ_i (Eq. (2.16)), which depend on the aforementioned potentials (Eq. (2.26)). Hence, the KS equations have to be solved in a self-consistent manner. Secondly, no explicit expression for the exact exchange-correlation functional E_{xc} is known so that approximations are needed. A selection of common approximate exchange-correlation functionals is discussed in the next section.

The KS orbitals Φ_i and the KS eigenvalues ϵ_i are a mathematical result of the minimization of the KS energy E_{KS}. Accordingly, the actual total energy of the system E_{tot} is not just a sum of the single particle energies $\sum_i \epsilon_i$ (see Sec. 3.6). Therefore, their physical meaning is limited. A detailed discussion about their meaning can be found in Refs. [Alm85, Koh96, Mar04, Koh06] and references therein. Nevertheless, the KS eigenvalues usually give a reasonable first approximation to the energy levels of the interacting system.

In summary, the KS equations present a recipe on how to obtain the electron ground state density by means of the KS orbitals and Eq. (2.16). Consequently, this determines the total ground state energy E_{tot} via Eq. (2.23). This was achieved by replacing the highly complex initial system of interacting electrons with a system of non-interacting electrons

under the utilization of the HK theorems. However, the KS scheme reintroduced wave functions in DFT through the kinetic energy of non-interacting electrons (Eq. (2.18)) and therefore, the $3N_{\mathrm{el}}$ degrees of freedom of the electrons appear in the formalism. Of course, the huge advantage of using wave functions is that the kinetic energy of non-interacting electrons, the major part of the full kinetic energy, is exact [Par89].

2.3 Approximations to exchange and correlation energy

The KS equations provide a procedure to obtain the exact ground state energy and density of the many-electron system. No explicit expression for the universal, exact exchange-correlation functional E_{xc} is known, though, so that approximations are needed. These approximations are usually called exchange-correlation functionals, too.

In general, the exchange-correlation energy is small compared to the total energy because most of the physics is already captured by the kinetic energy of non-interacting electrons and the Hartree energy, see Eq. (2.20). Hence, already relatively simple approximations often give reasonable results. However, this is not always the case (see Chap. 8) so that the employed approximate exchange-correlation functionals need to be validated against higher-order methods to enable predictive calculations. In the following, a selection of common density-functional approximations (DFAs) is briefly presented. More in-depth discussions can be found in Refs. [Mar04, Koh06, Coh12].

It is convenient to split the exchange-correlation energy E_{xc} into an exchange (E_{x}) and a correlation part (E_{c}), $E_{\mathrm{xc}} = E_{\mathrm{x}} + E_{\mathrm{c}}$ [Per03]. The exchange part is typically defined as

$$E_{\mathrm{x}}[n] = \langle \psi_{\mathrm{aux},0} | \hat{V}_{\text{el-el}} | \psi_{\mathrm{aux},0} \rangle - E_{\mathrm{H}}[n] \tag{2.31}$$

using the ground state wave function $\psi_{\mathrm{aux},0}$ of the KS auxiliary system defined in Eq. (2.15). The correlation part is the missing rest, namely,

$$\begin{aligned} E_{\mathrm{c}}[n] &= E_{\mathrm{xc}}[n] - E_{\mathrm{x}}[n] \\ &= \langle \psi_{\mathrm{el},0} | \hat{T}_{\mathrm{el}} + \hat{V}_{\text{el-el}} | \psi_{\mathrm{el},0} \rangle - \langle \psi_{\mathrm{aux},0} | \hat{T}_{\mathrm{el}} + \hat{V}_{\text{el-el}} | \psi_{\mathrm{aux},0} \rangle . \end{aligned} \tag{2.32}$$

2.3.1 Local-density approximation

The main idea of the local-density approximation (LDA) is that in a first order approximation the electron density n can be assumed as locally constant, i.e., that the inhomogeneous electron system can be treated as a locally homogeneous electron gas. Under this assumption, the exchange-correlation energy E_{xc} can be written as a weighted spatial average of the exchange-correlation energy per electron ϵ_{xc},

$$E_{\mathrm{xc}}^{\mathrm{LDA}}[n] = \int \mathrm{d}\boldsymbol{r}\, n(\boldsymbol{r}) \epsilon_{\mathrm{xc}}^{\mathrm{LDA}}\big(n(\boldsymbol{r})\big). \tag{2.33}$$

For every point in space, $\epsilon_{\mathrm{xc}}^{\mathrm{LDA}}(n)$ is the respective value for a homogeneous electron gas with density n. The exchange part $\epsilon_{\mathrm{x}}^{\mathrm{LDA}}$ is known exactly [Dir30],

$$\epsilon_{\mathrm{x}}^{\mathrm{LDA}}(n) = -\frac{3}{4}\left(\frac{3}{\pi}\right)^{1/3} n^{1/3}, \tag{2.34}$$

whereas the explicit form of the correlation part ϵ_{c} is unknown. Only its low- and high-density limits are known from the work of Wigner and of Gell-Mann and Brueckner, respectively [Mar04]. Therefore, accurate parametrizations of $\epsilon_{\mathrm{c}} = \epsilon_{\mathrm{xc}} - \epsilon_{\mathrm{x}}$ for intermediate densities were introduced on the basis of quantum Monte Carlo calculations [Cep80]. Amongst others, there exist parametrizations by Vosko, Wilk, and Nusair [Vos80], Perdew and Zunger [Per81], and Perdew and Wang [Per92].

The LDA exchange-correlation potential can be derived using Eqs. (2.30) and (2.33) and is given by

$$\hat{v}_{\mathrm{xc}}^{\mathrm{LDA}}(n) = \epsilon_{\mathrm{xc}}^{\mathrm{LDA}}(n) + n\frac{\partial \epsilon_{\mathrm{xc}}^{\mathrm{LDA}}(n)}{\partial n}. \tag{2.35}$$

2.3.2 Generalized gradient approximation

In order to treat inhomogeneities of the electron density n more accurately, the gradient of the density ∇n is taken into account in the generalized gradient approximation (GGA) of the exchange-correlation energy,

$$E_{\mathrm{xc}}^{\mathrm{GGA}}[n] = \int \mathrm{d}\boldsymbol{r}\, n(\boldsymbol{r}) \epsilon_{\mathrm{xc}}^{\mathrm{GGA}}\Big(n(\boldsymbol{r}), \nabla n(\boldsymbol{r})\Big). \tag{2.36}$$

The GGA is called a semi-local functional because it depends on the density gradient ∇n. There is no unique choice for $\epsilon_{\mathrm{xc}}^{\mathrm{GGA}}$ so that two different approaches exist in practice [Koh06]: 1) Deriving a functional form and parameters that satisfy as many formal properties (e.g., asymptotic behavior) as possible, e.g., as done by Perdew, Burke, and Ernzerhof (PBE) [Per96a], 2) fitting the parameters of a certain functional form to experimental data, e.g., as done by Becke, Lee, Yang, and Parr (BLYP) [Bec88a, Lee88].

In the physical community, the probably most used GGA functional is PBE [Per96a]. Its general form is given by

$$\epsilon_{\mathrm{xc}}^{\mathrm{GGA}}\Big(n(\boldsymbol{r}), \nabla n(\boldsymbol{r})\Big) = \epsilon_{\mathrm{xc}}^{\mathrm{LDA}}\Big(n(\boldsymbol{r})\Big) F_{\mathrm{xc}}\Big(n(\boldsymbol{r}), \nabla n(\boldsymbol{r})\Big). \tag{2.37}$$

The function F_{xc} is called enhancement factor and modifies the LDA exchange-correlation energy per electron $\epsilon_{\mathrm{xc}}^{\mathrm{LDA}}$ to account for the density gradient at the considered point. There have been many modifications to the PBE functional, e.g., revPBE [Zha98], RPBE [Ham99], PBEsol [Per08], PBEint [Fab10]; different GGA functionals such as AM05[4] [Arm05] have been proposed as well.

[4] The '05' in AM05 stands for the year of publication.

The exchange-correlation potential of GGA can be derived in the same fashion as in the LDA case but an additional term appears due to the density gradient

$$\begin{aligned} \hat{v}_{\mathrm{xc}}^{\mathrm{GGA}}(n,\nabla n) &= \epsilon_{\mathrm{xc}}^{\mathrm{GGA}}(n,\nabla n) + n\frac{\partial \epsilon_{\mathrm{xc}}^{\mathrm{GGA}}(n,\nabla n)}{\partial n} - \nabla\left(n\frac{\partial \epsilon_{\mathrm{xc}}^{\mathrm{GGA}}(n,\nabla n)}{\partial(\nabla n)}\right) \\ &= \epsilon_{\mathrm{xc}}^{\mathrm{GGA}}(n,\nabla n) + n\frac{\partial \epsilon_{\mathrm{xc}}^{\mathrm{GGA}}(n,\nabla n)}{\partial n} - 2\nabla\left(n(\nabla n)\frac{\partial \epsilon_{\mathrm{xc}}^{\mathrm{GGA}}(n,\nabla n)}{\partial|\nabla n|^2}\right). \end{aligned} \tag{2.38}$$

Here, the squared absolute value of the density $|\nabla n|^2$ was introduced since $\epsilon_{\mathrm{xc}}^{\mathrm{GGA}}$ only depends on the magnitude of the gradient $\left(\frac{\partial|\nabla n|^2}{\partial(\nabla n)} = 2\nabla n\right)$.

A step beyond the GGA functionals are the so-called meta-GGA functionals. These approximate functionals additionally include the second derivative of the electron density (kinetic energy density) of the KS orbitals [Per99, Sun15].

2.3.3 Hybrid functionals

Hybrid functionals are a further advance in approximating the universal, exact exchange-correlation functional. The initial idea was derived by Becke [Bec93a] using the adiabatic connection for the KS formalism [Har84]. In hybrid functionals, a DFA (LDA or GGA) is mixed with the Hartree-Fock (HF) exchange $E_{\mathrm{x}}^{\mathrm{HF}}$, the so-called exact exchange, which is defined as [Mar04, Koh06]

$$E_{\mathrm{x}}^{\mathrm{HF}} = -\frac{1}{2}\sum_{ij} f_i f_j \iint \mathrm{d}\boldsymbol{r}\,\mathrm{d}\tilde{\boldsymbol{r}}\,\frac{\Phi_i^*(\boldsymbol{r})\Phi_j(\boldsymbol{r})\Phi_j^*(\tilde{\boldsymbol{r}})\Phi_i(\tilde{\boldsymbol{r}})}{|\boldsymbol{r}-\tilde{\boldsymbol{r}}|}. \tag{2.39}$$

This expression is exact for wave functions that are a single Slater determinant. In DFT, the HF exchange is evaluated using the KS orbitals Φ_i. The HF exchange is non-local since its corresponding potential depends both on $\boldsymbol{r}$ and $\tilde{\boldsymbol{r}}$. Its explicit form will be presented below. Furthermore, the exchange in hybrid functionals is

$$E_{\mathrm{x}}^{\mathrm{hyb}}(\alpha) = \alpha E_{\mathrm{x}}^{\mathrm{HF}} + (1-\alpha)E_{\mathrm{x}}^{\mathrm{DFA}} \tag{2.40}$$

with the real-valued parameter $\alpha \in [0,1]$ determining the amount of HF exchange added. The value for α may be obtained by fitting to experimental data or by theoretical considerations. In general, the value of α can be system dependent [Mar11] and there are efforts to obtain it in an *ab initio* manner [Ric13, Ata13b].

Hybrid functionals typically reduce the so-called self-interaction error. The Hartree energy E_{H} (Eq. (2.19)) describes the classical Coulomb interaction between the electron density n and itself and thus includes the unphysical interaction of an electron with itself. This spurious interaction is called self-interaction [Per81] and is canceled in the exact exchange-correlation functional, but not in most of the approximate exchange-

correlation functionals, e.g., LDA and GGA. In HF theory, however, the diagonal terms ($i = j$) of the HF exchange (Eq. (2.39)) cancel exactly the one-electron self-interaction of the Hartree energy and thus the spurious one-electron self-interaction. Hence, including a fraction of HF exchange partially cures the self-interaction error of DFA.

One popular hybrid functional is the PBE0[5] functional [Per96b], which uses the PBE functional as DFA and $\alpha = 1/4$,

$$E_{\mathrm{xc}}^{\mathrm{PBE0}} = E_{\mathrm{xc}}^{\mathrm{PBE}} + \tfrac{1}{4}\left(E_{\mathrm{x}}^{\mathrm{HF}} - E_{\mathrm{x}}^{\mathrm{PBE}}\right). \tag{2.41}$$

Another widely used hybrid functional, especially in the chemical community, is the B3LYP functional [Bec93b, Ste94]. It employs three parameters[6] α_0, α_{x}, and α_{c}, which are fitted to experimental data,

$$E_{\mathrm{xc}}^{\mathrm{B3LYP}} = (1-\alpha_0)E_{\mathrm{x}}^{\mathrm{LDA}} + \alpha_0 E_{\mathrm{x}}^{\mathrm{HF}} + \alpha_{\mathrm{x}}\Delta E_{\mathrm{x}}^{\mathrm{B88}} + (1-\alpha_{\mathrm{c}})E_{\mathrm{c}}^{\mathrm{VWN}} + \alpha_{\mathrm{c}}E_{\mathrm{c}}^{\mathrm{LYP}} \tag{2.42}$$

with

$$\alpha_0 = 0.20, \quad \alpha_{\mathrm{x}} = 0.72, \quad \alpha_{\mathrm{c}} = 0.81. \tag{2.43}$$

Here, $\Delta E_{\mathrm{x}}^{\mathrm{B88}}$ is the gradient correction of the LDA exchange by Becke [Bec88a], $E_{\mathrm{c}}^{\mathrm{VWN}}$ the parametrization of the LDA correlation by Vosko, Wilk, and Nusair [Vos80], and $E_{\mathrm{c}}^{\mathrm{LYP}}$ the GGA correlation by Lee, Yang, and Parr [Lee88].

Since the HF exchange is orbital dependent, the functional derivative of the exchange-correlation functional E_{xc} with respect to the electron density n in Eq. (2.25) has to be modified. The HF exchange part of E_{xc} must be differentiated separately with respect to the KS orbitals Φ_i (analogously to the kinetic energy of non-interacting electrons T_{s}). This leads to a modified KS equation

$$\left(-\frac{\Delta}{2} + \hat{v}_{\mathrm{ext}}(\boldsymbol{r}) + \hat{v}_{\mathrm{H}}(\boldsymbol{r}) + \hat{v}_{\mathrm{xc}}^{\mathrm{DFA}}(\boldsymbol{r},\alpha)\right)\Phi_i(\boldsymbol{r}) + \alpha \int \mathrm{d}\tilde{\boldsymbol{r}}\, \hat{v}_{\mathrm{x}}^{\mathrm{HF}}(\boldsymbol{r},\tilde{\boldsymbol{r}})\Phi_i(\tilde{\boldsymbol{r}}) = \epsilon_i \Phi_i(\boldsymbol{r}) \tag{2.44}$$

with the α-dependent DFA exchange-correlation potential

$$\hat{v}_{\mathrm{xc}}^{\mathrm{DFA}}(\boldsymbol{r},\alpha) = \hat{v}_{\mathrm{xc}}^{\mathrm{DFA}}(\boldsymbol{r}) - \alpha \hat{v}_{\mathrm{x}}^{\mathrm{DFA}}(\boldsymbol{r}) \tag{2.45}$$

and the non-local HF exchange potential

$$\hat{v}_{\mathrm{x}}^{\mathrm{HF}}(\boldsymbol{r},\tilde{\boldsymbol{r}}) = -\sum_j f_j \frac{\Phi_j(\boldsymbol{r})\Phi_j^*(\tilde{\boldsymbol{r}})}{|\boldsymbol{r}-\tilde{\boldsymbol{r}}|}. \tag{2.46}$$

The external potential v_{ext}, the Hartree potential v_{H} and the DFA exchange-correlation potential $v_{\mathrm{xc}}^{\mathrm{DFA}}$ are given in Eqs. (2.28), (2.29), and (2.30), respectively. The potential

[5] The '0' in PBE0 stands for zero parameters in the functional.
[6] The '3' in B3LYP stands for these three parameters.

of the exchange part v_x^{DFA} follows from Eq. (2.30), too, by using the exchange E_x^{DFA} instead of the full exchange-correlation E_{xc}^{DFA}. Equation (2.44) is also called generalized Kohn-Sham equation [Sei96] and must be solved in a self-consistent manner as the normal KS equations.

2.3.4 Screened hybrid functionals

One property of the HF exchange is that it is an integral over the Coulomb interaction $1/|\boldsymbol{r}-\tilde{\boldsymbol{r}}|$, which is long ranged. However, the Coulomb interaction is screened in large systems and solids. In order to incorporate this[7], a range separation of the Coulomb interaction into a long-range (LR) and short-range (SR) part is introduced with the help of the error function

$$\frac{1}{|\boldsymbol{r}-\tilde{\boldsymbol{r}}|} = \underbrace{\frac{\operatorname{erfc}(\omega|\boldsymbol{r}-\tilde{\boldsymbol{r}}|)}{|\boldsymbol{r}-\tilde{\boldsymbol{r}}|}}_{\text{SR}} + \underbrace{\frac{\operatorname{erf}(\omega|\boldsymbol{r}-\tilde{\boldsymbol{r}}|)}{|\boldsymbol{r}-\tilde{\boldsymbol{r}}|}}_{\text{LR}} \tag{2.47}$$

with the real-valued screening parameter $\omega \geq 0$, also called inverse screening length. The higher the value of ω is, the stronger is the screening. Equation (2.40) is now modified in such a way that the DFA exchange is replaced by the HF exchange only in the short-range region,

$$E_x^{\text{scr.hyb}}(\alpha,\omega) = \alpha E_x^{HF,SR}(\omega) + (1-\alpha)E_x^{DFA,SR}(\omega) + E_x^{DFA,LR}(\omega). \tag{2.48}$$

A popular screened hybrid functional is HSE06[8] by Heyd, Scuseria, and Ernzerhof (HSE) [Hey03, Hey06, Kru06]. This functional employs PBE for the DFA part, $\alpha = 1/4$ as PBE0, and $\omega = 0.11\,\text{bohr}^{-1}$, which was determined by fitting to experimental data. In principle, the screening parameter ω should be determined system dependent just as α and there are approaches doing this in an *ab initio* manner [Ste10].

As for the hybrid functionals in the previous section, the KS orbitals for screened hybrid functionals are determined by the generalized Kohn-Sham equation (2.44). The only change is that the DFA exchange-correlation potential and the HF exchange potential become ω-dependent,

$$\hat{v}_{xc}^{DFA}(\boldsymbol{r},\alpha,\omega) = v_{xc}^{DFA}(\boldsymbol{r}) - \alpha\hat{v}_x^{DFA,SR}(\boldsymbol{r},\omega) \tag{2.49}$$

$$\hat{v}_x^{HF}(\boldsymbol{r},\tilde{\boldsymbol{r}},\omega) = \sum_j f_j \frac{\operatorname{erf}(\omega|\boldsymbol{r}-\tilde{\boldsymbol{r}}|)\Phi_j(\boldsymbol{r})\Phi_j^*(\tilde{\boldsymbol{r}})}{|\boldsymbol{r}-\tilde{\boldsymbol{r}}|}. \tag{2.50}$$

2.3.5 Functional families

In the previous sections, many different functionals approximating the exchange-correlation energy were introduced. Some of them can be summarized in a unified picture, the

[7] The screening also reduces the computational effort [Hey03].
[8] The '06' in HSE06 stands for the year of publication.

HSE family of functionals. The functionals of this family are characterized by the two parameters α (amount of added HF exchange) and ω (screening parameter of Coulomb interaction) and are denoted with HSE(α, ω). The HSE(α, ω) functional has the following exchange-correlation energy expression:

$$E_{\mathrm{xc}}^{\mathrm{HSE}}(\alpha,\omega) = E_{\mathrm{xc}}^{\mathrm{PBE}} + \alpha\Big(E_{\mathrm{x}}^{\mathrm{HF,SR}}(\omega) - E_{\mathrm{x}}^{\mathrm{PBE,SR}}(\omega)\Big), \quad \alpha \in [0,1], \quad \omega \geq 0. \tag{2.51}$$

The following DFAs are special elements of the HSE family and were presented in the previous sections:

$$\mathrm{HSE06} = \mathrm{HSE}\Big(\tfrac{1}{4}, 0.11\,\mathrm{bohr}^{-1}\Big) \tag{2.52}$$

$$\mathrm{PBE0} = \mathrm{HSE}\Big(\tfrac{1}{4}, 0\Big) \tag{2.53}$$

$$\mathrm{PBE} = \mathrm{HSE}(0,\omega). \tag{2.54}$$

The PBE functional has no added HF exchange ($\alpha = 0$) and thus, no dependence on ω. This means that the value of ω in Eq. (2.54) is irrelevant and is only kept for formal reasons.

2.3.6 Van der Waals corrections

All DFAs presented so far lack long-range van der Waals (vdW) interactions (dispersion) [Pér95]. Please note that there exist various definitions of the vdW interactions. In this thesis, we define it as the interaction between fluctuating multipoles. The vdW interactions arise from the correlated movement of electrons and there are three main approaches to incorporate them in DFT calculations: 1) Adding explicitly the leading $1/R^6$ vdW energy term with semi-empirical parameters to the exchange-correlation energy [Ahl77, Wu02, Gri04, Tka09], 2) constructing approximate exchange-correlation functionals that include a non-local correlation energy [And96, Dio04, Vyd08, Lee10], 3) using the random phase approximation for the correlation energy [Boh53, Ren12b].

In this thesis, we will concentrate on the first approach. This means the vdW energy E_{vdW} is explicitly added to the exchange-correlation energy $E_{\mathrm{xc}}^{\mathrm{DFA}}$ obtained from a DFA,

$$E_{\mathrm{xc}}^{\mathrm{DFA+vdW}} = E_{\mathrm{xc}}^{\mathrm{DFA}} + E_{\mathrm{vdW}}. \tag{2.55}$$

For the formulation of the vdW energy, we use the scheme by Tkatchenko-Scheffler (TS) [Tka09]. Like in other methods [Ahl77, Wu02, Gri04], the vdW energy E_{vdW} is written as a sum over all pairwise interatomic interactions between atoms I and J. In first order, the vdW interaction has a $1/R^6$ decay,

$$E_{\mathrm{vdW}} = -\frac{1}{2}\sum_{I}^{N_{\mathrm{nuc}}}\sum_{J\neq I}^{N_{\mathrm{nuc}}} f_{\mathrm{damp}}(\boldsymbol{R}_I,\boldsymbol{R}_J)\frac{C_{6IJ}}{|\boldsymbol{R}_I - \boldsymbol{R}_J|^6}. \tag{2.56}$$

The isotropic C_{6IJ} coefficients contain the information about the vdW interaction between atom I and J. The damping function f_{damp} helps to avoid singularities at close distances and double counting of correlation effects at intermediate ranges that are already included in the DFA.

An advantage of the TS scheme is that the heteronuclear C_{6IJ} coefficients do not have fixed empirical values, but that they are determined in each calculation from the ground state electron density n. Therefore, the C_{6IJ} coefficients reflect the chemical environment of atoms I and J. In general, they are given by

$$C_{6IJ}[n] = \frac{2C_{6II}[n]C_{6JJ}[n]}{\frac{\alpha_J^0}{\alpha_I^0}C_{6II}[n] + \frac{\alpha_I^0}{\alpha_J^0}C_{6JJ}[n]} \tag{2.57}$$

with the homonuclear C_{6II} coefficient and the static polarizability α_I^0 of atom I. The homonuclear C_{6II} coefficient is linked to the C_{6II}^{free} coefficient of the free isolated atom via the volume V_I of the atom in the molecule or solid and the volume V_I^{free} of the free atom by

$$C_{6II}[n] = C_{6II}^{\text{free}}\left(\frac{V_I[n]}{V_I^{\text{free}}}\right)^2. \tag{2.58}$$

The volume of the free atom V_I^{free} is defined as a volume integral weighted by the electron density of the free atom n_I^{free} [Joh05],

$$V_I^{\text{free}} = \int \mathrm{d}\boldsymbol{r}\,|\boldsymbol{r}|^3 n_I^{\text{free}}(\boldsymbol{r}). \tag{2.59}$$

In order to obtain the volume of an atom in a molecule or solid, the so-called Hirshfeld partitioning [Hir77] is employed. It allows to partition the electron density n of the system into atomic contributions with the help of a partitioning scheme p_I,

$$V_I[n] = \int \mathrm{d}\boldsymbol{r}\,|\boldsymbol{r}|^3 p_I(\boldsymbol{r})n(\boldsymbol{r}) \quad \text{with} \quad p_I(\boldsymbol{r}) = \frac{n_I^{\text{free}}(\boldsymbol{r})}{\sum_J^{N_{\text{nuc}}} n_J^{\text{free}}(\boldsymbol{r})}. \tag{2.60}$$

The values for the C_6^{free} coefficients and the static polarizabilities α^0 are taken from tabulated reference data [Chu04].

In principle, the functional form of f_{damp} can be choosen freely as long as it becomes zero at close ranges and one at long ranges. In the TS scheme, a Fermi-type function was chosen,

$$f_{\text{damp}}(\boldsymbol{R}_I, \boldsymbol{R}_J) = \frac{1}{1 + \exp\left[-d\left(\frac{|\boldsymbol{R}_I - \boldsymbol{R}_J|}{s_R\left(R_I^{\text{vdW}}[n] + R_J^{\text{vdW}}[n]\right)} - 1\right)\right]}. \tag{2.61}$$

R_I^{vdW} is the vdW radius of atom I in the molecule or solid and depends on the electron density n. d and s_{R} are parameters. The vdW radius R_I^{vdW} is linked to the vdW radius of the free atom $R_I^{\mathrm{vdW,free}}$ via the atomic volumes,

$$R_I^{\mathrm{vdW}}[n] = R_I^{\mathrm{vdW,free}} \left(\frac{V_I[n]}{V_I^{\mathrm{free}}} \right)^{1/3} . \tag{2.62}$$

The free atom vdW radius is derived from the vdW radius of noble gases. The steepness of the damping function is determined by d and a value of $d = 20$ is chosen. The vdW energy depends only slightly on the choice of d [Tka09]. The parameter s_{R} controls the onset of the vdW correction and depends on the underlying DFA. It is determined for each DFA by fitting to the S22 database that consists of binding energies for 22 pairs of small molecules [Jur06]. The so determined values of s_{R} are in the range around one.

It is important to note that in the TS scheme the contribution of the vdW energy E_{vdW} to the exchange-correlation potential $\hat{v}_{\mathrm{xc}}$ (Eq. (2.30)) via its functional derivative with respect to the electron density n is neglected. Hence, the vdW correction does not enter the KS equations (2.26). This means that after the KS equations are solved self-consistently with a DFA and the ground state electron density is obtained, the vdW energy of Eq. (2.56) is added to the total energy. Thus, this method can be seen as a post-processing step after a DFT calculation. A shortcoming of the TS scheme is that it includes only pairwise interatomic interactions and lacks the description of long-range electrodynamic response, e.g., screening. This response becomes crucial for large systems and there exists an extension to the TS scheme for finite-gap systems in order to include them [Tka12, Amb14].

3 Solving the Kohn-Sham equations with FHI-aims

While the previous chapter has outlined the theoretical framework of DFT and KS approach, this chapter discusses the numerical techniques used to solve the KS equations in a computer code. In this thesis, we focus on the Fritz Haber Institute *ab initio* molecular simulations (FHI-aims) package [Blu09] for our electronic-structure calculations. FHI-aims is an all-electron electronic-structure code, i.e., each electron is treated at the same level of theory. Accordingly, core electrons are taken into account in an explicit fashion in contrast to the approximate approach of pseudopotential methods.

This chapter is dedicated to briefly review the underlying principles of FHI-aims, which includes the discussion of the used basis functions, the numerical integration scheme, and the treatment of periodic systems. Additionally, we present in detail how the total energy is calculated in FHI-aims. This will be the cornerstone for our implementation of the stress tensor discussed in Chap. 5.

3.1 Self-consistent field method

The KS equations (2.26) have to be solved in a self-consistent manner as explained in Sec. 2.2. Figure 3.1 shows the flow chart of this self-consistent field (SCF) cycles used to obtain the solution. As a first step, an initial electron density $n_{\text{in}}^{(0)}$ has to be "guessed" in iteration $m = 0$. In the case of FHI-aims, the superposition of the free atom densities is used as initial guess. The Hartree (v_{H}) and exchange-correlation potential (v_{xc}) are then calculated according to Eqs. (2.29) and (2.30) from the initial density, respectively. Next, the KS equations (2.26) are solved numerically by diagonalization, which yields the orbitals $\Phi_i^{(0)}$. These are used to calculate the new density $n_{\text{out}}^{(0)}$ according to Eq. (2.16). In each iteration m, it is checked if the solution is self-consistent, e.g., if input and output density are numerically equal[1]: $n_{\text{in}}^{(m)} = n_{\text{out}}^{(m)}$. In practice, it is checked whether the root mean square of the difference between input and output density is below a certain threshold. If this is the case, the solution has been found and desired quantities such as

[1] In order to test for self-consistency, one can additionally check whether the change of the sum of eigenvalues and of the total energy between the current and the previous iteration is below a certain threshold.

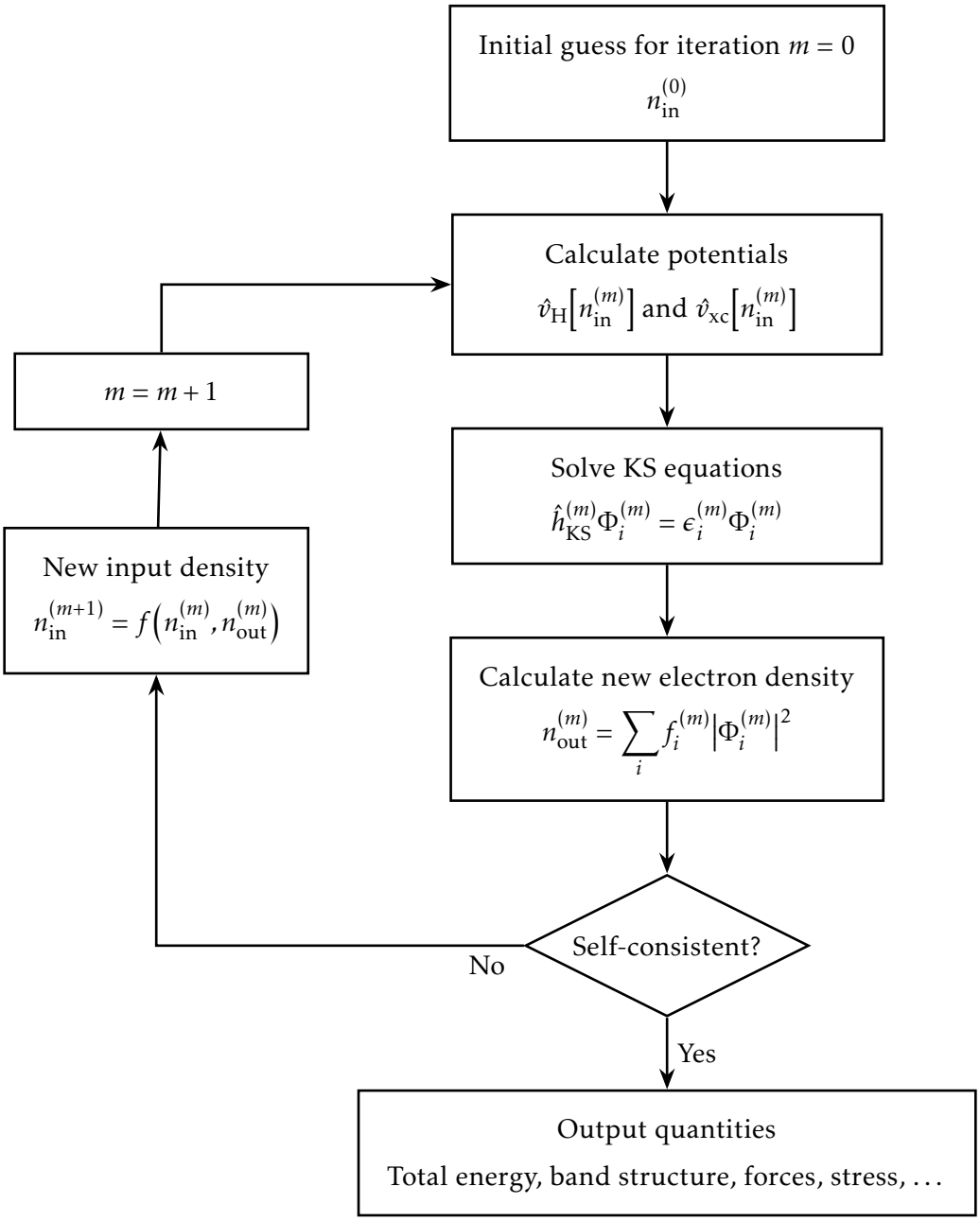

Figure 3.1: Flow chart of the self-consistent field cycle for the solution of the KS equations (2.26) adopted from [Mar04].

the total energy can be calculated. Otherwise, a new input density has to be constructed with the help of a function f. In the easiest case, a linear mixing between the input and output density can be used, $f\left(n_{\text{in}}^{(m)}, n_{\text{out}}^{(m)}\right) = (1-a)n_{\text{in}}^{(m)} + a n_{\text{out}}^{(m)}$ and $a \in [0,1]$. Now, one advances to the next iteration $m = 1$ and the cycle is closed by calculating the Hartree and exchange-correlation potential with the new input density $n_{\text{in}}^{(1)}$. This SCF cycle is repeated until self-consistency is achieved.

There exist different mixing schemes f that accelerate the convergence of the SCF cycle, e.g., the Pulay mixing scheme [Pul80]. The densities of previous iterations[2] are incorporated in the construction of the new input density in this scheme. Usually, a SCF cycle takes 10 to 20 iterations to converge to a reasonable accuracy for "well-behaved" systems.

3.2 Numeric atom-centered basis functions

A fundamental choice for the numerical solution of the KS equations (2.26) is the specific form of the basis functions utilized to span the one-electron Hilbert space. These basis functions φ_j are used to expand the KS orbitals

$$\Phi_i = \sum_j c_{ji} \varphi_j \tag{3.1}$$

with the expansion coefficients c_{ji}. In practice, this expansion has to be truncated. Therefore, one has to ensure that the set of basis functions is large enough and has sufficient flexibility for the expansion of the KS orbitals. There are two main categories of basis functions: extended and localized ones. A prominent representative of extended basis functions are plane waves. They are the natural choice to study periodic systems but are computationally expensive for localized (core) orbitals so that pseudopotentials are de facto required.

Conversely, FHI-aims utilizes localized numeric atom-centered basis functions of the following general form:

$$\varphi_i(\boldsymbol{r}) = \frac{u_{nl}(r)}{r} Y_{lm}(\theta, \phi) \tag{3.2}$$

using the real expression for the spherical harmonics

$$Y_{lm}(\theta,\phi) = \begin{cases} \Re\mathfrak{e}\, Y_{lm}^{\text{compl}}(\theta,\phi) & \text{for } m \geq 0 \\ \Im\mathfrak{m}\, Y_{lm}^{\text{compl}}(\theta,\phi) & \text{for } m < 0. \end{cases} \tag{3.3}$$

The radial part $u_{nl}(r)$ is numerically tabulated and fully flexible. The basis function index i summarizes the principal (n), angular (l), and magnetic (m) quantum number.

[2] For example, the densities from iteration $m-1$, $m-2$, $m-3$, and so forth.

The basis functions are real-valued by construction because Eq. (3.3) is used to obtain $Y_{lm}(\theta,\phi)$ from their complex definition $Y_{lm}^{\text{compl}}(\theta,\phi)$. Appendix B.1 explains how the exact form of the radial part $u_{nl}(r)$ is determined. The final three-dimensional form of the basis functions is then obtained by multiplying the generated radial functions $u_{nl}(r)$ with the $2l+1$ spherical harmonics $Y_{lm}(\theta,\phi)$ according to Eq. (3.2).

The utilization of atom-centered basis functions in FHI-aims implies that each atom has a set of basis functions associated with it. These basis functions depend on the species of the atom and are centered on the atom. Therefore, the basis set expansion in Eq. (3.1) takes the following explicit form:

$$\Phi_i(\boldsymbol{r}) = \sum_{J}^{N_{\text{nuc}}} \sum_{j} c_{ji}\varphi_j(\boldsymbol{r}-\boldsymbol{R}_J). \tag{3.4}$$

The sum runs over all atoms J and basis functions j that are associated with atom J, and $\boldsymbol{R}_J$ denotes the position of atom J.

3.3 Generalized eigenvalue problem

With the basis set expansion of Eq. (3.1), the minimization of the KS total energy E_{KS} with respect to the KS orbitals Φ_i in Eq. (2.23) becomes effectively a minimization with respect to the expansion coefficients c_{ji}. Furthermore, the difficult problem of solving the KS equations (2.26) can be cast into an algebraic problem. Substituting Φ_i in Eq. (2.26) with Eq. (3.1), multiplying from the left-hand side with φ_l^*, and integrating over the real space coordinates yields

$$\sum_j h_{lj}c_{ji} = \epsilon_i \sum_j s_{lj}c_{ji} \tag{3.5}$$

with the Hamilton matrix

$$h_{lj} = \langle\varphi_l|\hat{h}_{\text{KS}}|\varphi_j\rangle = \int \mathrm{d}\boldsymbol{r}\, \varphi_l^*(\boldsymbol{r})\hat{h}_{\text{KS}}\varphi_j(\boldsymbol{r}) \tag{3.6}$$

and the overlap matrix

$$s_{lj} = \langle\varphi_l|\varphi_j\rangle = \int \mathrm{d}\boldsymbol{r}\, \varphi_l^*(\boldsymbol{r})\varphi_j(\boldsymbol{r}), \tag{3.7}$$

where the previously introduced bra-ket notation (Eq. (2.17)) is used. Equation (3.5) is a generalized eigenvalue problem and can be solved by numerical eigenvalue solvers. Please note that for the numeric atom-centered basis functions of FHI-aims, the overlap matrix is not the unity matrix since the basis functions of different atoms are not orthonormal to each other.

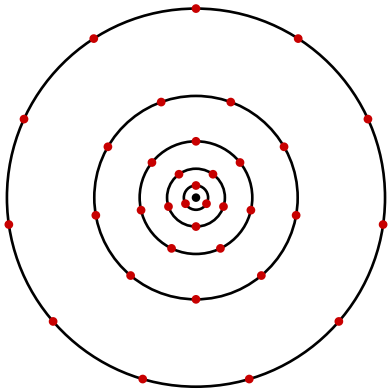

Figure 3.2: Two-dimensional schematic of the atom-centered grid of FHI-aims. The atom sits in the middle and the black circles are the spherical integration shells on which the red angular integration points are distributed.

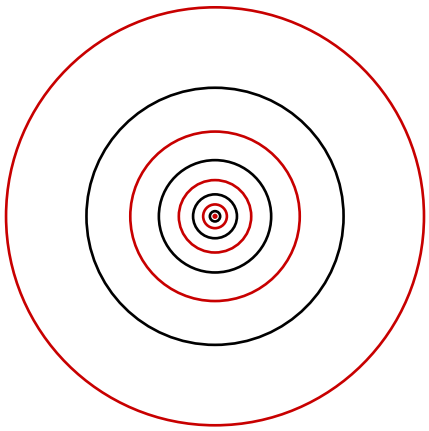

Figure 3.3: Two-dimensional schematic for the effect of the radial multiplier n_{mult}. The atom sits in the middle and the black circles are the integration shells for $n_{\text{mult}} = 1$. Increasing the n_{mult} to 2 adds the red integration shells.

3.4 Numerical integration

To ensure parallelization and accuracy, the real space numerical integration in FHI-aims is performed by employing a partitioning technique [Bec88b, Del90, Str96]. The integrand is divided into pieces, each of them localized at different atoms, and the individual pieces are then integrated by standard numeric methods. The partitioning of an integrand f is performed with the help of atom-centered partitioning functions[3] p_I so that integrals can be rewritten in the following way:

$$\int \mathrm{d}\boldsymbol{r}\, f(\boldsymbol{r}) = \sum_{I}^{N_{\text{nuc}}} \int \mathrm{d}\boldsymbol{r}\, p_I(\boldsymbol{r}) f(\boldsymbol{r}) \tag{3.8}$$

with

$$p_I(\boldsymbol{r}) = \frac{g_I(\boldsymbol{r})}{\sum_J g_J(\boldsymbol{r})}. \tag{3.9}$$

In principle, g_I is an arbitrary function that is strongly peaked at atom I. One choice is the n/r^2-type partitioning function suggested by Delley [Del90], which uses $g_I(\boldsymbol{r}) = n_I^{\text{free}}(\boldsymbol{r})/|\boldsymbol{r}|^2$ and $n_I^{\text{free}}(\boldsymbol{r})$ is the electron density of the isolated free atom I. In the case of the Stratmann partitioning scheme [Str96], a modified version of which has been

[3] The expression"partitioning function" in the context of integration must not be confused with the partition function from statistical mechanics.

implemented in FHI-aims (see App. B.3), the partitioning function also depends on the position of the atoms with respect to each other.

Each of the atom-centered pieces $p_I(\boldsymbol{r})f(\boldsymbol{r})$ in Eq. (3.8) is then integrated on a grid of overlapping atom-centered grids. Each of the atom-centered grids consists of N_r spherical integration shells $r(s)$ ($s = 1,\ldots,N_\mathrm{r}$) that are centered around the corresponding atom and extend up to an outermost shell at distance r_outer from the nucleus. In FHI-aims, the positions of the integration shells are determined according to Baker *et al.* [Bak94] by

$$r(s) = r_\mathrm{outer}\frac{\log\left[1-\left(s/(N_\mathrm{r}+1)^2\right)\right]}{\log\left[1-\left(N_\mathrm{r}/(N_\mathrm{r}+1)^2\right)\right]}. \tag{3.10}$$

On each shell, angular integration points are distributed so that spherical harmonics up to a certain order are integrated exactly. This kind of grid is called Lebedev grid and a version provided by Delley [Del96b] is employed. The number of angular integration points N_ang on each shell depends on the distance between shell and nucleus. More points are needed for far away shells than for those close to the nucleus since their circumference is larger. Figure 3.2 shows a two-dimensional schematic of the atom-centered grid in FHI-aims.

The accuracy of the grid can be increased uniformly by placing additional shells at integer fractions of the original grid. The radial multiplier n_mult denotes the denominator of these fractions. For example, a radial multiplier of 2 places additional shells at $s = \frac{1}{2}, s = \frac{3}{2}, \ldots, s = N_\mathrm{r} + \frac{1}{2}$, resulting in $2N_\mathrm{r}+1$ total shells. Figure 3.3 shows the effect of the radial multiplier. In general, there are $n_\mathrm{mult}(N_\mathrm{r}+1)-1$ integration shells in total.

3.5 Periodic systems

Solids can appear as ordered systems and thus form crystals in which the constituents are periodically arranged. Such periodic systems in three dimensions are described by a set of three lattice vectors $\boldsymbol{a}_n$, which define the unit cell of the crystal, and the basis, which specifies the position of the atoms within one unit cell. The lattice vectors can be written as the columns of a matrix $A = [\boldsymbol{a}_1\boldsymbol{a}_2\boldsymbol{a}_3]$ and the unit vectors of the reciprocal lattice $\boldsymbol{b}_n$ are given by

$$B = 2\pi\left(A^\mathrm{T}\right)^{-1} \tag{3.11}$$

with the matrix $B = [\boldsymbol{b}_1\boldsymbol{b}_2\boldsymbol{b}_3]$. The translation vector from the central unit cell to another unit cell $\boldsymbol{M}$ is $\boldsymbol{T}(\boldsymbol{M}) = A\cdot\boldsymbol{M}$ with $\boldsymbol{M} = (M_1, M_2, M_3)$ being a vector with integer numbers. $\boldsymbol{M} = (0,0,0)$ stands for the central unit cell. The periodicity of the crystal imposes constrictions on the form of the KS orbitals Φ_i, the so-called Bloch theorem [Mar04, Koh06],

$$\Phi_i^{(\boldsymbol{k})}(\boldsymbol{r}) = \mathrm{e}^{\mathrm{i}\boldsymbol{k}\cdot\boldsymbol{r}}u_i^{(\boldsymbol{k})}(\boldsymbol{r}) \quad \text{with} \quad u_i^{(\boldsymbol{k})}\left(\boldsymbol{r}+\boldsymbol{T}(\boldsymbol{M})\right) = u_i^{(\boldsymbol{k})}(\boldsymbol{r}). \tag{3.12}$$

Accordingly, KS orbitals that are periodically shifted by $\boldsymbol{T}(\boldsymbol{M})$ have to satisfy the condition

$$\Phi_i^{(\boldsymbol{k})}\Big(\boldsymbol{r}+\boldsymbol{T}(\boldsymbol{M})\Big) = \mathrm{e}^{\mathrm{i}\boldsymbol{k}\cdot\boldsymbol{T}(\boldsymbol{M})}\Phi_i^{(\boldsymbol{k})}(\boldsymbol{r}). \tag{3.13}$$

The KS orbitals and eigenvalues now depend on the additional quantum number $\boldsymbol{k}$, which is a vector in reciprocal space. The KS equations (2.26) can be solved separately for each $\boldsymbol{k}$-point and they are coupled through the electron density (see Eq. (2.16))

$$n(\boldsymbol{r}) = \frac{1}{V_{\mathrm{BZ}}}\int_{V_{\mathrm{BZ}}} \mathrm{d}\boldsymbol{k} \sum_i f_i^{(\boldsymbol{k})} |\Phi_i^{(\boldsymbol{k})}(\boldsymbol{r})|^2 \tag{3.14}$$

with V_{BZ} the volume of the Brillouin zone. The vector $\boldsymbol{k}$ is a continuous variable but in practice, it is sufficient to sample the Brillouin zone with a discrete and finite $\boldsymbol{k}$-point grid [Cha73, Mon76], thus replacing the integration by a summation. Still, the density of the $\boldsymbol{k}$-point grid is critical for the accuracy of a calculation. For instance, metals need denser grids than semiconductors and insulators due to their intricate Fermi surface, which has to be captured accurately [Koh06].

In the case of FHI-aims, Bloch-like generalized basis functions $\chi_{i,\boldsymbol{k}}(\boldsymbol{r})$ that fulfill Eq. (3.13) are used. They are derived from the atom-centered basis functions residing in different unit cells $\boldsymbol{M}$, $\varphi_{i,\boldsymbol{M}}(\boldsymbol{r}) = \varphi_i(\boldsymbol{r}-\boldsymbol{R}_I+\boldsymbol{T}(\boldsymbol{M}))$. These generalized basis functions are [Blu09]

$$\chi_i^{(\boldsymbol{k})}(\boldsymbol{r}) = \sum_{\boldsymbol{M}} \mathrm{e}^{\mathrm{i}\boldsymbol{k}\cdot\boldsymbol{T}(\boldsymbol{M})}\varphi_{i,\boldsymbol{M}}(\boldsymbol{r}). \tag{3.15}$$

Therefore, matrix elements like h_{ij} from Eq. (3.5) become $\boldsymbol{k}$-dependent:

$$h_{ij}^{(\boldsymbol{k})} = \langle \chi_i^{(\boldsymbol{k})} | \hat{h}_{\mathrm{KS}} | \chi_j^{(\boldsymbol{k})} \rangle. \tag{3.16}$$

For calculations, the matrix elements per unit cell are needed, denoted with $\bar{h}_{ij}^{(\boldsymbol{k})}$. Inserting Eq. (3.15) into Eq. (3.16) leads to two sums over the unit cells. Due to periodicity, they reduce to one sum for the matrix elements per unit cell,

$$\bar{h}_{ij}^{(\boldsymbol{k})} = \sum_{\boldsymbol{M}} \mathrm{e}^{\mathrm{i}\boldsymbol{k}\cdot\boldsymbol{T}(\boldsymbol{M})} \langle \varphi_{i,0} | \hat{h}_{\mathrm{KS}} | \varphi_{j,\boldsymbol{M}} \rangle, \tag{3.17}$$

in which the index 0 is a shorthand notation for the central unit cell. The sum over the unit cells $\boldsymbol{M}$ is finite due to the finite extent of all basis functions since they are bounded by a confinement potential (see App. B.1).

The matrix elements in Eq. (3.17) represent integrals over the whole space. However, it is more convenient to integrate them in separate pieces. Integrals over just one specific unit cell are calculated, and then all contributions are added up. Due to periodicity, all integrations can be performed in the central unit cell, which leads to

$$\sum_{\boldsymbol{M}} \langle \varphi_{i,0} | \hat{h}_{\mathrm{KS}} | \varphi_{j,\boldsymbol{M}} \rangle = \sum_{\boldsymbol{M},\boldsymbol{N}}{}' \int_V \mathrm{d}\boldsymbol{r}\, \varphi_{i,\boldsymbol{N}}(\boldsymbol{r}) \hat{h}_{\mathrm{KS}} \varphi_{j,\boldsymbol{M}}(\boldsymbol{r}) \tag{3.18}$$

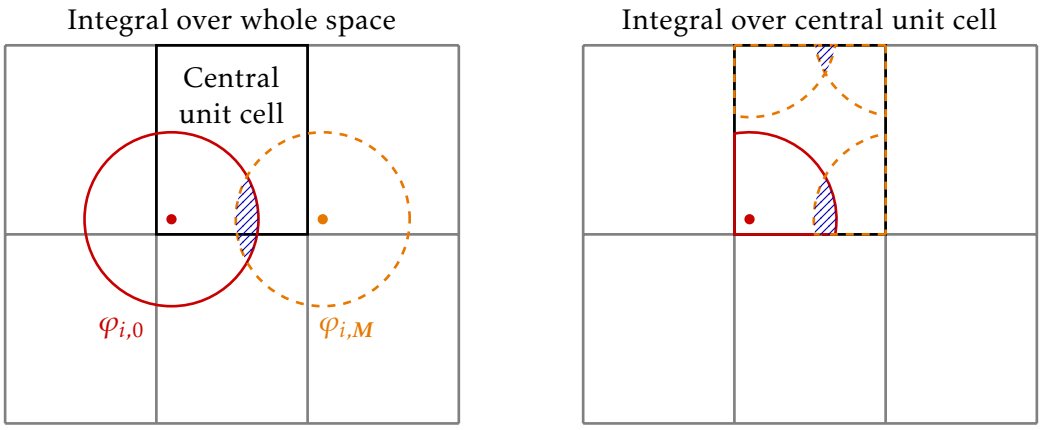

Figure 3.4: Illustration of two ways to calculate the overlap integral (blue stripes) between basis function $\varphi_{i,0}$ (red, solid) centered at the corner of the central unit cell (black frame) and one of its periodic images $\varphi_{i,\boldsymbol{M}}$ (orange, dashed). For simplicity, a spherical basis function and a rectangular unit cell are used. The left picture shows the straightforward approach: Both functions are integrated over the whole space to obtain the overlap integral. Alternatively, the integration can be separated into pieces lying inside individual unit cells, which can be mapped into the central unit cell due to periodicity. This approach yields the picture on the right hand side. There, the overlap integral is calculated by an integration over the central unit cell by considering those periodic images of the basis functions that extend into the central unit cell.

with V the volume of the central unit cell. The sum $\sum'_{\boldsymbol{M},\boldsymbol{N}}$ runs only over those unit cells that contain basis functions that have a non-zero contribution in the central unit cell. Figure 3.4 illustrates the location of these integration volumes. With Eq. (3.18), Eq. (3.17) becomes

$$\bar{h}_{ij}^{(\boldsymbol{k})} = \sum_{\boldsymbol{M},\boldsymbol{N}}{}' \mathrm{e}^{\mathrm{i}\boldsymbol{k}\cdot[\boldsymbol{T}(\boldsymbol{N})-\boldsymbol{T}(\boldsymbol{M})]} \int_V \mathrm{d}\boldsymbol{r}\, \varphi_{i,\boldsymbol{N}}(\boldsymbol{r}) \hat{h}_{\mathrm{KS}} \varphi_{j,\boldsymbol{M}}(\boldsymbol{r}) \tag{3.19}$$

so that it incorporates the Bloch phase factors. Analogously, all other inner products in Hilbert space are evaluated as integrals over the central unit cell in FHI-aims, e.g., a $\boldsymbol{k}$-dependent expression can be derived for the overlap matrix elements s_{ij} in Eq. (3.5).

3.6 Total energy in FHI-aims

This section lists all contributions to the total energy accounted for in FHI-aims. Detailed explanations and derivations are given in the corresponding publication [Blu09]. This list of terms then serves as a basis for the derivation of the stress tensor in Chap. 5. The

equations for the total energy E_{tot} (Eq. (2.23)) and the KS energy E_{KS} (Eq. (2.20)) are

$$E_{\text{tot}} = \min_{\{\Phi_i\}} \left[E_{\text{KS}}[\{\Phi_i\}] - \sum_i f_i \epsilon_i \Big(\langle \Phi_i | \Phi_i \rangle - 1 \Big) \right] + E_{\text{nuc-nuc}} \tag{3.20}$$

and

$$E_{\text{KS}}[n] = T_{\text{s}}[n] + E_{\text{H}}[n] + \int \mathrm{d}\boldsymbol{r}\, v_{\text{ext}}(\boldsymbol{r}) n(\boldsymbol{r}) + E_{\text{xc}}[n]. \tag{3.21}$$

3.6.1 Kinetic energy of non-interacting electrons

Non-relativistic kinetic energy

The kinetic energy in the non-relativistic case, see Eq. (2.18), is

$$T_{\text{s}}^{\text{non-rel}} = -\frac{1}{2} \sum_i f_i \langle \Phi_i | \Delta | \Phi_i \rangle. \tag{3.22}$$

Relativistic kinetic energy

In principle, the four-component Dirac equation has to be solved for the correct relativistic description of electrons. A scalar-relativistic Schrödinger equation can be derived from the Dirac equation by neglecting spin-orbit coupling [Blu09],

$$\left(-\nabla \cdot \frac{c^2}{2c^2 + \epsilon_i - \hat{v}} \nabla + \hat{v} \right) \Phi_i = \epsilon_i \Phi_i, \tag{3.23}$$

with c the speed of light and v the full potential of the system. The relativistic kinetic energy operator in Eq. (3.23) is approximated in the "scaled ZORA" (zeroth order regular approximation with scaled eigenvalues) approach [vLe94] as

$$\hat{t}_{\text{ZORA}} = -\nabla \cdot \frac{c^2}{2c^2 - \hat{v}} \nabla. \tag{3.24}$$

To maintain gauge invariance with respect to shifts in the potential zero, each eigenvalue ϵ_i in Eq. (3.23) is rescaled by the factor $1/(1 - \langle \Phi_i | \nabla \cdot \frac{c^2}{(2c^2 - \hat{v})^2} \nabla | \Phi_i \rangle)$ after the self-consistent solution has been found.

Another possible approximation of the relativistic kinetic energy operator in Eq. (3.23) is "atomic ZORA" (zeroth order regular approximation with on-site free-atom potentials) [Blu09]. Here, the full potential v in Eq. (3.24) is replaced by the on-site free-atom potential $v_{\text{free}}^{J(j)}$ of atom J with the associated basis function j and the kinetic energy operator becomes

$$\hat{t}_{\text{at.ZORA}} | \varphi_j \rangle = -\nabla \cdot \frac{c^2}{2c^2 - \hat{v}_{\text{free}}^{J(j)}} \nabla | \varphi_j \rangle. \tag{3.25}$$

In this case, no scaling of the eigenvalues is needed and the relativistic kinetic energy has the following form:

$$T_{\mathrm{s}}^{\mathrm{rel}} = \frac{1}{2}\sum_{JK}^{N_{\mathrm{nuc}}}\sum_{ijk} f_i c_{ij} c_{ik}\Big[\langle\varphi_j|\hat{t}_{\mathrm{at.ZORA}}|\varphi_k\rangle + \langle\varphi_k|\hat{t}_{\mathrm{at.ZORA}}|\varphi_j\rangle\Big]. \tag{3.26}$$

The on-site free-atom potentials in Eq. (3.25) are obtained by solving a one-dimensional differential equation for each orbital for non-spinpolarized spherically symmetric free atoms with the same scalar relativistic approximation and DFA as employed in the full calculation later. However, there are exceptions to this approach, e.g., for hybrid functionals, the underlying (semi-)local DFA without HF exchange is used. In principle, solving the four-component Dirac equation with exactly the same DFA as employed in the full calculation later would be desirable. Still, the presented approach produces reliable results in practice and the difference between "atomic ZORA" and "scaled ZORA" is very small (usually in the order of 0.1 meV per atom for heavy elements, less for lighter elements) [Blu09, DCD].

3.6.2 Electrostatics

The electrostatic energy is described by three terms: classical electron-electron interaction (Hartree term) E_{H}, electron-nuclei interaction E_{ext}, and nuclei-nuclei interaction $E_{\text{nuc-nuc}}$. These three terms cannot be treated separately in a numerical approach since they diverge under periodic boundary conditions. This problem can be avoided by treating electrons and nuclei together by defining a total electrostatic energy

$$E_{\mathrm{es}} = E_{\mathrm{H}} + E_{\mathrm{ext}} + E_{\text{nuc-nuc}}. \tag{3.27}$$

Then, only energy contributions arising from electrostatically neutral subsystems are handled, leading to a finite value of the total electrostatic energy.

To achieve a rapid and accurate description of the electrostatic interactions, the electron density n is partitioned into contributions n_I associated with the individual atoms I (see Sec. 3.4 for a discussion of the partitioning function p_I),

$$n_I(\boldsymbol{r} - \boldsymbol{R}_I) = \int \mathrm{d}\boldsymbol{r}\, p_I(\boldsymbol{r}) n(\boldsymbol{r}). \tag{3.28}$$

With this partitioning scheme, the Hartree potential (Eq. (2.29)) becomes

$$v_{\mathrm{H}}(\boldsymbol{r}) = \sum_{I}^{N_{\mathrm{nuc}}} v_{\mathrm{H}}^{I}(\boldsymbol{r} - \boldsymbol{R}_I) = \sum_{I}^{N_{\mathrm{nuc}}} \int_V \mathrm{d}\tilde{\boldsymbol{r}}\, \frac{n_I(\tilde{\boldsymbol{r}} - \boldsymbol{R}_I)}{|\boldsymbol{r} - \tilde{\boldsymbol{r}}|}. \tag{3.29}$$

Adding the external potential v_{ext} (Eq. (2.28)) defines the total electrostatic potential

$$v_{\text{es}}(\boldsymbol{r}) = \sum_{I}^{N_{\text{nuc}}} v_{\text{es}}^{I}(\boldsymbol{r} - \boldsymbol{R}_I) = \sum_{I}^{N_{\text{nuc}}} \Big[v_{\text{H}}^{I}(\boldsymbol{r} - \boldsymbol{R}_I) + v_{\text{ext}}^{I}(\boldsymbol{r} - \boldsymbol{R}_I) \Big]. \tag{3.30}$$

Accordingly, the total electrostatic energy, which includes the electron-electron, electron-nuclear, and nuclear-nuclear interaction, becomes

$$E_{\text{es}} = \frac{1}{2} \int_V \mathrm{d}\boldsymbol{r}\, n(\boldsymbol{r}) v_{\text{es}}(\boldsymbol{r}) + \frac{1}{2} \sum_{I}^{N_{\text{nuc}}} Z_I \left[v_{\text{H}}^{I}(0) + \sum_{J \neq I}^{N_{\text{nuc}}} v_{\text{es}}^{J}(\boldsymbol{R}_J - \boldsymbol{R}_I) \right]. \tag{3.31}$$

Here, $Z_I v_{\text{H}}^{I}(0)$ is the on-site term and it describes the interaction of atom I with its own electrons.

In practice, the total electrostatic potential is calculated in three steps: First, the electron density associated to the superposition of the isolated free atoms n_{free}^{I} is used to define the difference density

$$\delta n(\boldsymbol{r}) = n(\boldsymbol{r}) - \sum_{I}^{N_{\text{nuc}}} n_{\text{free}}^{I}(\boldsymbol{r} - \boldsymbol{R}_I) \tag{3.32}$$

with respect to the total density n (Eq. (2.16)). Second, this difference density δn is partitioned according to Eq. (3.28) and expanded in a multipole (MP) expansion δn_{MP}. This expansion yields an approximate description of the electron density n, the so-called multipole density

$$n_{\text{MP}}(\boldsymbol{r}) = \sum_{I}^{N_{\text{nuc}}} n_{\text{MP}}^{I}(\boldsymbol{r}) = \sum_{I}^{N_{\text{nuc}}} \Big[n_{\text{free}}^{I}(\boldsymbol{r} - \boldsymbol{R}_I) + \delta n_{\text{MP}}^{I}(\boldsymbol{r} - \boldsymbol{R}_I) \Big]. \tag{3.33}$$

Third, the potential v_{free}^{I} generated by the density n_{free}^{I} and nucleus I is calculated. This means that the external potential v_{ext}^{I} is included in the free-atom potential v_{free}^{I}. Furthermore, the potential δv_{es}^{I} generated by the density δn_{MP}^{I} is calculated so that the total electrostatic potential consists of these two terms,

$$v_{\text{es}}(\boldsymbol{r}) = \sum_{I}^{N_{\text{nuc}}} \Big[v_{\text{free}}^{I}(\boldsymbol{r} - \boldsymbol{R}_I) + \delta v_{\text{es}}^{I}(\boldsymbol{r} - \boldsymbol{R}_I) \Big]. \tag{3.34}$$

Here, the potentials v_{free}^{I} of the isolated free atoms are calculated as a cubic spline function on dense logarithmic grids, while the potential δv_{es}^{I} is split up into three contributions:

$$\delta v_{\text{es}}^{I}(\boldsymbol{r} - \boldsymbol{R}_I) = v_{\text{NU}}^{I}(\boldsymbol{r} - \boldsymbol{R}_I) + v_{\text{SR}}^{I}(\boldsymbol{r} - \boldsymbol{R}_I) + v_{\text{LR}}^{I}(\boldsymbol{r} - \boldsymbol{R}_I). \tag{3.35}$$

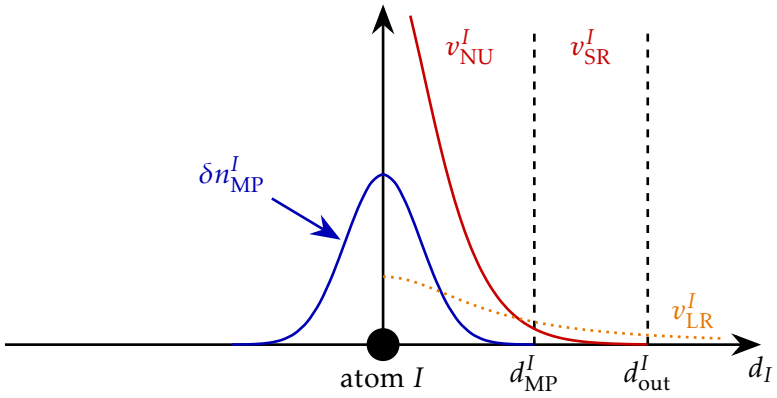

Figure 3.5: One-dimensional sketch of the different contributions and used radii for the calculation of the electrostatic potential in FHI-aims. The abscissa shows the distance d_I to atom I and the partitioned difference density δn^I_{MP} of atom I is depicted (blue). For distances less than d^I_{MP} where δn^I_{MP} is non-zero the potential v^I_{NU} (red, solid) is obtained by explicitly solving Poisson's equation. Outside the density, the potential is determined by the Ewald short-range term v^I_{SR} (red, solid), which extends up to d^I_{out}. Any long-range tails of the potential are accounted for by the Ewald long-range term v^I_{LR} (orange, dotted).

This potential is calculated with the help of the Ewald summation for multipole charges [Del96a]. The first term is the numerical potential v^I_{NU}, which solves the electrostatic potential explicitly for short ranges $d_I = |\boldsymbol{r} - \boldsymbol{R}_I| < d^I_{\mathrm{MP}}$ where the difference density δn^I_{MP} of atom I is non-zero, see Fig. 3.5. This is done by the Green's function for Poisson's equation of multipoles from classical electrostatics,

$$v^I_{\mathrm{NU}}(\boldsymbol{r}-\boldsymbol{R}_I) = \sum_{l,m} Y_{lm}(\theta_I,\phi_I)\left[\int_0^{d_I} \mathrm{d}\tilde{d}\,\frac{\tilde{d}^{l+2}}{d_I^{l+1}}\delta n_{I,lm}(\tilde{d}) + \int_{d_I}^{\infty} \mathrm{d}\tilde{d}\,\frac{d_I^{l}}{\tilde{d}^{l-1}}\delta n_{I,lm}(\tilde{d})\right]. \tag{3.36}$$

$Y_{lm}(\theta_I,\phi_I)$ is the real form of the spherical harmonics (Eq. (3.3)) with θ_I and ϕ_I the angles of vector $\boldsymbol{r}-\boldsymbol{R}_I$ in spherical coordinates. The $\delta n_{I,lm}$ are the multipole components of the difference density associated with atom I, $\delta n_{I,lm}(r) = \iint \mathrm{d}\phi\,\mathrm{d}\theta\,\sin\theta\, p_I(\boldsymbol{r})\delta n(\boldsymbol{r}) Y_{lm}(\theta,\phi)$. The other terms are the Ewald short-range (SR) potential [Del96a]

$$v^I_{\mathrm{SR}}(\boldsymbol{r}-\boldsymbol{R}_I) = \sum_{l,m} Q_{I,lm} E_{lm} F^{p(lm)}(d_I)(d_{I,x})^{X_{lm}}(d_{I,y})^{Y_{lm}}(d_{I,z})^{Z_{lm}}, \tag{3.37}$$

which extends up to a specific distance d^I_{out} from atom I, see Fig. 3.5, and the Ewald long-range (LR) potential [Del96a]

$$v^I_{\mathrm{LR}}(\boldsymbol{r}-\boldsymbol{R}_I) = \frac{4\pi}{V}\sum_{\boldsymbol{G}} \frac{\exp\left(-\frac{\kappa^2 G^2}{4}\right)}{G^2} S_I(\boldsymbol{G})\exp(\mathrm{i}\boldsymbol{G}\cdot\boldsymbol{r}) \tag{3.38}$$

with

$$S_I(\boldsymbol{G}) = \sum_{l,m} Q_{I,lm} G_{lm} \exp(-\mathrm{i}\boldsymbol{G}\cdot\boldsymbol{R}_I)\mathrm{i}^{D_{lm}}(G_x)^{A_{lm}}(G_y)^{B_{lm}}(G_z)^{C_{lm}}. \tag{3.39}$$

The coefficients E_{lm}, G_{lm}, the exponents A_{lm}, B_{lm}, C_{lm}, D_{lm}, X_{lm}, Y_{lm}, Z_{lm}, and the function $F^{p(lm)}(d)$ are expressions that only depend on the numbers l and m. The analytical expression for these terms can be found in the publication by Delley [Del96a]. The $Q_{I,lm}$ are the atomic multipoles, $Q_{I,lm} = \sqrt{\frac{4\pi}{2l+1}}\int \mathrm{d}r\, r^{l+2}\delta n_{I,lm}(r)$, $\boldsymbol{G} = (G_x, G_y, G_z)$ is a vector of the reciprocal lattice ($G = |\boldsymbol{G}|$), κ is the Ewald parameter, and $(d_{I,x}, d_{I,y}, d_{I,z}) = \boldsymbol{r} - \boldsymbol{R}_I$.

In periodic boundary conditions, the zero level of the electrostatic potential is not well defined. To achieve consistency across systems, the zero of the electrostatic potential is manually set to the spatial average of the potential δv_{es} generated by the difference density δn_{MP},

$$v_{\mathrm{avg}} = \frac{1}{V}\int_V \mathrm{d}\boldsymbol{r}\,\delta v_{\mathrm{es}}(\boldsymbol{r}). \tag{3.40}$$

Accordingly, the total electrostatic potential in Eq. (3.34) becomes[4]

$$v_{\mathrm{es}}(\boldsymbol{r}) = \sum_{I}^{N_{\mathrm{nuc}}}\left[v^I_{\mathrm{free}}(\boldsymbol{r}-\boldsymbol{R}_I) + \delta v^I_{\mathrm{es}}(\boldsymbol{r}-\boldsymbol{R}_I)\right] - v_{\mathrm{avg}}. \tag{3.41}$$

In order to reduce the error in the total electrostatic energy expression due to the multipole expansion to quadratic order with respect to the maximal angular momentum used in the expansion [Dun79], the total electrostatic energy (Eq. (3.31)) is calculated as follows:

$$E_{\mathrm{es}} = \int_V \mathrm{d}\boldsymbol{r}\left[n(\boldsymbol{r}) - \frac{1}{2}n_{\mathrm{MP}}(\boldsymbol{r})\right]v_{\mathrm{es}}(\boldsymbol{r}) + \frac{1}{2}\sum_{I}^{N_{\mathrm{nuc}}} Z_I\left[v^I_{\mathrm{H}}(0) + \sum_{J\neq I}^{N_{\mathrm{nuc}}} v^J_{\mathrm{es}}(\boldsymbol{R}_J - \boldsymbol{R}_I)\right]. \tag{3.42}$$

Here, the electron density n in Eq. (3.31) has been replaced by

$$\frac{1}{2}n(\boldsymbol{r}) \longrightarrow n(\boldsymbol{r}) - \frac{1}{2}n_{\mathrm{MP}}(\boldsymbol{r}). \tag{3.43}$$

[4] The $\boldsymbol{G} = 0$ term of the Ewald summation does not appear explicitly.

3.6.3 Exchange-correlation energy

LDA and GGA

For the LDA and GGA functionals, the exchange-correlation energy is calculated according to Eqs. (2.33) and (2.36), respectively,

$$E_{\mathrm{xc}}^{\mathrm{LDA}} = \int_V \mathrm{d}\boldsymbol{r}\, n(\boldsymbol{r}) \epsilon_{\mathrm{xc}}^{\mathrm{LDA}}\Big(n(\boldsymbol{r})\Big). \tag{3.44}$$

$$E_{\mathrm{xc}}^{\mathrm{GGA}}[n] = \int_V \mathrm{d}\boldsymbol{r}\, n(\boldsymbol{r}) \epsilon_{\mathrm{xc}}^{\mathrm{GGA}}\Big(n(\boldsymbol{r}), \nabla n(\boldsymbol{r})\Big). \tag{3.45}$$

Hybrid functionals

For hybrid functionals, we here discuss the one parameter case[5] for the sake of simplicity, where a fraction α of GGA exchange is replaced by HF exchange (with and without range separation). The respective exchange-correlation energy has the following form, see Secs. 2.3.3 and 2.3.4:

$$E_{\mathrm{xc}}^{\mathrm{scr.hyb}}(\alpha,\omega) = E_{\mathrm{xc}}^{\mathrm{GGA}} + \alpha\Big(E_{\mathrm{x}}^{\mathrm{HF,SR}}(\omega) - E_{\mathrm{x}}^{\mathrm{GGA,SR}}(\omega)\Big). \tag{3.46}$$

In the following, it is concisely described how the HF exchange energy is actually calculated in FHI-aims. The explanation is based on the publication by Ren *et al.* [Ren12a]. For a given basis set expansion as defined in Eq. (3.1), the HF exchange energy is defined as

$$E_{\mathrm{x}}^{\mathrm{HF}} = -\frac{1}{2}\sum_{ijkl} D_{jk} D_{il} (ij|kl). \tag{3.47}$$

The one-particle density matrix is defined using

$$D_{jk} = \sum_m f_m c_{jm} c_{km} \tag{3.48}$$

and the indices i, j, k, l run over all basis functions. The occupation numbers f_m and the expansions coefficients c_{jm} have been introduced before. The expression $(ij|kl)$ denotes the four-center two-electron Coulomb integral

$$(ij|kl) = \iint \mathrm{d}\boldsymbol{r}\, \mathrm{d}\tilde{\boldsymbol{r}}\, \varphi_i(\boldsymbol{r})\varphi_j(\boldsymbol{r}) v(|\boldsymbol{r}-\tilde{\boldsymbol{r}}|)\varphi_k(\tilde{\boldsymbol{r}})\varphi_l(\tilde{\boldsymbol{r}}) \tag{3.49}$$

with the Coulomb kernel $v(|\boldsymbol{r}|)$. No complex conjugate quantities appear since the basis functions are chosen to be real valued in FHI-aims, see Sec. 3.2. For PBE0, the Coulomb

[5] Functionals with more than one parameter can be handled analogously using the formalism for the calculation of the ingredients (exchange and/or correlation of LDA, GGA, or HF) discussed in this thesis.

kernel is simply the Coulomb potential $1/|\boldsymbol{r}|$, while $v(|\boldsymbol{r}|) = \mathrm{erfc}(\omega|\boldsymbol{r}|)/|\boldsymbol{r}|$ for HSE06 so that only the short-range part of the Coulomb potential is included.

With the help of the resolution of identity (RI) [VAl88], one can expand the product $\varphi_i(\boldsymbol{r})\varphi_j(\boldsymbol{r})$ of two basis functions (centered at atoms I and J, respectively) in a finite auxiliary product basis set $P_\mathfrak{m}(\boldsymbol{r})$,

$$\varphi_i(\boldsymbol{r})\varphi_j(\boldsymbol{r}) \approx \sum_\mathfrak{m} C_{ij}^\mathfrak{m} P_\mathfrak{m}(\boldsymbol{r}), \tag{3.50}$$

with the expansion coefficients $C_{ij}^\mathfrak{m}$. Using the auxiliary basis set, the HF exchange energy can be rewritten as

$$E_\mathrm{x}^\mathrm{HF} = -\frac{1}{2}\sum_{\substack{ijkl\\ \mathfrak{mn}}} D_{jk}D_{il}\left[C_{ij}^\mathfrak{m} V_\mathfrak{mn} C_{kl}^\mathfrak{n}\right] \tag{3.51}$$

with the Coulomb matrix

$$V_\mathfrak{mn} = (\mathfrak{m}|\mathfrak{n}) = \iint \mathrm{d}\boldsymbol{r}\,\mathrm{d}\tilde{\boldsymbol{r}}\, P_\mathfrak{m}(\boldsymbol{r}) v(|\boldsymbol{r}-\tilde{\boldsymbol{r}}|) P_\mathfrak{n}(\tilde{\boldsymbol{r}}). \tag{3.52}$$

In the so-called RI-V formalism, the error in the four-center Coulomb integrals that stems from the product basis expansion is minimized [Vah93] by choosing the expansion coefficients to be

$$C_{ij}^\mathfrak{m} = \sum_\mathfrak{n} (ij|\mathfrak{n}) V_\mathfrak{nm}^{-1}. \tag{3.53}$$

With the so-called RI-LVL formalism [Ihr15], the computational effort can be further reduced within negligible losses in accuracy by using a locally restricted expansion,

$$\varphi_i(\boldsymbol{r})\varphi_j(\boldsymbol{r}) \approx \sum_{\mathfrak{m}\in\mathcal{P}(IJ)} C_{ij}^\mathfrak{m} P_\mathfrak{m}(\boldsymbol{r}), \tag{3.54}$$

with $\mathcal{P}(IJ) = \mathcal{P}(I) \cup \mathcal{P}(J)$. The set of all auxiliary basis functions that are centered at atom I is denoted with $\mathcal{P}(I)$. For a basis product $\varphi_i\varphi_j$, this means that the index $\mathfrak{m}$ runs only over those auxiliary basis functions that are centered on atom I or J. Consequently, the expansion coefficients become

$$C_{ij}^\mathfrak{m} = \begin{cases} \displaystyle\sum_{\mathfrak{n}\in\mathcal{P}(IJ)} (ij|\mathfrak{n}) L_\mathfrak{nm}^{IJ} & \text{for } \mathfrak{m}\in\mathcal{P}(IJ) \\ 0 & \text{else} \end{cases} \tag{3.55}$$

with $L^{IJ} = \left(V^{IJ}\right)^{-1}$ being the inverse of the Coulomb matrix that includes only auxiliary basis functions centered at atom I or J. With this locally restricted expansion, Eq. (3.51) becomes

$$E_\mathrm{x}^\mathrm{HF} = -\frac{1}{2}\sum_{IJ}^{N_\mathrm{nuc}} \sum_{\substack{i,j,k,l\in\mathcal{B}(IJ)\\ \mathfrak{m},\mathfrak{n}\in\mathcal{P}(IJ)}} D_{jk}D_{il}\left[C_{ij}^\mathfrak{m} V_\mathfrak{mn} C_{kl}^\mathfrak{n}\right] \tag{3.56}$$

with $\mathcal{B}(IJ) = \mathcal{B}(I) \cup \mathcal{B}(J)$ the set of all basis functions that are centered on atom I or J – similar to $\mathcal{P}(IJ)$.

Van der Waals correction

According to Eq. (2.56), the correction for the vdW interactions is

$$E_{\mathrm{vdW}} = -\frac{1}{2} \sum_{I}^{N_{\mathrm{nuc}}} \sum_{J \neq I}^{N_{\mathrm{nuc}}} f_{\mathrm{damp}}(\boldsymbol{R}_I, \boldsymbol{R}_J) \frac{C_{6IJ}}{|\boldsymbol{R}_I - \boldsymbol{R}_J|^6}, \tag{3.57}$$

and the form of the damping function f_{damp} is given in Eq. (2.61). For periodic systems, the vdW correction is calculated by explicitly including the periodic images of the atoms in the summations. Since the $1/R^6$ function falls off quickly with increasing distance, only few neighboring unit cells are needed to obtain converged results.

4 Calculating electrical band conductivities with BoltzTraP

This thesis solely focuses on electronic band transport, which is one of the possible macroscopic charge transport mechanisms in organic semiconductors. As explained in the introduction (Chap. 1), other possible transport mechanisms are electronic hopping and coupled electron-phonon transport. Band transport can be a dominant contribution to the electrical conductivity for highly ordered organic crystals at low temperatures. The BoltzTraP code [Mad06] is used in order to estimate electrical band conductivities from electronic band structures of crystals. Therefore, this chapter briefly summarizes the underlying methodology and how the formalism is used for the calculations of charge carrier concentrations and electrical band conductivities.

4.1 Band conductivity from Boltzmann transport equation

The electrical band conductivity ς being a tensor of rank two can be obtained by solving the semiclassical Boltzmann transport equation. For a constant external electrical field and using the relaxation time approximation, the electrical band conductivity of a crystal is [Mah96, Mad06]

$$\varsigma(E_\mathrm{F}, T) = -\int \mathrm{d}\epsilon \, \frac{\partial f(\epsilon, E_\mathrm{F}, T)}{\partial \epsilon} \Xi(\epsilon). \tag{4.1}$$

Here, f is the Fermi function,

$$f(\epsilon, E_\mathrm{F}, T) = \frac{1}{1 + \exp\left(\frac{\epsilon - E_\mathrm{F}}{k_\mathrm{B} T}\right)}, \tag{4.2}$$

with the Fermi level E_F, the Boltzmann constant k_B, and the temperature T. The transport distribution function $\Xi(E)$ is a tensor of rank two defined as

$$\Xi(\epsilon) = \frac{1}{N_\mathrm{k}} \sum_{i,\boldsymbol{k}} \delta\Big(\epsilon - \epsilon_i(\boldsymbol{k})\Big) \tau_{i,\boldsymbol{k}} \boldsymbol{v}_i(\boldsymbol{k}) \otimes \boldsymbol{v}_i(\boldsymbol{k}). \tag{4.3}$$

The sum runs over all bands i and $\boldsymbol{k}$-points in the Brillouin zone. N_k is the number of sampled $\boldsymbol{k}$-points, $\tau_{i,\boldsymbol{k}}$ the relaxation time, and ϵ_i the energy of band i. The group velocities $\boldsymbol{v}_i$ of the electrons in the crystal are given by

$$\boldsymbol{v}_i(\boldsymbol{k}) = \frac{\partial \epsilon_i(\boldsymbol{k})}{\partial \boldsymbol{k}}. \tag{4.4}$$

The relaxation time $\tau_{i,\boldsymbol{k}}$ introduced as an approximation is an effective measure how fast the system returns to its equilibrium state from non-equilibrium, e.g., after an electron is scattered. In this approximation, it only depends on the band index i and the direction of $\boldsymbol{k}$. Due to the derivative of the Fermi function in Eq. (4.1), only bands close to the band gap (i.e. Fermi level) contribute to the conductivity. In first order approximation the relaxation time can be assumed to be (a) band index and (b) direction independent, which further simplifies the formalism. Hence, we use a constant relaxation time τ for our studies.

In order to calculate electrical band conductivities, we compute the band energies $\epsilon_i(\boldsymbol{k})$ on a fine $\boldsymbol{k}$-point grid and pass them to BoltzTraP. The code performs then a Fourier expansion of these band energies and calculates the conductivity tensor ς divided by the relaxation time τ according to Eq. (4.1). Because the relaxation time is unknown, we are not able to calculate absolute values for the conductivity. However, we can still investigate trends of the conductivity under pressure assuming that the relaxation time stays constant.

4.2 Determining the Fermi level and charge carrier concentrations

The conductivity calculated by BoltzTraP depends on the Fermi level E_F besides the temperature, see Eq. (4.1). Therefore, the Fermi level has to be determined based on our calculations. For intrinsic semiconductors, the Fermi level lies between the valance and conduction band and its exact position depends on the type and amount of doping as well as on the temperature T [Ash76]. n-doping induces an excess of negative charge carriers (electrons) and shifts the Fermi level towards the conduction band; p-doping induces an excess of positive charge carriers (holes) and shifts the Fermi level towards the valence band. In the intrinsic case, the charge carrier concentration of electrons and holes must be the same due to charge carrier conservation.

The electron density per energy range is given by the product of density of states (DOS) and Fermi function f (Eq. (4.2)) [Ash76]. The total charge carrier concentration of electrons n_c is then given by the concentration of electrons above the conduction band minimum (CBM), i.e.,

$$n_\mathrm{c} = \int_{E_\mathrm{CBM}}^{\infty} \mathrm{d}\epsilon\, f(\epsilon, E_\mathrm{F}, T)\mathrm{DOS}(\epsilon). \tag{4.5}$$

The total charge carrier concentration of holes p_v is given by the concentration of holes below the valence band maximum (VBM)[1], i.e.,

$$p_\mathrm{v} = \int_{-\infty}^{E_\mathrm{VBM}} \mathrm{d}\epsilon \Big(1 - f(\epsilon, E_\mathrm{F}, T)\Big) \mathrm{DOS}(\epsilon). \tag{4.6}$$

Hence, Eqs. (4.5) and (4.6) allow to determine the Fermi level for a specific temperature T. For the case of n-doping (p-doping) with a specific charge carrier density n_c (p_v), we numerically solve Eq. (4.5) (Eq. (4.6)) for the Fermi level E_F; for the intrinsic case, the equation $n_\mathrm{c} = p_\mathrm{v}$ is solved numerically. Additionally, the solution yields the intrinsic charge carrier concentration $n_\mathrm{i} = n_\mathrm{c} = p_\mathrm{v}$.

[1] Since we consider holes, the distribution $(1 - f)$ instead of f is used.

Part II

Derivation and implementation of stress tensor

5 Stress in crystals

The strain tensor ε of rank two describes the elastic deformation of a crystal relative to a reference state, see Fig. 5.1. This corresponds to a linear transformation of the crystal structure, i.e., the atomic positions $\boldsymbol{R}_I$ and lattice vectors $\boldsymbol{a}_n$ are transformed according to

$$R_{I,\alpha}(\varepsilon) = \sum_{\beta} (\delta_{\alpha\beta} + \varepsilon_{\alpha\beta}) R_{I,\beta}(0) \tag{5.1}$$

$$a_{\alpha n}(\varepsilon) = \sum_{\beta} (\delta_{\alpha\beta} + \varepsilon_{\alpha\beta}) a_{\beta n}(0) \tag{5.2}$$

with respect to the zero strain reference $\boldsymbol{R}_I(0)$ and $\boldsymbol{a}_n(0)$, respectively. α, β denote the Cartesian components. The strain tensor is defined to be symmetric since an asymmetric component corresponds to a rigid rotation of the crystal [Nye85]. Straining a crystal leads to a response, called stress, similar to atomic forces, which are a response to the displacement of atoms. For a unit cell with volume V, the stress tensor σ is defined as the first order change in the total energy of the unit cell E_{tot} under a symmetrical, infinitesimal strain deformation ε [Nye85, Nag11],

$$\sigma_{\lambda\mu} = \frac{1}{V} \frac{\partial E_{\text{tot}}}{\partial \varepsilon_{\lambda\mu}} \bigg|_{\varepsilon=0} . \tag{5.3}$$

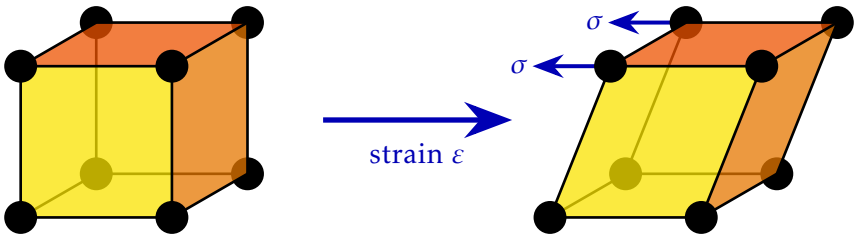

Figure 5.1: The strain ε describes the elastic deformation of a crystal structure. In response to the distorted lattice, the stress σ arises, which drives the crystal back to its equilibrium position.

Since the strain tensor is symmetric per definition, the stress tensor is symmetric as well and thus, consists of six independent entries. Although the definition of Eq. (5.3) is unique, a practical implementation in an electronic-structure code depends very much on the numerical details chosen for the DFT formalism, e.g., on the basis set type.

Historically, Nielsen and Martin [Nie83, Nie85] first demonstrated that the stress can be efficiently and accurately assessed in a DFT framework. For this purpose, they employed a plane-wave basis set expansion (together with norm-conserving pseudopotentials) and the local-density approximation. In later works, the stress tensor implementation for plane waves was extended to ultra-soft pseudopotentials [Foc95] including the contributions of the generalized orthonormality condition. Thonhauser *et al.* [Tho02] as well as Nagasako *et al.* [Nag11] reported the strain derivatives for the linearized augmented plane wave method. The former derived a surface term due to the discontinuities at the boundaries between muffin tins and interstitial region and the latter presented a correction because the number of plane waves in the interstitial region changes under strain. For the projector augmented-wave method, Kresse *et al.* [Kre99] as well as Torrent *et al.* [Tor08] derived the stress tensor and discussed the additional terms arising from the compensating charges of this method. Kudin *et al.* [Kud00] discussed the implementation of the stress tensor for Gaussian-type orbitals while evaluating the electrostatic contributions entirely in real space using a fast multipole method. Doll *et al.* [Dol04, Dol10] employed Gaussian-type orbitals, too, and included the strain derivatives for Hartree-Fock calculations. In addition, Soler *et al.* [Sol02] presented the strain derivatives for numeric atom-centered orbitals with norm-conserving pseudopotentials calculating the electrostatics by Fast Fourier Transformation (FFT).

For this thesis, we derive the analytic strain derivatives, i.e., the stress tensor components, in the all-electron, numeric atom-centered orbital based density-functional formalism of FHI-aims. For this purpose, the general mathematical formulae and relations of strain derivatives are presented followed by a detailed derivation of the various contributions to the stress tensor arising from the total energy detailed in Sec. 3.6. Finally, details of the numerical implementation are given as well as how the stress tensor can be used to optimize crystal structures under external pressure. The derivations in this chapter follow the results published in [Knu15].

5.1 Fundamental formulae for strain derivatives

5.1.1 Properties of strain derivatives

The total energy derivative with respect to the strain in Eq. (5.3) can be written as

$$\left.\frac{\partial E_{\text{tot}}}{\partial \varepsilon_{\lambda\mu}}\right|_{\varepsilon=0} = \sum_i \frac{\partial E_{\text{tot}}(u_i)}{\partial u_i} \left.\frac{\partial u_i}{\partial \varepsilon_{\lambda\mu}}\right|_{\varepsilon=0}, \tag{5.4}$$

where the chain rule was used and the sum runs over all parameters u_i that enter the total energy and change under a strain transformation. For specified numerical and computational settings (basis set, integration grids, and DFA), the total energy solely depends on the chemical species (mass, nuclear charge, and electronic configuration) and the positions of the individual atoms. Because of periodic boundary conditions, the latter also includes the lattice vectors $\boldsymbol{a}_n$, since the periodic images of an atom with coordinate vector $\boldsymbol{R}_I$ are given by $\boldsymbol{R}'_I = \boldsymbol{R}_I + \sum_n M_n \boldsymbol{a}_n$ with M_n being integer numbers. Accordingly, the atomic positions in the unit cell and the lattice vectors are the only quantities changing under a strain transformation and their respective strain derivatives are derived below. There is no contributions from the coefficients for the basis set expansion c_{ij} in Eq. (3.1) because the total energy is minimized with respect to them (see Sec. 3.3), i.e., $\frac{\partial E_{\text{tot}}}{\partial c_{ij}} = 0$. Since the atom-centered basis functions (see Sec. 3.2) and the real space grid (see Sec. 3.4) used for the electronic degrees of freedom move with the respective nuclear degrees of freedom, their contributions to the strain derivatives need to be accounted for as well. However, some contributions to the total energy do not depend directly on the atomic positions or the lattice vectors. Instead, they depend on derived quantities. These are the volume of the system V and the reciprocal lattice $\boldsymbol{G}$-vectors. To achieve a more concise formalism, the strain derivatives for these quantities are derived here as well.

5.1.2 Strain derivative of position vectors

Following the respective strain transformation given in Eq. (5.1), the strain derivative of a general position vector $\boldsymbol{R}$ is

$$\left.\frac{\partial R_\alpha}{\partial \varepsilon_{\lambda\mu}}\right|_{\varepsilon=0} = \sum_\beta \delta_{\alpha\lambda}\delta_{\beta\mu} R_\beta = \delta_{\alpha\lambda} R_\mu. \tag{5.5}$$

In many cases, terms $f(\boldsymbol{r}_{\text{AB}})$ appear that do not depend on the absolute position but on position differences $\boldsymbol{r}_{\text{AB}} = \boldsymbol{r}_{\text{A}} - \boldsymbol{r}_{\text{B}}$. Following the chain rule in Eq. (5.4), we thus obtain

$$\left.\frac{\partial f(\boldsymbol{R}_{\text{AB}})}{\partial \varepsilon_{\lambda\mu}}\right|_{\varepsilon=0} = \frac{\partial f(\boldsymbol{R}_{\text{AB}})}{\partial R_{\text{A},\lambda}} R_{\text{A},\mu} + \frac{\partial f(\boldsymbol{R}_{\text{AB}})}{\partial R_{\text{B},\lambda}} R_{\text{B},\mu} = \frac{\partial f(\boldsymbol{R}_{\text{AB}})}{\partial R_{\text{A},\lambda}} (R_{\text{A},\mu} - R_{\text{B},\mu}). \tag{5.6}$$

Since the function $f(\boldsymbol{R}_{AB})$ depends only on the difference $\boldsymbol{R}_{\text{A}} - \boldsymbol{R}_{\text{B}}$, the derivative of the second summand can be changed from $\frac{\partial}{\partial R_{\text{B},\lambda}}$ to $-\frac{\partial}{\partial R_{\text{A},\lambda}}$. Please note that the here derived relations apply to the electronic degrees of freedom as well.

5.1.3 Strain derivative of lattice vectors

Following the respective strain transformation given in Eq. (5.2), the strain derivative of a lattice vector $\boldsymbol{a}_n$ is

$$\left.\frac{\partial a_{\alpha n}}{\partial \varepsilon_{\lambda\mu}}\right|_{\varepsilon=0} = \sum_\beta \delta_{\alpha\lambda}\delta_{\beta\mu}a_{\beta n} = \delta_{\alpha\lambda}a_{\mu n}. \tag{5.7}$$

5.1.4 Strain derivative of unit cell volume

The volume of the unit cell V can be calculated with the matrix of the lattice vectors A,

$$V = |\det A|. \tag{5.8}$$

With the help of Eq. (5.2), the strained volume is obtained:

$$V(\varepsilon) = |\det A(\varepsilon)| = \left|\det(\mathbb{1}+\varepsilon)\right| V(0) = \left|\sum_\alpha (1+\varepsilon_{\alpha\alpha})\right| V(0). \tag{5.9}$$

In the last step, the determinant was expanded up to first order in the strain. Taking the strain derivative of Eq. (5.9) leads to

$$\left.\frac{\partial V}{\partial \varepsilon_{\lambda\mu}}\right|_{\varepsilon=0} = \sum_\alpha \delta_{\alpha\lambda}\delta_{\alpha\mu}V = \delta_{\lambda\mu}V. \tag{5.10}$$

5.1.5 Strain derivative of reciprocal lattice vectors

In order to investigate how the unit vectors of the reciprocal lattice $\boldsymbol{b}_n$ behave under strain, we use the matrix of these unit vectors B and Eqs. (3.11) and (5.2) to obtain

$$B(\varepsilon) = 2\pi\left(\mathbb{1}+\varepsilon^{\mathrm{T}}\right)^{-1}\left(A^{\mathrm{T}}\right)^{-1} = \left(\mathbb{1}-\varepsilon^{\mathrm{T}}\right)B(0), \tag{5.11}$$

where we expanded the matrix inverse up to first order in the strain. The component-wise notation of Eq. (5.11) is

$$b_{\alpha n}(\varepsilon) = \sum_\beta (\delta_{\beta\alpha} - \varepsilon_{\beta\alpha})b_{\beta n}(0) \tag{5.12}$$

and hence, the strain derivative is

$$\left.\frac{\partial b_{\alpha n}}{\partial \varepsilon_{\lambda\mu}}\right|_{\varepsilon=0} = -\sum_\beta \delta_{\beta\lambda}\delta_{\alpha\mu}b_{\beta n} = -\delta_{\alpha\mu}b_{\lambda n}. \tag{5.13}$$

A general vector of the reciprocal lattice $\boldsymbol{G}$ is a linear combination of the three unit reciprocal lattice vectors,

$$\boldsymbol{G} = s_1\boldsymbol{b}_1 + s_2\boldsymbol{b}_2 + s_3\boldsymbol{b}_3, \tag{5.14}$$

with s_1, s_2, s_3 being integer numbers. Applying the result from Eq. (5.13) gives

$$\left.\frac{\partial G_\alpha}{\partial \varepsilon_{\lambda\mu}}\right|_{\varepsilon=0} = -\delta_{\alpha\mu}\Big(s_1 b_{\lambda 1} + s_2 b_{\lambda 2} + s_3 b_{\lambda 3}\Big) = -\delta_{\alpha\mu} G_\lambda. \tag{5.15}$$

Hence, for a quantity $f(\boldsymbol{G})$ that depends on the $\boldsymbol{G}$-vector, the strain derivative becomes

$$\left.\frac{\partial f(\boldsymbol{G})}{\partial \varepsilon_{\lambda\mu}}\right|_{\varepsilon=0} = -\sum_\alpha \frac{\partial f(\boldsymbol{G})}{\partial G_\alpha}\delta_{\alpha\mu} G_\lambda = -\frac{\partial f(\boldsymbol{G})}{\partial G_\mu} G_\lambda. \tag{5.16}$$

5.1.6 Strain derivative of integrals over the unit cell volume

Many quantities are calculated by integrals over the central unit cell, see Sec. 3.5. As a consequence, the integral boundaries change under strain, which has to be accounted for. Let us consider the integral of an arbitrary function f over the unit cell volume V,

$$I(V) = \int_V \mathrm{d}\boldsymbol{r}\, f(\boldsymbol{r}). \tag{5.17}$$

In order to take the strain derivative of this expression, we need to change the integration variable to fractional coordinates[1] $\boldsymbol{s}$, which are linked to the Cartesian coordinates $\boldsymbol{r}$ by

$$\boldsymbol{r} = A \cdot \boldsymbol{s}. \tag{5.18}$$

Using the transformation theorem for integrals and Eq. (5.8), the change of integration variables yields

$$I(V) = V \int_0^1 \mathrm{d}\boldsymbol{s}\, f(\boldsymbol{s}), \tag{5.19}$$

and the integration limits symbolize that the three components of the fractional coordinates lie in the range from 0 to 1. Taking the strain derivative of this transformed integral, using Eq. (5.10), and transforming it back results in

$$\left.\frac{\partial I(V)}{\partial \varepsilon_{\lambda\mu}}\right|_{\varepsilon=0} = \delta_{\lambda\mu} I(V) + \int_V \mathrm{d}\boldsymbol{r}\left.\frac{\partial f(\boldsymbol{r})}{\partial \varepsilon_{\lambda\mu}}\right|_{\varepsilon=0}. \tag{5.20}$$

The first term arises due to the finite integration limits, which change under strain, and we will call it Jacobian term from here on.

[1] Fractional coordinates mean that position vectors are expressed in the basis of the lattice vectors instead of the usual standard Cartesian basis.

5.2 Derivation of all stress tensor contributions

We will now determine the strain derivatives of all total energy contributions detailed in Sec. 3.6. For this purpose, we will reduce the strain derivatives to derivatives with respect to position vectors, which are known from the atomic force calculations [Blu09, Geh09]. The notation is simplified by leaving out the explicit notation that the derivative is evaluated at the point $\varepsilon = 0$ for the remainder of this thesis.

5.2.1 Kohn-Sham orbitals

We start with the KS orbitals Φ_i, which appear in most terms. Their strain derivative can be calculated using the basis set expansion (Eq. (3.4)) and Eq. (5.6),

$$\frac{\partial \Phi_i(\boldsymbol{r})}{\partial \varepsilon_{\lambda\mu}} = \sum_J^{N_{\text{nuc}}} \sum_j c_{ji} \frac{\partial \varphi_j(\boldsymbol{r} - \boldsymbol{R}_J)}{\partial R_{J,\lambda}} \Big(R_{J,\mu} - r_\mu \Big). \tag{5.21}$$

The strain derivative of the gradient of a KS orbital can be performed analogously,

$$\frac{\partial}{\partial \varepsilon_{\lambda\mu}} \frac{\partial \Phi_i(\boldsymbol{r})}{\partial R_{K,\nu}} = \sum_J^{N_{\text{nuc}}} \sum_j c_{ji} \frac{\partial^2 \varphi_j(\boldsymbol{r} - \boldsymbol{R}_J)}{\partial R_{J,\lambda} \partial R_{K,\nu}} \Big(R_{J,\mu} - r_\mu \Big), \tag{5.22}$$

which means that the Hessian of the basis functions is required for such strain derivatives.

5.2.2 Normalization factor

The strain derivative of the normalization factor in Eq. (3.20) yields

$$\frac{\partial F_{\text{norm}}}{\partial \varepsilon_{\lambda\mu}} = -\delta_{\lambda\mu} \sum_i f_i \epsilon_i \langle \Phi_i | \Phi_i \rangle - 2 \sum_i f_i \epsilon_i \langle \tfrac{\partial \Phi_i}{\partial \varepsilon_{\lambda\mu}} | \Phi_i \rangle, \tag{5.23}$$

and the strain derivative of the occupation numbers f_i is neglected since it turns out that their contribution plays no role for all considered cases in this thesis (see Chap. 6). The inner product of the two KS orbitals yields two terms according to Eqs. (2.17) and (5.20). Replacing $\epsilon_i \langle \Phi_i | \Phi_i \rangle$ in the first term in Eq. (5.23) by $\langle \Phi_i | \epsilon_i | \Phi_i \rangle$ and $\epsilon_i | \Phi_i \rangle$ by the generalized KS equation (2.44) yields

$$\frac{\partial F_{\text{norm}}}{\partial \varepsilon_{\lambda\mu}} = -\delta_{\lambda\mu} \Big[T_{\text{s}} + 2\alpha E_{\text{x}}^{\text{HF}} + \sum_i f_i \langle \Phi_i | \Big(\hat{v}_{\text{es}} + \hat{v}_{\text{xc}}^{\text{DFA}}(\alpha) \Big) | \Phi_i \rangle \Big] - 2 \sum_i f_i \epsilon_i \langle \tfrac{\partial \Phi_i}{\partial \varepsilon_{\lambda\mu}} | \Phi_i \rangle \tag{5.24}$$

with the help of Eqs. (2.18)/(3.26), (2.39), and (3.30).

5.2.3 Kinetic energy of non-interacting electrons

Non-relativistic kinetic energy

It is important to consider the change of the Laplace operator $\Delta_{\boldsymbol{r}}$ in Eq. (3.22) under a strain transformation. The change of a position vector $\boldsymbol{r}$ under such a transformation is given by Eq. (5.1) and the respective inverse relation (up to first order in the strain) is $r_\alpha(0) = \sum_\beta (\delta_{\alpha\beta} - \varepsilon_{\alpha\beta}) r_\beta(\varepsilon)$. Accordingly, the derivative with respect to positions transforms as

$$\frac{\partial}{\partial r_\alpha(\varepsilon)} = \sum_\beta \frac{\partial r_\beta(0)}{\partial r_\alpha(\varepsilon)} \frac{\partial}{\partial r_\beta(0)} = \frac{\partial}{\partial r_\alpha(0)} - \sum_\beta \varepsilon_{\alpha\beta} \frac{\partial}{\partial r_\beta(0)}. \tag{5.25}$$

Thus, the Laplace operator becomes (up to first order in the strain)

$$\Delta_{\boldsymbol{r}}(\varepsilon) = \sum_\alpha \left(\frac{\partial}{\partial r_\alpha(\varepsilon)} \right)^2 = \sum_\alpha \left(\frac{\partial}{\partial r_\alpha(0)} \right)^2 - 2 \sum_{\alpha,\beta} \varepsilon_{\alpha\beta} \frac{\partial}{\partial r_\alpha(0)} \frac{\partial}{\partial r_\beta(0)}. \tag{5.26}$$

Hence, the strain derivative of the Laplace operator is

$$\frac{\partial}{\partial \varepsilon_{\lambda\mu}} \Delta_{\boldsymbol{r}} = -2 \frac{\partial}{\partial r_\lambda} \frac{\partial}{\partial r_\mu}, \tag{5.27}$$

which requires the Hessian of the orbitals. Applying this result to the non-relativistic kinetic energy (Eq. (3.22)), which is an inner product of KS orbitals, yields the strain derivative

$$\frac{\partial T_\mathrm{s}^\text{non-rel}}{\partial \varepsilon_{\lambda\mu}} = \delta_{\lambda\mu} T_\mathrm{s}^\text{non-rel} - \sum_i f_i \left[\langle \tfrac{\partial \Phi_i}{\partial \varepsilon_{\lambda\mu}} | \Delta | \Phi_i \rangle - \langle \Phi_i | \tfrac{\partial}{\partial r_\lambda} \tfrac{\partial}{\partial r_\mu} | \Phi_i \rangle \right]. \tag{5.28}$$

Scalar relativistic kinetic energy

The strain derivative of the scalar relativistic kinetic energy (Eq. (3.26)) including the Jacobian term is

$$\frac{\partial T_\mathrm{s}^\mathrm{rel}}{\partial \varepsilon_{\lambda\mu}} = \delta_{\lambda\mu} T_\mathrm{s}^\mathrm{rel} + \sum_{JK}^{N_\mathrm{nuc}} \sum_{ijk} f_i c_{ij} c_{ik} \left[\langle \tfrac{\partial \varphi_j}{\partial \varepsilon_{\lambda\mu}} | \hat{t}_\text{at.ZORA} | \varphi_k \rangle + \langle \partial \varphi_k | \tfrac{\partial}{\partial \varepsilon_{\lambda\mu}} \left(\hat{t}_\text{at.ZORA} | \varphi_j \rangle \right) \right]. \tag{5.29}$$

The last derivative can be expressed in real space with the help of Eq. (5.6) as

$$\frac{\partial}{\partial \varepsilon_{\lambda\mu}} \left(\hat{t}_\text{at.ZORA} \varphi_j(\boldsymbol{r} - \boldsymbol{R}_J) \right) = \frac{\partial}{\partial R_{J,\lambda}} \left(\hat{t}_\text{at.ZORA} \varphi_j(\boldsymbol{r} - \boldsymbol{R}_J) \right) \left(R_{J,\mu} - r_\mu \right) \tag{5.30}$$

since the derivative of the full expression $\hat{t}_\text{at.ZORA} | \varphi_j \rangle$ with respect to atomic coordinates is known.

5.2.4 Electrostatics

Taking the strain derivative of the total electrostatic energy (Eq. (3.42)) results in many different terms that cannot be further simplified,

$$\begin{aligned}\frac{\partial E_{\text{es}}}{\partial \varepsilon_{\lambda\mu}} = \delta_{\lambda\mu}\int_V \mathrm{d}\boldsymbol{r}\left[n(\boldsymbol{r}) - \frac{1}{2}n_{\text{MP}}(\boldsymbol{r})\right]v_{\text{es}}(\boldsymbol{r}) + \int_V \mathrm{d}\boldsymbol{r}\left[n(\boldsymbol{r}) - \frac{1}{2}n_{\text{MP}}(\boldsymbol{r})\right]\frac{\partial v_{\text{es}}(\boldsymbol{r})}{\partial \varepsilon_{\lambda\mu}} \\ + \int_V \mathrm{d}\boldsymbol{r}\left[\frac{\partial n(\boldsymbol{r})}{\partial \varepsilon_{\lambda\mu}} - \frac{1}{2}\frac{\partial n_{\text{MP}}(\boldsymbol{r})}{\partial \varepsilon_{\lambda\mu}}\right]v_{\text{es}}(\boldsymbol{r}) + \frac{1}{2}\sum_{I,J\neq I}^{N_{\text{nuc}}} Z_I \frac{\partial v^J_{\text{es}}(\boldsymbol{R}_J - \boldsymbol{R}_I)}{\partial \varepsilon_{\lambda\mu}}.\end{aligned} \tag{5.31}$$

The terms can be regrouped using Eqs. (2.16) and (2.17),

$$\begin{aligned}\frac{\partial E_{\text{es}}}{\partial \varepsilon_{\lambda\mu}} = \sum_i f_i\Big[\delta_{\lambda\mu}\langle\Phi_i|\hat{v}_{\text{es}}|\Phi_i\rangle + \langle\Phi_i|\tfrac{\partial \hat{v}_{\text{es}}}{\partial \varepsilon_{\lambda\mu}}|\Phi_i\rangle + 2\langle\tfrac{\partial \Phi_i}{\partial \varepsilon_{\lambda\mu}}|\hat{v}_{\text{es}}|\Phi_i\rangle\Big] \\ - \delta_{\lambda\mu}\frac{1}{2}\int_V \mathrm{d}\boldsymbol{r}\, n_{\text{MP}}(\boldsymbol{r})v_{\text{es}}(\boldsymbol{r}) - \frac{1}{2}\int_V \mathrm{d}\boldsymbol{r}\left[n_{\text{MP}}(\boldsymbol{r})\frac{\partial v_{\text{es}}(\boldsymbol{r})}{\partial \varepsilon_{\lambda\mu}} + \frac{\partial n_{\text{MP}}(\boldsymbol{r})}{\partial \varepsilon_{\lambda\mu}}v_{\text{es}}(\boldsymbol{r})\right] \\ + \frac{1}{2}\sum_{I,J\neq I}^{N_{\text{nuc}}} Z_I \frac{\partial v^J_{\text{es}}(\boldsymbol{R}_J - \boldsymbol{R}_I)}{\partial \varepsilon_{\lambda\mu}}.\end{aligned} \tag{5.32}$$

The strain derivative of the multipole density n_{MP} can be evaluated using the partitioning into single atom contributions (Eq. (3.33)),

$$\frac{\partial n_{\text{MP}}(\boldsymbol{r})}{\partial \varepsilon_{\lambda\mu}} = \sum_I^{N_{\text{nuc}}} \frac{\partial n^I_{\text{MP}}(\boldsymbol{r} - \boldsymbol{R}_I)}{\partial \varepsilon_{\lambda\mu}} = \sum_I^{N_{\text{nuc}}} \frac{\partial n^I_{\text{MP}}(\boldsymbol{r} - \boldsymbol{R}_I)}{\partial R_{I,\lambda}}\big(R_{I,\mu} - r_\mu\big). \tag{5.33}$$

The strain derivative of the on-site term $Z_I v^I_{\text{H}}(0)$ (the atom interacts with its own electrons) that appears in Eq. (3.42) vanishes since the atom and its electron density transform equally under a strain deformation. A rigorous mathematical proof can be found in App. C.1.

The strain derivative of the total electrostatic potential v_{es} in Eq. (5.32) requires some more work. We have to calculate the individual strain derivatives of Eq. (3.41) together with Eqs. (3.35) and (3.40). The terms v^I_{free}, v^I_{NU}, and v^I_{SR} only depend on position vectors, thus, their derivatives are simply

$$\frac{\partial v^I_{\text{free}}(\boldsymbol{r} - \boldsymbol{R}_I)}{\partial \varepsilon_{\lambda\mu}} = \frac{\partial v^I_{\text{free}}(\boldsymbol{r} - \boldsymbol{R}_I)}{\partial R_{I,\lambda}}\big(R_{I,\mu} - r_\mu\big) \tag{5.34}$$

$$\frac{\partial v^I_{\text{NU}}(\boldsymbol{r} - \boldsymbol{R}_I)}{\partial \varepsilon_{\lambda\mu}} = \frac{\partial v^I_{\text{NU}}(\boldsymbol{r} - \boldsymbol{R}_I)}{\partial R_{I,\lambda}}\big(R_{I,\mu} - r_\mu\big) \tag{5.35}$$

$$\frac{\partial v^I_{\text{SR}}(\boldsymbol{r} - \boldsymbol{R}_I)}{\partial \varepsilon_{\lambda\mu}} = \frac{\partial v^I_{\text{SR}}(\boldsymbol{r} - \boldsymbol{R}_I)}{\partial R_{I,\lambda}}\big(R_{I,\mu} - r_\mu\big). \tag{5.36}$$

The most complicated term is v_{LR}^I (Eq. (3.38)) because it depends on volume V, positions $\boldsymbol{r}$, $\boldsymbol{R}_I$, and $\boldsymbol{G}$-vectors. Using Eq. (5.4) yields

$$\begin{aligned}\frac{\partial v_{\mathrm{LR}}^I(\boldsymbol{r}-\boldsymbol{R}_I)}{\partial \varepsilon_{\lambda\mu}} = \frac{v_{\mathrm{LR}}^I(\boldsymbol{r}-\boldsymbol{R}_I)}{\partial r_\lambda} r_\mu + \frac{\partial v_{\mathrm{LR}}^I(\boldsymbol{r}-\boldsymbol{R}_I)}{\partial R_{I,\lambda}} R_{I,\mu} \\ - \frac{\partial v_{\mathrm{LR}}^I(\boldsymbol{r}-\boldsymbol{R}_I)}{\partial G_\mu} G_\lambda + \frac{\partial v_{\mathrm{LR}}^I(\boldsymbol{r}-\boldsymbol{R}_I)}{\partial V} \delta_{\lambda\mu} V.\end{aligned} \tag{5.37}$$

Evaluating the individual derivatives results in the final expression

$$\frac{\partial v_{\mathrm{LR}}^I(\boldsymbol{r}-\boldsymbol{R}_I)}{\partial \varepsilon_{\lambda\mu}} = \frac{4\pi}{V} \sum_{\boldsymbol{G}} \frac{\exp\left(-\frac{\kappa^2 G^2}{4}\right)}{G^2} \exp(\mathrm{i}\boldsymbol{G}\cdot\boldsymbol{r}) \left[S_I(\boldsymbol{G})\Lambda_{\lambda\mu}(\boldsymbol{G}) - G_\lambda \Gamma_{I,\mu}(\boldsymbol{G})\right] \tag{5.38}$$

with

$$\Lambda_{\lambda\mu}(\boldsymbol{G}) = -\delta_{\lambda\mu} + \left(\frac{2}{G^2} + \frac{\kappa^2}{2}\right) G_\lambda G_\mu \tag{5.39}$$

$$\Gamma_{I,\mu}(\boldsymbol{G}) = \sum_{l,m} Q_{I,lm} G_{lm} \exp(-\mathrm{i}\boldsymbol{G}\cdot\boldsymbol{R}_I) \mathrm{i}^{D_{lm}} \gamma_\mu^{lm}(\boldsymbol{G}) \tag{5.40}$$

$$\gamma_\mu^{lm}(\boldsymbol{G}) = \frac{\partial}{\partial G_\mu} \left[(G_x)^{A_{lm}} (G_y)^{B_{lm}} (G_z)^{C_{lm}}\right]. \tag{5.41}$$

See App. C.2 for an explicit derivation of the individual derivatives of v_{LR}^I. The strain derivative of the average potential v_{avg} (Eq. (3.40)) only contains already calculated derivatives (the ones of δv_{es}, Eq. (3.35), i.e., v_{NU}^I, v_{SR}^I, and v_{LR}^I), so that no new contribution have to be calculated,

$$\frac{\partial v_{\mathrm{avg}}}{\partial \varepsilon_{\lambda\mu}} = \frac{1}{V} \int_V \mathrm{d}\boldsymbol{r}\, \frac{\partial \delta v_{\mathrm{es}}(\boldsymbol{r})}{\partial \varepsilon_{\lambda\mu}}. \tag{5.42}$$

Here, no Jacobian term appears due to the prefactor $1/V$.

5.2.5 Exchange-correlation energy

LDA

Using the chain rule and the definition of the exchange-correlation potential $\hat{v}_{\mathrm{xc}}^{\mathrm{LDA}}$ (Eq. (2.35)), the strain derivative of the exchange-correlation energy for the LDA functional (Eq. (3.44)) becomes

$$\begin{aligned}\frac{\partial E_{\mathrm{xc}}^{\mathrm{LDA}}}{\partial \varepsilon_{\lambda\mu}} &= \delta_{\lambda\mu} E_{\mathrm{xc}}^{\mathrm{LDA}} + \int_V \mathrm{d}\boldsymbol{r}\, \frac{\partial n(\boldsymbol{r})}{\partial \varepsilon_{\lambda\mu}} \left[\epsilon_{\mathrm{xc}}^{\mathrm{LDA}}(n) + n(\boldsymbol{r}) \frac{\partial \epsilon_{\mathrm{xc}}^{\mathrm{LDA}}(n)}{\partial n}\right] \\ &= \delta_{\lambda\mu} E_{\mathrm{xc}}^{\mathrm{LDA}} + 2 \sum_i f_i \langle \tfrac{\partial \Phi_i}{\partial \varepsilon_{\lambda\mu}} | \hat{v}_{\mathrm{xc}}^{\mathrm{LDA}}(n) | \Phi_i \rangle.\end{aligned} \tag{5.43}$$

There are again two terms due to the integration over the unit cell volume and the integral was rewritten according to Eqs. (2.16) and (2.17).

GGA

Since the exchange-correlation energy of GGA functionals (Eq. (3.45)) depends additionally on the density gradient ∇n, an additional term arises in the strain derivative,

$$\begin{aligned}\frac{\partial E_{\mathrm{xc}}^{\mathrm{GGA}}}{\partial \varepsilon_{\lambda\mu}} = \delta_{\lambda\mu} E_{\mathrm{xc}}^{\mathrm{GGA}} + \int_V \mathrm{d}\boldsymbol{r}\, \frac{\partial n(\boldsymbol{r})}{\partial \varepsilon_{\lambda\mu}} \left[\epsilon_{\mathrm{xc}}^{\mathrm{GGA}} + n(\boldsymbol{r}) \frac{\partial \epsilon_{\mathrm{xc}}^{\mathrm{GGA}}}{\partial n} \right] \\ + 2 \int_V \mathrm{d}\boldsymbol{r}\, n(\boldsymbol{r}) \left((\nabla n) \cdot \frac{\partial \nabla n}{\partial \varepsilon_{\lambda\mu}} \right) \frac{\partial \epsilon_{\mathrm{xc}}^{\mathrm{GGA}}}{\partial |\nabla n|^2}.\end{aligned} \tag{5.44}$$

The term in parentheses in the last line is a scalar product of vectors. A local exchange-correlation potential for GGA is defined, which includes only the partial derivative with respect to the density n,

$$\hat{v}_{\mathrm{xc,loc}}^{\mathrm{GGA}} = \epsilon_{\mathrm{xc}}^{\mathrm{GGA}} + n \frac{\partial \epsilon_{\mathrm{xc}}^{\mathrm{GGA}}}{\partial n}, \tag{5.45}$$

and the last line can be expanded using Eq. (2.16) and the product rule for derivatives,

$$\begin{aligned}\frac{\partial E_{\mathrm{xc}}^{\mathrm{GGA}}}{\partial \varepsilon_{\lambda\mu}} = \delta_{\lambda\mu} E_{\mathrm{xc}}^{\mathrm{GGA}} + 2 \sum_i f_i \langle \tfrac{\partial \Phi_i}{\partial \varepsilon_{\lambda\mu}} | \hat{v}_{\mathrm{xc,loc}}^{\mathrm{GGA}}(n) | \Phi_i \rangle \\ + 4 \sum_i f_i \int_V \mathrm{d}\boldsymbol{r}\, n(\boldsymbol{r}) (\nabla n) \cdot \left[\frac{\partial \Phi_i}{\partial \varepsilon_{\lambda\mu}} \nabla \Phi_i + \frac{\partial \nabla \Phi_i}{\partial \varepsilon_{\lambda\mu}} \Phi_i \right] \frac{\partial \epsilon_{\mathrm{xc}}^{\mathrm{GGA}}}{\partial |\nabla n|^2}.\end{aligned} \tag{5.46}$$

Hybrid functionals

The strain derivative of the HF exchange energy in the locally restricted expansion (Eq. (3.56)) is

$$\frac{\partial E_{\mathrm{x}}^{\mathrm{HF}}}{\partial \varepsilon_{\lambda\mu}} = -\frac{1}{2} \sum_{IJ}^{N_{\mathrm{nuc}}} \sum_{\substack{i,j,k,l \in \mathcal{B}(IJ) \\ \mathfrak{m},\mathfrak{n} \in \mathcal{P}(IJ)}} D_{jk} D_{il} \left[C_{ij}^{\mathfrak{m}} \frac{\partial V_{\mathfrak{m}\mathfrak{n}}}{\partial \varepsilon_{\lambda\mu}} C_{kl}^{\mathfrak{n}} + 2 \frac{\partial C_{ij}^{\mathfrak{m}}}{\partial \varepsilon_{\lambda\mu}} V_{\mathfrak{m}\mathfrak{n}} C_{kl}^{\mathfrak{n}} \right]. \tag{5.47}$$

In this case, no Jacobian terms arise since the integration domains of the Coulomb integrals are the whole space. In the following, we will use the notation $i(I)$ to indicate that the basis function i is centered on atom I. The strain derivative of the Coulomb matrix is given by

$$\begin{aligned}\frac{\partial V_{\mathfrak{m}(I)\mathfrak{n}(J)}}{\partial \varepsilon_{\lambda\mu}} &= \frac{\partial V_{\mathfrak{m}(I)\mathfrak{n}(J)}}{\partial R_{I,\lambda}} R_{I,\mu} + \frac{\partial V_{\mathfrak{m}(I)\mathfrak{n}(J)}}{\partial R_{J,\lambda}} R_{J,\mu} \\ &= \frac{\partial V_{\mathfrak{m}(I)\mathfrak{n}(J)}}{\partial R_{I,\lambda}} \left(R_{I,\mu} - R_{J,\mu} \right),\end{aligned} \tag{5.48}$$

a detailed proof of which is given in App. C.3. For the expansion coefficients, we obtain an analogous result

$$\begin{aligned}\frac{\partial C^{\mathfrak{m}(\mathfrak{M})}_{i(I)j(J)}}{\partial \varepsilon_{\lambda\mu}} &= \frac{\partial C^{\mathfrak{m}(\mathfrak{M})}_{i(I)j(J)}}{\partial R_{I,\lambda}} R_{I,\mu} + \frac{\partial C^{\mathfrak{m}(\mathfrak{M})}_{i(I)j(J)}}{\partial R_{J,\lambda}} R_{J,\mu} \\ &= \frac{\partial C^{\mathfrak{m}(\mathfrak{M})}_{i(I)j(J)}}{\partial R_{I,\lambda}} \Big(R_{I,\mu} - R_{J,\mu} \Big),\end{aligned} \tag{5.49}$$

where $\mathfrak{M}$ is either atom I or J and a detailed proof can be found in App. C.4. Using the relations derived in this section, the strain derivative of the hybrid exchange-correlation energy (Eq. (3.46)) is

$$\begin{aligned}\frac{\partial E^{\text{scr.hyb}}_{\text{xc}}(\alpha,\omega)}{\partial \varepsilon_{\lambda\mu}} &= \frac{\partial E^{\text{GGA}}_{\text{xc}}}{\partial \varepsilon_{\lambda\mu}} - \alpha \frac{\partial E^{\text{GGA,SR}}_{\text{x}}(\omega)}{\partial \varepsilon_{\lambda\mu}} \\ &\quad - \frac{\alpha}{2} \sum_{IJ}^{N_{\text{nuc}}} \sum_{\substack{i,j,k,l \in \mathcal{B}(IJ) \\ \mathfrak{m},\mathfrak{n} \in \mathcal{P}(IJ)}} D_{jk} D_{il} \Big(R_{I,\mu} - R_{J,\mu} \Big) \left[C^{\mathfrak{m}}_{ij} \frac{\partial V_{\mathfrak{m}\mathfrak{n}}(\omega)}{\partial R_{I,\lambda}} + 2 \frac{\partial C^{\mathfrak{m}}_{ij}}{\partial R_{I,\lambda}} V_{\mathfrak{m}\mathfrak{n}}(\omega) \right] C^{\mathfrak{n}}_{kl}.\end{aligned} \tag{5.50}$$

The strain derivative of the GGA exchange-correlation energy has been derived in the previous section (see Eq. (5.46)).

Van der Waals correction

The strain derivative of the vdW correction (Eq. (3.57)) is

$$\frac{\partial E_{\text{vdW}}}{\partial \varepsilon_{\lambda\mu}} = -\frac{1}{2} \sum_{I,J}^{N_{\text{nuc}}} \frac{C_{6IJ}}{|\boldsymbol{R}_I - \boldsymbol{R}_J|^6} \left[\frac{\partial f_{\text{damp}}(\boldsymbol{R}_I, \boldsymbol{R}_J)}{\partial R_{I,\lambda}} - 6 \frac{R_{I,\lambda} - R_{J,\lambda}}{|\boldsymbol{R}_I - \boldsymbol{R}_J|^2} \right] \Big(R_{I,\mu} - R_{J,\mu} \Big). \tag{5.51}$$

Here, the change of the C_6 coefficients and of the damping function f_{damp} (i.e., the change of the included vdW radii) under strain is neglected since they seem to be negligible in practice [Buč13].

5.3 Summary of terms – the stress tensor

We will now collect all contributions to the stress tensor derived in the previous sections. The terms with the Kronecker delta in Eq. (5.24) are rearranged to their respective energy category. Hence, the stress tensor is

$$\sigma_{\lambda\mu} = \sigma^{\text{norm}}_{\lambda\mu} + \sigma^{\text{kin}}_{\lambda\mu} + \sigma^{\text{es,nuc}}_{\lambda\mu} + \sigma^{\text{es,el}}_{\lambda\mu} + \sigma^{\text{es,MP}}_{\lambda\mu} + \sigma^{\text{xc}}_{\lambda\mu} + \sigma^{\text{vdW}}_{\lambda\mu} \tag{5.52}$$

with

$$\sigma_{\lambda\mu}^{\text{norm}} = -\frac{2}{V}\sum_i f_i \langle \frac{\partial \Phi_i}{\partial \varepsilon_{\lambda\mu}} | \epsilon_i | \Phi_i \rangle \tag{5.53}$$

$$\sigma_{\lambda\mu}^{\text{kin,non-rel}} = -\frac{1}{V}\sum_i f_i \langle \frac{\partial \Phi_i}{\partial \varepsilon_{\lambda\mu}} | \Delta | \Phi_i \rangle + \frac{1}{V}\sum_i f_i \langle \Phi_i | \frac{\partial}{\partial r_\lambda}\frac{\partial}{\partial r_\mu} | \Phi_i \rangle \tag{5.54}$$

$$\sigma_{\lambda\mu}^{\text{kin,rel}} = \frac{1}{V}\sum_{JK}^{N_{\text{nuc}}}\sum_{ijk} f_i c_{ij} c_{ik}\Big[\langle \frac{\partial \varphi_j}{\partial \varepsilon_{\lambda\mu}} | \hat{t}_{\text{at.ZORA}} | \varphi_k \rangle + \langle \partial \varphi_k | \frac{\partial}{\partial \varepsilon_{\lambda\mu}}\big(\hat{t}_{\text{at.ZORA}} | \varphi_j \rangle\big)\Big] \tag{5.55}$$

$$\sigma_{\lambda\mu}^{\text{es,nuc}} = \frac{1}{2V}\sum_{I,J\neq I}^{N_{\text{nuc}}} Z_I \frac{\partial v_{\text{es}}^J(\boldsymbol{R}_J - \boldsymbol{R}_I)}{\partial \varepsilon_{\lambda\mu}} \tag{5.56}$$

$$\sigma_{\lambda\mu}^{\text{es,el}} = \frac{1}{V}\sum_i f_i \Big[\langle \Phi_i | \frac{\partial \hat{v}_{\text{es}}}{\partial \varepsilon_{\lambda\mu}} | \Phi_i \rangle + 2\langle \frac{\partial \Phi_i}{\partial \varepsilon_{\lambda\mu}} | \hat{v}_{\text{es}} | \Phi_i \rangle\Big] \tag{5.57}$$

$$\begin{aligned}\sigma_{\lambda\mu}^{\text{es,MP}} = &-\delta_{\lambda\mu}\frac{1}{2V}\int_V \mathrm{d}\boldsymbol{r}\, n_{\text{MP}}(\boldsymbol{r}) v_{\text{es}}(\boldsymbol{r}) - \frac{1}{2V}\int_V \mathrm{d}\boldsymbol{r}\, n_{\text{MP}}(\boldsymbol{r})\frac{\partial v_{\text{es}}(\boldsymbol{r})}{\partial \varepsilon_{\lambda\mu}} \\ &- \frac{1}{2V}\sum_I^{N_{\text{nuc}}}\int_V \mathrm{d}\boldsymbol{r}\, \frac{\partial n_{\text{MP}}^I(\boldsymbol{r}-\boldsymbol{R}_I)}{\partial R_{I,\lambda}}\big(R_{I,\mu} - r_\mu\big) v_{\text{es}}(\boldsymbol{r})\end{aligned} \tag{5.58}$$

$$\sigma_{\lambda\mu}^{\text{xc,LDA}} = \delta_{\lambda\mu}\frac{1}{V}\Big(E_{\text{xc}}^{\text{LDA}} - \sum_i f_i \langle \Phi_i | \hat{v}_{\text{xc}}^{\text{LDA}} | \Phi_i \rangle\Big) + \frac{2}{V}\sum_i f_i \langle \frac{\partial \Phi_i}{\partial \varepsilon_{\lambda\mu}} | \hat{v}_{\text{xc}}^{\text{LDA}}(n) | \Phi_i \rangle \tag{5.59}$$

$$\begin{aligned}\sigma_{\lambda\mu}^{\text{xc,GGA}} = &\,\delta_{\lambda\mu}\frac{1}{V}\Big(E_{\text{xc}}^{\text{GGA}} - \sum_i f_i \langle \Phi_i | \hat{v}_{\text{xc}}^{\text{GGA}} | \Phi_i \rangle\Big) + \frac{2}{V}\sum_i f_i \langle \frac{\partial \Phi_i}{\partial \varepsilon_{\lambda\mu}} | \hat{v}_{\text{xc,loc}}^{\text{GGA}}(n) | \Phi_i \rangle \\ &+ \frac{4}{V}\sum_i f_i \int_V \mathrm{d}\boldsymbol{r}\, n(\boldsymbol{r})(\nabla n)\cdot\Big[\frac{\partial \Phi_i}{\partial \varepsilon_{\lambda\mu}}\nabla\Phi_i + \frac{\partial \nabla \Phi_i}{\partial \varepsilon_{\lambda\mu}}\Phi_i\Big]\frac{\partial \epsilon_{\text{xc}}^{\text{GGA}}}{\partial |\nabla n|^2}\end{aligned} \tag{5.60}$$

$$\begin{aligned}\sigma_{\lambda\mu}^{\text{xc,scr.hyb}} = &\,\sigma_{\lambda\mu}^{\text{xc,GGA}} - \alpha\sigma_{\lambda\mu}^{\text{x,GGA,SR}}(\omega) - \delta_{\lambda\mu}\frac{2\alpha}{V}E_{\text{x}}^{\text{HF,SR}}(\omega) \\ &- \frac{\alpha}{2V}\sum_{IJ}^{N_{\text{nuc}}}\sum_{\substack{i,j,k,l\in\mathcal{B}(IJ)\\ \mathfrak{m},\mathfrak{n}\in\mathcal{P}(IJ)}} D_{jk}D_{il}\big(R_{I,\mu} - R_{J,\mu}\big)\Big[C_{ij}^{\mathfrak{m}}\frac{\partial V_{\mathfrak{m}\mathfrak{n}}(\omega)}{\partial R_{I,\lambda}} + 2\frac{\partial C_{ij}^{\mathfrak{m}}}{\partial R_{I,\lambda}}V_{\mathfrak{m}\mathfrak{n}}(\omega)\Big]C_{kl}^{\mathfrak{n}}\end{aligned} \tag{5.61}$$

$$\sigma_{\lambda\mu}^{\text{vdW}} = -\frac{1}{2V}\sum_{I,J}^{N_{\text{nuc}}}\frac{C_{6IJ}}{|\boldsymbol{R}_I - \boldsymbol{R}_J|^6}\Big[\frac{\partial f_{\text{damp}}(\boldsymbol{R}_I,\boldsymbol{R}_J)}{\partial R_{I,\lambda}} - 6\frac{R_{I,\lambda} - R_{J,\lambda}}{|\boldsymbol{R}_I - \boldsymbol{R}_J|^2}\Big]\big(R_{I,\mu} - R_{J,\mu}\big). \tag{5.62}$$

The strain derivative of the total electrostatic potential has been calculated before,

$$\frac{\partial v_{\text{es}}(\boldsymbol{r})}{\partial \varepsilon_{\lambda\mu}} = \sum_I^{N_{\text{nuc}}}\Big[\frac{\partial v_{\text{free}}^I(\boldsymbol{r}-\boldsymbol{R}_I)}{\partial \varepsilon_{\lambda\mu}} + \frac{\partial v_{\text{NU}}^I(\boldsymbol{r}-\boldsymbol{R}_I)}{\partial \varepsilon_{\lambda\mu}} + \frac{\partial v_{\text{SR}}^I(\boldsymbol{r}-\boldsymbol{R}_I)}{\partial \varepsilon_{\lambda\mu}} + \frac{\partial v_{\text{LR}}^I(\boldsymbol{r}-\boldsymbol{R}_I)}{\partial \varepsilon_{\lambda\mu}}\Big] - \frac{\partial v_{\text{avg}}}{\partial \varepsilon_{\lambda\mu}}, \tag{5.63}$$

and the individual derivatives can be looked up in Eqs. (5.34), (5.35), (5.36), (5.38), and (5.42). The strain derivatives of the KS orbitals Φ_i and their gradients are given in Eqs. (5.21) and (5.22), respectively. Please note that Eqs. (5.53), (5.54), (5.55), (5.57), (5.59), (5.60), and (5.61) includes Pulay terms of the form $\langle \frac{\partial \varphi_j}{\partial \varepsilon_{\lambda\mu}} | \ldots | \varphi_k \rangle$ that depend on the strain derivative of the orbitals analogously to the Pulay corrections of atomic forces [Pul69].

5.4 Implementation details

It is advantageous to compute terms of the stress tensor with the same bra and ket together in an actual computation to reduce the numerical effort. Furthermore, this practice avoids taking differences of large numbers and thereby leads to a reduction of numerical errors. In detail, this grouping means that the terms of the form $\langle \varphi_j | \ldots | \varphi_k \rangle$ of Eqs. (5.54)/(5.55), (5.57), and (5.59)/(5.60)/(5.61) are computed together as one integral. The same is done for terms of the form $\langle \frac{\partial \varphi_j}{\partial \varepsilon_{\lambda\mu}} | \ldots | \varphi_k \rangle$ of Eqs. (5.53), (5.54)/(5.55), (5.57), and (5.59)/(5.60)/(5.61).

The calculation of the stress tensor involves integrals of quantities f_I and g_I and their derivatives that are centered on the same atom I, i.e., $\int \mathrm{d}\boldsymbol{r}\, \frac{\partial f_I(\boldsymbol{r})}{\partial r_\alpha} g_I(\boldsymbol{r})$. The integrands of these on-site terms are typically multiple orders of magnitude larger than those of off-site terms (quantities centered at different atoms), especially for heavy elements. Accordingly, even minute relative numerical inaccuracies, e.g., due to relatively sparse integration grids used for light settings (see App. B.4) or in the derivatives of the spherical harmonics, can result in notable absolute numerical inaccuracies for the stress tensor – even for a single on-site term. In the next two subsections, we will point out the problematic terms and how these issues can be circumvented.

5.4.1 Kinetic on-site correction

The term $\langle \Phi_i | \Delta | \Phi_i \rangle$ of the non-relativistic kinetic energy (Eq. (3.22)) can be numerically inaccurate for sparse integration grids. This inaccuracy stems from the on-site terms, i.e., the inner products of basis functions j and j' located on the same atom J, namely

$$T_\mathrm{s}^{\text{non-rel,on-site}} = -\frac{1}{2} \sum_J^{N_\mathrm{nuc}} \sum_{i,j,j'} f_i c_{ij} c_{ij'} \langle \varphi_j | \Delta | \varphi_{j'} \rangle. \tag{5.64}$$

Analytically, the strain derivative of this term and each of its summands $\langle \varphi_j | \Delta | \varphi_{j'} \rangle$ should be zero since only quantities centered on one atom appear. However, this is not always the case in a numerical calculation: Since both basis functions are located on the same atom, they have a huge overlap, and small numerical inaccuracies in such a

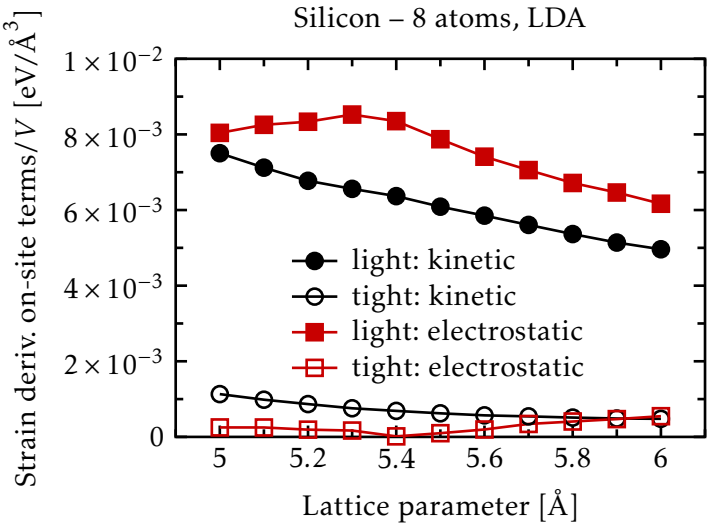

Figure 5.2: Absolute value of strain derivatives divided by unit cell volume V of kinetic (black circles, Eq. (5.64)) and electrostatic on-site terms (red squares, Eq. (5.66)) at different lattice parameters. These terms are analytically zero but might be non-vanishing in an actual numerical calculation and therefore, they are omitted, see text. For light integration grids (filled symbols), the strain derivatives of the on-site terms are clearly non-zero whereas they become significantly smaller for tight grids (open symbols). A denser integration grid (going from light to tight) captures more accurately the overlap of the wave functions centered at the same atom. See App. B.4 for more details about the used integration grid. The calculations were performed for a diamond unit cell of silicon (8 atoms) with the LDA functional.

large term can effectively prevent these terms from vanishing as explained above. See Fig. 5.2 for a comparison between different integrations grids for the strain derivative of this on-site term. To correct for this erroneous behavior, the on-site term (Eq. (5.64)) is omitted from Eq. (5.28) and therefore,

$$\frac{\partial T_\mathrm{s}^\text{non-rel}}{\partial \varepsilon_{\lambda\mu}} = \delta_{\lambda\mu} T_\mathrm{s}^\text{non-rel} - \sum_{J}^{N_\text{nuc}} \sum_{K\neq J}^{N_\text{nuc}} \sum_{ijk} f_i c_{ij} c_{ik} \left[\left\langle \frac{\partial \varphi_j}{\partial \varepsilon_{\lambda\mu}} \middle| \Delta \middle| \varphi_k \right\rangle - \left\langle \varphi_j \middle| \frac{\partial}{\partial r_\lambda} \frac{\partial}{\partial r_\mu} \middle| \varphi_k \right\rangle \right]. \tag{5.65}$$

Here, J and K specify the atoms the basis functions j and k are associated with, respectively, and it is enforced that atom K is different from atom J.

5.4.2 Electrostatic on-site correction

A similar problem occurs for the electrostatics. In Eq. (3.42), special care has to be taken of the strain derivative of the integral involving the term $n_\mathrm{MP}(\boldsymbol{r}) v_\mathrm{es}(\boldsymbol{r})$. One part of the total electrostatic potential v_es includes the sum of the potentials of the free atoms

$\sum_I v^I_{\text{free}}(\boldsymbol{r}-\boldsymbol{R}_I)$ (Eq. (3.41)) and the multipole density n_{MP} is built up from the sum of the electron density of the free atoms $\sum_I n^I_{\text{free}}(\boldsymbol{r}-\boldsymbol{R}_I)$ and a residual part (Eq. (3.33)). Hence, the total electrostatic energy in Eq. (3.42) involves a term that corresponds to the sum of the Hartree energy of the isolated free atoms,

$$E_{\text{es,free}} = -\frac{1}{2}\sum_I \int_V \mathrm{d}\boldsymbol{r}\, n^I_{\text{free}}(\boldsymbol{r}-\boldsymbol{R}_I) v^I_{\text{free}}(\boldsymbol{r}-\boldsymbol{R}_I). \tag{5.66}$$

Analytically, the strain derivative of this term is zero since it includes only contributions of isolated free atoms. However, numerical inaccuracies can prevent this term from vanishing, especially for sparse integration grids, as explained above. See Fig. 5.2 for a comparison between different integrations grids for the strain derivatives of this on-site term. To correct for this erroneous behavior, we explicitly leave out the strain derivative of the on-site term (Eq. (5.66)), which is

$$\begin{aligned}\frac{\partial E_{\text{es,free}}}{\partial \varepsilon_{\lambda\mu}} &= \delta_{\lambda\mu} E_{\text{es,free}} \\ &\quad - \frac{1}{2}\sum_I \int_V \mathrm{d}\boldsymbol{r}\left(R_{I,\mu} - r_\mu\right)\left[n^I_{\text{free}}(\boldsymbol{r}-\boldsymbol{R}_I)\frac{\partial v^I_{\text{free}}(\boldsymbol{r}-\boldsymbol{R}_I)}{\partial R_{I,\lambda}} + \frac{\partial n^I_{\text{free}}(\boldsymbol{r}-\boldsymbol{R}_I)}{\partial R_{I,\lambda}} v^I_{\text{free}}(\boldsymbol{r}-\boldsymbol{R}_I)\right],\end{aligned} \tag{5.67}$$

during the calculation of the electrostatic contributions. Together with the correction for the kinetic energy in the previous section, this allows to reduce the numerical inaccuracies by roughly one order of magnitude.

5.5 Finite differences stress tensor

In order to check the accuracy of the implemented analytical derivatives of the stress tensor (see Chap. 6), we also calculate the stress tensor numerically via finite differences of the total energies of distorted structures. This numerical procedure has been implemented in FHI-aims by V. Atalla [Ata13a]. Without accounting for space group symmetry, this requires the total energy calculation of twelve slightly distorted structures, i.e., two strain transformations $\varepsilon_{\lambda\mu} = \Delta h$ and $\varepsilon_{\lambda\mu} = -\Delta h$ for each of the six independent components of the stress tensor. The numerical derivative using the symmetric difference quotient is

$$\sigma_{\lambda\mu} = \frac{1}{V}\frac{E_{\text{tot}}(\varepsilon_{\lambda\mu}=\Delta h) - E_{\text{tot}}(\varepsilon_{\lambda\mu}=-\Delta h)}{2\Delta h} + \mathcal{O}(\Delta h^2). \tag{5.68}$$

On the one hand, the displacement Δh must be small enough to ensure that the two-point numerical derivative yields reasonable results. On the other hand, Δh must not be too small at the same time. Otherwise, the differences become too small, which

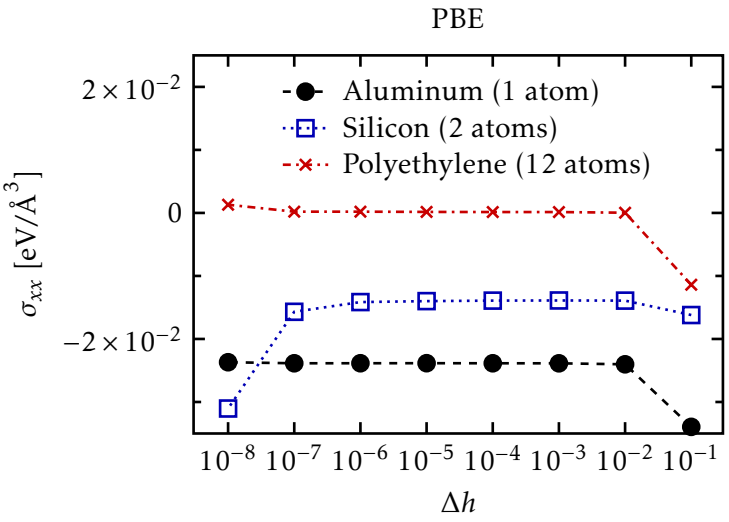

Figure 5.3: Convergence of the finite differences stress tensor σ with respect to distortion Δh (Eq. (5.68)), which is used for reference purposes in this thesis in order to validate the analytical derivatives of the stress tensor in Chap. 6. The ordinate shows the component σ_{xx}. Around $\Delta h = 10^{-4}$, the stress tensor changes by values lower than 1 meV/Å^{-3}, which means that $\Delta h = 10^{-4}$ is a safe choice and yields accurate results. Decreasing Δh too much leads to large numerical rounding errors and a loss in accuracy. Calculations with Δh above 10^{-2} become inaccurate, too, since the displacement is becoming too big. The calculations were performed at fixed numerical settings with the PBE functional.

leads to large numerical rounding errors. The convergence analysis with respect to the displacement Δh, see Fig. 5.3, shows that the value $\Delta h = 10^{-4}$ chosen for all calculations presented in this thesis is reasonable. With this choice, we are in agreement with literature suggestions [Gol13], which propose values $\Delta h < 10^{-2}$.

5.6 Unit cell optimization with external pressure

The stress tensor can be used to optimize the unit cell of a crystal structure. For this, the forces acting on the lattice vectors $\boldsymbol{a}_n$ are required, which we define as the negative derivative of the total energy E_{tot} with respect to the lattice vectors,

$$\boldsymbol{F}_n^{\text{lat}} = -\frac{\partial E_{\text{tot}}}{\partial \boldsymbol{a}_n}. \tag{5.69}$$

Since the stress tensor depends only on the atomic positions and the lattice vectors, Eq. (5.4) becomes

$$V\sigma_{\lambda\mu} = \sum_{I}^{N_{\text{nuc}}} \frac{\partial E_{\text{tot}}}{\partial R_{I,\lambda}} R_{I,\mu} + \sum_{n=1}^{3} \frac{\partial E_{\text{tot}}}{\partial a_{\lambda n}} a_{\mu n}, \tag{5.70}$$

where the strain derivatives have been evaluated according to Eqs. (5.5) and (5.7). The derivatives of the total energy with respect to the atomic positions are the atomic forces,

$$F_{I,\lambda} = -\frac{\partial E_{\text{tot}}}{\partial R_{I,\lambda}}. \tag{5.71}$$

Here, $F_{I,\lambda}$ is component λ of the force acting on atom I. Solving Eq. (5.70) for the lattice vector derivative yields the forces acting on the lattice vectors,

$$F^{\text{lat}}_{\lambda n} = -V \sum_{\mu=1}^{3} \sigma_{\lambda\mu} \left(A^{-1}\right)_{n\mu} - \sum_{\mu=1}^{3} \sum_{I}^{N_{\text{nuc}}} F_{I,\lambda} R_{I,\mu} \left(A^{-1}\right)_{n\mu} \tag{5.72}$$

with A the matrix of the lattice vectors. $F^{\text{lat}}_{\lambda n}$ is component λ of the force acting on lattice vector $\boldsymbol{a}_n$.

Together with the atomic forces, the lattice vector forces can be used to optimize the structure of the unit cell and the position of the atoms of a crystal. A generalized coordinate vector is defined, $\boldsymbol{X} = \{a_{x1}, a_{y1}, \ldots, a_{z3}, R_{1,x}, R_{1,y}, \ldots, R_{N,z}\}$, in order to treat atoms and lattice vectors on equal footing. This vector contains the lattice vectors and atomic positions. In addition, the corresponding generalized force vector is defined as $\boldsymbol{F} = \{F^{\text{lat}}_{x1}, F^{\text{lat}}_{y1}, \ldots, F^{\text{lat}}_{z3}, F_{1,x}, F_{1,y}, \ldots, F_{N,z}\}$ containing the lattice vector forces and atomic forces. The vectors $\boldsymbol{X}$ and $\boldsymbol{F}$ as well as the total energy E_{tot} can be used as an input for an optimization scheme to obtain the local minimum of the crystal structure, e.g., the Broyden-Fletcher-Goldfarb-Shanno algorithm or the trust region method [Noc06]. The optimization algorithms in FHI-aims have been extended by V. Atalla to include lattice degrees of freedom [Ata13a].

The above described method to optimize crystal structures can be extended to the case where external pressure is acting on the crystal. When external hydrostatic pressure p_{ext} is applied to the crystal, the enthalpy $H(S,p)$ has to be minimized instead of the total (inner) energy $E_{\text{tot}}(S,V)$ of the underlying system. The enthalpy is given by

$$H(S,p) = E_{\text{tot}}(S,V) + p_{\text{ext}} V \tag{5.73}$$

with V the volume of the system. It is immediately apparent that the atomic forces are not affected by the external pressure, however, there is an additional contribution to the stress tensor since the unit cell volume depends on the strain. Using Eq. (5.10) to calculate the contribution of the external pressure yields the total stress of the system

$$\sigma^{\text{tot}}_{\lambda\mu} = \sigma_{\lambda\mu} + \delta_{\lambda\mu} p_{\text{ext}}, \tag{5.74}$$

and $\sigma_{\lambda\mu}$ is given in Eq. (5.52). Finding the local minimum under pressure works exactly as described above: $\sigma_{\lambda\mu}$ in Eq. (5.72) is just replaced by $\sigma^{\text{tot}}_{\lambda\mu}$ from Eq. (5.74) and the enthalpy H is used instead of the total energy E_{tot}.

Since the numerical optimization schemes obtain only local minima, it is unlikely that one can directly observe phase transitions between different crystal structures under pressure if there is an energy barrier between different structures as it is often the case. Especially, transitions will be observed too late, i.e., at a much higher pressures compared to the actual transition pressure. In order to overcome such barriers, molecular dynamics simulations at temperatures greater than 0 K are required. This means that systems under pressure usually stay within their initial crystal structure during optimization unless they are significantly distorted in the beginning.

6 Validation

In this chapter, the implementation of the stress tensor in FHI-aims is validated by extensively comparing the stress obtained from analytical gradients (Sec. 5.3), in short analytical stress, and the stress from finite differences (Sec. 5.5), in short numerical stress. Since numerous aspects are considered, this validation is divided into three sections: First, a large variety of crystal systems and chemical species is investigated. The main focus lies on the diagonal elements of the stress tensor, but its off-diagonal elements are considered, too. Furthermore, the consistency of the analytical stress with respect to the chosen DFA, basis set size, and unit cell size is investigated as well as the performance of the implementation. The second section addresses the usage of the analytical stress tensor for the unit cell optimization described in Sec. 5.6. Therefore, the change from a cubic to a fcc unit cell for aluminum is investigated. In the last section, the optimization of crystals under pressures, briefly explained in Sec. 5.6, is discussed. This is exemplified by the investigation of the transition pressure for the phase transition of silicon from the diamond to the β-tin structure. The validation in Sec. 6.1 follows the results published in [Knu15].

6.1 Stress tensor

Unless noted otherwise, all calculations of the analytical stress tensor in this section are performed with the n/r^2-type partitioning function described in Sec. 3.4. The effect of this and the "modified Stratmann" partitioning function on the stress tensor is discussed in Sec. 6.1.4.

6.1.1 Different crystals

The analytical implementation of the stress tensor is tested with various different crystal systems, chemical species and computational settings. At different lattice parameters around the equilibrium geometry, the numerical and analytical stress are computed by single point calculations. Figure 6.1 shows a plot of such calculations for silicon. If the crystal system has more than one lattice parameter, each one is separately varied while keeping the other ones fixed. The differences between the numerical and analytical stress

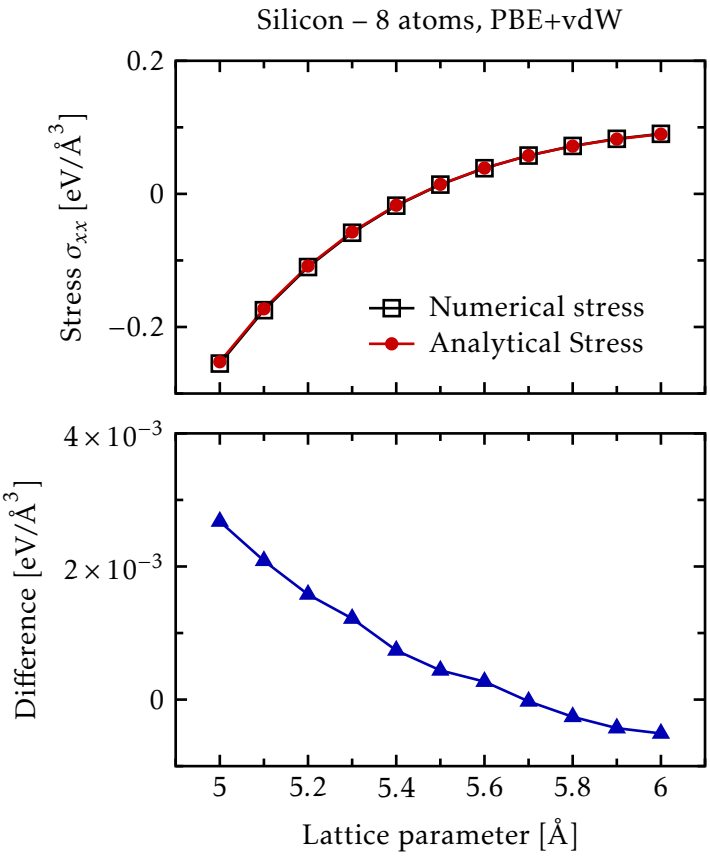

Figure 6.1: Comparison between numerical (black open squares) and analytical (red filled circles) stress for a silicon crystal at different lattice parameters. The top figure shows the resulting stress for both types and the bottom figure the difference between the two. The calculations were performed for a diamond unit cell of silicon (8 atoms) with the PBE functional and vdW corrections.

are then evaluated by calculating the mean of these differences as well as the maximum of the absolute differences and the standard deviation. Additionally, we determine the relative values of the maximum absolute difference.

In Tab. 6.1, the results for a broad range of crystals and computational settings (DFA, relativistic and spin treatment) are listed. We find that our analytical implementation is very accurate by comparing to the numerical stress for all tested crystal systems and DFAs. The mean difference, maximum absolute difference, and standard deviation of the difference between these two quantities are always in the range of a few meV/Å^3 or below, i.e., in the order of magnitude of the numerical error of the numerical stress tensor (see Sec. 5.5). Also, the relative values of the maximum absolute difference are

Table 6.1: Mean difference, maximum absolute difference, relative maximum absolute difference, and standard deviation of the difference between numerical and analytical stress for different crystals. All values are given in units of meV/Å^3 except for the relative maximum absolute difference, which is given in %. For the listed systems, the crystal, its structure, and the total number of atoms in the unit cell are given. Under computational settings, the used DFA is noted as well as the chosen relativistic treatment (no entry means non-relativistic). Additionally, a collinear spin treatment was used for iron. It is also listed, which lattice parameter is varied and which corresponding stress component (σ_{ii}) is evaluated.

Crystal	#Atoms	Comp. settings	Latt. par.	σ_{ii}	Mean diff.	Max. diff.	Rel. max. diff.	Std. dev.
Aluminum (fcc)	4	PBE	a	xx	0.6	3.1	0.9	1.3
Ammonia (cubic)	16	HSE06+vdW	a	xx	−0.3	0.4	1.1	0.1
Benzene (orthorhombic)	48	HSE06+vdW	a	xx	−0.4	0.9	0.7	0.5
			b	yy	−1.4	1.8	0.2	0.4
			c	zz	−0.1	0.6	0.3	0.5
Carbon dioxide (cubic)	12	HSE06+vdW	a	xx	−0.5	0.6	0.7	0.1
Gold (fcc)	4	PBE, rel.	a	xx	0.6	2.2	0.3	0.7
Graphite (hexagonal)	4	PBE+vdW	a	xx	−4.1	6.7	0.4	1.5
			c	zz	−0.9	1.3	0.9	0.2
Hexamine (bcc)	22	HSE06+vdW	a	xx	−0.2	0.2	0.2	0.0
Iron (bcc)	1	PBE, rel., coll. spin	a	xx	0.0	0.3	0.0	0.1
		PBE0, rel., coll. spin	a	xx	−0.5	6.5	0.3	3.0
Naphthalene (monoclinic)	36	HSE06+vdW	a	xx	−0.1	0.4	0.5	0.3
			b	yy	−1.1	1.8	0.6	0.7
			c	zz	−1.9	2.3	0.3	0.3
Sodium (bcc)	2	PBE	a	xx	−0.1	0.3	0.6	0.1
Sodium chloride (rock salt)	2	PBE	a	xx	0.3	0.6	0.6	0.2
Silicon (diamond)	8	LDA	a	xx	0.8	1.8	0.8	0.7
		PBE+vdW	a	xx	0.7	2.7	1.1	1.1
		PBE0	a	xx	1.0	2.7	1.0	0.9
		HSE06	a	xx	1.0	2.7	1.0	0.9
Silicon carbide (wurtzite)	4	PBE	a	xx	1.8	2.5	0.4	0.8
			c	zz	0.2	0.8	0.2	0.5
Urea (tetragonal)	16	HSE06+vdW	a	xx	−0.2	0.4	0.4	0.1
			c	zz	−1.4	1.7	0.6	0.3

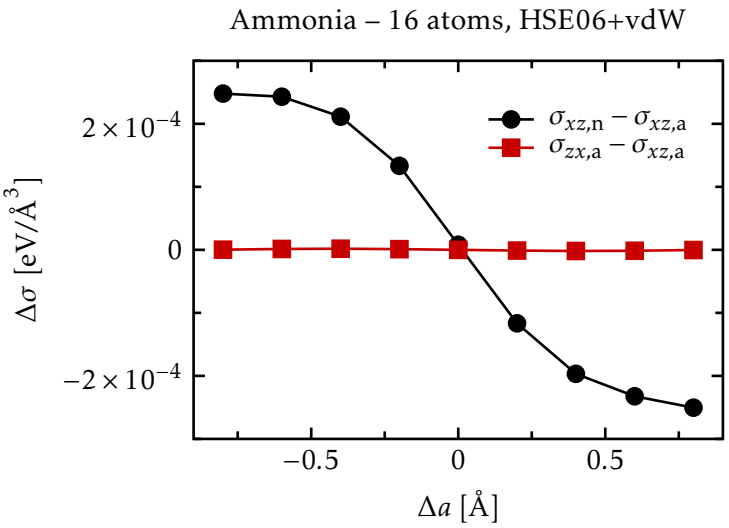

Figure 6.2: Off-diagonal stress for a strained cubic unit cell with lattice vectors $(a, 0, \Delta a)$, $(0, a, 0)$, and $(\Delta a, 0, a)$. Black circles: Difference between the off-diagonal element xz of numerical ($\sigma_{xz,\mathrm{n}}$) and analytical ($\sigma_{xz,\mathrm{a}}$) stress. Red squares: Difference between the off-diagonal elements of lower ($\sigma_{zx,\mathrm{a}}$) and upper ($\sigma_{xz,\mathrm{a}}$) triangle of the analytical stress. The calculations were performed for a unit cell of ammonia (16 atoms) with the HSE06 functional and vdW corrections at a lattice parameter $a = 5.1$ Å.

always 1 % or below. Furthermore, no constant offset, systematic variation, or regular pattern could be found in the respective deviations.

So far, we have only looked at the diagonal elements of the stress tensor. We next address the off-diagonal elements at an exemplary system. In general, it suffices to calculate the upper (lower) triangle of the stress tensor since it is symmetric by definition. However, to test the numerical accuracy of our implementation, we calculate the full stress tensor and compare the off-diagonal elements. Figure 6.2 demonstrates that the difference between upper and lower triangle is vanishingly small. In addition, it shows that the off-diagonal elements of the analytical stress are very accurate in comparison to the numerical stress, too. In summary, not only the diagonal elements of the analytical stress are accurate but also the off-diagonal ones and our implementation reproduces nicely the symmetry of the stress tensor.

6.1.2 Different functionals

As a further test, calculations with all LDA, GGA and hybrid functionals available within FHI-aims were performed. Table 6.2 lists the resulting difference between the numerical and analytical stress for a silicon crystal and shows that our implementation is consistent across all tested DFAs.

Table 6.2: Difference between numerical and analytical stress in units of meV/Å^3 for different DFAs. The calculations were performed for a diamond unit cell of silicon (8 atoms) at a lattice parameter of 5.2 Å.

	AM05	B3LYP	BLYP	HF	HSE06	PBE	PBE0
Difference	1.4	1.9	1.8	1.8	1.8	1.8	1.8

	PBEint	PBEsol	PBEsol0	PW-LDA	PZ-LDA	revPBE	RPBE
Difference	1.4	1.8	1.8	1.5	1.4	1.7	1.7

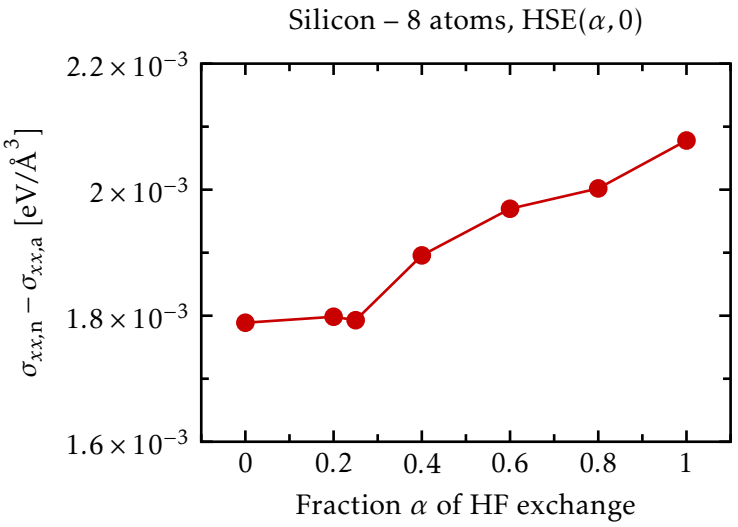

Figure 6.3: Difference between numerical ($\sigma_{xx,\mathrm{n}}$) and analytical ($\sigma_{xx,\mathrm{a}}$) stress for different fractions α of HF exchange. The calculations were performed for a diamond unit cell of silicon (8 atoms) with the HSE(α, 0) functional (Sec. 2.3.5) at a lattice parameter of 5.2 Å.

Furthermore, the fraction α of the HF exchange for hybrid functionals (Sec. 2.3.5) can be varied to check the accuracy of the analytical stress. For a silicon crystal, the difference to the numerical stress stays almost constant, see Fig. 6.3, and scales only weakly with α showing that we have a consistent implementation.

6.1.3 Basis set and unit cell size

Next, we demonstrate the consistency of the analytical stress with respect to the basis set and unit cell size. The difference between numerical and analytical stress stays almost constant when the basis set size is increased, see Fig. 6.4. Figure 6.5 shows that the

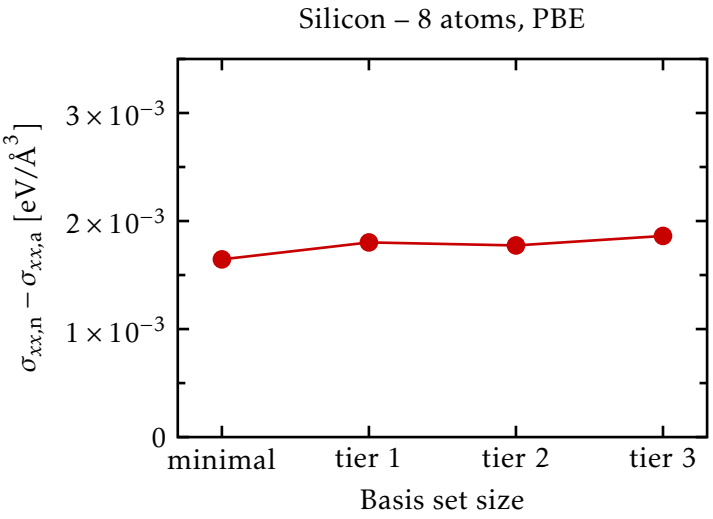

Figure 6.4: Difference between numerical ($\sigma_{xx,\mathrm{n}}$) and analytical ($\sigma_{xx,\mathrm{a}}$) stress for increasing basis set size. The higher the tier in FHI-aims, the more basis functions are included, see App. B.1. For more details about the used basis set, see App. B.2. The calculations were performed for a diamond unit cell of silicon (8 atoms) with the PBE functional at a lattice parameter of 5.2 Å.

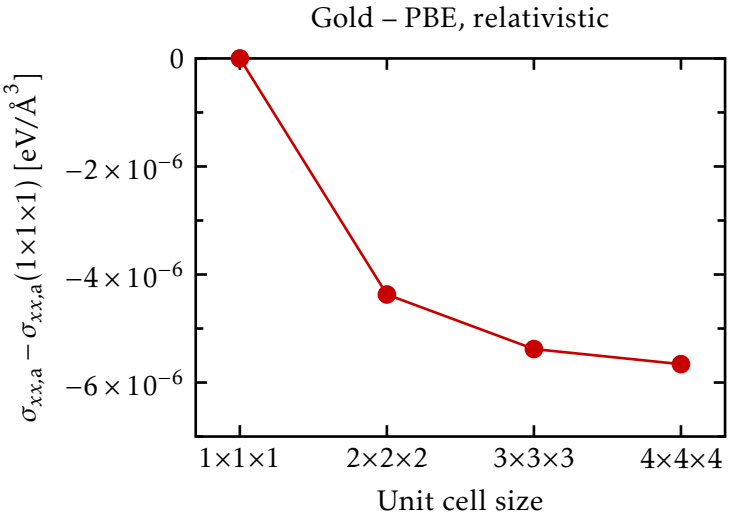

Figure 6.5: Change of the analytical stress for increasing unit cell sizes relative to a 1×1×1 unit cell, which contains 1 atom. The calculations were performed for fcc unit cells of gold with the PBE functional and relativistic treatment at a lattice parameter of 4.0 Å.

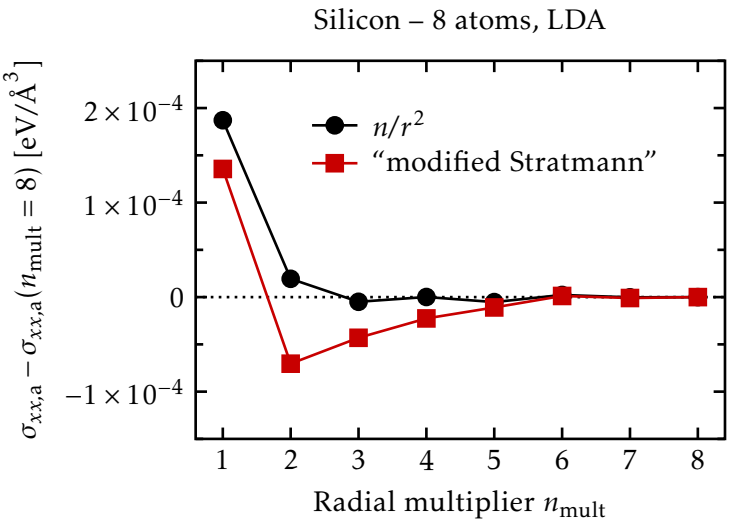

Figure 6.6: Change of the analytical stress for increasing integration grid densities relative to the densest used grid. The behavior for the two different partitioning functions for integration described in the text is shown. Increasing the radial multiplier increases the number of spherical integration shells around every atom, and therefore, leads to a denser integration grid, see Sec. 3.4. For more details about the used integration grid, see App. B.4. The calculations were performed for a diamond unit cell of silicon (8 atoms) with the LDA functional at a lattice parameter of 5.2 Å.

analytical stress stays constant within numerical limitations when the size of the unit cell is increased.

6.1.4 Partitioning functions for integration

In general, the partitioning function in Eq. (3.9), which is used for the numerical integration (Eq. (3.8)), changes under strain, and therefore, contributes to the stress tensor. However, in the limit of an infinitively dense integration grid, this additional contribution vanishes.

The n/r^2-type partitioning function uses $g_I(\boldsymbol{r}) = n_I^{\text{free}}(\boldsymbol{r})/|\boldsymbol{r}|^2$ with $n_I^{\text{free}}(\boldsymbol{r})$ being the electron density of the isolated free atom I (see Sec. 3.4). For such a partitioning function the contribution to the stress tensor will be small because the partitioning functions move equally with the atoms under a strain transformation and most integrands are built up from atom-centered quantities. Figure 6.6 shows that the contribution of the integration grid for a n/r^2-type partitioning function is considerably below 1 meV/Å^3 (thus, below the numerical accuracy) and the analytical stress converges rapidly by increasing the grid density.

We expect to get bigger contributions to the stress tensor compared to the n/r^2-type

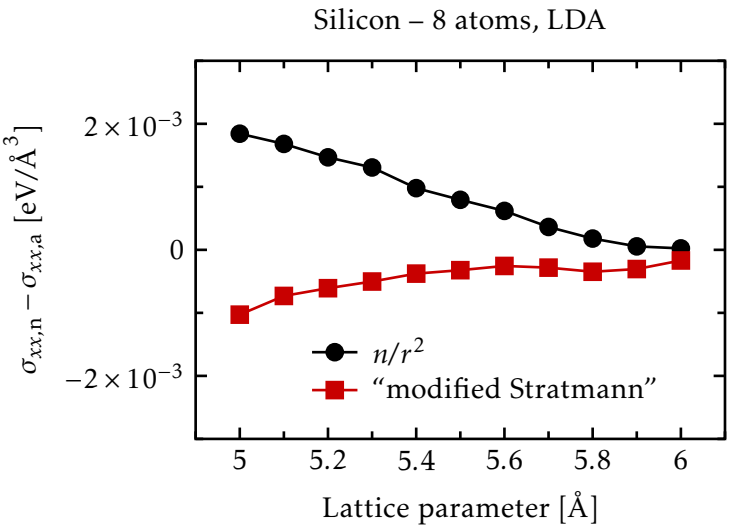

Figure 6.7: Difference between numerical ($\sigma_{xx,\mathrm{n}}$) and analytical ($\sigma_{xx,\mathrm{a}}$) stress for two different partitioning functions for integration, see text. The calculations were performed for a diamond unit cell of silicon (8 atoms) with the LDA functional.

partitioning function, if the partitioning function depends on the position of the atoms with respect to each other, which is the case for the "modified Stratmann" partitioning function (see App. B.3). However, Fig. 6.6 shows that the contribution of the "modified Stratmann" partitioning function is in the same order as for the n/r^2-type partitioning function. The only difference is that the analytical stress convergence is slower with increasing integration grid density, but this is insignificant since the differences are below the target numerical accuracy required for practical calculations.

In summary, the contribution of the integration grid to the stress tensor is very small (considerably below 1 meV/Å^3) and therefore, we neglect this contribution. Figure 6.7 shows that using the "modified Stratmann" partitioning function does not lead to larger deviations in the difference between numerical and analytical stress compared to the n/r^2-type partitioning function.

6.1.5 Timings

In this section, the efficiency of our analytical stress implementation in the FHI-aims code is investigated. In order to test the performance of the computation of the analytical stress, we compare the computing time for total energy, forces, analytical stress, and numerical stress. For this purpose, we measure how much additional time the computation takes relative to the time for a total-energy computation. For LDA and PBE, the computation of the analytical stress including forces takes roughly double the time of

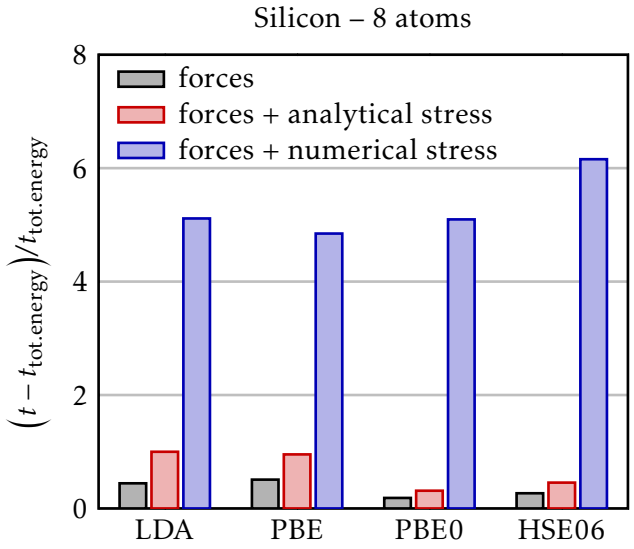

Figure 6.8: Comparison between the computing time for forces, forces + analytical stress, and forces + numerical stress for different DFAs. We take the difference between the time $t_{\text{tot.energy}}$ for a total-energy computation and time t for a computation of one of the quantities listed before. Then, the value relative to $t_{\text{tot.energy}}$ is plotted. The calculations were performed for a diamond unit cell of silicon (8 atoms) at a lattice parameter of 5.2 Å.

a total-energy computation, see Fig. 6.8 (the additional time is one times the time of a total-energy computation). The time in addition to a total-energy computation[1] is only doubled compared to the computation of forces. This is a very good result if one considers that three derivatives have to be calculated for the forces, however, nine derivatives (three for forces and six for stress tensor) are needed for the analytical stress including forces. The additional cost for the computation of the analytical stress including forces is significantly lower for hybrid functionals since several terms of the HF exchange energy computation can be reused (compare Eqs. (3.56) and (5.50)) and the evaluation of the individual HF exchange terms dominates the overall computing time.

The additional time for the computation of the numerical stress including forces is roughly five to six times the time for a total-energy computation for all tested DFAs, see Fig. 6.8. While this might be still computationally feasible for LDA and GGA functionals, it is definitely a heavy burden for unit cell optimizations with hybrid functionals. For instance, the total-energy computation with the LDA functional in Fig. 6.8 takes 140 seconds on 12 CPUs. Using the PBE0 functional, it takes about 4800 seconds on 24 CPUs.

[1] Even for the total energy, we only consider computations converged to a degree of self-consistency that yields accurate forces. In this case, the stress tensor is converged, too.

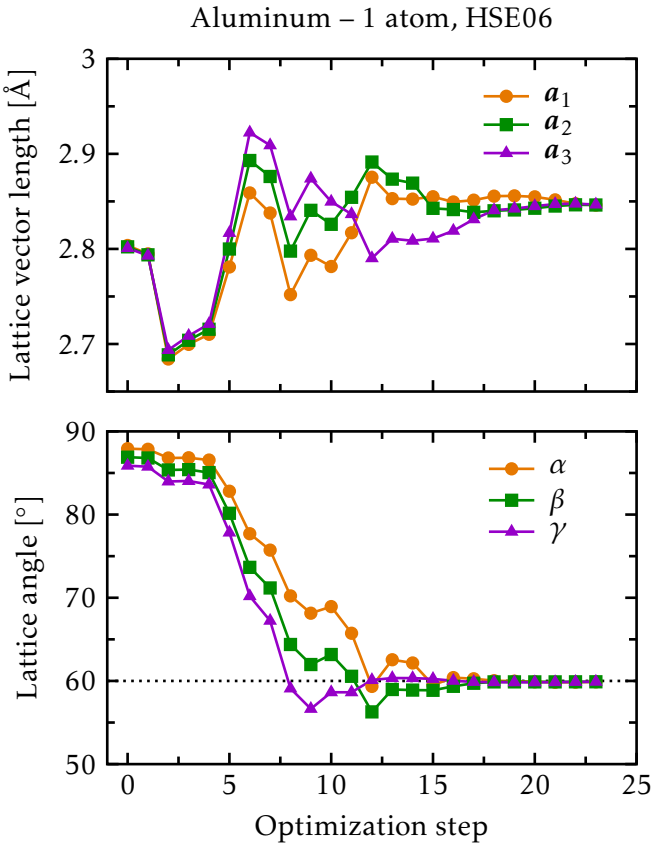

Figure 6.9: Change of the unit cell geometry during the optimization procedure. The starting point is a slightly distorted simple cubic unit cell with one aluminum atom. The top figure shows the length of the three lattice vectors $\boldsymbol{a}_1$, $\boldsymbol{a}_2$, $\boldsymbol{a}_3$ during optimization and the bottom figure the three angles α, β, γ between the lattice vectors. The angle of the fcc structure (60 °) is shown as a dotted line. The calculations were performed with the HSE06 functional.

6.2 Unit cell optimization

In order to verify that the unit cell optimization scheme (Sec. 5.6) based on the analytical stress works, a simple cubic unit cell with one aluminum atoms is set up. We then expect that the optimization will lead to the optimal equilibrium structure for aluminum (fcc for all temperatures below the melting point [Tot03]). However, starting with a perfect symmetric simple cubic unit cell does not work since the energy barrier to break the symmetry is too large. Distorting the three lattice vectors by about 0.1 Å in an asymmetric way enables the optimization procedure to find the fcc structure as an energy minimum, see Fig. 6.9. At the end of the optimization, all three lattice vectors

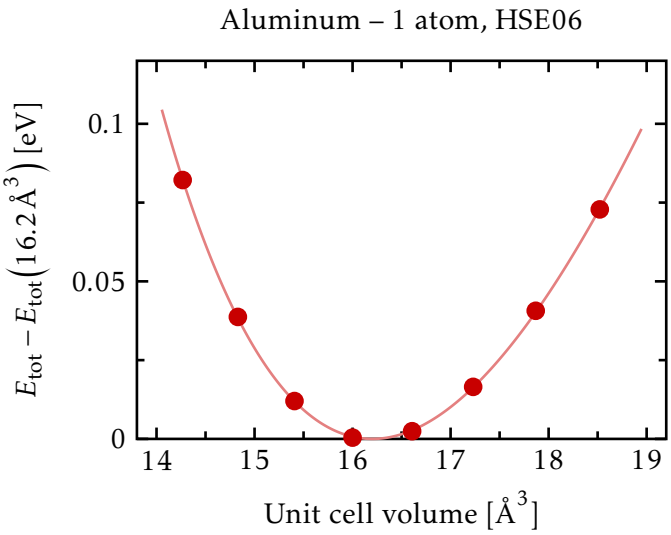

Figure 6.10: Change of the total energy of aluminum for different unit volumes relative to the minimal total energy. The solid, light red line is a fit of the data points with the Murnaghan equation of state (Eq. (6.1)). The calculations were performed for a fcc unit cell of aluminum (1 atom) with the HSE06 functional.

have the same length and the angles between them are 60 °, which corresponds exactly to the primitive unit cell of the fcc structure[2]. The lattice parameter of the obtained fcc unit cell is 4.022 Å.

In general, the optimal lattice parameter of cubic crystal structures can also be determined by calculating the total energy E_{tot} for different unit cell volumes V and then fitting the obtained data points to the Murnaghan equation of state [Mur44],

$$E_{tot}(V) = E_0 + \frac{B_0 V}{B_0'}\left[\frac{(V_0/V)^{B_0'}}{B_0' - 1} + 1\right] - \frac{B_0 V_0}{B_0' - 1}, \tag{6.1}$$

with the following fitting parameters: E_0 is the minimal energy at the optimal volume V_0, B_0 the bulk modulus at zero pressure, and B_0' its derivative with respect to pressure, which is assumed to be constant under pressure. Doing such a fit for aluminum in the fcc structure with the same computational settings as used in Fig. 6.9 yields an optimal volume of 16.2 Å^3 for the primitive fcc unit cell, see Fig. 6.10. This corresponds to a lattice parameter of 4.017 Å, which is very close to the value obtained from the unit cell optimization (4.022 Å). The total energy of the aluminum crystal obtained from the unit cell optimization is 0.6 meV lower than the total energy calculated at the optimal volume

[2] The lattice vectors of the primitive fcc unit cell are $(0, a/2, a/2)$, $(a/2, 0, a/2)$, and $(a/2, a/2, 0)$ with a the lattice parameter.

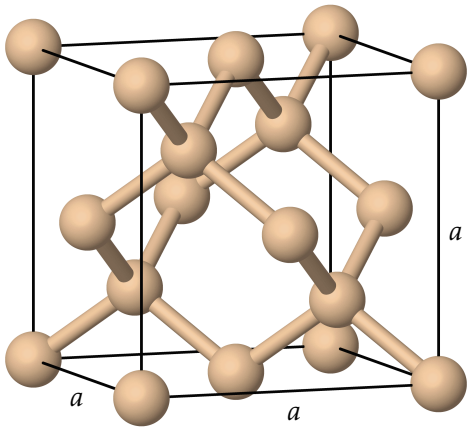

Figure 6.11: Cubic unit cell of silicon in the diamond structure with lattice parameter $a = 5.4\,\text{Å}$. The unit cell contains 8 non-equivalent atoms.

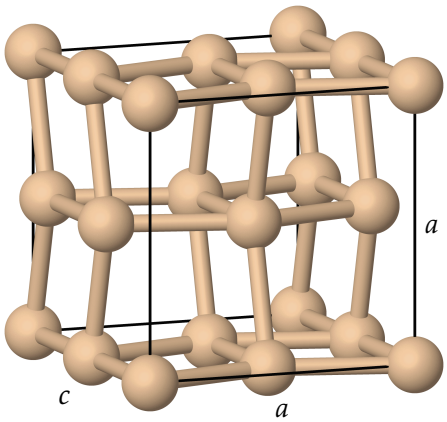

Figure 6.12: Tetragonal unit cell of silicon in the β-tin structure with lattice parameter $a = 4.8\,\text{Å}$ and ratio $c/a = 1.12$. The unit cell contains 8 non-equivalent atoms.

obtained from the fit with the Murnaghan equation of state (Eq. (6.1)). In summary, it has been demonstrated that a unit cell optimization with the analytical stress tensor yields accurate results.

6.3 Optimization under external pressure

In the last section of this chapter, the unit cell optimization with external hydrostatic pressure is validated. This is done by investigating the transition pressure between the diamond and the β-tin structure of silicon. The study of the stability of different silicon crystal structures has been one of the early successes of DFT [Yin82]. Figures 6.11 and 6.12 show the respective structures of silicon.

In order to calculate the transition pressure between the diamond and β-tin structure, we do a unit cell optimization at different external hydrostatic pressures for each of the two structures according to Sec. 5.6. From the resulting geometry, the enthalpy H (Eq. (5.73)) is determined. Figure 6.13 shows that at low pressures the diamond structure is preferred. At high pressure, the β-tin structure becomes favorable. The reason for this behavior is that the diamond structure is a relatively open structure (there is a lot of "empty" space between the silicon atoms) compared to the more compact β-tin structure. Determining the intersection between the two enthalpy curves in Fig. 6.13 yields the transition pressure $p_\text{t} = 10.14\,\text{GPa}$.

The transition pressure between diamond and β-tin structure can also be determined by calculating the total energy of the two structures for different volumes. Figure 6.14

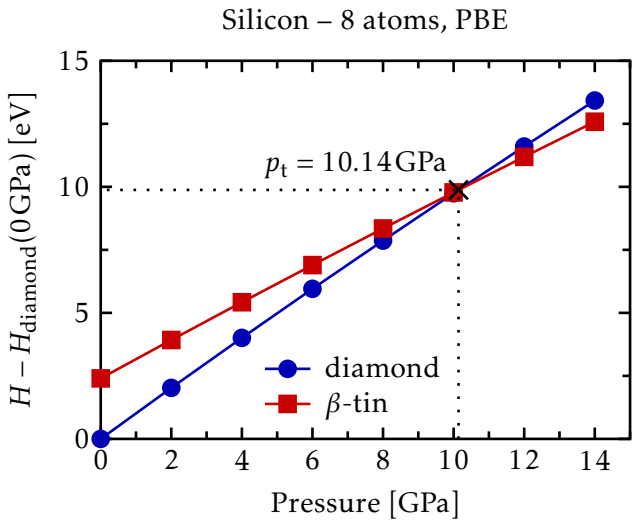

Figure 6.13: Change of enthalpy H of diamond (blue circles) and β-tin structure (red squares) of silicon under pressure relative to the enthalpy of the diamond structure at zero pressure. The transition pressure p_t between the two structures is determined by interpolating between the data points. The calculations were performed for unit cells containing 8 silicon atoms with the PBE functional.

shows the result of these calculations together with fits with the Murnaghan equation of state (Eq. (6.1)). For the β-tin structure, a ratio $c/a = 1.12$ was used for all volumes, see Fig. 6.12. For our chosen computational settings, this ratio is the optimal one for the equilibrium geometry and for the scope of this study, it is sufficient to keep the ratio constant for all calculated volumes. The Maxwell construction [Rei98] allows to determine the transition pressure between diamond and β-tin structure by calculating the slope of the common tangent of the two corresponding energy-volume curves. This yields a transition pressure of $p_t = 10.17\,\text{GPa}$ in close agreement with the value obtained from the unit cell optimization with external pressure (10.14 GPa). These two values are in the range of experimental and theoretical values reported in [Qiu12], too. Hence, we have demonstrated that we can accurately describe materials under external pressure with the analytical stress tensor.

6.4 Summary

In this chapter, we demonstrated the excellent accuracy of our implementation of the stress tensor based on the analytical strain derivatives that have been derived in Chap. 5. For all considered crystal systems and chemical species, the difference between analytical and numerical stress tensor are in the order of the numerical error of the numerical

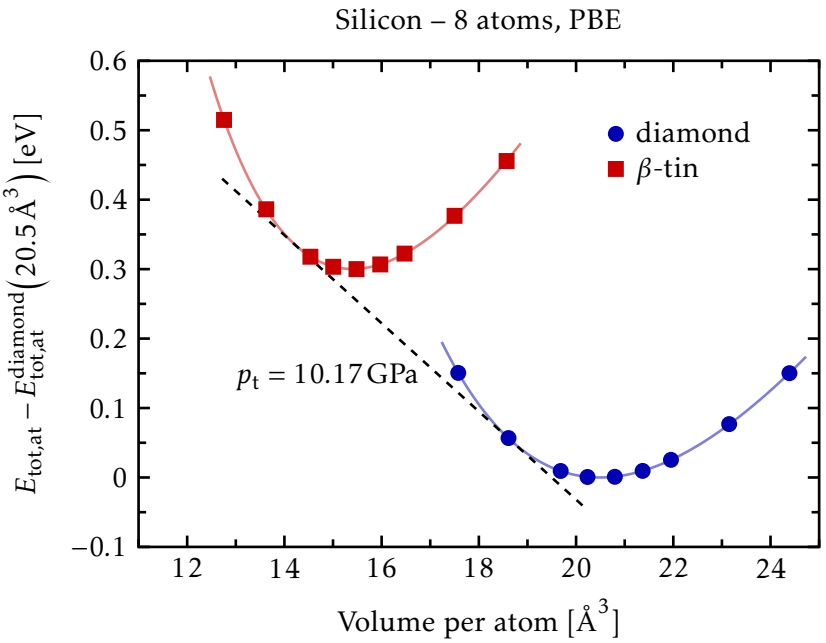

Figure 6.14: Change of the total energy per atom $E_{tot,at}$ of diamond (blue circles) and β-tin structure (red squares) of silicon for different volumes per atom relative to the minimal total energy of the diamond structure. For the β-tin structure, a ratio $c/a = 1.12$ was used for all volumes. The solid, light-colored lines are fits of the data points with the Murnaghan equation of state (Eq. (6.1)). The dashed black line is the common tangent between the two curves and its negative slope is the transition pressure p_t between the two structures. The calculations were performed for unit cells containing 8 silicon atoms with the PBE functional.

stress tensor. The implementation is consistent with respect to the basis set and unit cell size and allows to considerably speed up calculations with respect to the numerical stress tensor especially for hybrid functionals. Finally, it was demonstrated that the analytical stress tensor is well suited to optimize unit cells of crystal structures including optimizations under external pressure.

Part III

Application to organic crystals

7 Anthracene

One class of organic semiconductors are molecular crystals, i.e., crystals that consist of individual small organic molecules. Such a molecule is for example anthracene ($C_{14}H_{10}$), which is composed of three fused benzene rings forming a planar rod-like molecule (see Fig. 7.1). As it is the case for benzene, all carbon atoms are sp^2 hybridized and the remaining overlapping p orbitals of each carbon atom form delocalized π bonds that span the whole molecule. Accordingly, anthracene possesses a delocalized π-electron system.

The photoconductivity of crystalline anthracene was already discovered in 1906, however, this discovery was forgotten until its rediscovery around 1960 [Kar89]. Anthracene was then used in scintillation detectors for high energy particles and became a prototype of an organic photoconductor. It is possible to produce anthracene single crystals of high quality and purity [Kal58, Ono77, Kar01a] with high charge carrier mobilities [Kar01b]. Charge carriers (electrons and holes) can be generated inside the crystal by injecting them from the attached electrodes or by optical excitation [Pop62, Nak64, Wil70, Wil72, Pro75].

Out investigation of crystalline anthracene under hydrostatic pressure is divided into two parts: First, its equilibrium geometry is characterized and we discuss which DFAs are suitable for the description of this system. Based on the optimized equilibrium geometry, the electronic band structure is discussed. Second, the change of the geometry, band structure, and macroscopic properties (intrinsic charge carrier concentration and electrical band conductivity) under pressure is investigated in detail and it is demonstrated how they depend on each other. We start by briefly summarizing which numerical settings were used for the calculations of crystalline anthracene.

7.1 Numerical settings

The standard tight integration grid of FHI-aims is used. In order to ensure a convergence of total energy differences within few meV per atom, the "tier 1+" basis set (App. D.1) is used. The Brillouin zone is sampled by a very dense $\boldsymbol{k}$-point grid of size 8×12×6 which

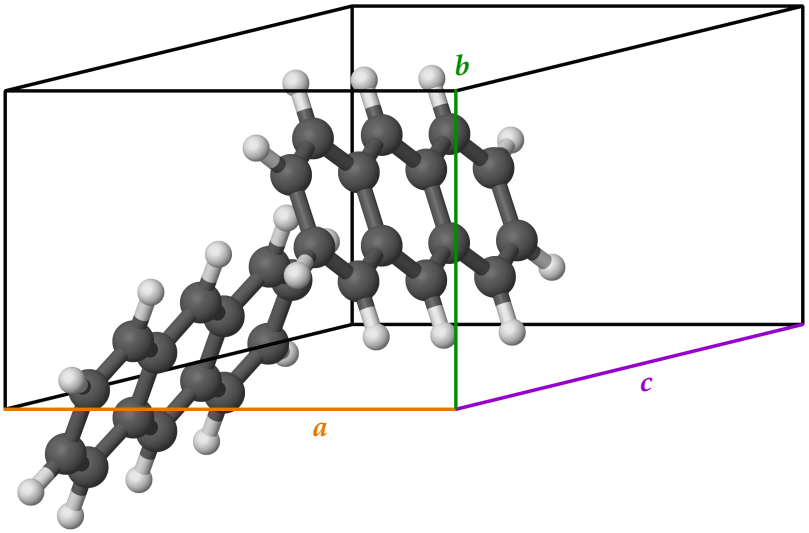

Figure 7.1: Monoclinic unit cell of crystalline anthracene with the three lattice vectors $\boldsymbol{a}$, $\boldsymbol{b}$, $\boldsymbol{c}$. Carbon atoms are gray, hydrogen atoms white. The geometry from Exp. [Cha82] (Tab. 7.1) is displayed.

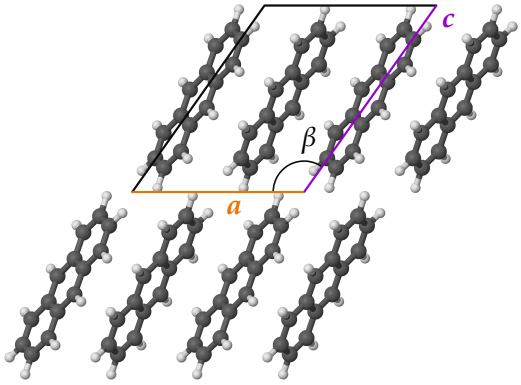

Figure 7.2: View along lattice vector $\boldsymbol{b}$ for crystalline anthracene. The monoclinic cell angle β (measured between $\boldsymbol{a}$ and $\boldsymbol{c}$) is displayed. Carbon atoms are gray, hydrogen atoms white. The unit cell is indicated by the box. This view shows the layered structure of the crystal.

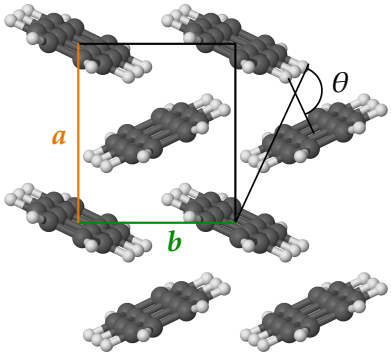

Figure 7.3: View along lattice vector $\boldsymbol{c}$ for crystalline anthracene. Carbon atoms are gray, hydrogen atoms white. The unit cell is indicated by the box. This view shows the herringbone structure of the molecules and the herringbone angle θ.

allows for accurate band structures[1]. Overall, these settings deliver a good accuracy within acceptable computational cost. More details about the basis set and $\boldsymbol{k}$-point grid convergence and can be found in Apps. D.2.1 and D.3.1. The LDA, PBE, and HSE06 functionals together with vdW corrections are used as DFAs for the study of anthracene.

7.2 Properties at zero pressure

We characterize the properties of crystalline anthracene at zero pressure, i.e., its geometry and its electronic band structure. For the geometry, we first summarize the experimental available data and then discuss the optimized geometry obtained by different DFAs.

7.2.1 Geometry

Experimental Geometry

The unit cell of crystalline anthracene is monoclinic and consists of two inequivalent anthracene molecules, see Fig. 7.1. In total, there are 28 carbon and 20 hydrogen atoms. Along lattice vector $\boldsymbol{c}$ the molecules are arranged in layers, see Fig. 7.2. Within these layers, the molecules are rotated with respect to each other forming a so-called herringbone structure, see Fig. 7.3. The herringbone angle θ measures the angle between the normal vectors of the molecular planes of two inequivalent molecules. The crystal structure of anthracene has been investigated by Mason *et al.* with X-ray measurements at a temperature of 95 K [Mas64] and by Chaplot *et al.* with neutron diffraction measurement at a temperature of 16 K [Cha82]. The unit cell parameters and herringbone angles are very similar in both experiments and the individual values can be found in Tab. 7.1. In this table, the monoclinic angle is $\beta = \angle(\boldsymbol{a}, \boldsymbol{c})$. Another X-ray measurement has been performed by Oehzelt *et al.* at ambient temperature [Oeh02] (see Tab. 7.1). Their unit cell parameters are in good agreement with the other two experiments mentioned above, but the unit cell volume is slightly larger due to thermal expansion. However, there is a larger difference (16 °) for the herringbone angle.

Optimized geometry

We have optimized the geometry (atomic positions and unit cell) of crystalline anthracene for different DFAs and Tab. 7.1 shows the resulting unit cell parameters and herringbone angle. The LDA functional underestimates the unit cell volume by 9 % and

[1] As in the case of polyacetylene (see Chap. 8), dense $\boldsymbol{k}$-point grids are needed to accurately describe strong local band dispersion. Also, the dispersion locally increases under pressure (see Fig. 7.11), which has to be captured accurately. Please note that a total energy convergence (considerably below 1 meV per atom) could be achieved with a less dense $\boldsymbol{k}$-point grid (see Fig. D.3).

Table 7.1: Unit cell parameters and herringbone angle θ of the optimized unit cell of crystalline anthracene for different DFAs. The expression $\angle(\boldsymbol{a},\boldsymbol{b})$ denotes the angle between lattice vector $\boldsymbol{a}$ and $\boldsymbol{b}$. For comparison, the experimentally measured parameters are listed. Exp. [Mas64] was performed at a temperature of 95 K, Exp. [Cha82] at a temperature of 16 K and Exp. [Oeh02] at ambient temperature.

DFA	$\lvert\boldsymbol{a}\rvert$ [Å]	$\lvert\boldsymbol{b}\rvert$ [Å]	$\lvert\boldsymbol{c}\rvert$ [Å]	$\angle(\boldsymbol{a},\boldsymbol{b})$ [°]	$\angle(\boldsymbol{a},\boldsymbol{c})$ [°]	$\angle(\boldsymbol{b},\boldsymbol{c})$ [°]	V [Å^3]	θ [°]
LDA	8.09	5.85	10.87	90.3	126.5	89.5	413.3	131.8
PBE	9.66	6.33	11.54	90.7	119.8	92.2	611.3	112.7
PBE+vdW	8.27	5.95	11.08	90.0	124.7	90.0	448.5	131.3
HSE06	9.07	6.16	11.15	90.0	114.6	89.6	565.9	115.9
HSE06+vdW	8.22	5.90	11.03	90.0	124.6	90.0	439.8	131.1
Exp. [Mas64]	8.44	6.00	11.12	90.0	125.6	90.0	457.9	140.1
Exp. [Cha82]	8.37	6.00	11.12	90.0	125.4	90.0	455.2	140.4
Exp. [Oeh02]	8.55	6.02	11.17	90.0	124.6	90.0	473.2	124.7

the PBE (HSE06) functional overestimates the unit cell volume by 34 % (24 %) compared to experimental measurements at low temperatures [Mas64, Cha82]. Not too surprisingly, the inclusion of vdW corrections on top of the PBE (HSE06) functional yields good agreement with a deviation of only −2 % (−4 %). These results clearly show that accounting for vdW interactions is essential for anthracene, as expected for a molecular crystal. An inclusion of zero-point vibrations is expected to increase the unit cell volumes and therefore, further improve the agreement between calculations with vdW corrections and experiment.

The cell angles of the monoclinic structure are reproduced reasonably well by all considered DFAs. The best agreement with experiment is achieved with the PBE+vdW and HSE06+vdW functionals, which yield a deviation of less than 1° for the monoclinic angle and the other two cell angles are 90.0° in exact agreement with experiment. Larger uncertainties are found for the herringbone angle in all cases. The PBE and HSE functional predict a herringbone angle that is considerably smaller than all experimentally ones in Tab. 7.1 (difference in the range of 12° to 28°). Including vdW corrections improves the herringbone angles. However, they still differ by about 10° from experimental values. Please note that similar deviations in the herringbone angle are also found when comparing different experiments (see Tab. 7.1).

It was shown that vdW corrections are essential for the correct description of the geometry of crystalline anthracene. Since there is no qualitative difference between the geometry obtained by the PBE+vdW and HSE06+vdW functional, all further geometry optimizations for anthracene are performed with the PBE+vdW functional with two exceptions. We revisit the HSE06+vdW functional to discuss its influence on the electronic structure and on the behavior of the band gap under pressure.

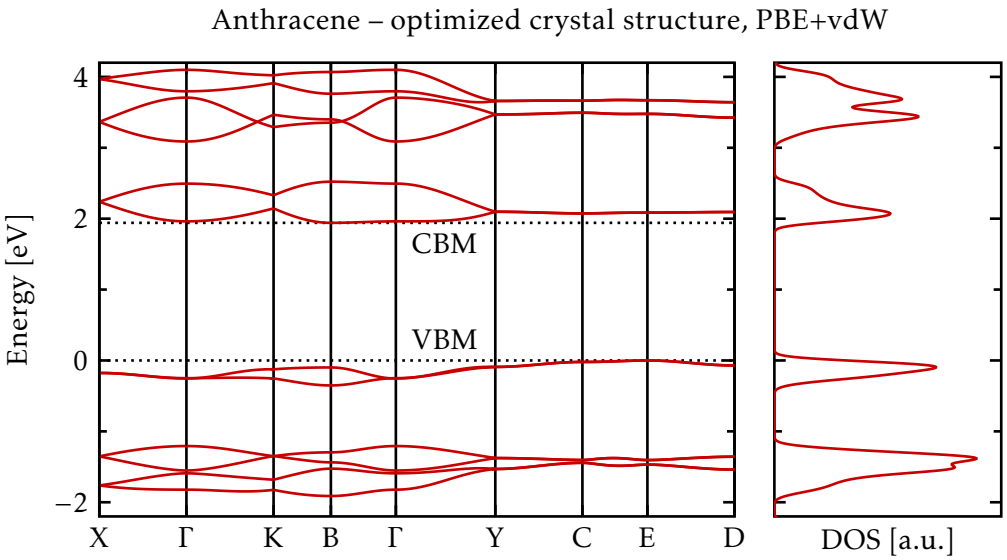

Figure 7.4: Left: Electronic band structure of crystalline anthracene. The valence band maximum (VBM) and conduction band minimum (CBM) are indicated. There is an indirect band gap between point E and B. The energy zero was set to the valence band maximum and the coordinates of the special $\boldsymbol{k}$-points can be found in App. D.4. Right: Corresponding density of states (DOS) in arbitrary units with a Gaussian broadening of 0.05 eV. The calculations were performed for the optimized crystal structure with the PBE functional and vdW corrections. For each band segment between the special $\boldsymbol{k}$-points, 50 values have been calculated.

7.2.2 Electronic band structure

As a next step, we investigate and characterize the electronic band structure of crystalline anthracene, which is needed to understand the behavior of the electronic properties under pressure. For this study, the optimized geometry obtained in Sec. 7.2.1 is used. The calculated electronic band structure for crystalline anthracene is displayed in Fig. 7.4 and is consistent with previously calculated band structures [Hum03, Fed11][2]. The bands are very flat in the region of the VBM and CBM, which implies weak electronic band transport at zero pressure. We find an indirect KS band gap of 1.94 eV between point E and B and the smallest direct KS gap of 2.04 eV is at point B. The coordinates of the special $\boldsymbol{k}$-points are given in App. D.4. Photoemission and photoconductivity measurements yield an electronic band gap of approximately 4.0 eV without specifying whether the gap is direct or indirect [Bäs72, Bel74, Seb83]. Hence, the gap experimentally determined by photoemission is twice as large as the calculated band gap with the PBE+vdW functional. This result is not surprising because the KS band gap of

[2] Some labels of the special $\boldsymbol{k}$-points used in this thesis (see App. D.4) differ from the labels in the specified references.

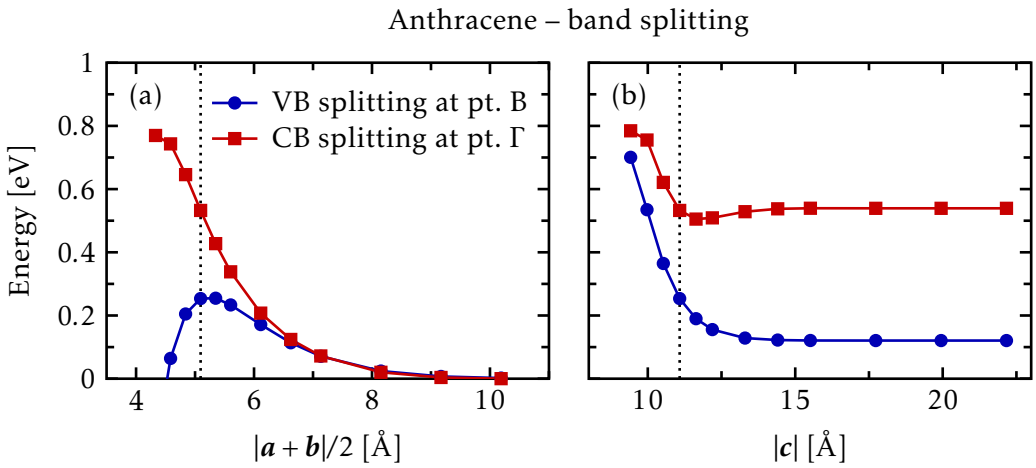

Figure 7.5: Splitting of both valence (blue circles, VB) and conduction bands (red squares, CB) for different lengths of the lattice vectors. (a): The lattice vectors $\boldsymbol{a}$ and $\boldsymbol{b}$ are both uniformly scaled. One molecule is fixed at the cell boundary and the other one is kept in the middle of the unit cell. Therefore, $|\boldsymbol{a}+\boldsymbol{b}|/2$ measures the distance between the centroids of two inequivalent neighboring molecules, see Fig. 7.3. Please note that there is a crossing of the valence bands at point B close to $|\boldsymbol{a}+\boldsymbol{b}|/2 = 4.5\,\text{Å}$, which implies that the blue curve assumes the value zero. (b): The lattice vector $\boldsymbol{c}$ is uniformly scaled. Therefore, $|\boldsymbol{c}|$ measures the distance between the centroids of two molecules in the direction of the long molecular axis, see Fig. 7.2. The black, dotted line indicates the equilibrium length in both figures.

DFT calculations and the gap measured by photoemission (or photoabsorption) are two different quantities [Per83, Mar04, Cap06] since the KS band gap is derived from the eigenvalue spectrum of the non-interacting auxiliary system described in Sec. 2.2. Higher-level methods such as GW[3] are required to achieve quantitatively correct band gaps [Oni02, Rin05].

One distinctive feature of the electronic band structure of anthracene is a splitting of both valence and conduction bands due to the interaction between the anthracene molecules. The valence band is split at point B and the conduction band between point B and Γ, see Fig. 7.4. Figure 7.5 illustrates that the band splitting is directly related to the intermolecular interactions. Increasing the distance between the molecules inside the crystal decreases the degree of splitting. Scaling the lattice vectors $\boldsymbol{a}$ and $\boldsymbol{b}$ uniformly and keeping one molecule fixed at the cell boundary and the other one in the middle of the unit cell changes the distance between the molecular planes. Therefore, increasing $\boldsymbol{a}$ and $\boldsymbol{b}$ leads to a vanishing band splitting, see Fig. 7.5(a). The distance between the molecules in the direction of their long molecular axis is changed by scaling lattice

[3] GW is an approximation for the self-energy of the many-body system. G stands for the single particle Green's function and W for the screened Coulomb interaction.

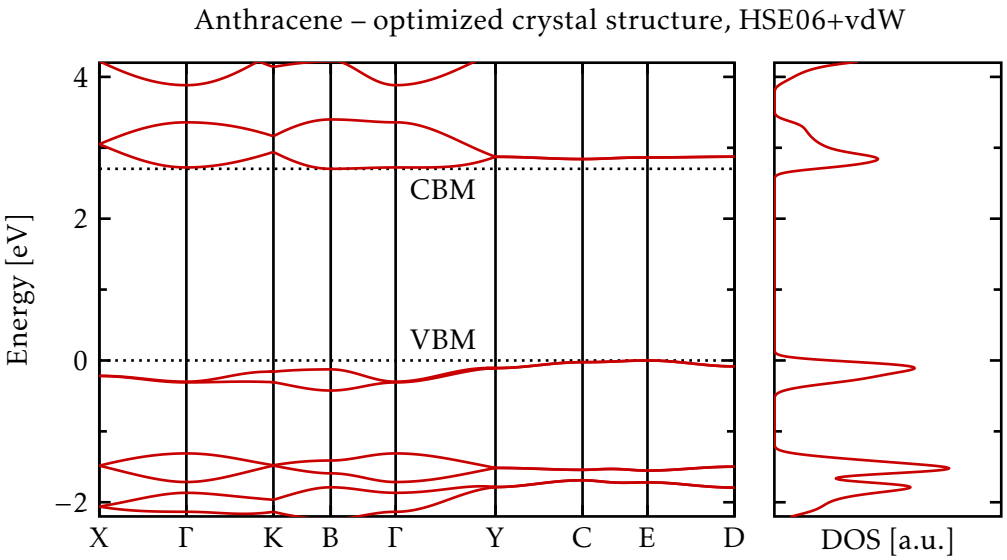

Figure 7.6: Electronic band structure and density of states (DOS) of crystalline anthracene as in Fig. 7.4 with the difference that the calculations were performed with the HSE06 functional and vdW corrections as well as the corresponding optimized crystal structure.

vector $\boldsymbol{c}$ uniformly. Increasing this lattice vector decreases the band splitting, too, see Fig. 7.5(b). However, the splitting stays non-zero even at large distances. The reason for this is that the distance between the molecules in $\boldsymbol{ab}$ direction stays constant if $\boldsymbol{c}$ is scaled, see Fig. 7.2. Hence, the intermolecular interactions between the π electrons of the aromatic rings are still present causing the non-zero band splitting at large lengths of $\boldsymbol{c}$. Increasing $\boldsymbol{a}$ and $\boldsymbol{b}$ leads to the case that only molecular interactions in the direction of the long molecular axis remain, see Fig. 7.3. In this case, only the few atoms at the top and bottom of the molecules contribute, which is not enough to cause a non-vanishing band splitting.

In the previous section, it was shown that the PBE+vdW functional yields qualitatively the same geometry as the HSE06+vdW functional. In order to underline that the PBE+vdW functional is well suited for our needs, the band structure of crystalline anthracene has been calculated with the HSE06+vdW functional in Fig. 7.6. It can be seen that the shape of the individual bands does not change in comparison to Fig. 7.4. The bands are only shifted with respect to each other. For this reason, the DOS of the PBE+vdW and HSE06+vdW functional are very similar, too. Due to the shift of the bands, the indirect KS band gap between point E and B increases from 1.94 eV (PBE+vdW) to 2.70 eV and the smallest direct KS gap at point B from 2.04 eV (PBE+vdW) to 2.84 eV. In principle, the experimental gap of about 4 eV could be obtained by increasing the value of α in the HSE(α, 0.11 bohr^{-1}) functional (Sec. 2.3.5).

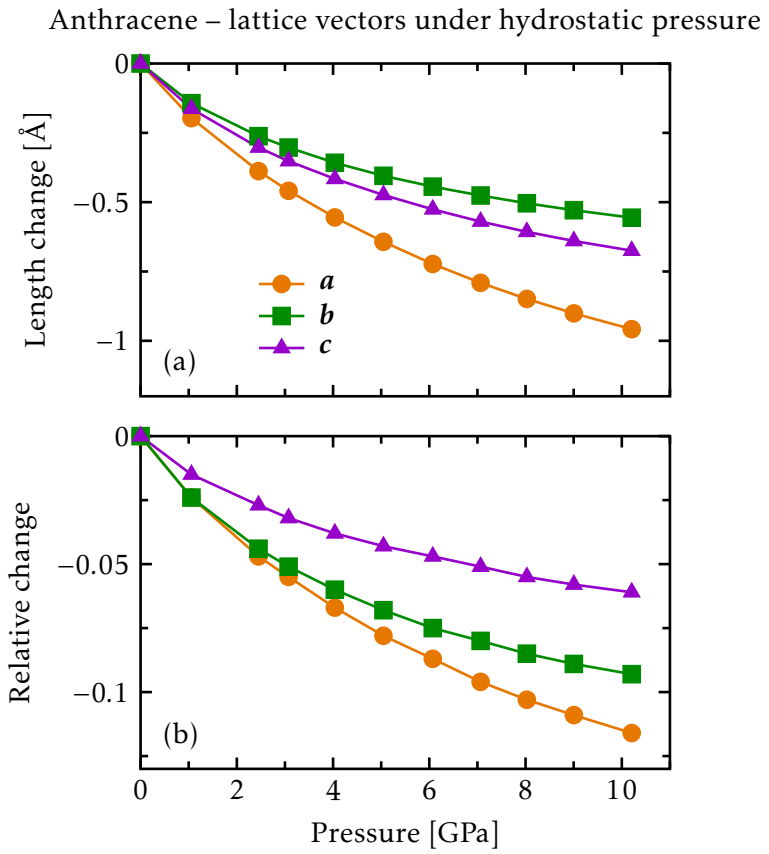

Figure 7.7: Change of lattice vectors under hydrostatic pressure. (a): Absolute length change of the three lattice vectors. (b): Relative length change of the three lattice vectors.

7.3 Behavior under hydrostatic pressure

We now investigate the behavior of crystalline anthracene under hydrostatic pressure. First, we discuss the changes in the geometry and compare to experimental results. The changes in the geometry affect the electronic band structure, which in turn influences macroscopic properties (intrinsic charge carrier concentration and electrical band conductivity). The changes of the electrical band conductivity under hydrostatic pressure are analyzed in detail and it is shown that the behavior of the conductivity can be attributed to specific changes in the band structure.

7.3.1 Geometry

Figures 7.7 and 7.8 show the behavior of the anthracene geometry under hydrostatic pressure. Since the anthracene crystal is weakly bonded by vdW interactions in all three

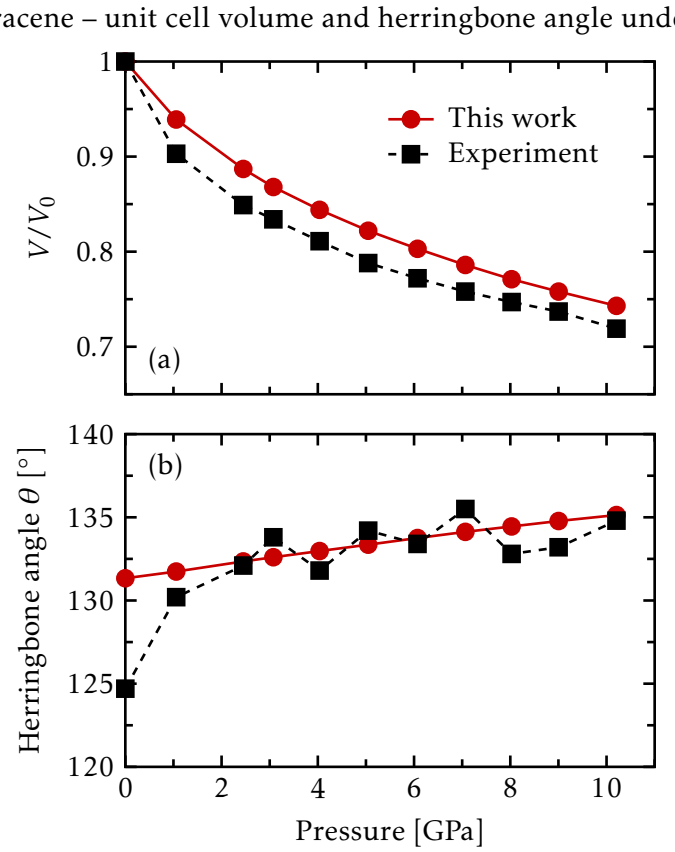

Figure 7.8: (a): Change of unit cell volume V relative to the volume at zero pressure V_0 under hydrostatic pressure. (b): Change of the herringbone angle θ (see Fig. 7.3) under hydrostatic pressure. For both figures, the calculated (red circles) and experimental values (black squares) [Oeh02] are shown.

spatial directions (see Sec. 7.2.1), a strong, non-linear compression of all three lattice vectors occurs at small pressure, see Fig. 7.7. As the pressure increases, the contraction becomes linear. On a relative scale, lattice vector $\boldsymbol{a}$ is compressed the most and lattice vector $\boldsymbol{c}$ the least. The layer structure of the molecules is aligned along $\boldsymbol{c}$, see Fig. 7.2, and there is less empty space between the molecules in this direction than in the direction of $\boldsymbol{a}$ and $\boldsymbol{b}$, see Fig. 7.3.

The computed change of the unit cell volume under hydrostatic pressure is in good qualitative agreement with experimental results from Oehzelt *et al.* [Oeh02], see Fig. 7.8(a). Figure 7.8(b) shows that the herringbone angle increases under hydrostatic pressure. The reason for this is that lattice vector $\boldsymbol{a}$ decreases stronger than lattice vector $\boldsymbol{b}$ on a relative scale (see Fig. 7.7(b)), i.e., the molecules approach each other

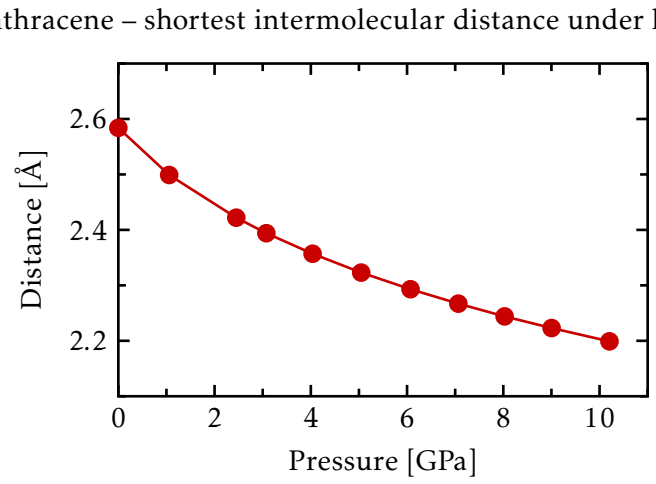

Figure 7.9: Change of shortest intermolecular distance under hydrostatic pressure, i.e., shortest distance between carbon and hydrogen atoms on different molecules.

faster in the direction of $\boldsymbol{a}$ than $\boldsymbol{b}$. In order to achieve a larger distance between the inequivalent molecules in the direction of $\boldsymbol{a}$, the herring bone angle increases, see Fig. 7.3. Qualitatively, this is also in agreement with the measurements from Oehzelt *et al.* [Oeh02], even quantitatively for higher pressures. For low pressures (up to 2 GPa), the measured (125 ° at 0 GPa) and calculated angles (131 ° at 0 GPa) differ. At zero pressure, other experiments have found herringbone angles around 140 ° as discussed before (see Tab. 7.1).

Since the unit cell is compressed under pressure, the shortest distance between carbon and hydrogen atoms on different molecules decreases significantly, too, see Fig. 7.9. Accordingly, the interaction between the molecules increases as well, which influences the band splitting as shown before.

7.3.2 Electronic band structure

Figure 7.10 shows that the electronic band gap of anthracene decreases under hydrostatic pressure. At the PBE level, it decreases by 0.60 eV (30 %) from 1.94 eV at 0 GPa to 1.35 eV at 10.2 GPa. The band gap stays indirect between point E and B over the whole calculated pressure range. As the molecules come closer to each other under pressure the interaction between them increases as shown before. Therefore, the splitting of both valence and conduction bands increases with increasing pressure, see Figs. 7.11 and 7.12, and in addition, the valence bands start to split at point Γ. Figure 7.11 also shows that the curvature of the segment $\overline{\mathrm{X\Gamma K}}$ in the conduction band and of the segment $\overline{\mathrm{CED}}$ in the valence band significantly increases under pressure. This means that electronic band

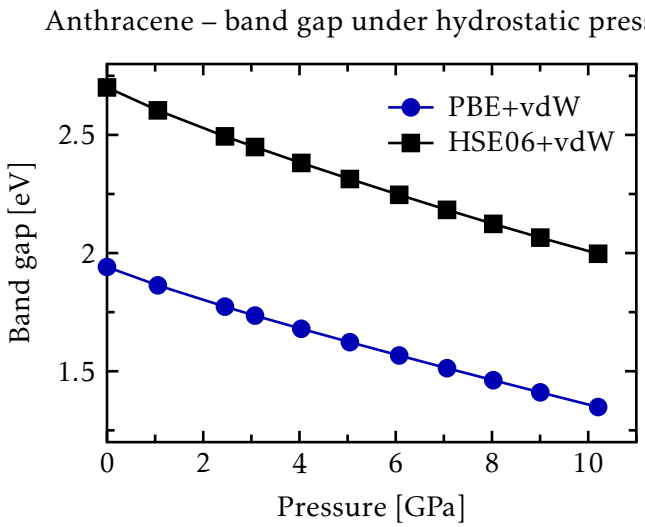

Figure 7.10: Change of electronic band gap under hydrostatic pressure for the PBE+vdW (blue circles) and HSE06+vdW functional (black squares). The band gap stays indirect between point E and B and is shown for the PBE+vdW functional in Fig. 7.11.

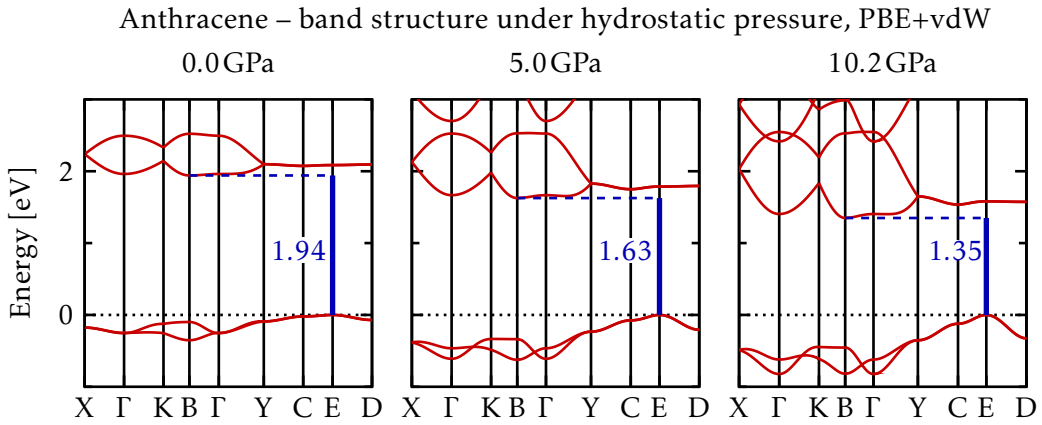

Figure 7.11: Sections from calculated electronic band structure near the valence band maximum (black, dotted line) for different pressures for the PBE+vdW functional. For each band segment between the special ***k***-points, 50 values have been calculated.

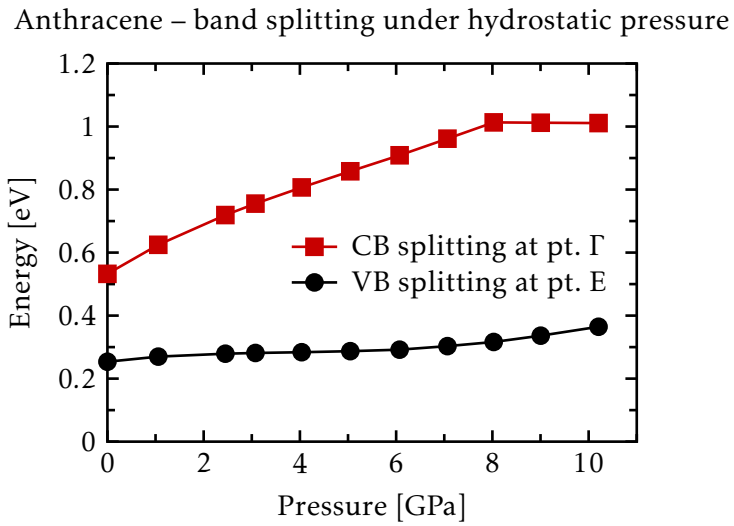

Figure 7.12: Splitting of valence (black circles, VB) and conduction bands (red squares, CB) under hydrostatic pressure.

transport is enhanced under pressure, which will be investigated in the next section.

A comparison between the PBE+vdW and HSE06+vdW functional shows that both functionals yield a similar behavior of the band gap under pressure, see Fig. 7.10. In the case of the HSE06+vdW functional, the band gap decreases by 0.70 eV (26 %) from 2.70 eV at 0 GPa to 2.00 eV at 10.2 GPa. This means that the band offset between the two functionals (see Sec. 7.2.2) stays almost constant and that the PBE+vdW functional is also well-suited to predict trends in the band structure under pressure.

7.3.3 Macroscopic transport properties

In this section, we consider electrical band conductivities of anthracene for the intrinsic case as well as n- and p-doping with a charge carrier concentration of $10^{19}\,\mathrm{cm}^{-3}$ at zero pressure. The temperature is chosen to be 300 K unless noted otherwise. According to Sec. 4.2, the intrinsic charge carrier concentration n_i has been determined, see Fig. 7.13(a). It can be seen that the concentration increases exponentially under hydrostatic pressure. This behavior is expected because the band gap E_gap decreases nearly linearly under pressure (see Fig. 7.10) and the charge carrier concentration of an intrinsic semiconductor (with Fermi level not close to the VBM or CBM) has the following approximate proportionality [Ash76]:

$$n_\mathrm{i} \propto \exp\left(-\frac{E_\mathrm{gap}}{2k_\mathrm{B}T}\right). \tag{7.1}$$

Anthracene – Intrinsic charge carrier concentr. and Fermi level under hydr. press.

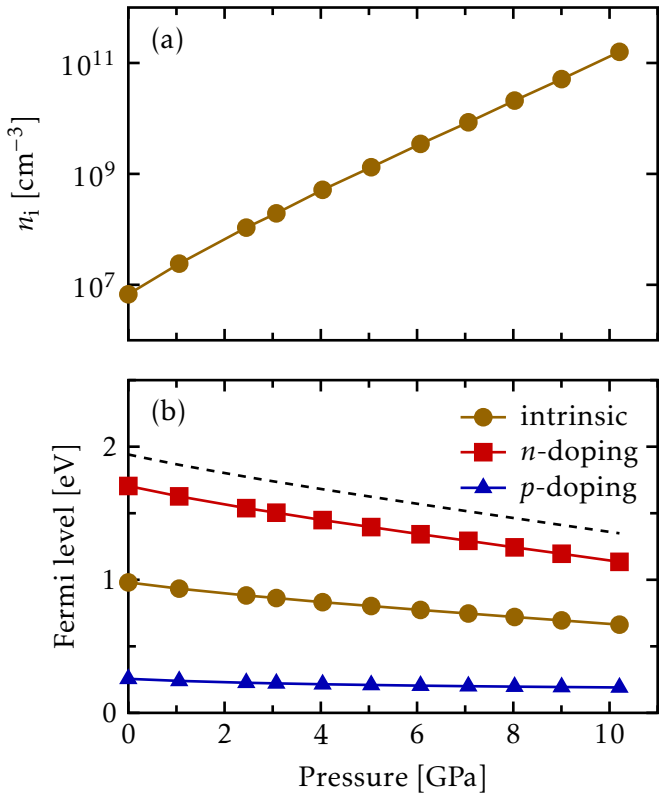

Figure 7.13: (a): Change of the intrinsic charge carrier concentration n_i under pressure. (b): Change of the Fermi level under pressure. The VBM is set to zero and the CBM is indicated by the black, dashed line. In the intrinsic case (brown circles), the Fermi level lies in the middle of the band gap. A doping with a charge carrier concentration of $10^{19}\,\mathrm{cm}^{-3}$ at zero pressure brings the Fermi level closer to the CBM in the n-doping case (red squares) and closer to the VBM in the p-doping case (blue triangles).

Figure 7.13(b) shows the Fermi level for all three cases (intrinsic, n-, p-doping), which has been determined according to Sec. 4.2. In the intrinsic case, the Fermi level lies in the middle of the band gap. It gets closer to the CBM (VBM) for n-doping (p-doping). Unfortunately, no experimentally measured charge carrier densities could be found in the literature preventing a comparison of the calculated values. Under hydrostatic pressure, the relative positions of the Fermi level are preserved for the three different cases. This means the Fermi level stays in the middle of the band gap for the intrinsic case and it keeps the same distance to the CBM (VBM) for n-doping (p-doping).

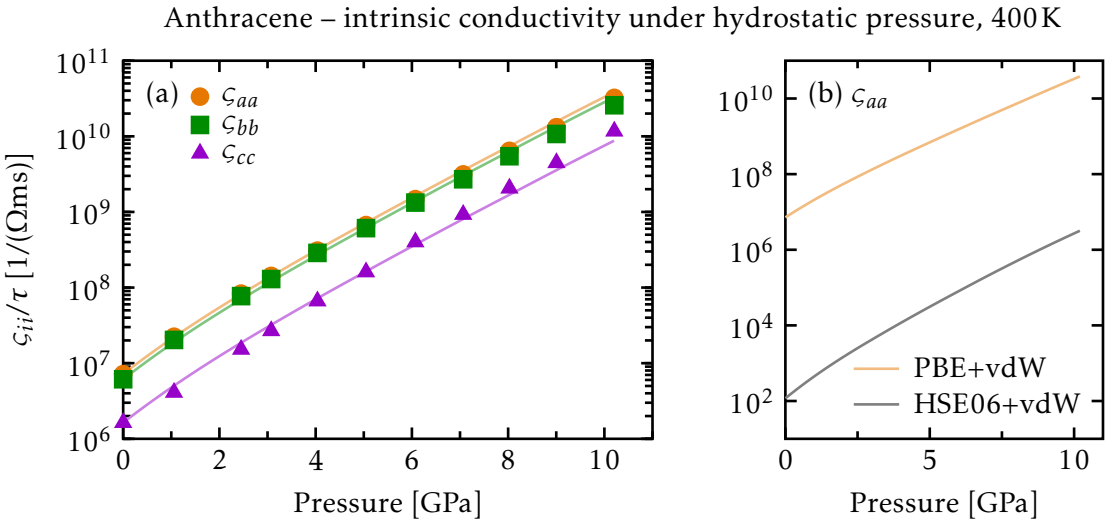

Figure 7.14: (a): Change of the quantity ς_{ii}/τ in the intrinsic case under hydrostatic pressure for the directions along the three lattice vectors $i = a, b, c$. The solid, light-colored lines are the approximations with Eq. (7.2) and $\varsigma_{ii}(0)$ as starting point. The temperature was increased to 400 K in order to avoid numerical difficulties due to low conductivity values. (b): Comparison between the PBE+vdW and HSE06+vdW functional for the approximation of ς_{aa} with Eq. (7.2), The curve of the PBE+vdW functional is the same one as displayed in (a).

Intrinsic band conductivity

Knowing the position of the Fermi level for different pressures, the quantity ς/τ can be calculated with BoltzTraP, which allows to investigate trends in the electrical band conductivity ς under the assumption of a constant relaxation time τ, see Sec. 4.1. Figure 7.14(a) shows the change of ς_{ii}/τ in the direction of the three lattice vectors $i = a, b, c$ under hydrostatic pressure for the intrinsic case. There is a strong increase by four orders of magnitude between the pressures 0 GPa and 10.2 GPa. This behavior is expected since the intrinsic charge carrier concentration increases exponentially under pressure (see Fig. 7.13(a)). It can also be seen that the electronic transport is highest (by one order of magnitude) along the lattice vectors $\boldsymbol{a}$ and $\boldsymbol{b}$, i.e., in the direction of the herringbone-stacking. This is expected since this is the direction of the largest intermolecular interactions as shown in Sec. 7.2.2.

For an intrinsic semiconductor (with Fermi level not close to the VBM or CBM) the conductivity ς is determined in first order approximation by the charge carrier concentration (see Eq. (7.1)). Thus, the following proportionality holds [Ash76]:

$$\varsigma(p) \propto \exp\left(-\frac{E_{\mathrm{gap}}(p)}{2k_{\mathrm{B}}T}\right) \tag{7.2}$$

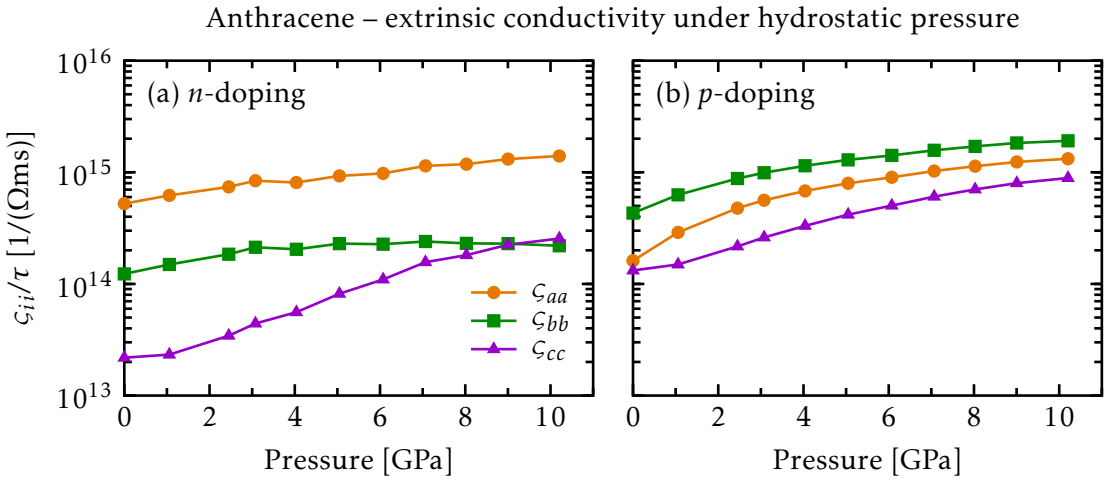

Figure 7.15: Change of the quantity ς_{ii}/τ in the doped case with a charge carrier concentration of $10^{19}\,\mathrm{cm}^{-3}$ at zero pressure under hydrostatic pressure for the directions along the three lattice vectors $i = a, b, c$.

with temperature T. We use the value of ς_{ii}/τ at zero pressure as starting point and $E_{\mathrm{gap}}(p)$ from Fig. 7.10. Figure 7.14(a) shows that this approximation reproduces ς_{ii}/τ very well. This means that the change in intrinsic conductivity under pressure mainly stems from the change of the band gap under pressure and that other effects (changes in the form of the band structure) only play a minor role.

The band gaps of the PBE+vdW and HSE06+vdW functional follow the same trend; they are only shifted against each other by an approximately constant factor (see Fig. 7.10). Therefore, the approximation to the intrinsic conductivity (Eq. (7.2)) shows the same trend for both functionals, see Fig. 7.14(b). However, ς_{ii}/τ is much lower for the HSE06+vdW functional due to the larger band gap. This means that fewer free charge carriers are present in the valence and conduction bands (see Eq. (7.1)).

Extrinsic band conductivity

However, this is different for the doped case. For doping with a charge carrier concentration of $10^{19}\,\mathrm{cm}^{-3}$ at zero pressure, see Fig. 7.13(b), the Fermi level is close to the CBM or VBM and remains in this region even under pressure. This means that a change in the band gap does not have a big influence on the conductivity. Instead, changes of the bands near the CBM or VBM affect the conductivity depending where the Fermi level is closer to. Figure 7.15 shows the change of ς_{ii}/τ in the direction of the three lattice vectors $i = a, b, c$ for n- and p-doping with a charge carrier concentration of $10^{19}\,\mathrm{cm}^{-3}$ at zero pressure under hydrostatic pressure.

For n-doping, ς_{aa}/τ and ς_{cc}/τ increase under pressure, however, ς_{bb}/τ increases only

slightly in the beginning and stays roughly constant afterwards, see Fig. 7.15(a). This behavior can be explained by looking at the change of the bands near the CBM (Fig. 7.11). The segments $\overline{\mathrm{X\Gamma K}}$ and $\overline{\mathrm{K\,B\Gamma}}$ in the band structure correspond mainly to the directions along lattice vector $\boldsymbol{a}$ and $\boldsymbol{c}$, respectively. In these two segments, the curvature, i.e., the group velocity (Eq. (4.4)), of the bands increases significantly under pressure. A larger group velocity translates into a larger conductivity since the latter is proportional to the outer product of the group velocity, see Eqs. (4.1) and (4.3). This explains the increase of ς_{aa}/τ and ς_{cc}/τ under pressure near the CBM (Fig. 7.11). The segment $\overline{\Gamma\mathrm{Y}}$ in the band structure corresponds to the directions along lattice vector $\boldsymbol{b}$. There, the curvature of the bands hardly changes under pressure, thus ς_{bb}/τ changes only slightly.

For p-doping, all three conductivities increase under pressure roughly uniformly, see Fig. 7.15(b). Figure 7.11 shows that the curvature of the valence band in the segment $\overline{\mathrm{CED}}$, which includes the VBM, increases under pressure. Since this segment includes the directions of all three lattice vectors, the relative increase of ς_{aa}/τ, ς_{bb}/τ and ς_{cc}/τ under pressure is approximately the same.

Comparison to experiment

Pohl *et al.* [Poh62] measured an increasing electrical conductivity with increasing pressure for a crystalline anthracene sample in agreement with our findings. However, many experimental details are unknown so that further and more detailed comparisons are not possible. Kajiwara *et al.* [Kaj67] measured an increasing electron mobility with increasing pressure for anthracene crystals. Mobility μ_e and electrical conductivity ς are related by [Ash76]

$$\varsigma = e n_\mathrm{c} \mu_\mathrm{e} \tag{7.3}$$

with n_c the charge carrier concentration of electrons and e the elementary charge. All microscopic effects of the Boltzmann transport equation that affect the conductivity are combined in the macroscopic mobility. Due to Eq. (7.3), the measured increase in mobility translates to an increase in conductivity under pressure (n_c increases under pressure, too, since the volume of the unit cell decreases), which supports our findings. Additionally, experiments [Pot69, Kar01b] report that the electron mobility is highest along lattice vector $\boldsymbol{a}$ and the hole mobility is highest along lattice vector $\boldsymbol{b}$. This is consistent with our results, see Fig. 7.15. For n-doping (p-doping), the conductivity is dominated by electrons (holes) and the highest conductivity is along lattice vector $\boldsymbol{a}$ ($\boldsymbol{b}$).

7.4 Summary

The geometric and electronic properties of crystalline anthracene have been investigated in detail at zero pressure and under hydrostatic pressure in this chapter. We find that GGA functionals are sufficient to describe the geometric properties of anthracene and

it is important to include vdW corrections to obtain reasonable unit cell volumes. The interaction between the molecules in the crystal lead to a splitting of valence and conduction bands. This interaction is enhanced under hydrostatic pressure because the crystal gets compressed, and in turn, the band splitting increases. Due to the band gap reduction under pressure, the charge carrier concentration and the electrical band conductivity strongly increase in the intrinsic case. The intrinsic conductivity is one order of magnitude larger along the lattice vectors $\boldsymbol{a}$ and $\boldsymbol{b}$ than in the direction of lattice vector $\boldsymbol{c}$. The changes in the band structure near the CBM and VBM determine the behavior of conductivity in the doped case. The extrinsic conductivity is highest along lattice vector $\boldsymbol{a}$ ($\boldsymbol{b}$) for n-doping (p-doping), which is in agreement with experimental measurements.

8 Polyacetylene

Organic crystals that consist of conjugated polymers form another class of organic semiconductors. The most fundamental and simplest polymer in this class is polyacetylene (IUPAC name: polyethyne). This polymer is a formally infinite, linear chain of sp^2 hybridized carbon atoms each having one bonded hydrogen atom. In a crystal, two of these chains are periodically repeated. The chains can have *cis* or *trans* configuration; in our studies, we exclusively investigate *trans*-polyacetylene (TPA). In 1977, it was discovered that the electrical conductivity of polyacetylene can be increased by many orders of magnitude to values comparable to metals through doping [Chi77, Shi77]. By introducing molecules that accept or donate electrons, *n*- or *p*-type semiconducting polyacetylene can be produced [Chi78b, Chi78a, Kwa79, Gha86]: *p*-doping can be achieved by adding electron accepting substances such as halides or arsenic pentafluoride. Consequently, the carbon chain becomes partially oxidized, i.e., electrons are lost. Analogously, *n*-doping is obtained by adding electron donating substances such as alkali metals. In this case, the carbon chain becomes partially reduced, i.e., electrons are gained. It is possible to produce highly crystalline polyacetylene film with highly oriented carbon chains [Lei84, Moo87, Cao91]. The crystalline structure of polyacetylene is robust against moderate doping and no significant loss in crystallinity occurs [Moo87, Cao91].

Experiments [Fin82, Yan83, Kah87, Moo87, Zhu92] have shown that crystalline polyacetylene has a broken symmetry ground state: The bond lengths between the carbon atoms in the polymer are not equal. Instead, there is an alternation between longer (single) and shorter (double) bonds (Peierl's distortion). The length difference between the two different bonds is specified either by the bond length alternation (BLA) or the dimerization (Δz), see Fig. 8.1. These two quantities are approximately related by: $\mathrm{BLA} \approx \sqrt{3}\Delta z$. Quite early, 1D model Hamiltonians such as the Su-Schrieffer-Heeger (SSH) one [Su79], which account for electron-phonon interaction on a parametric basis, were able to rationalize the dimerization. However, the SSH Hamiltonian does not include electron-electron interaction so that several subsequent studies [Wu87, Bré89, Kön90] have investigated the role of electron-electron interaction and electron correlation on the dimerization.

Standard DFT calculations with LDA or GGA functionals have problems reproducing the correct ground state of TPA. They give dimerizations that are too small or even

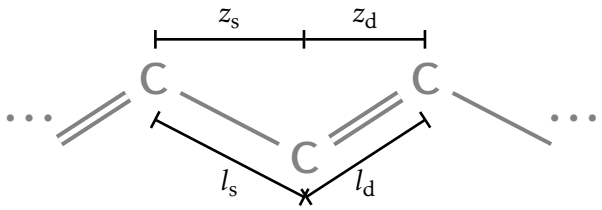

Figure 8.1: Sketch showing how the alternation between single and double bonds is measured for the carbon (C) chain of *trans*-polyacetylene (hydrogen atoms are omitted). The bond length alternation (BLA) measures the difference between the length of a single and a double bond. The dimerization Δz measures the difference between the distance of single bonded and double bonded carbon atoms along the chain direction.

zero [Ash89, Vog90, Suh95, Cho97, Hir98, Kör12] mainly due to the self-interaction error (see Sec. 2.3.3). Hybrid functionals do better in predicting the right dimerization [Suh95, Cho97, Hir98, Kör12]. However, they employ at least one parameter, namely the amount α of added HF exchange. In general, α is system dependent [Mar11] and in the case of polyacetylene, the dimerization depends strongly on α. There are efforts to obtain α in an *ab initio* manner by using quasiparticle corrections obtained by *GW* calculations [Ata13b, Ric13]. However, it is unclear if such a procedure is possible in the case of polyacetylene. For an isolated chain, Körzdörfer *et al.* [Kör12] have demonstrated that no single value of α is able to yield the correct dimerization and simultaneously a vanishing many-electron self-interaction error. They have investigated finite conjugated carbon chains (polyenes) of increasing length and have calculated the dimerizations for different chain lengths with the quantum chemistry method CCSD(T)[1]. The so obtained length-dimerization curve is closely reproduced by the HSE$(\alpha, 0)$ functional (Sec. 2.3.5) with $\alpha = 0.4573$ (i.e. no screening and no vdW corrections). However, they have demonstrated that this value of α yields an increasing many-electron self-interaction error with increasing chain length. Since Körzdörfer *et al.* have only focused on the isolated chain, it is unclear to which extent this statement holds in the bulk material given that interchain interactions affect the electronic structure considerably (see below). In spite of the fact that high-level calculations such as CCSD(T) are capable of producing very accurate results, their excruciating computational cost limits their applicability to non-periodic systems with the number of atoms in the order of ten. A detailed comparison to experiments is also difficult because there are no accurately measured dimerizations available for crystalline TPA.

Our investigation of crystalline TPA under hydrostatic pressure is divided into three parts: First, its equilibrium geometry is characterized and we discuss which DFAs are suitable for the description of this system. This includes a critical discussion of the

[1] CCSD(T) stands for the coupled cluster method with a full treatment of single and double excitations and a perturbative treatment of triple excitations.

dimerization in dependence of the chosen DFA. Based on the optimized equilibrium geometry, the electronic band structure is studied. Second, the behavior of dimerization and electronic band structure properties is investigated under uniaxial strain along the carbon chain and uniform biaxial strain in both orthogonal directions. This helps us to understand which properties are influenced by which geometry changes and it allows to investigate which features change between the two limiting cases: isolated chains and bulk system. Third, the change of the geometry, band structure, and macroscopic properties (intrinsic charge carrier concentration and electrical band conductivity) under pressure is investigated in detail and it is demonstrated how they depend on each other. We start by briefly summarizing which numerical settings were used for the calculation of crystalline TPA.

8.1 Numerical settings

The standard tight integration grid of FHI-aims is used. In order to ensure a convergence of total energy differences below 1 meV per atom, the "tier 1+" basis set (App. D.1) is used. It is known in the literature [Min87, Ash89, Sun02] that the number of $\boldsymbol{k}$-points along the carbon chain is critical for the correct description of the dimerization. Therefore, we ensure that the $\boldsymbol{k}$-point grid is converged with respect to the dimerization (convergence below 10^{-3} Å) and with respect to total energy differences (convergence below 1 meV per atom). This level of convergence is achieved by sampling the Brillouin zone with a very dense $\boldsymbol{k}$-point grid of size 8×4×24[2]. Overall, these settings deliver a good accuracy within acceptable computational cost. More details about the basis set convergence and the $\boldsymbol{k}$-point grid can be found in Apps. D.2.2 and D.3.2. The LDA and PBE functional as well as the HSE family of functionals (Sec. 2.3.5) are used as DFAs for the study of TPA. Here, we use a fixed screening parameter $\omega = 0.11\,\text{bohr}^{-1}$ for the HSE family of functionals and the notation is abbreviated as follows: $\text{HSE}(\alpha) = \text{HSE}(\alpha, 0.11\,\text{bohr}^{-1})$.

8.2 Properties at zero pressure

We characterize the properties of crystalline TPA at zero pressure, i.e., its geometry and its electronic band structure. For the geometry, we first summarize the available experimental data and then discuss the dimerization and optimized unit cell obtained by different DFAs.

[2] In addition to the convergence of the dimerization and of total energy differences, dense $\boldsymbol{k}$-point grids are needed to accurately describe the strong local band dispersion that is present in the band structure of TPA, e.g., in the segment $\overline{\text{YD}}$ and $\overline{\text{BΓ}}$ in Fig. 8.8. Also, the dispersion locally increases under pressure (see Fig. 8.19), which has to be captured accurately.

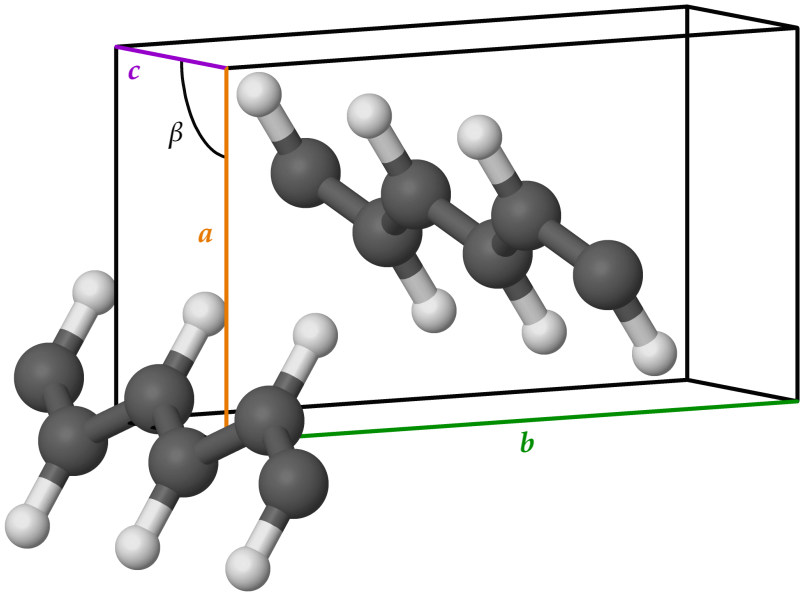

Figure 8.2: Unit cell of crystalline *trans*-polyacetylene in the $P2_1/a$ structure with the three lattice vectors $\boldsymbol{a}$, $\boldsymbol{b}$, $\boldsymbol{c}$, and the monoclinic cell angle β (measured between $\boldsymbol{a}$ and $\boldsymbol{c}$). In the direction of $\boldsymbol{c}$, two periodic images were added in order to highlight the two chains. Carbon atoms are gray, hydrogen atoms white. The geometry from Exp. [Kah87] (Tab. 8.1) is displayed.

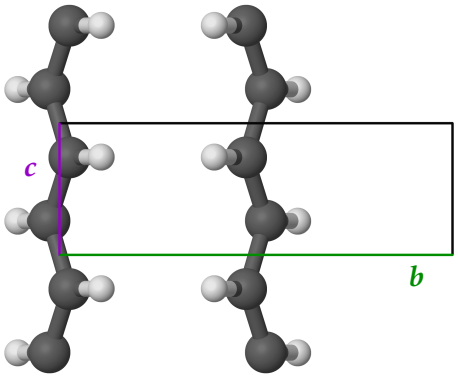

Figure 8.3: View along lattice vector $\boldsymbol{a}$ for crystalline *trans*-polyacetylene. In the direction of $\boldsymbol{c}$, two periodic images were added in order to highlight the two chains. Carbon atoms are gray, hydrogen atoms white. The unit cell is indicated by the box.

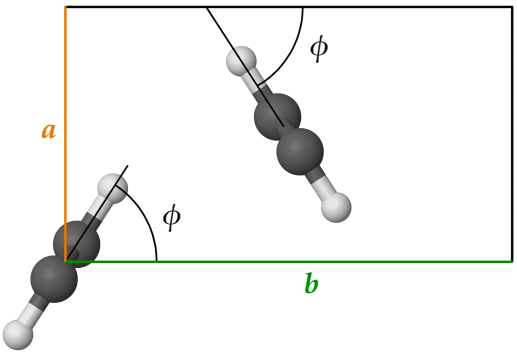

Figure 8.4: View along lattice vector $\boldsymbol{c}$ for crystalline *trans*-polyacetylene. Carbon atoms are gray, hydrogen atoms white. The unit cell is indicated by the box. This view shows the setting angle ϕ.

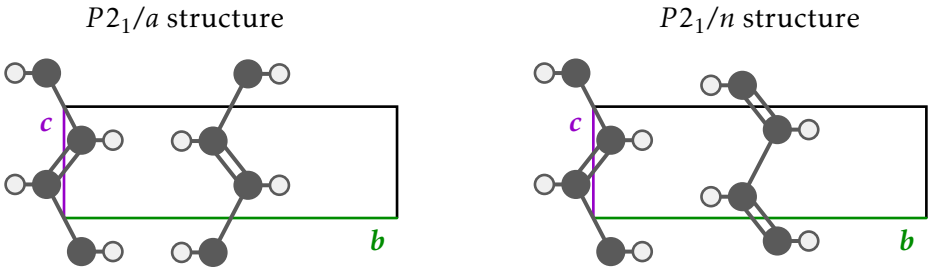

Figure 8.5: Sketches showing $P2_1/a$ (left) and $P2_1/n$ (right) structure of *trans*-polyacetylene. The view is along lattice vector $\boldsymbol{a}$ and carbon atoms are gray, hydrogen atoms white. The unit cells are indicated by the boxes. For $P2_1/a$, the alternation between single and double bonds is in-phase between the two chains, whereas for $P2_1/n$, the alternation is in anti-phase.

8.2.1 Geometry

Experimental geometry

The unit cell of crystalline TPA is monoclinic of and consists of two inequivalent parallel unsaturated carbon chains, see Figs. 8.2, 8.3, and 8.4. The chains are oriented along lattice vector $\boldsymbol{c}$ and there are four carbon and four hydrogen atoms per unit cell in total. The chains are rotated with respect to each other around the lattice vector $\boldsymbol{c}$. The setting angle ϕ measures this rotation relative to the $\boldsymbol{bc}$ plane, see Fig. 8.4. Two different crystalline domains, namely $P2_1/a$ and $P2_1/n$ have been suggested [Fin82, Kah87], see Fig. 8.5. The two structures can be converted into each other by shifting one chain by $\boldsymbol{c}/2$ with respect the other. For the $P2_1/a$ structure, the alternating pattern of single and double bonds is in-phase between the two chains, whereas, it is in anti-phase for the $P2_1/n$ structure. Consequently, the shortest distance between carbon and hydrogen atoms on different chains is smaller for the $P2_1/a$ structure, which implies a stronger interaction between the chains. This thesis focuses on the $P2_1/a$ structure since both structures behave qualitatively similar under pressure in our studies.

X-ray studies of crystal structure of TPA have been performed by several experiments [Fin82, Kah87, Zhu92]. The unit cell parameters and setting angle are very similar in all experiments and the individual values can be found in Tab. 8.1. In this table, the monoclinic angle is $\beta = \angle(\boldsymbol{a}, \boldsymbol{c})$. For crystalline TPA, experiments [Fin82, Yan83, Kah87] have measured a dimerization $\Delta z \sim 0.05\,\text{Å}$.

Dimerization for different DFAs

For the investigation of the dimerization, we start with the experimental unit cell of Exp. [Kah87], see Tab. 8.1, and then calculate the total energy-dimerization curve for different DFAs. Figure 8.6 shows that the LDA and PBE functional fail to predict the right ground state of TPA as expected. A dimerization $\Delta z = 0$ is obtained, which means

Table 8.1: Unit cell parameters and setting angle ϕ of optimized unit cell of crystalline TPA for different DFAs. The expression $\angle(\boldsymbol{a},\boldsymbol{b})$ denotes the angle between lattice vector $\boldsymbol{a}$ and $\boldsymbol{b}$. For comparison, the experimentally measured parameters are listed. For all experiments, no specific temperature was given.

DFA	$\lvert\boldsymbol{a}\rvert$ [Å]	$\lvert\boldsymbol{b}\rvert$ [Å]	$\lvert\boldsymbol{c}\rvert$ [Å]	$\angle(\boldsymbol{a},\boldsymbol{b})$ [°]	$\angle(\boldsymbol{a},\boldsymbol{c})$ [°]	$\angle(\boldsymbol{b},\boldsymbol{c})$ [°]	V [Å^3]	ϕ [°]
HSE(0.25)	4.77	8.23	2.47	75.5	100.3	90.8	92.6	47.3
HSE(0.25)+vdW	4.00	7.40	2.45	89.2	88.6	104.2	70.2	48.2
HSE(0.50)+vdW	3.90	7.52	2.44	89.3	93.1	108.0	67.9	46.7
HSE(0.75)+vdW	3.82	7.44	2.42	88.8	94.8	107.8	65.4	45.6
HSE(1.00)+vdW	3.75	7.38	2.41	88.7	95.9	107.8	63.1	44.7
Exp. [Fin82]	4.24	7.32	2.46	90.0	91.5	90.0	76.3	55
Exp. [Kah87]	4.18	7.34	2.46	90.0	90.5	90.0	75.5	57
Exp. [Zhu92]	4.10	7.39	2.46	90.0	92	90.0	74.5	55

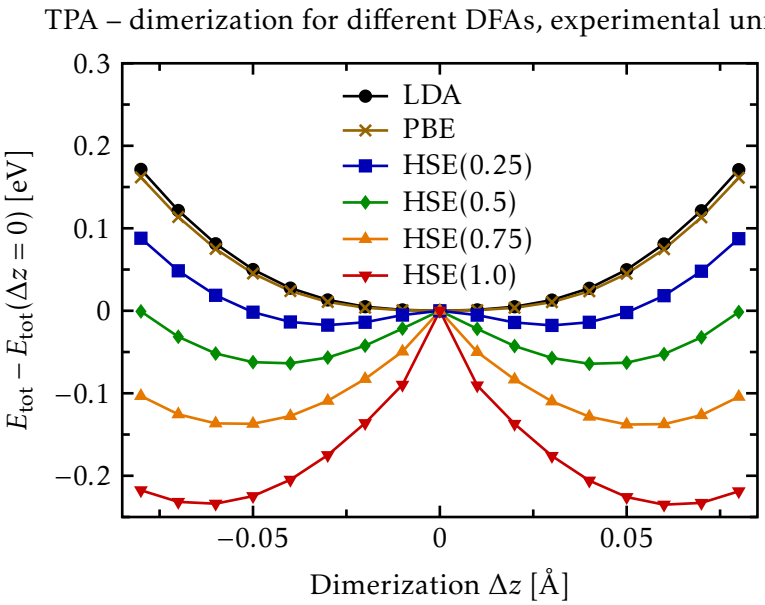

Figure 8.6: Predicted dimerization Δz of crystalline TPA for different DFAs. The ordinate shows the total energy relative to the value of $\Delta z = 0$ for each curve. The energy-dimerization curve is shown for the LDA and PBE functional as well as the HSE(α) functional (Sec. 2.3.5) with different α. The calculations were performed for the experimental unit cell of Exp. [Kah87], see Tab. 8.1. The atomic positions are first optimized for each DFA, and the atoms are then positioned according to the dimerization. For the resulting structures, the total energy is calculated.

that all carbon-carbon bonds have the same length. Therefore, the system is metallic since there is one free electron per carbon atom in this case. As mentioned previously, the broken symmetry ground state is correctly obtained by using a hybrid functional such as HSE. It can be seen in Fig. 8.6 that the dimerization depends on the amount of added HF exchange α. The higher α, the higher is the dimerization.

Our calculations show that (at least) hybrid functionals are clearly needed to describe the internal geometry of TPA correctly since LDA and GGA functionals are insufficient for this task. Qualitatively, the results of Tab. 8.1 do not change upon including vdW corrections. Next, we discuss how hybrid functionals perform for the description of the unit cell of crystalline TPA.

Optimized unit cell: The full picture

We have optimized the geometry (atomic positions and unit cell) of crystalline TPA for the HSE(α) functional (Sec. 2.3.5) with different α and Tab. 8.1 shows the resulting unit cell parameters and setting angle. As was already shown in the case of crystalline anthracene (see Sec. 7.2.1), vdW interactions are needed to obtain reasonable unit cell volumes. Lattice vector $\boldsymbol{c}$ is barely sensitive to the chosen DFA since it this is the direction of the carbon chains, i.e., the strong covalent bonds. In contrast, lattice vector $\boldsymbol{a}$ and $\boldsymbol{b}$ are overestimated if no vdW corrections are included. This result shows clearly that the bonding between the individual carbon chains of crystalline TPA is predominantly of vdW nature. In addition, Tab. 8.1 shows that unit cell volume and setting angle decrease for increasing α of the HSE(α)+vdW functional. As mentioned before, vdW interactions have no direct influence on the dimerization but an indirect one due to the changes in the lattice vectors.

In comparison to experimental values, the unit cell volume and lattice vector lengths of the HSE(α)+vdW functional agree reasonably well. However, we obtain a triclinic unit cell instead of a monoclinic one. The largest difference is for the angle between lattice vector $\boldsymbol{b}$ and $\boldsymbol{c}$. The experimental one is 90°, the calculated one is about 110°. As in the case of crystalline anthracene for the herringbone angle (see Sec. 7.2.1), larger differences are also found for the setting angle for all considered DFAs. They differ by about 10° from experimental values. The orientation of the chains with respect to each other and the unit cell parameters are interrelated because they determine the interaction strength between the chains. Since our calculated unit cell parameters are not in exact agreement with the experimental values, it is not surprising that the setting angle differs, too.

It was shown that vdW corrections are essential for the adequate description of the geometry of crystalline TPA, analogously to crystalline anthracene. The HSE(α)+vdW functional is able to yield unit cells and setting angles with reasonable agreement to experiments for all considered α. As a last step, we combine the dimerization study with the optimized unit cell.

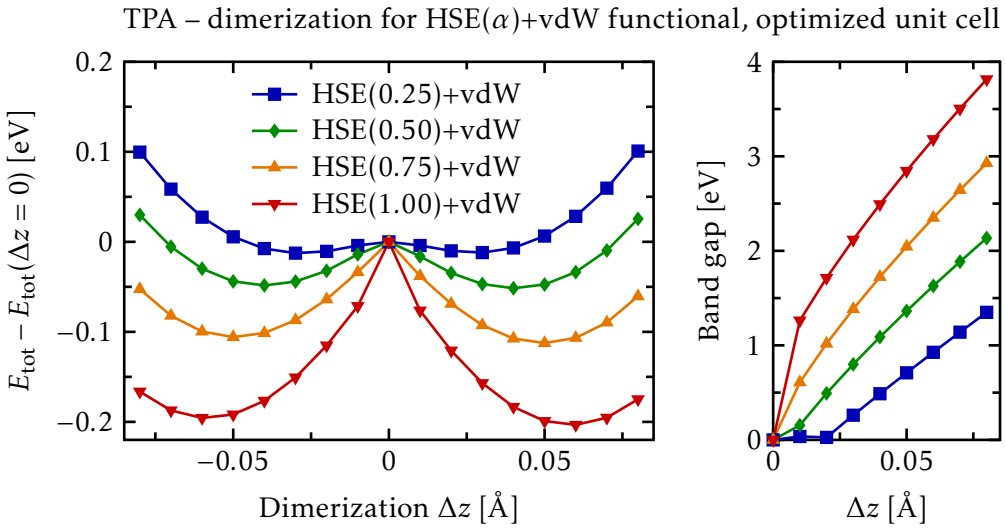

Figure 8.7: Left: Predicted dimerization Δz of crystalline TPA for different values of α of the HSE(α)+vdW functional (Sec. 2.3.5). The ordinate shows the total energy relative to the value of $\Delta z = 0$ for each curve. Right: Dependence of the band gap on Δz and on the used α. The calculations were performed by taking the unit cell of the fully optimized structure for each value of α (Tab. 8.1) and positioning the atoms according to the dimerization. Afterwards the positions of the hydrogen atoms are optimized (everything else is kept fixed) and total energy as well as band gap of the resulting structure are calculated.

Table 8.2: Dimerization Δz for different α of the HSE(α)+vdW functional (Sec. 2.3.5). The dimerizations are obtained by a cubic spline interpolation of the total energy-dimerization curves in Fig. 8.7.

α	0.25	0.5	0.75	1.0
Δz [Å]	0.028	0.040	0.050	0.058

For each value of α of the HSE(α)+vdW functional, the total energy-dimerization curve is calculated for the corresponding unit cells given in Tab. 8.1. As already seen previously in Fig. 8.6, the dimerization increases with increasing α, see Fig. 8.7 and Tab. 8.2. Extrapolating the dimerizations for finite and isolated conjugated carbon chains of increasing length calculated with CCSD(T) by Körzdörfer *et al.* [Kör12] yields $\Delta z \sim 0.047$ Å. The electronic band gap of crystalline TPA depends strongly on the dimerization, too, see Fig. 8.7, besides the fact that it depends on α.

As explained in the beginning of this chapter, it is unclear whether there is a value of α that yields a quantitatively correct description for all properties of crystalline TPA. Comparison to Körzdörfer *et al.* shows that the properties of TPA sensitively depend on

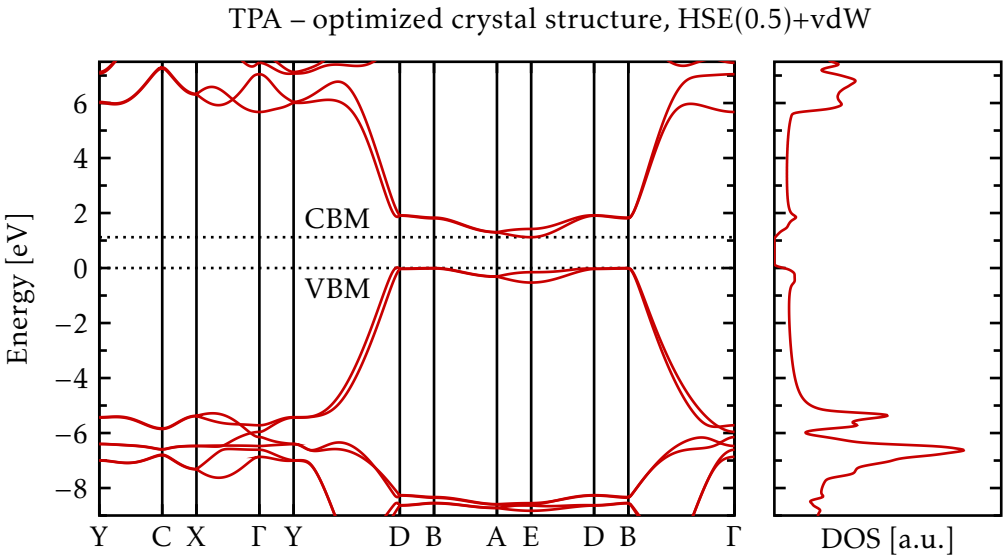

Figure 8.8: Left: Electronic band structure of crystalline TPA. The valence band maximum (VBM) and conduction band minimum (CBM) are indicated. There is an indirect band gap between point B and E. The energy zero was set to the valence band maximum and the coordinates of the special $\boldsymbol{k}$-points can be found in App. D.4. Right: Corresponding density of states (DOS) in arbitrary units with a Gaussian broadening of 0.05 eV. The calculations were performed for the optimized crystal structure with the HSE(0.5) functional and vdW corrections. For each band segment between the special $\boldsymbol{k}$-points, 50 values have been calculated.

the value of α and on the environment. For instance, the extrapolated CCSD(T) value of $\Delta z \sim 0.047$ Å lies between our calculated dimerizations with the screened HSE(α)+vdW functional for $\alpha = 0.5$ and 0.75 (see Tab. 8.2), while Körzdörfer *et al.* find $\alpha = 0.4573$ more appropriate in their calculations with the unscreened HSE(α, 0) functional. Therefore, we have chosen both $\alpha = 0.5$ and 0.75, which yields reliable results for quantities we are interested in. The predicted dimerization is large enough, $\Delta z \sim 0.04$ Å and 0.05 Å, respectively (see Tab. 8.2), and the band gap is large enough so that the system becomes semiconducting as soon as $\Delta z \neq 0$, which is not the case for $\alpha = 0.25$, see Fig. 8.7. By choosing a certain value for α, we cannot expect to correctly reproduce absolute values for TPA. However, we are confident that we can correctly describe trends since our starting geometry has qualitatively the correct features (non-zero dimerization, large enough band gap).

8.2.2 Electronic band structure

As a next step, we investigate and characterize the electronic band structure of crystalline TPA, which is needed to understand the behavior of the electronic properties under

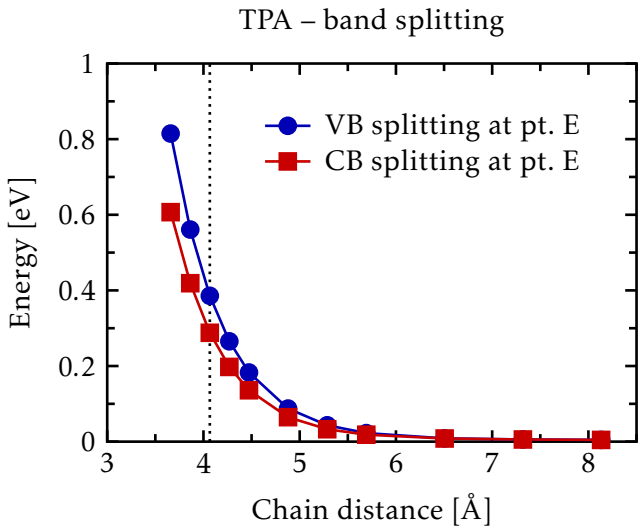

Figure 8.9: Splitting of valence (blue circles, VB) and conduction bands (red squares, CB) for different distances between the carbon chains. The black, dotted line indicates the equilibrium distance. The distance between the chains is changed by scaling the lattice vectors $\boldsymbol{a}$ and $\boldsymbol{b}$ uniformly and keeping one chain fixed at the cell boundary and the other one in the middle of the unit cell, see Fig. 8.4.

pressure. For this study, the optimized geometry obtained in Sec. 8.2.1 is used. The calculated electronic band structure for TPA is displayed in Fig. 8.8 and is consistent with previously calculated band structures [Vog89, Pus02, Tia04][3]. The bands are relatively flat in the region of the VBM and CBM meaning that electronic band transport is rather weak at zero pressure. We find an indirect KS band gap of 1.12 eV between point B and E and the smallest direct KS gap of 1.27 eV is at point E. The coordinates of the special $\boldsymbol{k}$-points are given in App. D.4. An indirect optical absorption gap of 1.1 eV and a direct gap of 1.4 eV is reported by Fincher *et al.* [Fin79]. In general, optical absorption experiments report values of about 1.5 eV [Tan80, Mos82, Bri86, Lei88]. We stress that we do not equate the electronic band gap with the optical absorption gap, however, it is reassuring that the two values are in the same order of magnitude since they are correlated with each other to some extent.

As in the case of anthracene, there is a splitting of both valence and conduction bands due to the interaction between the carbon chains. The valence band and the conduction band are split at point E, see Fig. 8.8. Figure 8.9 illustrates that the band splitting is directly related to the interchain interactions. Increasing the distance between the carbon chains inside the crystal decreases the amount of the splitting. In the limit of

[3] Some labels of the special $\boldsymbol{k}$-points used in this thesis (see App. D.4) differ from the labels in the specified references.

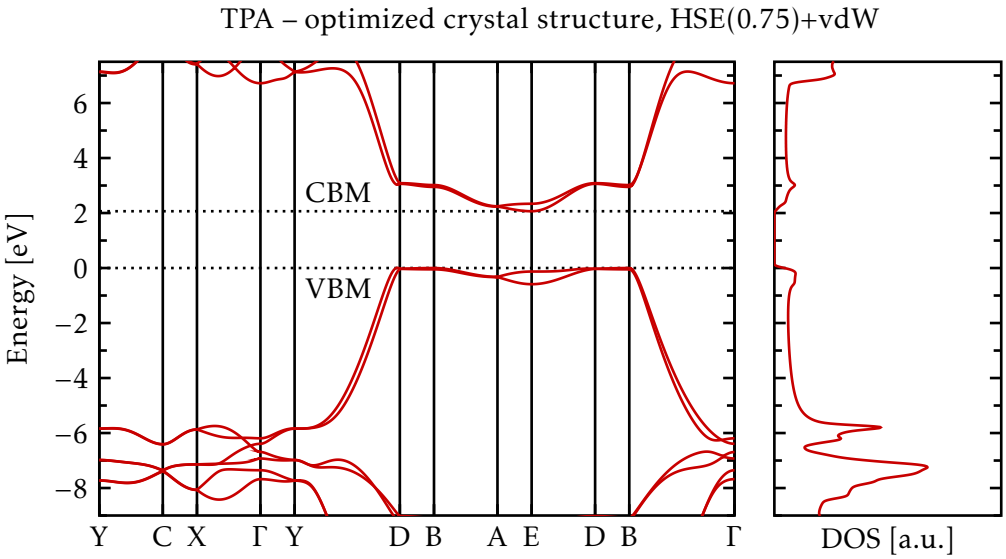

Figure 8.10: Electronic band structure and density of states (DOS) of crystalline TPA as in Fig. 8.8 with the difference that the calculations were performed with the HSE(0.75) functional and vdW corrections as well as the corresponding optimized crystal structure.

isolated chains, the band splitting vanishes and valence as well as conduction band become completely flat.

Qualitatively, the electronic band structure and DOS calculated with the HSE(α)+vdW functional for $\alpha = 0.5$ and 0.75 show no qualitative difference (compare Fig. 8.8 and Fig. 8.10). It can be seen that the shape of the individual bands does not change qualitatively. The bands are shifted with respect to each other so that the indirect KS band gap between point B and E increases from 1.12 eV ($\alpha = 0.5$) to 2.07 eV and the smallest direct KS gap at point E from 1.27 eV ($\alpha = 0.5$) to 2.19 eV. The splitting of the VBM increases from 0.38 eV ($\alpha = 0.5$) to 0.46 eV while the splitting of the CBM decreases from 0.30 eV ($\alpha = 0.5$) to 0.27 eV.

8.3 Behavior under strain

In this section, the behavior of the dimerization and of electronic band structure properties under strain is investigated. As a zero strain reference, the optimized unit cell from Sec. 8.2.1 is used. The unit cell is strained in the z direction (ε_{zz}), i.e., along the carbon chains, and uniformly in the x and y directions ($\varepsilon_{xx} = \varepsilon_{yy}$), which changes the interchain distance. The atomic positions are then optimized inside the distorted unit cell. This allows to create two dimensional contour plots for the strain dependency of the investigated quantities and to investigate which features change how between bulk

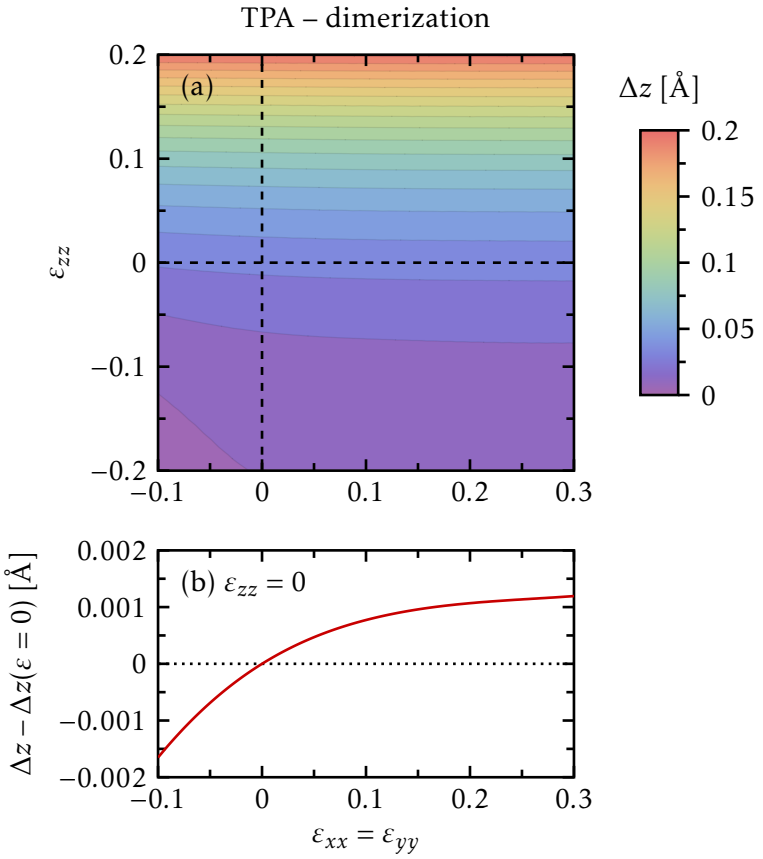

Figure 8.11: (a): Contour plot for the dimerization Δz of crystalline TPA under strain ε. The crystal is strained in the z direction along the carbon chains and uniformly in the x and y directions. (b): Cut through the contour plot in (a) along the line $\varepsilon_{zz} = 0$. The ordinate shows the dimerization Δz relative to the zero strain reference.

($\varepsilon_{xx} = \varepsilon_{yy} = 0$) and isolated chain limit ($\varepsilon_{xx}, \varepsilon_{yy} \to \infty$).

Figure 8.11(a) shows such a contour plot for the dimerization of the carbon chains. It can be seen that the dimerization depends strongly on ε_{zz}, i.e., the length of lattice vector $\boldsymbol{c}$. In contrast, the dimerization depends only minimally on $\varepsilon_{xx}/\varepsilon_{yy}$, i.e., the distance between the chains as long as the carbon atoms inside the chains are not squeezed together significantly (negative ε_{zz}). Still, the change of the dimerization from zero strain to more distant chains ($\varepsilon_{xx} = \varepsilon_{yy} = 0.3$) is about 0.001 Å (see Fig. 8.11(b)), which corresponds to a change in α (the amount of added HF exchange) of roughly 0.03 (see Tab. 8.2).

For the splitting of the valence and conduction bands at point E, the dependence on the strain direction is reversed in comparison to the dimerization, see Figs. 8.12 and 8.13.

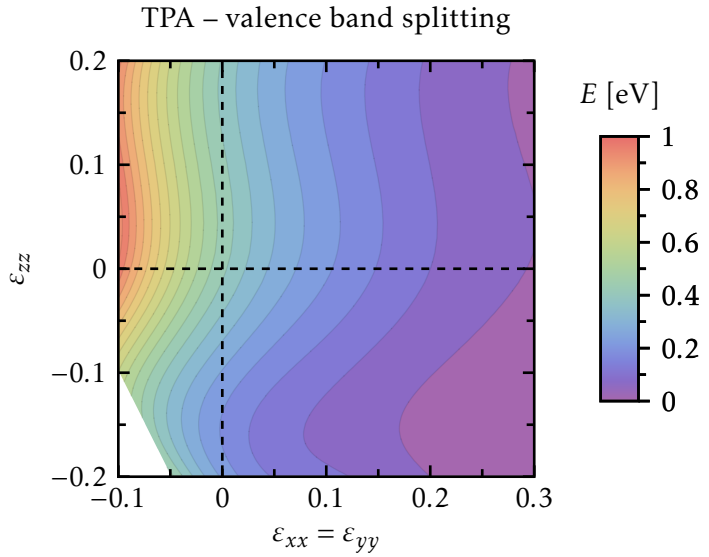

Figure 8.12: Contour plot for the splitting of the valence band at point E of crystalline TPA under strain ε. The crystal is strained in the z direction along the carbon chains and uniformly in the x and y directions. The lower left corner is left open since the band gap in this region is zero and the bands are crossing.

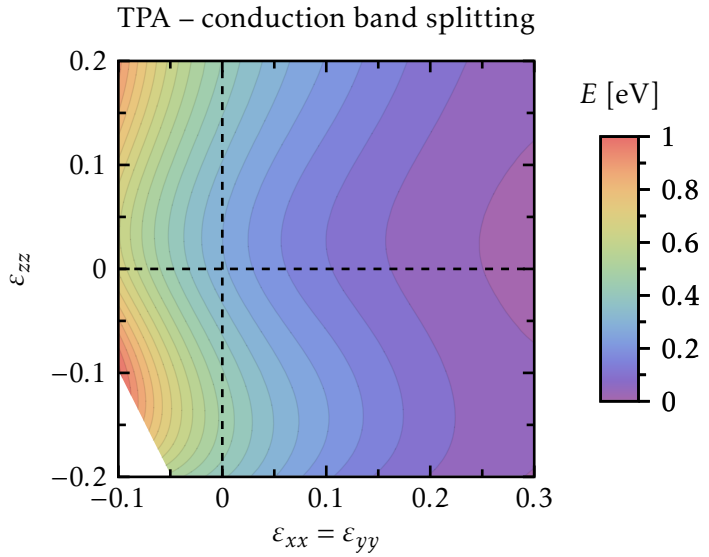

Figure 8.13: Contour plot for the splitting of the conduction band at point E of crystalline TPA under strain ε. The crystal is strained in the z direction along the carbon chains and uniformly in the x and y directions. The lower left corner is left open since the band gap in this region is zero and the bands are crossing.

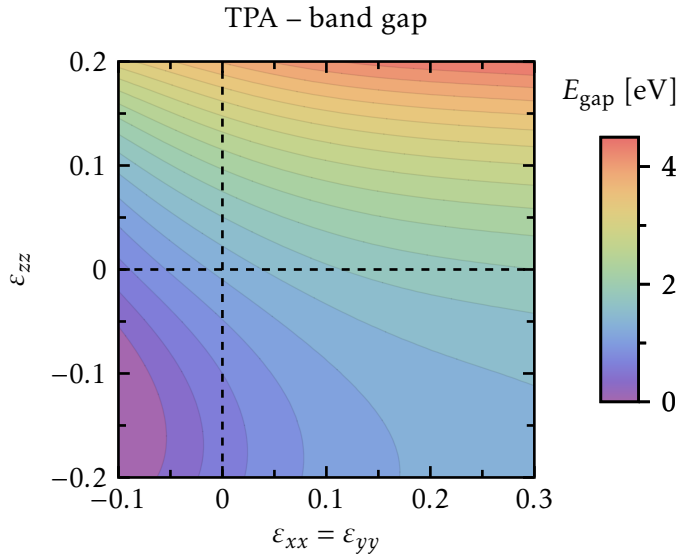

Figure 8.14: Contour plot for the band gap E_{gap} of crystalline TPA under strain ε. The crystal is strained in the z direction along the carbon chains and uniformly in the x and y directions.

The splitting depends strongly on $\varepsilon_{xx}/\varepsilon_{yy}$ but only slightly on ε_{zz}. As already seen in Fig. 8.9, the band splitting increases with decreasing interchain distance, i.e., decreasing $\varepsilon_{xx}/\varepsilon_{yy}$. The dependence of the splitting on ε_{zz} shows no clear behavior. Upon changing ε_{zz}, i.e., the lattice vector $\boldsymbol{c}$, the carbon atoms move sideways within the chains and in addition, the chains move with respect to each other in order to adjust the interchain distance. This behavior modifies the interchain interactions in a non-linear way and thereby the band splitting.

The behavior of the band gap under strain depends both on the dimerization and the band splitting. Larger dimerizations mean a larger band gap, see Fig. 8.7, and larger splittings of valence and conduction bands mean a smaller band gap, see Fig. 8.8. The interplay of these two effects can be seen in Fig. 8.14. Increasing $\varepsilon_{xx}/\varepsilon_{yy}$ as well as ε_{zz} increases the band gap. Thus, we expect that crystalline TPA behaves the other way round under hydrostatic pressure since this compresses the unit cell, which corresponds to decreasing $\varepsilon_{xx}/\varepsilon_{yy}$ and ε_{zz}, and therefore leads to a decrease in the band gap.

All shown contour plots for the strained unit cell are qualitatively the same for the HSE(0.75)+vdW functional and the dimerization changes by the same amount (about 0.001 Å) when going from the zero strain reference to more distant chains. Since the dimerization and the band gap sensitively depend on the amount of added HF exchange α (see Fig. 8.7), the actual numbers differ between the HSE(0.5)+vdW and HSE(0.75)+vdW functional.

Our strain studies show that the dimerization of the carbon chain only slightly changes

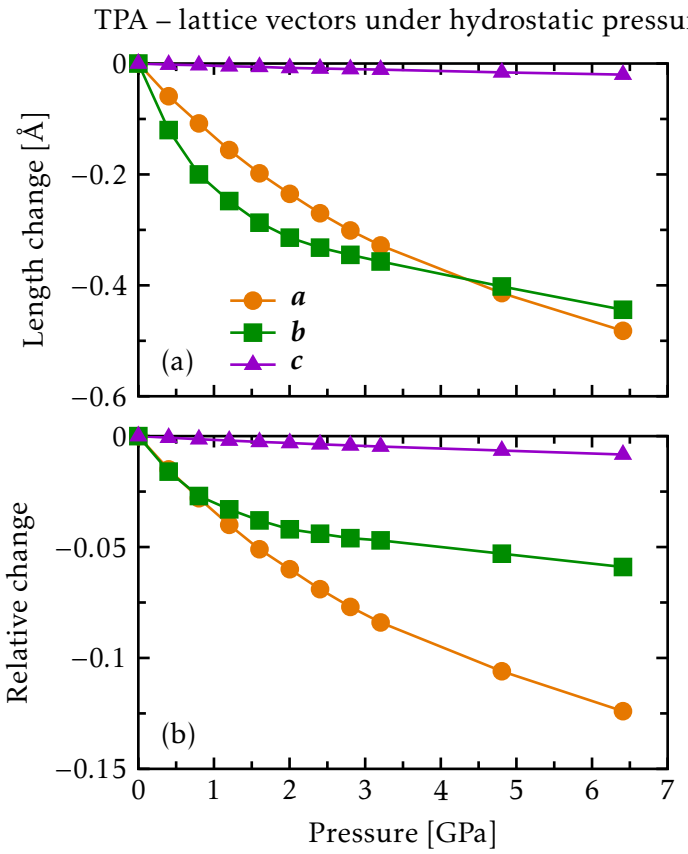

Figure 8.15: Change of lattice vectors under hydrostatic pressure. (a): Absolute length change of the three lattice vectors. (b): Relative length change of the three lattice vectors.

with the distance between the chains. This means that the dimerizations of single (isolated) TPA chains and crystalline TPA are comparable. Still, there is a slight difference (about 0.001 Å) between isolated and interacting chains, which in turn correspond to changes in α. Hence, a direct comparison between the values of α for bulk systems and isolated chains is not possible. In contrast to the dimerization, the electronic-structure properties sensitively depend on the interactions between the chains so that these properties significantly differ for bulk system and isolated chain. This suggests that not every result for the isolated chain can be directly transfered to the bulk system and vice versa.

8.4 Behavior under hydrostatic pressure

In the previous section, we have investigated the behavior of the dimerization and of electronic band structure properties under strain. However, the strained unit cell has

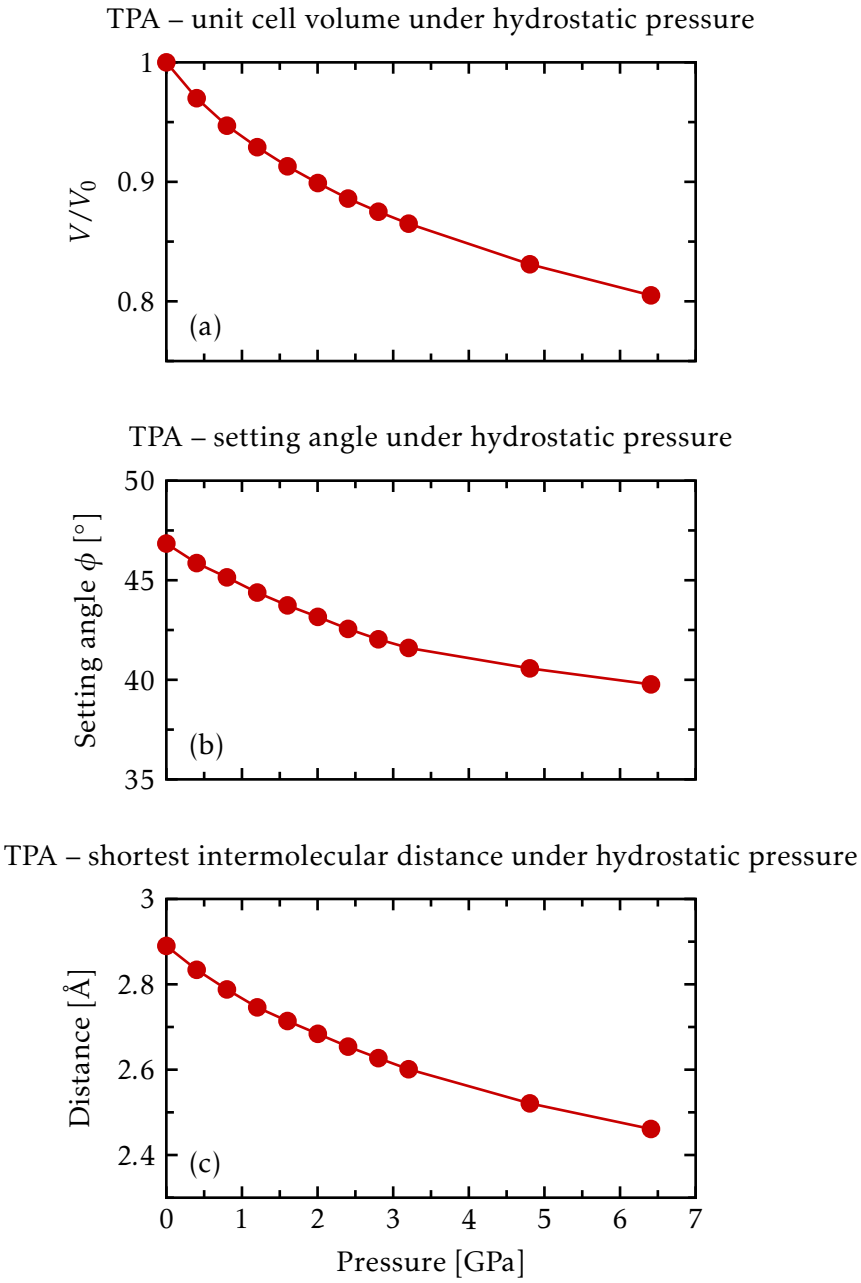

Figure 8.16: (a): Change of unit cell volume V relative to the volume at zero pressure V_0 under hydrostatic pressure. (b): Change of the setting angle ϕ (see Fig. 8.4) under hydrostatic pressure. (c): Change of shortest interchain distance under hydrostatic pressure, i.e., the shortest distance between carbon and hydrogen atoms on different chains.

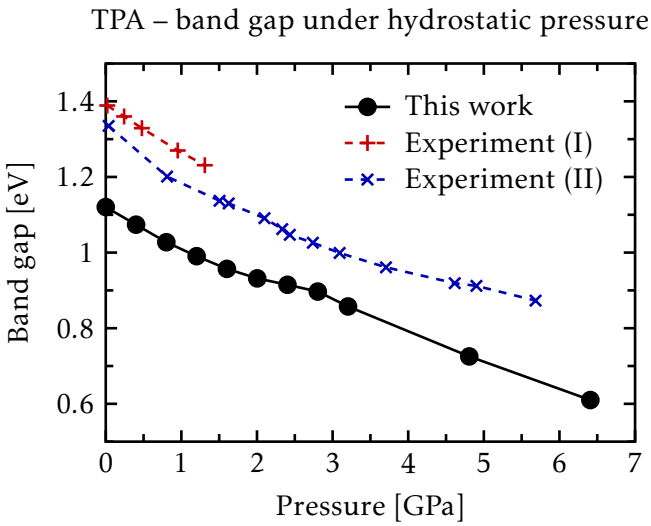

Figure 8.17: Change of electronic band gap under hydrostatic pressure. The band gap is indirect between point B and E up to 2.8 GPa. Afterwards, the band gap is direct at point E, see Figs. 8.18 and 8.19. Experiment (I) [Mos82] and experiment (II) [Bri86] show results of optical absorption measurements under hydrostatic pressure.

been kept fixed. In order to get a more realistic picture and to allow for changes of the other lattice vectors when one lattice vectors changes, we apply hydrostatic pressure to crystalline TPA. First, we discuss the changes in the geometry and these changes affect the electronic band structure, which in turn influences the electrical conductivity. The changes of the electrical conductivity under hydrostatic pressure are analyzed in detail and it is shown that the behavior of the conductivity can be attributed to specific changes in the band structure.

8.4.1 Geometry

Figures 8.15 and 8.16 show how the geometry of the TPA crystal system behaves under hydrostatic pressure. The lattice vector $\boldsymbol{c}$, which is in direction of the carbon chains, hardly changes under pressure due to the strong covalent bonds. In the other two directions, $\boldsymbol{a}$ and $\boldsymbol{b}$, the crystal is only weakly bonded by vdW interactions (see Sec. 8.2.1) and thus, much softer so that a strong, non-linear compression occurs at small pressure. As the pressure increases, the contraction becomes linear. On a relative scale, lattice vector $\boldsymbol{a}$ is compressed the most and lattice vector $\boldsymbol{c}$ the least. Figure 8.16(b) shows that the setting angle decreases under hydrostatic pressure. The reason for this is that lattice vector $\boldsymbol{a}$ decreases stronger than lattice vector $\boldsymbol{b}$ on a relative scale (see Fig. 8.15(b)), i.e., the chains approach each other faster in the direction of $\boldsymbol{a}$ than $\boldsymbol{b}$. In order to achieve

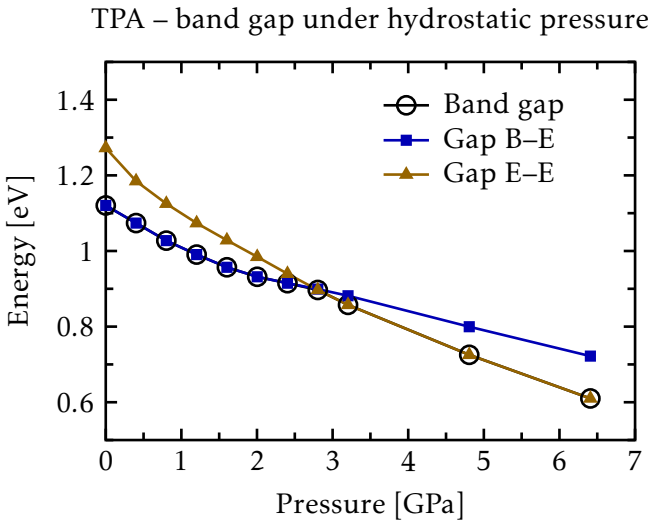

Figure 8.18: Change of the energy gap between point B and E (blue squares) and of the energy gap at point E (brown triangles) under hydrostatic pressure. The position of these gaps is displayed in Fig. 8.19. For reference, the band gap (empty black circles) from Fig. 8.17 is shown, too.

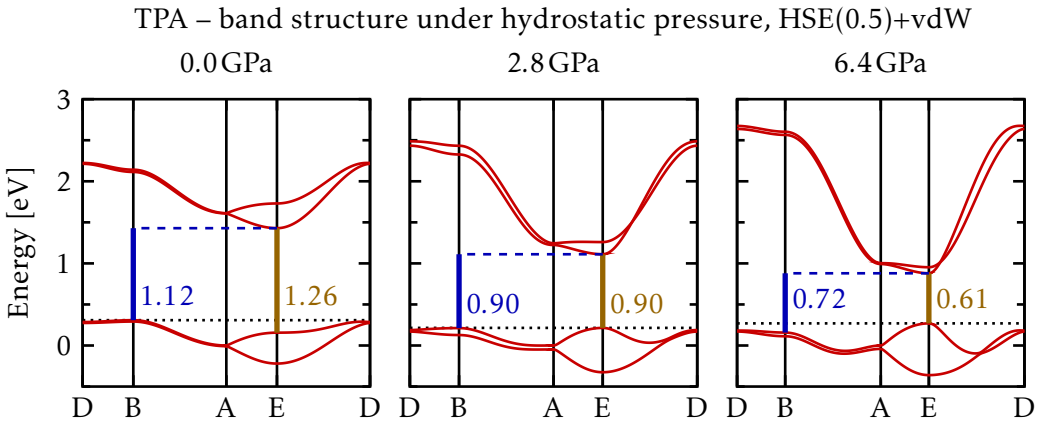

Figure 8.19: Sections from calculated electronic band structure near the valence band maximum (black, dotted line) for different pressures. The calculations were performed with the HSE(0.5) functional and vdW corrections. For each band segment between the special $\boldsymbol{k}$-points, 50 values have been calculated.

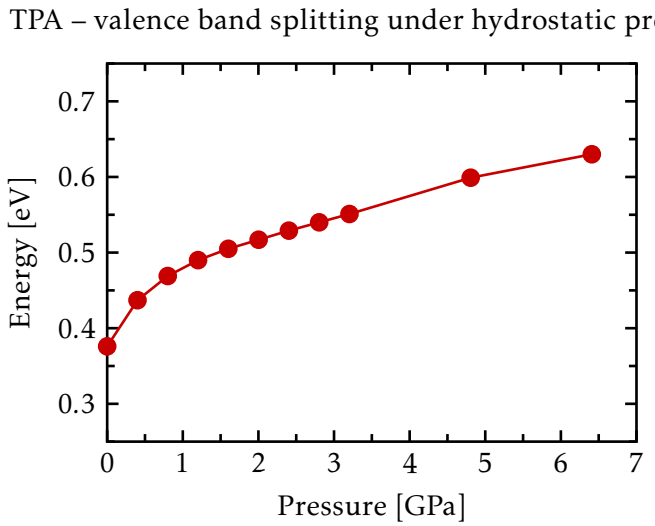

Figure 8.20: Splitting of valence band at point E under hydrostatic pressure.

a larger distance between the equivalent chains in the direction of $\boldsymbol{a}$, the setting angle decreases, see Fig. 8.4. The unit cell compression goes hand in hand with a decrease in the shortest distance between carbon and hydrogen atoms on different chains, see Fig. 8.16(c). In turn, this translates in an increased interaction between the chains, which also affects the electronic structure.

8.4.2 Electronic band structure

Figure 8.17 shows that the electronic band gap of TPA decreases under hydrostatic pressure as expected from Fig. 8.14. It decreases by 0.51 eV (46 %) from 1.12 eV at 0 GPa to 0.61 eV at 6.4 GPa. There is a transition from an indirect (between point B and E) to a direct band gap (at point E) at about 2.8 GPa as shown in Fig. 8.18: As the carbons chains come closer to each other under pressure, the increased interaction enhances the splitting of the valence bands, see Figs. 8.19 and 8.20. At about 2.8 GPa, the splitting at point E becomes so large that E becomes the VBM (instead of point B). Since the CBM is lowered under pressure but stays at point E, the band gap becomes direct. This is the reason for the kink in our data in Fig. 8.17. Figure 8.19 also shows that the curvature of the segments $\overline{\mathrm{BA}}$ and $\overline{\mathrm{ED}}$ in the conduction band significantly increases under pressure.

Comparing our results to optical absorption experiments [Mos82, Bri86], see Fig. 8.17, shows that we reproduce the trend of the band gap under pressure very well. However, these experiments do not report the nature of the band gap (direct/indirect) so that we cannot verify the transition from an indirect to a direct band gap.

For the HSE(0.75)+vdW functional, the electronic band gap shows similar, but quali-

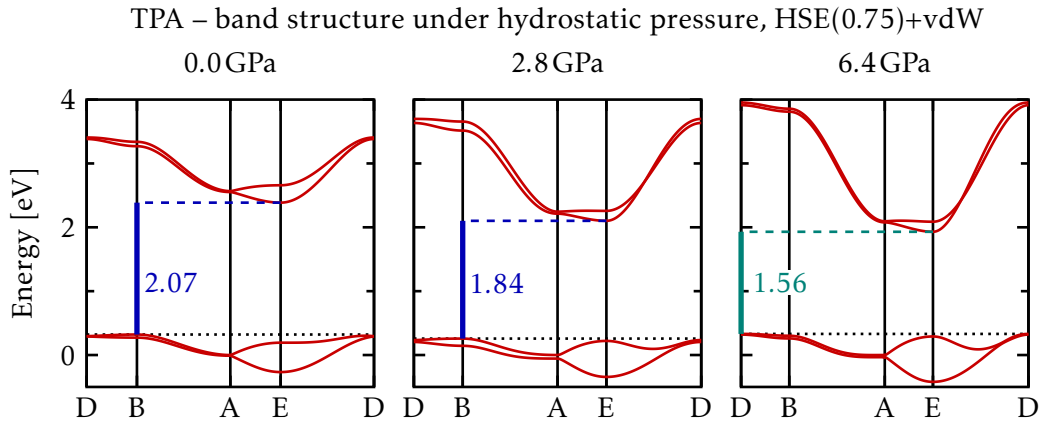

Figure 8.21: Sections from calculated electronic band structure near the valence band maximum (black, dotted line) for different pressures. The calculations were performed with the HSE(0.75) functional and vdW corrections. For each band segment between the special $\boldsymbol{k}$-points, 50 values have been calculated.

tatively and quantitatively different effects compared to the HSE(0.5)+vdW functional. It decreases by 0.51 eV (25 %) from 2.07 eV at 0 GPa to 1.56 eV at 6.4 GPa. However, it stays indirect: The splitting of the valence bands at point E increases (see Fig. 8.21), but due to the fact that the valence band at point E lies initially lower, the splitting under pressure is not large enough to make point E the VBM in the considered pressure region. Instead, the VBM changes from point B to D at about 4.5 GPa.

8.4.3 Macroscopic transport properties

In this section, we consider electrical conductivities of TPA for the intrinsic case as well as n- and p-doping with a very high charge carrier concentration of $10^{21}\,\mathrm{cm}^{-3}$ at zero pressure. This concentration is among the highest values reported by experiments. The temperature is set to 300 K. According to Sec. 4.2, the intrinsic charge carrier concentration n_i has been determined, see Fig. 8.22(a). It can be seen that the concentration increases roughly exponentially under hydrostatic pressure. As in the case of anthracene (see Sec. 7.3.3), this behavior is expected: The band gap E_gap decreases approximately linearly under pressure (see Fig. 8.17) and the intrinsic charge carrier concentration has approximate proportionality shown in Eq. (7.1).

Figure 8.22(b) shows the Fermi level for all three cases (intrinsic, n-, p-doping), which has been determined according to Sec. 4.2. In the intrinsic case, the Fermi level lies in the middle of the band gap. It gets close to the CBM (VBM) for n-doping (p-doping) and TPA becomes almost metallic. This is consistent with experimental findings, which report metallic behavior of TPA for charge carrier densities around $10^{22}\,\mathrm{cm}^{-3}$ [Shi67,

TPA – Intrinsic charge carrier concentration and Fermi level under hydr. press.

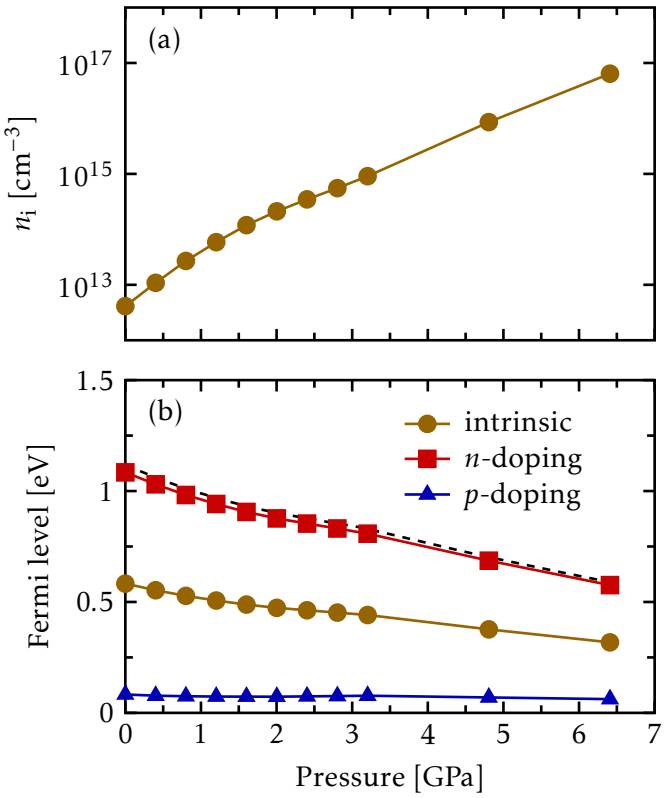

Figure 8.22: (a): Change of the intrinsic charge carrier concentration n_i under pressure. (b): Change of the Fermi level under pressure. The VBM is set to zero and the CBM is indicated by the black, dashed line. In the intrinsic case (brown circles), the Fermi level lies in the middle of the band gap. A doping with a charge carrier concentration of 10^{21} cm^{-3} at zero pressure brings the Fermi level close to the CBM in the n-doping case (red squares) and close to the VBM in the p-doping case (blue triangles).

Wei79, Väk93]. Under hydrostatic pressure, the relative positions of the Fermi level are preserved for the three different cases. This means the Fermi level stays in the middle of the band gap for the intrinsic case and it keeps the same distance to the CBM (VBM) for n-doping (p-doping).

Intrinsic band conductivity

Knowing the position of the Fermi level for different pressures, the quantity ς/τ can be calculated with BoltzTraP, which allows to investigate trends in the electrical band conductivity ς in the constant relaxation time approximation, see Sec. 4.1. Figure 8.23

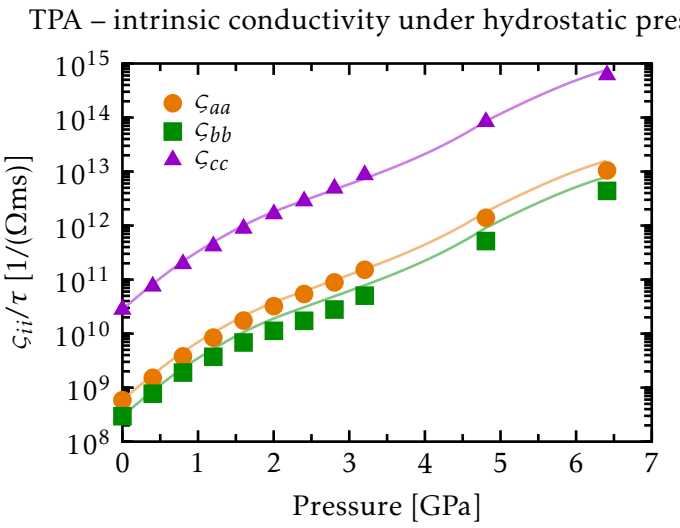

Figure 8.23: Change of the quantity ς_{ii}/τ in the intrinsic case under hydrostatic pressure for the directions along the three lattice vectors $i = a, b, c$. The solid, light-colored lines are the approximations with Eq. (7.2) and $\varsigma_{ii}(0)$ as starting point.

shows the change of ς_{ii}/τ in the direction of the three lattice vectors $i = a, b, c$ under hydrostatic pressure for the intrinsic case. There is a strong increase by four orders of magnitude between the pressures 0 GPa and 6.4 GPa. This behavior is expected since the intrinsic charge carrier concentration increases roughly exponentially under pressure (see Fig. 8.22(a)). In comparison to anthracene, this increase is stronger. ς/τ increases by the same relative amount for anthracene but the pressure increase is 10.2 GPa in this case. It can also be seen that the electronic transport is highest (by two orders of magnitude) along the lattice vector $\boldsymbol{c}$, i.e., along the carbon chains. This is not too surprising since this is the direction of the conjugated bonds.

Equation (7.2) can be used again for approximating the behavior of the conductivity under pressure together with the value of ς_{ii}/τ at zero pressure as starting point and $E_{\mathrm{gap}}(p)$ from Fig. 8.17. Figure 8.23 shows that this approximation reproduces ς_{ii}/τ very well as in the case of anthracene. This means that the change in intrinsic conductivity under pressure mainly stems from the change of the band gap under pressure and that other effects (changes in the form of the band structure) only play a minor role.

Extrinsic band conductivity

However, this is different in the case of doping as already explained for anthracene, see Sec. 7.3.3. For a doping with a charge carrier concentration of $10^{21}\,\mathrm{cm}^{-3}$ at zero pressure (see Fig. 8.22(b)), the Fermi level gets very close to the CBM or VBM so that changes of

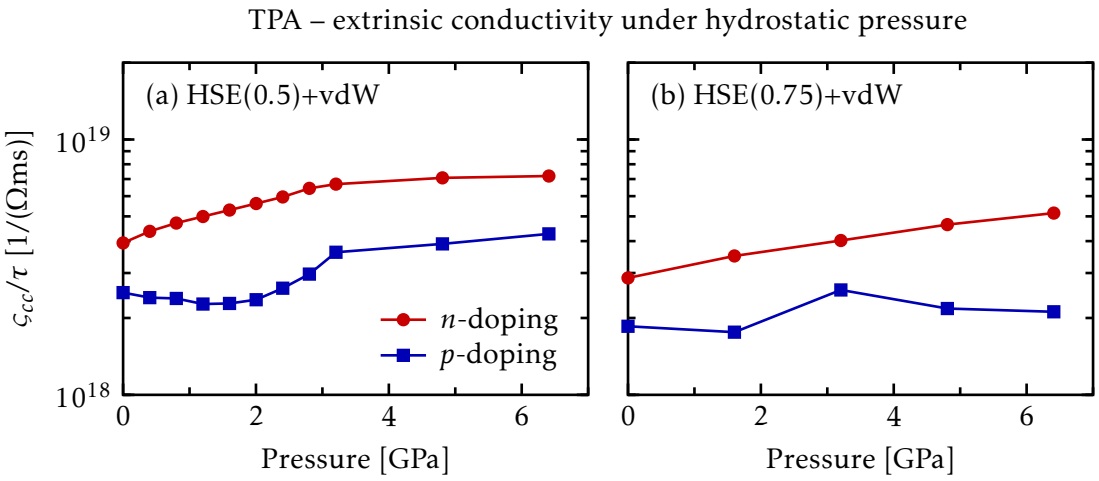

Figure 8.24: Change of the quantity ς_{cc}/τ in the doped case with a charge carrier concentration of $10^{21}\,\mathrm{cm}^{-3}$ at zero pressure under hydrostatic pressure. (a): Calculation with the HSE(0.5) functional and vdW corrections. (b): Calculation with the HSE(0.75) functional and vdW corrections.

the band gap do not have a big influence on the conductivity. Instead, the effect of small changes of the band curvature close to the CBM or VBM become visible. Figure 8.24(a) shows the change of ς_{cc}/τ for n- and p-doping with a charge carrier concentration of $10^{21}\,\mathrm{cm}^{-3}$ at zero pressure under hydrostatic pressure. Since the conductivity along the carbon chains is two orders of magnitude larger than in the other two directions, similar to the intrinsic case, we have focused on ς_{cc} for the remainder of this chapter.

For n-doping, the ς_{cc}/τ increases under pressure but not nearly as much as in the intrinsic case (Fig. 8.23) since the Fermi level is already close to the CBM. This increase comes from the increasing band curvature around the CBM in the segments $\overline{\mathrm{BA}}$ and $\overline{\mathrm{ED}}$ under pressure, see Fig. 8.19. As explained in Sec. 7.3.3, a larger curvature means a higher conductivity.

For p-doping, we have the interesting case that ς_{cc}/τ first decreases under pressure and then starts to rise around 2 GPa, see Fig. 8.24(a). This can be understood by looking at the behavior of the valence band under pressure in Fig. 8.19. For low pressures, the VBM is at point B and there the band curvature decreases under pressure leading to a decrease in conductivity. For pressures above 2 GPa, point E comes close to the VBM, which strongly increases the conductivity since now two channels for conduction exist. Beyond 3 GPa, point E is the VBM and point B is getting out of reach, which flattens the increase. Still, the ς_{cc}/τ increases for higher pressures since the band curvature around point E also increases under pressure.

HSE(0.75)+vdW functional

For the HSE(0.75)+vdW functional, we find the same behavior of ς_{ii}/τ ($i = a, b, c$) under hydrostatic pressure for the intrinsic case. The change in electrical conductivity is likewise dominated by the change of the electronic band gap and the dominant transport direction is along the carbon chain. However, ς_{ii}/τ is smaller by eight orders of magnitudes since the band gap is much larger than for the HSE(0.5)+vdW functional. In the n-doped case (Fig. 8.24(b)), the conductivity behaves similarly since the bands around the CBM behave similarly in comparison to the HSE(0.5)+vdW functional, see Fig. 8.21. The p-doped case (Fig. 8.24(b)) displays a different behavior because the VBM behaves differently compared to the HSE(0.5)+vdW functional, see Fig. 8.21. Still, there is a decrease of the conductivity at low pressure because the band curvature around point B decreases. The trend at higher pressures is determined by the behavior of the valence bands near point D, B, and E.

Comparison to experiment

In a previous section, we have stated that in our calculation, the electrical conductivity along the carbon chains is two orders of magnitude larger than in the other two directions for the doped case. Similar levels of anisotropy in the conductivity have been found in experiments with doped TPA [Tsu92].

In order to check the consistency of our calculated electrical conductivity data, we can determine the relaxation time τ by taking experimental data. Väkiparta *et al.* [Väk93] report for an oriented TPA film at a temperature of 300 K an electrical conductivity of about $10^5\,(\Omega\mathrm{m})^{-1}$ for a charge carrier concentration of about $5\times10^{21}\,\mathrm{cm}^{-3}$. For such an oriented film, the conductivity is dominated by the transport direction along the carbon chains. From Fig. 8.24(a), the value $\varsigma_{cc}/\tau \sim 5\times10^{18}\,(\Omega\mathrm{ms})^{-1}$ allows to estimate the relaxation time $\tau \sim 2\times10^{-13}\,\mathrm{s}$. This relaxation time is consistent with the time scale of the carbon-carbon stretching vibration, which occurs on similar time scales ($10^{-14}\,\mathrm{s}$ to $10^{-13}\,\mathrm{s}$ [Kuz80, Bri86]). For electronic transport along the carbon chains, we expect that the vibrations of the carbon atoms are the main source for the scattering of charge carriers. In conclusion, our estimation of the relaxation time nicely shows that our data is consistent with experimental values.

8.5 Summary

The geometric and electronic properties of crystalline TPA have been investigated in detail at zero pressure and under hydrostatic pressure in this chapter. We find that (at least) hybrid functionals are mandatory to correctly describe the dimerization of the carbon chains. It is also important to include vdW corrections in order to obtain unit cell volumes that are not too big. The interaction between the chains in the crystal lead

to a splitting of valence and conduction bands. Straining the unit cell along the carbon chains influences the dimerization the most. Straining the unit cell in the other two directions has the biggest effect on the band splitting. Combining these two effects leads to a non-trivial behavior of the band gap. Furthermore, our strain study demonstrates that a one-to-one comparison between properties of bulk TPA and isolated chains of TPA is not always valid. Therefore, it is unclear for instance if statements about the value of α (the amount of added HF exchange) can be directly transfered from one system to the other. Under hydrostatic pressure, the crystal gets compressed along lattice vector $\boldsymbol{a}$ and $\boldsymbol{b}$ and the band gap is reduced in good agreement with experimental measurements. The compression leads to an increased interchain interaction, and in turn, the splitting of the valence band increases. This causes a transition from an indirect to a direct band gap. The reduction of the band gap strongly increases the charge carrier concentration and the electrical band conductivity in the intrinsic case. The changes in the band structure near the CBM and VBM determine the behavior of conductivity in the doped case. The conductivity is two orders of magnitude larger along the carbon chains than in the directions of the other two lattice vectors for the intrinsic and doped case. This is in agreement with experiments, which find a similar directional dependence for the doped case.

Our comparisons between the HSE(0.5)+vdW and HSE(0.75)+vdW functional show that there is no qualitative difference in the description of TPA under hydrostatic pressure. The corresponding geometries and electronic band structures are very similar and display the same features. Therefore, the intrinsic and extrinsic electrical conductivities show the same qualitative behavior under hydrostatic pressure for both functionals. However, the exact shape depends on the details of the band structure, which differs slightly between both functionals.

9 Summary and outlook

In this thesis, we have successfully used DFT with different approximations of the exchange-correlation functional for the investigation of organic semiconductors under hydrostatic pressure and we have explained the associated changes of their electronic-structure properties. On the one hand, this required a systematic assessment of the accuracy of the employed approximations since the interactions in such systems are driven by exchange-correlation effects. On the other hand, this required the derivation and implementation of the stress tensor in the numeric, atom-centered orbitals based all-electron electronic-structure code FHI-aims. For the stress tensor, Jacobi terms have been considered since the boundaries of integrals over the unit cell change under strain, and the contributions of the atom-centered basis functions, which move under strain, have been included as well. Naturally, all contributions that arise from the kinetic, electrostatic, and exchange-correlation energy of DFT have been accounted for. The electrostatic contributions required a full derivation of the strain derivatives of the Ewald summation for multipole charges. Furthermore, the contributions of a pairwise $1/R^6$ vdW correction scheme and of the HF exchange needed for hybrid functionals have been included – two contributions that we have shown to be essential for organic crystals.

We have investigated the accuracy of our stress tensor implementation by performing extensive benchmark calculations for a wide range of inorganic and organic crystals and it has been demonstrated that accurate numerical results can be achieved even for sparse integration grids by explicitly leaving out terms that are analytically zero. The comparison between the stress tensor calculated via our analytical derivatives and the one calculated via finite differences has shown that the difference is always in the range of a few meV/Å^3 or below, which is comparable to the magnitude of the numerical error. Furthermore, the same level of accuracy has been demonstrated for all DFAs available within FHI-aims. Our implementation is consistent with respect to the basis set and unit cell size, too. This means that the difference stays constant upon changing the size of one of these quantities. In comparison to the finite difference method, the calculation of the analytical stress tensor allows a speedup of at least a factor of three to five for hybrid functionals. This speedup is especially valuable since DFT calculations with hybrid functionals are much more time consuming than calculations with LDA or GGA

functionals. Finally, it has been demonstrated that our implemented stress tensor is well suited to optimize unit cells of crystal structures under pressure.

We have applied this implementation to the prototypical organic crystals anthracene and TPA in order to study their behavior under hydrostatic pressure. For both crystals, vdW corrections are needed to correctly describe the interactions between the molecules or chains inside the crystal. For anthracene, there is no qualitative difference in the geometry and the electronic band structure between GGA and hybrid functionals. However, hybrid functionals (or higher-level methods such as *GW*) are required to achieve quantitatively correct band gaps. In contrast, it is crucial to use hybrid functionals for TPA in order to obtain the correct symmetry breaking ground state, i.e., an alternation of shorter (double) and longer (single) bonds between the carbon atoms of the polymer chain (Peierl's distortion). As a matter of fact, LDA and GGA functionals give geometries for TPA in which all bonds have the same length, which in turn results in an erroneous metallic ground state. In part, hybrid functionals are able to cure this deficiency of (semi-)local DFAs. However, the amount α of added HF exchange included in such hybrid functionals is a parameter and both the dimerization and the band gap sensitively depend on it. For isolated TPA chains, comparisons with higher-level CCSD(T) calculations have shown that no value of α is able to yield the correct dimerization of the carbon chains and simultaneously a vanishing many-electron self-interaction error [Kör12]. It is however unclear if such a statement also holds for crystalline TPA, (a) since no high-level CCSD(T) calculations for this system are available (or even possible with reasonable numerical effort) and (b) since the electronic structure of TPA significantly differs in the bulk and isolated chain limit. For these reasons, we have systematically discussed how the actual value of $\alpha \in [0, 1]$ affects the properties in TPA and to which extent this changes in bulk systems. Generally, a value of α between 0.5 and 0.75 yields qualitatively correct trends with respect to experiments.

The electronic band structures of crystalline anthracene and TPA display a splitting of both valence and conduction bands due to the interactions between the molecules or chains. Hydrostatic pressure leads to a strong compression of the crystal structures along the weakly bonded crystal directions, thereby giving rise to stronger intermolecular or interchain interactions. Consequently, the splitting of the bands is increased. Accordingly, the electronic band gap decreases under hydrostatic pressure for both organic crystals, and in the case of TPA, the increased splitting of the valence band causes the transition from an indirect to a direct band gap.

Furthermore, we have used the Boltzmann transport equation in the constant relaxation time approximation in order to investigate how these microscopic properties affect macroscopic equilibrium (charge carrier concentration) and non-equilibrium properties (electrical band conductivity). Again, both organic semiconductors display a similar behavior. In the intrinsic case, applying pressure leads to a strong increase in conductivity due to the increase in charge carrier concentration associated with the band gap reduction. The behavior of the conductivity in the *n*- and *p*-doped case can be attributed

to the changes of the band structure near the CBM and VBM, respectively. In general, the band curvatures get stronger under pressure, thereby increasing the conductivity. Our calculated pressure-dependent band gap and electrical conductivity data is consistent with experimental measurements. This shows that our theoretical approach is able to yield reliable results and predictions. We can conclude that in the case of anthracene and TPA, electronic transport properties are enhanced by increasing the interactions between the constituents. In practice, this can be achieved by applying external pressure as demonstrated in our calculations.

This thesis has focused on electronic band transport as described parametrically by the Boltzmann transport equation in the constant relaxation time approximation. This allowed qualitative insights into how pressure induced changes in the electronic structure affect macroscopic transport on a relative scale; reliable and accurate quantitative predictions are however not possible in this formalism: On the one hand, the relaxation time does depend on temperature and pressure, which linearly affects the electrical conductivity. On the other hand, an even larger influence on the conductivity can arise from the band gap renormalization due to lattice vibrations [Car05] since the intrinsic conductivity depends exponentially on the electronic band gap as shown in Chaps. 7 and 8. For quantitative calculations, a more rigorous treatment of electronic band transport that accounts for such effects is required, e.g., using lifetimes derived from first principles [Xu14] or using the Kubo-Greenwood theory [Hol11, Fre14], which requires the calculation of the current-current correlation functions via molecular dynamics simulations. Research along these lines obviously constitutes a promising extension of this thesis.

Still, band transport is not the only mechanism determining the electrical conductivity in these organic semiconductors as already discussed in the introduction (Chap. 1). Achieving a unified assessment of electronic transport that also accounts for the contributions arising from electronic hopping, coupled electron-phonon transport (e.g. polarons), and ionic effects is obviously the final – scientifically extremely challenging – goal in this field of research. For accurate device simulations, this data, i.e., the full dependence of electronic material properties and scattering mechanisms on temperature, pressure, and charge carrier densities, is desirable. Still, the band structures and their pressure-induced changes presented in this thesis lay the founding for mesoscopic to macroscopic device simulations (e.g. via $\boldsymbol{k} \cdot \boldsymbol{p}$ perturbation theory [Yan14]).

Appendices

A Atomic units

In the system of atomic units the following physical constants are set to unity:

- electron charge e
- electron mass m_e
- reduced Planck constant $\hbar$
- electrostatic constant $1/(4\pi\epsilon_0)$

Therefore, charges and masses are measured in multiples of e and m_e, respectively.

B Details of FHI-aims

B.1 Radial part of basis functions

The radial part $u_{nl}(r)$ of the atom-centered basis functions in Eq. (3.2) is determined by the numerical solution of a Schrödinger-like radial equation

$$\left(-\frac{1}{2}\frac{\partial}{\partial r}+\frac{l(l+1)}{r^2}+v_{\text{shape}}(r)+v_{\text{cut}}(r)\right)u_{nl}(r)=\epsilon_n u_{nl}(r). \tag{B.1}$$

The potential v_{shape} determines the main shape of the radial function and the confining potential v_{cut} ensures a smooth decay to zero of the radial functions beyond a certain distance $r \geq r_{\text{cut}}$. The analytical form of the confining potential is chosen as

$$v_{\text{cut}}(r)=\begin{cases}0 & \text{for } r \leq r_{\text{onset}}\\ \frac{s}{(r-r_{\text{cut}})^2}\exp\left(\frac{w}{r-r_{\text{onset}}}\right) & \text{for } r_{\text{onset}} < r < r_{\text{cut}}\\ \infty & \text{for } r \geq r_{\text{cut}}\end{cases} \tag{B.2}$$

with a global scaling parameter s, the onset r_{onset} of the confining potential and its width w. For the distances, the relation $r_{\text{cut}} = r_{\text{onset}} + w$ holds. Typical values of these parameters are $s = 200\,\text{Ha}$, $r_{\text{cut}} = 6\,\text{Å}$, and $w = 2\,\text{Å}$. The radial functions $u_{nl}(r)$ are generated for each atom species in two steps:

1. v_{shape} in Eq. (B.1) is set to the self-consistent radial potential $(v_{\text{ext}} + v_{\text{H}} + v_{\text{xc}})$ in Eq. (2.27) for the isolated free atom. The solution for the free-atom electrons forms the so-called "minimal" basis set, which depends on the used DFA.

2. In order to increase the flexibility of the basis set, additional basis functions are constructed iteratively in the following way (DFA independent):

   a) A pool of candidate radial functions is generated by solving Eq. (B.1) for various choices of v_{shape}. It is either the potential of doubly positive charged free ions or a hydrogen-like z/r potential with z a real number.

b) Starting from the "minimal" basis set, each candidate radial function is added to the current basis in turn. The radial function that gives the best improvement of the LDA total energy for dimers of the given species is then added permanently to the current basis.

c) Step b) is repeated until no further significant improvement of the total energy is found.

d) The selected additional radial functions of step b) are grouped together in so-called tiers, namely "tier 1", "tier 2", and so on. The successive basis sets are hierarchical. For example, a "tier 2" basis set adds further radial functions while including the radial functions of the "minimal" and "tier 1" basis set as well.

B.2 Silicon basis functions

Table B.1 shows the shorthand notation for the parameters used to obtain the radial functions of silicon for those basis sets that were used for the study of the analytical stress for different basis set sizes in Sec. 6.1.3.

B.3 "Modified Stratmann" partitioning function

Here, the partitioning function for integrals proposed by Stratmann *et al.* [Str96] is briefly reviewed and the modified implementation in FHI-aims is presented.

The goal is to find an expression for the function $g_I(\boldsymbol{r})$ in Eq. (3.9) that is strongly peaked around atom I. For this purpose, confocal elliptical coordinates $\mu_{IJ}(\boldsymbol{r})$ between pairs of atoms are defined,

$$\mu_{IJ}(\boldsymbol{r}) = \frac{|\boldsymbol{r}-\boldsymbol{R}_I| - |\boldsymbol{r}-\boldsymbol{R}_J|}{|\boldsymbol{R}_I - \boldsymbol{R}_J|}, \tag{B.3}$$

where $\boldsymbol{R}_I$ and $\boldsymbol{R}_J$ are the positions of atom I and atom J, respectively. The range of the coordinates is limited to $-1 \leq \mu_{IJ}(\boldsymbol{r}) \leq 1$. Next a piecewise function h is defined,

$$h(\mu_{IJ}, a) = \begin{cases} 1, & \mu_{IJ} \leq -a \\ k(\mu_{IJ}, a), & -a < \mu_{IJ}(\boldsymbol{r}) < a \\ -1, & \mu_{IJ} \geq a, \end{cases} \tag{B.4}$$

with the threshold a. In practice, an empirically determined value of $a = 0.64$ is used. The function k is required to be continuously differentiable at $\mu_{IJ} = \pm a$. The proposed form of Stratmann *et al.* for k is

$$k(\mu_{IJ}, a) = \frac{1}{16}\left[35\left(\frac{\mu_{IJ}}{a}\right) - 35\left(\frac{\mu_{IJ}}{a}\right)^3 + 21\left(\frac{\mu_{IJ}}{a}\right)^5 - 5\left(\frac{\mu_{IJ}}{a}\right)^7\right]. \tag{B.5}$$

Table B.1: Shorthand notation for the parameters used to obtain the radial functions for silicon according to Eq. (B.1). For the confinement potential v_{cut}, $r_{\text{onset}} = 4$Å and $w_{\text{cut}} = 2$Å was used (see Eq. (B.2)). The minimal basis consist of the radial functions of the occupied orbitals of spherically symmetric free atoms with noble gas configuration and quantum numbers of the additional valence functions. H(nl, z) denotes a hydrogen-like radial function for the Coulomb potential z/r with radial and angular quantum numbers n and l, respectively. $X^{2+}(nl)$ denotes a n, l function for the doubly positive charged ion of element X. Each tier includes the basis functions of the lower tiers.

	Si
minimal	[Ne]+3s3p
tier 1	H(3d, 4.2)
	H(2p, 1.4)
	H(4f, 6.2)
	Si^{2+}(3s)
tier 2	H(3d, 9.2)
	H(5g, 9.4)
	H(4p, 4.0)
	H(1s, 0.65)
tier 3	Si^{2+}(3d)
	H(3s, 2.6)
	H(4f, 8.4)
	H(3d, 3.4)
	H(3p, 7.8)

With the function h from Eq. (B.4), the so-called cell function s is defined,

$$s(\mu_{IJ}, a) = \tfrac{1}{2}\Big[1 - h(\mu_{IJ}, a)\Big]. \tag{B.6}$$

The values of s are in the range between 0 and 1. The function $g_I(\boldsymbol{r})$ is given by

$$g_I(\boldsymbol{r}) = \prod_{J \neq I}^{N_{\text{nuc}}} s(\mu_{IJ}(\boldsymbol{r}), a). \tag{B.7}$$

Due to the definition of h and the threshold a in Eq. (B.4), the distance from which an atom can contribute to the partitioning function is restricted. For atoms J that have a large distance to the integration point $\boldsymbol{r}$ and atom I, $\mu_{IJ}(\boldsymbol{r})$ approaches -1 (see Eq. (B.3)) and consequently, the cell s function becomes 1 (see Eq. (B.6)). Nevertheless, the distance up to which an atom contributes can be very large. This poses a problem for periodic systems because it would lead to large integration volumes. In order to solve this problem, the partitioning function by Stratmann *et al.* as described above has been

Table B.2: Integration grids of silicon. The specification of the light and tight integration grid are shown here. N_r specifies the number of spherical integration shells around each atom, r_outer the extend of the grid, n_mult the radial multiplier, N_ang the number of angular integration points, and $N_\mathrm{tot,atom}$ the total number of grid points per atom. See also Sec. 3.4.

	light grid	tight grid
N_r	42	42
r_outer	5 Å	7 Å
n_mult	1	2
$\min(N_\mathrm{ang})$	50	50
$\max(N_\mathrm{ang})$	302	434
$N_\mathrm{tot,atom}$	5 604	17 918

implemented in FHI-aims with a small modification: Only atoms J that are closer to the integration point $\boldsymbol{r}$ than the cut-off radius r^J_cut of their confining potential v^J_cut (see Eq. (B.2)) are allowed to contribute. To avoid discontinuities, the following interpolation scheme is employed for the cell function s in Eq. (B.6):

$$s_\mathrm{mod}(\mu_{IJ}(\boldsymbol{r}), a) = \Big(1 - u_J(\boldsymbol{r})\Big) + u_J(\boldsymbol{r}) s(\mu_{IJ}(\boldsymbol{r}), a) \tag{B.8}$$

with

$$u_J(\boldsymbol{r}) = \begin{cases} 1, & d_J \leq b\, r^J_\mathrm{cut} \\ v_J(\boldsymbol{r}), & b\, r^\mathrm{cut}_J < d_J < r^J_\mathrm{cut} \\ 0, & d_J \geq r^J_\mathrm{cut} \end{cases} \tag{B.9}$$

and

$$v_J(\boldsymbol{r}) = \frac{1}{2} + \frac{1}{2} \cos\left[\pi \frac{d_J / r^J_\mathrm{cut} - b}{1 - b}\right]. \tag{B.10}$$

Here, $d_J = |\boldsymbol{r} - \boldsymbol{R}_J|$ is the distance between integration point $\boldsymbol{r}$ and atom J. The transition threshold b has been chosen as $b = 0.8$. In summary, this modification allows to use the Stratmann partitioning function together with a restricted atom list without introducing any discontinuities.

B.4 Silicon integration grid

In Tab. B.2, the specifications of the light and tight integration grid for silicon are shown, which were used for the study of the numerical correction terms in Secs. 5.4.1 and 5.4.2. The distribution of the angular grid points and integration shells for both integrations grids is shown in Figs. B.1 and B.2, respectively.

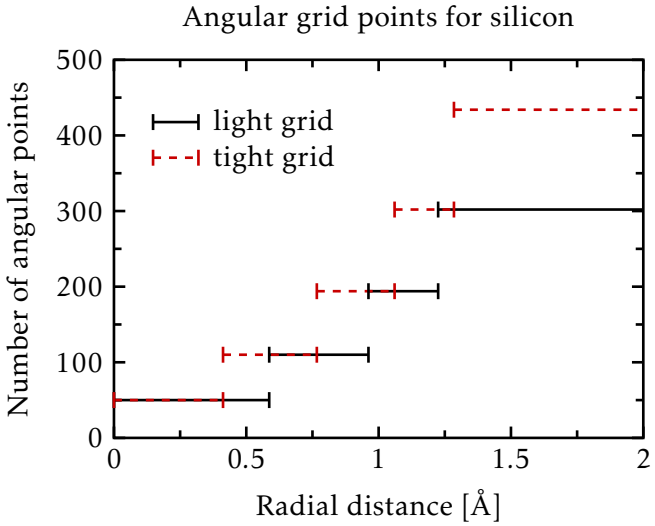

Figure B.1: Number of angular integration points for silicon in dependence of the radial distance from the nucleus. For the tight integration grid (red, dashed), the number of points increases faster with increasing distance and is overall larger in the most distant region in comparison to the light integration grid (black, solid). The number of integration points stays constant beyond 2 Å.

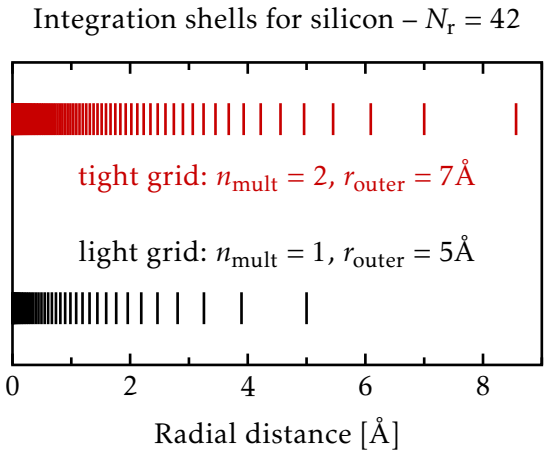

Figure B.2: Spherical integration shells for silicon. The position of these shells around a silicon atom is shown and they are determined by Eq. (3.10). The light integration grid (black, bottom) uses a radial multiplier $n_{mult} = 1$ and an extension of the shells $r_{outer} = 5$ Å. For the tight integration grid (red, top) the values are $n_{mult} = 2$ and $r_{outer} = 7$ Å.

C Details of stress tensor derivation

C.1 Strain derivative of on-site Hartree term

We want to show that the strain derivative of the Hartree potential $v_{\mathrm{H}}^{I}(\boldsymbol{r}-\boldsymbol{R}_I)$ vanishes for $\boldsymbol{r}=\boldsymbol{R}_I$. Starting with the definition from Eq. (3.29) and using Eqs. (5.6) and (5.20), yields

$$\begin{aligned}\frac{\partial v_{\mathrm{H}}^{I}(\boldsymbol{r}-\boldsymbol{R}_I)}{\partial \varepsilon_{\lambda\mu}} = \delta_{\lambda\mu} v_{\mathrm{H}}^{I}(\boldsymbol{r}-\boldsymbol{R}_I) &+ \int_V \mathrm{d}\tilde{\boldsymbol{r}}\,(\tilde{r}_\mu - R_{I,\mu})\frac{\partial n_I(\tilde{\boldsymbol{r}}-\boldsymbol{R}_I)}{\partial \tilde{r}_\lambda}\frac{1}{|\boldsymbol{r}-\tilde{\boldsymbol{r}}|} \\ &+ \int_V \mathrm{d}\tilde{\boldsymbol{r}}\,(\tilde{r}_\mu - r_\mu) n_I(\tilde{\boldsymbol{r}}-\boldsymbol{R}_I)\frac{\partial}{\partial \tilde{r}_\lambda}\frac{1}{|\boldsymbol{r}-\tilde{\boldsymbol{r}}|}.\end{aligned} \tag{C.1}$$

Next, we use integration by parts on the third term and the boundary term vanishes on the surface of the unit cell. Together with the product rule of derivatives, we obtain

$$\begin{aligned}\int_V \mathrm{d}\tilde{\boldsymbol{r}}\,(\tilde{r}_\mu - r_\mu) n_I(\tilde{\boldsymbol{r}}-\boldsymbol{R}_I)\frac{\partial}{\partial \tilde{r}_\lambda}\frac{1}{|\boldsymbol{r}-\tilde{\boldsymbol{r}}|} = &-\delta_{\lambda\mu} v_{\mathrm{H}}^{I}(\boldsymbol{r}-\boldsymbol{R}_I) \\ &- \int_V \mathrm{d}\tilde{\boldsymbol{r}}\,(\tilde{r}_\mu - r_\mu)\frac{\partial n_I(\tilde{\boldsymbol{r}}-\boldsymbol{R}_I)}{\partial \tilde{r}_\lambda}\frac{1}{|\boldsymbol{r}-\tilde{\boldsymbol{r}}|}.\end{aligned} \tag{C.2}$$

The two Kronecker delta terms in Eqs. (C.1) and (C.2) cancel each other. In the case $\boldsymbol{r}=\boldsymbol{R}_I$, the two integrals cancel each other, too, and the strain derivative vanishes.

C.2 Derivatives of Ewald long-range term

Here, the individual derivatives of the Ewald long-range term (Eqs. (3.38) and (5.37)) are shown. The derivatives with respect to the position vectors are

$$\frac{\partial v_{\mathrm{LR}}^{I}(\boldsymbol{r}-\boldsymbol{R}_I)}{\partial r_\lambda} r_\mu = \frac{4\pi}{V}\sum_{\boldsymbol{G}} \mathrm{i}G_\lambda r_\mu \frac{\exp\left(-\frac{\kappa^2 G^2}{4}\right)}{G^2} S_I(\boldsymbol{G})\exp(\mathrm{i}\boldsymbol{G}\cdot\boldsymbol{r}), \tag{C.3}$$

$$\frac{v^I_{\mathrm{LR}}(\boldsymbol{r}-\boldsymbol{R}_I)}{\partial R_{I,\lambda}} R_{I,\mu} = -\frac{4\pi}{V}\sum_{\boldsymbol{G}} \mathrm{i}G_\lambda R_{I,\mu} \frac{\exp\left(-\frac{\kappa^2 G^2}{4}\right)}{G^2} S_I(\boldsymbol{G})\exp(\mathrm{i}\boldsymbol{G}\cdot\boldsymbol{r}), \tag{C.4}$$

and the volume derivative is

$$\frac{\partial v^I_{\mathrm{LR}}(\boldsymbol{r}-\boldsymbol{R}_I)}{\partial V}\delta_{\lambda\mu}V = -v^I_{\mathrm{LR}}(\boldsymbol{r}-\boldsymbol{R}_I)\delta_{\lambda\mu}V. \tag{C.5}$$

For the $\boldsymbol{G}$-vector, the following derivatives are needed

$$\frac{\partial S_I(\boldsymbol{G})}{\partial G_\mu} = \Gamma_{I,\mu}(\boldsymbol{G}) - \mathrm{i}R_{I,\mu}S_I(\boldsymbol{G}) \tag{C.6}$$

and

$$\frac{\partial}{\partial G_\mu}\left(\frac{\exp\left(-\frac{\kappa^2 G^2}{4}\right)}{G^2}\right) = -\frac{\exp\left(-\frac{\kappa^2 G^2}{4}\right)}{G^2}\left(\frac{2}{G^2}+\frac{\kappa^2}{2}\right)G_\mu. \tag{C.7}$$

The definitions of $S_I(\boldsymbol{G})$ and $\Gamma_{I,\mu}(\boldsymbol{G})$ are given in Eqs. (3.39) and (5.40), respectively. With this, the derivative of the Ewald long-range term with respect to the $\boldsymbol{G}$-vector is

$$\begin{aligned}\frac{\partial v^I_{\mathrm{LR}}(\boldsymbol{r}-\boldsymbol{R}_I)}{\partial G_\mu}G_\lambda = &-\frac{4\pi}{V}\sum_{\boldsymbol{G}}\frac{\exp\left(-\frac{\kappa^2 G^2}{4}\right)}{G^2}\exp(\mathrm{i}\boldsymbol{G}\cdot\boldsymbol{r})G_\lambda \\ &\times\left[G_\mu S_I(\boldsymbol{G})\left(\frac{2}{G^2}+\frac{\kappa^2}{2}\right) - \Gamma_{I,\mu}(\boldsymbol{G}) - \mathrm{i}r_\mu S_I(\boldsymbol{G}) + iR_{I,\mu}S_I(\boldsymbol{G})\right].\end{aligned} \tag{C.8}$$

Since for the strain derivative of $v_{\mathrm{LR}}(\boldsymbol{r})$ the negative of the $\boldsymbol{G}$-vector derivative is needed (Eq. (5.37)), the terms of the position vectors derivative (Eqs. (C.3) and (C.4)) cancel completely with the third and fourth term in Eq. (C.8). Together with Eq. (C.5), the final expression for the strain derivative of $v_{\mathrm{LR}}(\boldsymbol{r})$ is obtained and presented in Eq. (5.38).

C.3 Position derivative of Coulomb matrix

We want to show that the derivative of the Coulomb matrix $V_{\mathfrak{mn}}$ (Eq. (3.52)) can be changed from $\frac{\partial}{\partial R_{I,\lambda}}$ to $-\frac{\partial}{\partial R_{J,\lambda}}$. We will use the notation $\mathfrak{m}(I)$ to indicate that the auxiliary basis function $\mathfrak{m}$ is centered on atom I. In addition, we will employ integration by parts (IP) and the boundary terms vanish for the Coulomb integral since the basis functions are zero at infinity:

$$\frac{\partial V_{\mathfrak{m}(I)\mathfrak{n}(J)}}{\partial R_{I,\lambda}} = \iint \mathrm{d}\boldsymbol{r}\,\mathrm{d}\tilde{\boldsymbol{r}}\,\frac{\partial P_{\mathfrak{m}}(\boldsymbol{r}-\boldsymbol{R}_I)}{\partial R_{I,\lambda}} v(|\boldsymbol{r}-\tilde{\boldsymbol{r}}|)P_{\mathfrak{n}}(\tilde{\boldsymbol{r}}-\boldsymbol{R}_J)$$

$$
\begin{aligned}
&= -\iint \mathrm{d}\boldsymbol{r}\,\mathrm{d}\tilde{\boldsymbol{r}}\,\tfrac{\partial P_{\mathfrak{m}}(\boldsymbol{r}-\boldsymbol{R}_I)}{\partial r_\lambda} v(|\boldsymbol{r}-\tilde{\boldsymbol{r}}|) P_{\mathfrak{n}}(\tilde{\boldsymbol{r}}-\boldsymbol{R}_J) \\
&\overset{IP}{=} \iint \mathrm{d}\boldsymbol{r}\,\mathrm{d}\tilde{\boldsymbol{r}}\, P_{\mathfrak{m}}(\boldsymbol{r}-\boldsymbol{R}_I) \tfrac{\partial v(|\boldsymbol{r}-\tilde{\boldsymbol{r}}|)}{\partial r_\lambda} P_{\mathfrak{n}}(\tilde{\boldsymbol{r}}-\boldsymbol{R}_J) \\
&= -\iint \mathrm{d}\boldsymbol{r}\,\mathrm{d}\tilde{\boldsymbol{r}}\, P_{\mathfrak{m}}(\boldsymbol{r}-\boldsymbol{R}_I) \tfrac{\partial v(|\boldsymbol{r}-\tilde{\boldsymbol{r}}|)}{\partial \tilde{r}_\lambda} P_{\mathfrak{n}}(\tilde{\boldsymbol{r}}-\boldsymbol{R}_J) \\
&\overset{IP}{=} \iint \mathrm{d}\boldsymbol{r}\,\mathrm{d}\tilde{\boldsymbol{r}}\, P_{\mathfrak{m}}(\boldsymbol{r}-\boldsymbol{R}_I) v(|\boldsymbol{r}-\tilde{\boldsymbol{r}}|) \tfrac{\partial P_{\mathfrak{n}}(\tilde{\boldsymbol{r}}-\boldsymbol{R}_J)}{\partial \tilde{r}_\lambda} \\
&= -\iint \mathrm{d}\boldsymbol{r}\,\mathrm{d}\tilde{\boldsymbol{r}}\, P_{\mathfrak{m}}(\boldsymbol{r}-\boldsymbol{R}_I) v(|\boldsymbol{r}-\tilde{\boldsymbol{r}}|) \tfrac{\partial P_{\mathfrak{n}}(\tilde{\boldsymbol{r}}-\boldsymbol{R}_J}{\partial R_{J,\lambda}} \\
&= -\frac{\partial V_{\mathfrak{m}(I)\mathfrak{n}(J)}}{\partial R_{J,\lambda}}.
\end{aligned}
\tag{C.9}
$$

We have used that $\frac{\partial v(|\boldsymbol{r}-\tilde{\boldsymbol{r}}|)}{\partial r_\lambda} = -\frac{\partial v(|\boldsymbol{r}-\tilde{\boldsymbol{r}}|)}{\partial \tilde{r}_\lambda}$.

C.4 Position derivative of locally restricted expansion coefficients

We want to show that the derivative of the expansion coefficients $C_{ij}^{\mathfrak{m}}$ (Eq. (3.53)) can be changed from $\frac{\partial}{\partial R_{I,\lambda}}$ to $-\frac{\partial}{\partial R_{J,\lambda}}$. We will use the notation $i(I)$ to indicate that the basis function i is centered on atom I. In addition, we will employ integration by parts (IP) and the boundary terms vanish for the Coulomb integrals since the basis functions are zero at infinity.

First, we will separately show that the derivative for each of the two factors $(ij|\mathfrak{n})$ and $L_{\mathfrak{n}\mathfrak{m}}^{IJ}$ in Eq. (3.53) can be changed and we begin with the Coulomb integral for the case that $\mathfrak{n}$ is centered on atom I:

$$
\begin{aligned}
\frac{\partial(i(I)j(J)|\mathfrak{n}(I))}{\partial R_{I,\lambda}} &= \iint \mathrm{d}\boldsymbol{r}\,\mathrm{d}\tilde{\boldsymbol{r}}\, \tfrac{\partial \varphi_i(\boldsymbol{r}-\boldsymbol{R}_I)}{\partial R_{I,\lambda}} \varphi_j(\boldsymbol{r}-\boldsymbol{R}_J) v(|\boldsymbol{r}-\tilde{\boldsymbol{r}}|) P_{\mathfrak{n}}(\tilde{\boldsymbol{r}}-\boldsymbol{R}_I) \\
&\quad + \iint \mathrm{d}\boldsymbol{r}\,\mathrm{d}\tilde{\boldsymbol{r}}\, \varphi_i(\boldsymbol{r}-\boldsymbol{R}_I)\varphi_j(\boldsymbol{r}-\boldsymbol{R}_J) v(|\boldsymbol{r}-\tilde{\boldsymbol{r}}|) \tfrac{\partial P_{\mathfrak{n}}(\tilde{\boldsymbol{r}}-\boldsymbol{R}_I)}{\partial R_{I,\lambda}} \\
&= -\iint \mathrm{d}\boldsymbol{r}\,\mathrm{d}\tilde{\boldsymbol{r}}\, \tfrac{\partial \varphi_i(\boldsymbol{r}-\boldsymbol{R}_I)}{\partial r_\lambda} \varphi_j(\boldsymbol{r}-\boldsymbol{R}_J) v(|\boldsymbol{r}-\tilde{\boldsymbol{r}}|) P_{\mathfrak{n}}(\tilde{\boldsymbol{r}}-\boldsymbol{R}_I) \\
&\quad - \iint \mathrm{d}\boldsymbol{r}\,\mathrm{d}\tilde{\boldsymbol{r}}\, \varphi_i(\boldsymbol{r}-\boldsymbol{R}_I)\varphi_j(\boldsymbol{r}-\boldsymbol{R}_J) v(|\boldsymbol{r}-\tilde{\boldsymbol{r}}|) \tfrac{\partial P_{\mathfrak{n}}(\tilde{\boldsymbol{r}}-\boldsymbol{R}_I)}{\partial \tilde{r}_\lambda} \\
&\overset{IP}{=} \iint \mathrm{d}\boldsymbol{r}\,\mathrm{d}\tilde{\boldsymbol{r}}\, \varphi_i(\boldsymbol{r}-\boldsymbol{R}_I) \tfrac{\partial \varphi_J(\boldsymbol{r}-\boldsymbol{R}_J)}{\partial r_\lambda} v(|\boldsymbol{r}-\tilde{\boldsymbol{r}}|) P_{\mathfrak{n}}(\tilde{\boldsymbol{r}}-\boldsymbol{R}_I) \\
&\quad + \iint \mathrm{d}\boldsymbol{r}\,\mathrm{d}\tilde{\boldsymbol{r}}\, \varphi_i(\boldsymbol{r}-\boldsymbol{R}_I)\varphi_j(\boldsymbol{r}-\boldsymbol{R}_J) \tfrac{\partial v(|\boldsymbol{r}-\tilde{\boldsymbol{r}}|)}{\partial r_\lambda} P_{\mathfrak{n}}(\tilde{\boldsymbol{r}}-\boldsymbol{R}_I)
\end{aligned}
\tag{C.10}
$$

$$
\begin{aligned}
&+ \iint \mathrm{d}\boldsymbol{r}\,\mathrm{d}\tilde{\boldsymbol{r}}\,\varphi_i(\boldsymbol{r}-\boldsymbol{R}_I)\varphi_j(\boldsymbol{r}-\boldsymbol{R}_J)\tfrac{\partial v(|\boldsymbol{r}-\tilde{\boldsymbol{r}}|)}{\partial \tilde{r}_\lambda} P_{\mathfrak{n}}(\tilde{\boldsymbol{r}}-\boldsymbol{R}_I) \\
&= -\iint \mathrm{d}\boldsymbol{r}\,\mathrm{d}\tilde{\boldsymbol{r}}\,\varphi_i(\boldsymbol{r}-\boldsymbol{R}_I)\tfrac{\partial \varphi_J(\boldsymbol{r}-\boldsymbol{R}_J)}{\partial R_{J,\lambda}} v(|\boldsymbol{r}-\tilde{\boldsymbol{r}}|)P_{\mathfrak{n}}(\tilde{\boldsymbol{r}}-\boldsymbol{R}_I) \\
&= -\frac{\partial (i(I)j(J)|\mathfrak{n}(I))}{\partial R_{J,\lambda}}.
\end{aligned}
$$

We have used that $\frac{\partial v(|\boldsymbol{r}-\tilde{\boldsymbol{r}}|)}{\partial r_\lambda} = -\frac{\partial v(|\boldsymbol{r}-\tilde{\boldsymbol{r}}|)}{\partial \tilde{r}_\lambda}$. From this result, we can derive the same relation if $\mathfrak{n}$ is centered on atom J by swapping $i(I)$ with $j(J)$ in the Coulomb integral, which changes nothing per definition (Eq. (3.49)) and then substituting the variable name I with J and J with I, respectively, and the same for the variables i and j. Hence, we obtain

$$
\frac{\partial (i(I)j(J)|\mathfrak{n}(J))}{\partial R_{I,\lambda}} = -\frac{\partial (i(I)j(J)|\mathfrak{n}(J))}{\partial R_{J,\lambda}}. \tag{C.11}
$$

Next, we consider the inverse Coulomb matrix L^{IJ}. The derivative $\frac{\partial}{\partial X}$ of an inverse matrix A^{-1} is given by $\frac{\partial A^{-1}}{\partial X} = -A^{-1}\frac{\partial A}{\partial X}A^{-1}$. Additionally, we will need that the derivatives of the on-site terms of the Coulomb matrix vanish, i.e., $\frac{\partial V_{\mathfrak{m}(I)\mathfrak{n}(I)}}{\partial R_{I,\lambda}} = 0$, which follows from Eq. (C.9). However, this is not true for the inverse Coulomb matrix and it does not matter for the following derivation on which atom the auxiliary basis functions $\mathfrak{m}$ and $\mathfrak{n}$ are centered. With this said, the derivative of the inverse Coulomb matrix becomes

$$
\begin{aligned}
\frac{\partial L^{IJ}_{\mathfrak{nm}}}{\partial R_{I,\lambda}} &= -\sum_{\mathfrak{r},\mathfrak{s}\in\mathcal{P}(IJ)} L^{IJ}_{\mathfrak{nr}}\frac{\partial V^{IJ}_{\mathfrak{rs}}}{\partial R_{I,\lambda}}L^{IJ}_{\mathfrak{sm}} \\
&= -\sum_{\substack{\mathfrak{r}\in\mathcal{P}(I)\\ \mathfrak{s}\in\mathcal{P}(J)}} L^{IJ}_{\mathfrak{nr}}\frac{\partial V^{IJ}_{\mathfrak{r}(I)\mathfrak{s}(J)}}{\partial R_{I,\lambda}}L^{IJ}_{\mathfrak{sm}} - \sum_{\substack{\mathfrak{r}\in\mathcal{P}(J)\\ \mathfrak{s}\in\mathcal{P}(I)}} L^{IJ}_{\mathfrak{nr}}\frac{\partial V^{IJ}_{\mathfrak{r}(J)\mathfrak{s}(I)}}{\partial R_{I,\lambda}}L^{IJ}_{\mathfrak{sm}} \\
&= \sum_{\mathfrak{r},\mathfrak{s}\in\mathcal{P}(IJ)} L^{IJ}_{\mathfrak{nr}}\frac{\partial V^{IJ}_{\mathfrak{rs}}}{\partial R_{J,\lambda}}L^{IJ}_{\mathfrak{sm}} \\
&= -\frac{\partial L^{IJ}_{\mathfrak{nm}}}{\partial R_{J,\lambda}},
\end{aligned} \tag{C.12}
$$

where we have used Eq. (C.9).

Now, we have all the necessary relations and we can tend to the expansion coefficients

using Eqs. (C.10), (C.11), and (C.12),

$$\begin{aligned}\frac{\partial C_{ij}^{\mathfrak{m}}}{\partial R_{I,\lambda}} &= \sum_{\mathfrak{n}\in\mathcal{P}(IJ)}\left[\frac{\partial (ij|\mathfrak{n})}{\partial R_{I,\lambda}} L_{\mathfrak{n}\mathfrak{m}}^{IJ} + (ij|\mathfrak{n})\frac{\partial L_{\mathfrak{n}\mathfrak{m}}^{IJ}}{\partial R_{I,\lambda}}\right] \\ &= -\sum_{\mathfrak{n}\in\mathcal{P}(IJ)}\left[\frac{\partial (ij|\mathfrak{n})}{\partial R_{J,\lambda}} L_{\mathfrak{n}\mathfrak{m}}^{IJ} + (ij|\mathfrak{n})\frac{\partial L_{\mathfrak{n}\mathfrak{m}}^{IJ}}{\partial R_{J,\lambda}}\right] \\ &= -\frac{\partial C_{ij}^{\mathfrak{m}}}{\partial R_{J,\lambda}}.\end{aligned} \tag{C.13}$$

For the inverse Coulomb matrix $L_{\mathfrak{n}\mathfrak{m}}^{IJ}$, the change of the derivative does not depend on which atom the auxiliary basis functions $\mathfrak{m}$ and $\mathfrak{n}$ are centered. For the Coulomb integral $(ij|\mathfrak{n})$, there are only two possibilities, either $\mathfrak{n}$ is centered on atom I or J. Both cases are covered by Eqs. (C.10) and (C.11) and we can change the derivative.

D Organic crystals

D.1 Hydrogen and carbon basis functions

Table D.1 shows the shorthand notation for the parameters used to obtain the radial functions of hydrogen and carbon for the different tiers. In addition, we used the basis set "tier 1+". For hydrogen (carbon), this basis set includes "tier 1" plus the $1s$ ($4f$) radial function from "tier 2" as well as the $3d$ radial function from "tier 2" for the construction of the auxiliary basis set (Eq. (3.50)) in the case of hybrid functionals.

Table D.1: Shorthand notation for the parameters used to obtain the radial functions for hydrogen and carbon according to Eq. (B.1). For the confinement potential v_{cut}, $r_{\text{onset}} = 4$Å and $w_{\text{cut}} = 2$Å was used (see Eq. (B.2)). The minimal basis consist of the radial functions of the occupied orbitals of spherically symmetric free atoms with noble gas configuration and quantum numbers of the additional valence functions. H(nl, z) denotes a hydrogen-like radial function for the Coulomb potential z/r with radial and angular quantum numbers n and l, respectively. Each tier includes the basis functions of the lower tiers.

	H	C
minimal	$1s$	[He]+$2s3p$
tier 1	H($2s$, 2.1)	H($2p$, 1.7)
	H($2p$, 3.5)	H($3d$, 6.0)
		H($2s$, 4.9)
tier 2	H($1s$, 0.85)	H($4f$, 9.8)
	H($2p$, 3.7)	H($3p$, 5.2)
	H($2s$, 1.2)	H($3s$, 4.3)
	H($3d$, 7.0)	H($5g$, 14.4)
		H($3d$, 6.2)
tier 3	H($4f$, 11.2)	H($2p$, 5.6)
	H($3p$, 4.8)	H($2s$, 1.4)
	H($4d$, 9.0)	H($3d$, 4.9)
	H($3s$, 3.2)	H($4f$, 11.2)

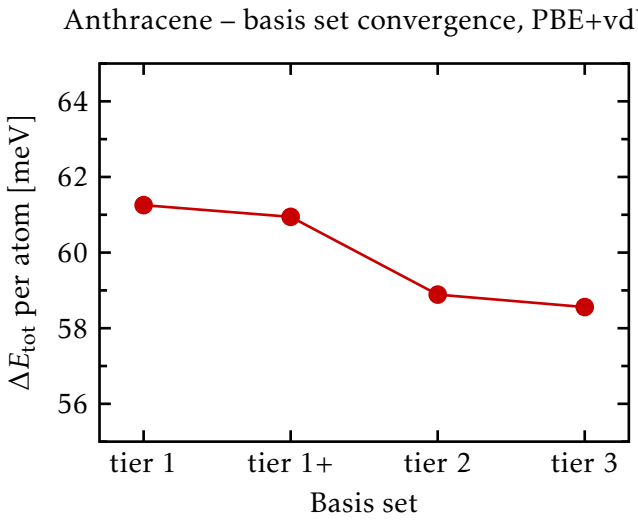

Figure D.1: Total energy difference convergence with respect to the basis set size for crystalline anthracene. ΔE_{tot} is defined as the difference between two times the total energy of an isolated anthracene molecule and crystalline anthracene, $\Delta E_{\text{tot}} = 2E_{\text{tot}}^{\text{mol}} - E_{\text{tot}}^{\text{crys}}$, and the ordinate shows ΔE_{tot} per atom. The definition of the basis sets is given in App. D.1. The calculations were performed for the experimental structure of Exp. [Cha82], see Tab. 7.1, with the PBE functional, vdW corrections and a $\boldsymbol{k}$-point grid of size 8×12×6.

D.2 Basis set convergence

D.2.1 Anthracene

Figure D.1 shows the total energy difference convergence with respect to the basis set size for crystalline anthracene. It can be seen that the "tier 2" basis set is already well converged. The "tier 1+" basis set is converged within a few meV per atom which provides already a good accuracy within acceptable computational cost and is well-suited for our purposes. Therefore, we choose the "tier 1+" basis set for the anthracene calculations.

D.2.2 Polyacetylene

Figure D.2 shows the total energy difference convergence with respect to the basis set size for crystalline TPA. For the PBE+vdW and HSE(0.5, 0.11 bohr^{-1})+vdW functional, the total energy difference is already well converged below 1 meV per atom for all considered basis sets. We choose the "tier 1+" basis set for the TPA calculations, which provides a good accuracy within acceptable computational cost and is well-suited for our purposes.

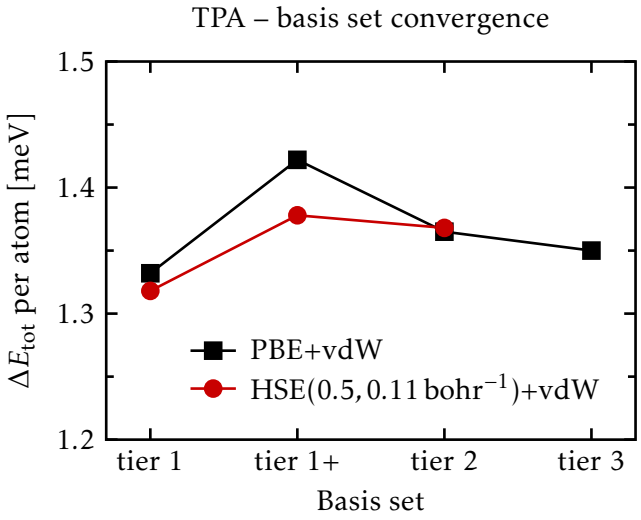

Figure D.2: Total energy difference convergence with respect to the basis set size for crystalline TPA. ΔE_{tot} is defined as the difference between the $P2_1/a$ and the $P2_1/n$ structure, $\Delta E_{tot} = E_{tot}^{P2_1/a} - E_{tot}^{P2_1/n}$, and the ordinate shows ΔE_{tot} per atom. The definition of the basis sets is given in App. D.1. The calculations were performed for the experimental structure of Exp. [Kah87], see Tab. 8.1 with the PBE (black squares) as well as the HSE(0.5, 0.11 bohr^{-1}) functional (red circles, Sec. 2.3.5), vdW corrections and a ***k***-point grid of size 8×4×24. For calculations with the HSE(0.5, 0.11 bohr^{-1}) functional, the "tier 2" basis is the largest possible basis set.

D.3 *k*-point convergence

D.3.1 Anthracene

The notation $N_a \times N_b \times N_c$ specifies the number of ***k***-points along the first, second and third axis of the Brillouin zone. N_a, N_b, and N_c are chosen to be different because the lattice vectors ***a***, ***b***, and ***c*** have different lengths, see Sec. 7.2.1. In order to obtain a uniform sampling of the Brillouin zone, the values of N_a, N_b, and N_c correspond roughly reciprocally to the lengths of ***a***, ***b***, and ***c***. Figure D.3 shows the total energy convergence with respect to the size of the ***k***-point grid for crystalline anthracene. It can be seen that the total energy is already well converged below 1 meV per atom for a ***k***-point grid of size 2×3×1 and extremely well converged for denser ***k***-point grids since crystalline anthracene is a semiconductor which requires only a sparse ***k***-point grid in general [Koh06]. In order to ensure that we obtain accurate band structures under pressure, we choose a safe ***k***-point grid of size 8×12×6.

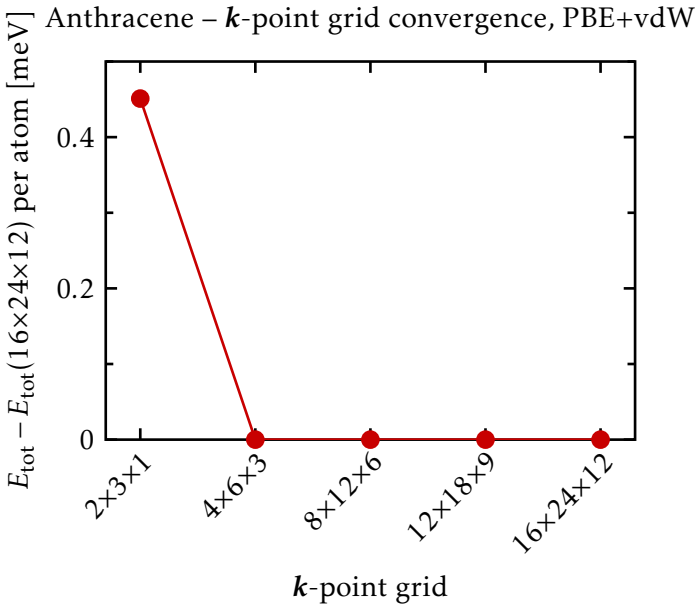

Figure D.3: Total energy convergence with respect to the size of $\boldsymbol{k}$-point grid for crystalline anthracene. The ordinate shows the total energy per atom relative to the value of 16×24×12. The calculations were performed with the PBE functional, vdW corrections and the "tier 2" basis set (App. D.1).

D.3.2 Polyacetylene

The notation $N_a \times N_b \times N_c$ specifies the number of $\boldsymbol{k}$-points along the first, second and third axis of the Brillouin zone. N_a, N_b, and N_c are chosen to be different because the lattice vectors $\boldsymbol{a}$, $\boldsymbol{b}$, and $\boldsymbol{c}$ have different lengths, see Sec. 8.2.1. In order to obtain a uniform sampling of the Brillouin zone, the values of N_a, N_b, and N_c correspond roughly reciprocally to the lengths of $\boldsymbol{a}$, $\boldsymbol{b}$, and $\boldsymbol{c}$. Figure D.4 shows the total energy convergence with respect to the size of the $\boldsymbol{k}$-point grid for crystalline TPA. It can be seen that the total energy is already well reasonably converged to a value of about 1 meV per atom for a $\boldsymbol{k}$-point grid of size 6×3×12. For denser $\boldsymbol{k}$-point grids, the total energy is well converged below 1 meV per atom. However, the dimerization Δz depends critically on the number of $\boldsymbol{k}$-points N_c along the carbon chain, i.e., along lattice vector $\boldsymbol{c}$ [Min87, Ash89, Sun02]. Figure D.5 shows that a value of $N_c = 24$ yields well converged results for the dimerization. Therefore, we choose a safe $\boldsymbol{k}$-point grid of size 8×4×24, which yields a convergence of the dimerization below 10^{-3} Å and of the total energy below 1 meV per atom. In addition, this $\boldsymbol{k}$-point grid allows for accurate band structures under pressure.

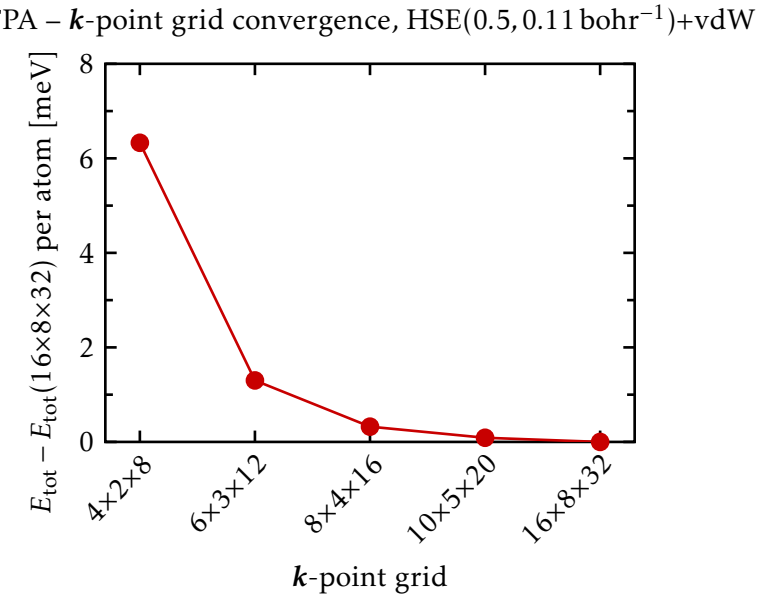

Figure D.4: Total energy convergence with respect to the size of ***k***-point grid for crystalline TPA. The ordinate shows the total energy per atom relative to the value of 16×8×32. The calculations were performed for the experimental structure of Exp. [Kah87], see Tab. 8.1, with the HSE(0.5, 0.11 bohr^{-1}) functional, vdW corrections and the "tier 2" basis set (App. D.1).

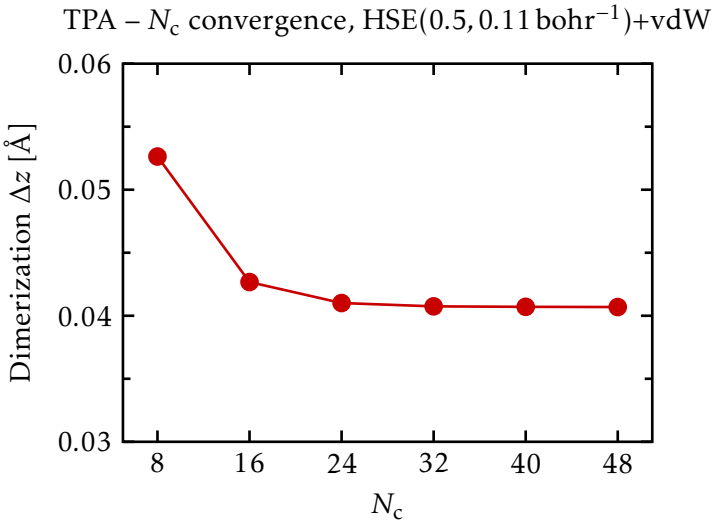

Figure D.5: Convergence of dimerization Δz of carbon chain with respect to the number of ***k***-points N_c along the carbon chain for crystalline TPA. The crystal structures have been fully optimized for each N_c value and the calculations were performed with the HSE(0.5, 0.11 bohr^{-1}) functional, vdW corrections and the "tier 1+" basis set (App. D.1). In the other two directions, the number of ***k***-points has been fixed to $N_a = 8$ and $N_b = 4$.

Table D.2: Fractional coordinates of special $\boldsymbol{k}$-points. This means $\boldsymbol{k} = s_a\boldsymbol{b}_a + s_b\boldsymbol{b}_b + s_c\boldsymbol{b}_c$ with the reciprocal lattice vectors $\boldsymbol{b}_a$, $\boldsymbol{b}_b$, and $\boldsymbol{b}_c$ corresponding to the lattice vectors $\boldsymbol{a}$, $\boldsymbol{b}$, and $\boldsymbol{c}$, respectively.

Name	s_a	s_b	s_c
Γ	0.0	0.0	0.0
A	0.5	0.0	0.5
B	0.0	0.0	0.5
C	0.5	0.5	0.0
D	0.0	0.5	0.5
E	0.5	0.5	0.5
K	0.4	0.0	0.2
X	0.5	0.0	0.0
Y	0.0	0.5	0.0

D.4 Coordinates of special $\boldsymbol{k}$-points

Table D.2 lists the coordinates of all special $\boldsymbol{k}$-points inside the Brillouin zone that were used for the calculations of the band structures in this thesis.

Publications

- **F. Knuth**, C. Carbogno, V. Atalla, V. Blum, and M. Scheffler. *All-electron formalism for total energy strain derivatives and stress tensor components for numeric atom-centered orbitals.* Computer Physics Communications **190**, 33 (2015).

Curriculum Vitae

For reasons of data protection, the curriculum vitae is not included in the online version.

Selbständigkeitserklärung

Hiermit versichere ich, alle Hilfsmittel und Hilfen angegeben zu haben und auf dieser Grundlage die Arbeit selbstständig verfasst zu haben. Die Arbeit wurde nicht schon einmal in einem früheren Promotionsverfahren angenommen oder als ungenügend beurteilt.

Berlin, den

Franz Knuth

Acknowledgments

First of all, I would like to thank Matthias Scheffler for giving me the opportunity to carry out my Ph.D. studies at the theory department of the Fritz Haber Institute. It is a great place to learn from many excellent scientists. I further want to thank my two supervisors Christian Carbogno and Volker Blum. Thank you for your kind and constant support as well as for teaching me computational and material science and the details of FHI-aims.

A special thanks goes to my long standing office mate Lydia Nemec. Thank you for sharing your knowledge about condensed matter physics as well as about running big calculations and for creating an enjoyable atmosphere. I thank (in alphabetical order) Viktor Atalla, Björn Bieniek, Oliver Hofmann, Arvid Ihrig, and Sergey Levchenko for fruitful scientific discussions. A big thanks goes to all former and present members of the theory department for their great help and for having fun with them during conferences, workshops, and summer/end-of-the-year parties.

I would like to thank the careful eyes of all my proof readers: Christian Carbogno, Volker Blum, and Judith Specht.

Finally, I like to thank my parents for their constant support. My special gratitude goes to Judith for her patience, support and love. You always encouraged me and you were always there for me.

Bibliography

[Ahl77] R. Ahlrichs, R. Penco, and G. Scoles. *Intermolecular forces in simple systems*. Chemical Physics **19**, 119 (1977).

[Alm85] C.-O. Almbladh and U. von Barth. *Exact results for the charge and spin densities, exchange-correlation potentials, and density-functional eigenvalues*. Physical Review B **31**, 3231 (1985).

[Amb14] A. Ambrosetti, A. M. Reilly, R. A. DiStasio, and A. Tkatchenko. *Long-range correlation energy calculated from coupled atomic response functions*. The Journal of Chemical Physics **140**, 18A508 (2014).

[And96] Y. Andersson, D. C. Langreth, and B. I. Lundqvist. *van der Waals Interactions in Density-Functional Theory*. Physical Review Letters **76**, 102 (1996).

[Arm05] R. Armiento and A. E. Mattsson. *Functional designed to include surface effects in self-consistent density functional theory*. Physical Review B **72**, 085108 (2005).

[Ash76] N. W. Ashcroft and N. D. Mermin. *Solid State Physics*. Holt, Rinehart and Winston (1976).

[Ash89] J. Ashkenazi, W. Pickett, H. Krakauer, C. Wang, B. Klein, and S. Chubb. *Ground state of trans-polyacetylene and the Peierls mechanism*. Physical Review Letters **62**, 2016 (1989).

[Ata13a] V. Atalla. *Density-functional theory and beyond for organic electronic materials*. Ph.D. thesis, Technischen Universität Berlin (2013).

[Ata13b] V. Atalla, M. Yoon, F. Caruso, P. Rinke, and M. Scheffler. *Hybrid density functional theory meets quasiparticle calculations: A consistent electronic structure approach*. Physical Review B **88**, 165122 (2013).

[Bak94] J. Baker, J. Andzelm, A. Scheiner, and B. Delley. *The effect of grid quality and weight derivatives in density functional calculations*. The Journal of Chemical Physics **101**, 8894 (1994).

[Bäs72] H. Bässler and H. Killesreiter. *Hot Carrier Injection into Molecular Crystals and Its Relevance to the Field Dependence of Photocurrents*. physica status solidi (b) **53**, 183 (1972).

[Bec88a] A. D. Becke. *Correlation energy of an inhomogeneous electron gas: A coordinate-space model*. The Journal of Chemical Physics **88**, 1053 (1988).

[Bec88b] A. D. Becke and R. M. Dickson. *Numerical solution of Poisson's equation in polyatomic molecules*. The Journal of Chemical Physics **89**, 2993 (1988).

[Bec93a] A. D. Becke. *A new mixing of Hartree–Fock and local density-functional theories*. The Journal of Chemical Physics **98**, 1372 (1993).

[Bec93b] A. D. Becke. *Density-functional thermochemistry. III. The role of exact exchange*. The Journal of Chemical Physics **98**, 5648 (1993).

[Bel74] A. I. Belkind and V. V. Grechov. *Energy Levels of Polyacene Crystals*. physica status solidi (a) **26**, 377 (1974).

[Blu09] V. Blum, R. Gehrke, F. Hanke, P. Havu, V. Havu, X. Ren, K. Reuter, and M. Scheffler. *Ab initio molecular simulations with numeric atom-centered orbitals*. Computer Physics Communications **180**, 2175 (2009).

[Boh53] D. Bohm and D. Pines. *A Collective Description of Electron Interactions: III. Coulomb Interactions in a Degenerate Electron Gas*. Physical Review **92**, 609 (1953).

[Bré89] J. L. Brédas and A. J. Heeger. *Comment on "Electron Correlation and Bond Alternation in Polymers"* (1989).

[Bri86] A. Brillante, M. Hanfland, K. Syassen, and J. Hocker. *Optical studies of polyacetylene under pressure*. Physica B+C **139-140**, 533 (1986).

[Buč13] T. Bučko, S. Lebègue, J. Hafner, and J. G. Ángyán. *Tkatchenko-Scheffler van der Waals correction method with and without self-consistent screening applied to solids*. Physical Review B **87**, 064110 (2013).

[Bur90] J. H. Burroughes, D. D. C. Bradley, A. R. Brown, R. N. Marks, K. Mackay, R. H. Friend, P. L. Burns, and A. B. Holmes. *Light-emitting diodes based on conjugated polymers*. Nature **347**, 539 (1990).

[Cao91] Y. Cao, P. Smith, and A. J. Heeger. *Mechanical and electrical properties of polyacetylene films oriented by tensile drawing*. Polymer **32**, 1210 (1991).

[Cap06] K. Capelle. *A Bird's-Eye View of Density-Functional Theory*. arXiv:cond-mat/0211443v5 [cond-mat.mtrl-sci] (2006).

[Car05] M. Cardona and M. L. W. Thewalt. *Isotope effects on the optical spectra of semiconductors*. Reviews of Modern Physics **77**, 1173 (2005).

[Cep80] D. M. Ceperley and B. J. Alder. *Ground State of the Electron Gas by a Stochastic Method*. Physical Review Letters **45**, 566 (1980).

[Cha73] D. J. Chadi and M. L. Cohen. *Special Points in the Brillouin Zone*. Physical Review B **8**, 5747 (1973).

[Cha82] S. L. Chaplot, N. Lehner, and G. S. Pawley. *The Structure of Anthracene-d_{10} at 16 K using Neutron Diffraction*. Acta Crystallographica Section B **38**, 483 (1982).

[Chi77] C. K. Chiang, C. R. Fincher, Y. W. Park, A. J. Heeger, H. Shirakawa, E. J. Louis, S. C. Gau, and A. G. MacDiarmid. *Electrical Conductivity in Doped Polyacetylene*. Physical Review Letters **39**, 1098 (1977).

[Chi78a] C. K. Chiang, M. A. Druy, S. C. Gau, A. J. Heeger, E. J. Louis, A. G. MacDiarmid, Y. W. Park, and H. Shirakawa. *Synthesis of highly conducting films of derivatives of polyacetylene, $(CH)_x$*. Journal of the American Chemical Society **100**, 1013 (1978).

[Chi78b] C. K. Chiang, S. C. Gau, C. R. Fincher, Y. W. Park, a. G. MacDiarmid, and a. J. Heeger. *Polyacetylene, $(CH)_x$: n-type and p-type doping and compensation*. Applied Physics Letters **33**, 18 (1978).

[Cho97] C. H. Choi, M. Kertesz, and A. Karpfen. *The effects of electron correlation on the degree of bond alternation and electronic structure of oligomers of polyacetylene*. The Journal of Chemical Physics **107**, 6712 (1997).

[Chu04] X. Chu and A. Dalgarno. *Linear response time-dependent density functional theory for van der Waals coefficients*. The Journal of Chemical Physics **121**, 4083 (2004).

[Coh12] A. J. Cohen, P. Mori-Sánchez, and W. Yang. *Challenges for Density Functional Theory*. Chemical Reviews **112**, 289 (2012).

[DCD] *Comparing Solid State DFT Codes, Basis Sets and Potentials*. http://molmod.ugent.be/deltacodesdft, accessed on 21 August 2015.

[Del90] B. Delley. *An all-electron numerical method for solving the local density functional for polyatomic molecules*. The Journal of Chemical Physics **92**, 508 (1990).

[Del96a] B. Delley. *Fast Calculation of Electrostatics in Crystals and Large Molecules*. The Journal of Physical Chemistry **100**, 6107 (1996).

[Del96b] B. Delley. *High order integration schemes on the unit sphere*. Journal of Computational Chemistry **17**, 1152 (1996).

[Dio04] M. Dion, H. Rydberg, E. Schröder, D. C. Langreth, and B. I. Lundqvist. *Van der Waals Density Functional for General Geometries*. Physical Review Letters **92**, 246401 (2004).

[Dir30] P. A. M. Dirac. *Note on Exchange Phenomena in the Thomas Atom*. Mathematical Proceedings of the Cambridge Philosophical Society **26**, 376 (1930).

[Dol04] K. Doll, R. Dovesi, and R. Orlando. *Analytical Hartree-Fock gradients with respect to the cell parameter for systems periodic in three dimensions*. Theoretical Chemistry Accounts **112**, 394 (2004).

[Dol10] K. Doll. *Analytical stress tensor and pressure calculations with the CRYSTAL code*. Molecular Physics **108**, 223 (2010).

[Dun79] B. I. Dunlap, J. W. D. Connolly, and J. R. Sabin. *On some approximations in applications of Xα theory*. The Journal of Chemical Physics **71**, 3396 (1979).

[Fab10] E. Fabiano, L. A. Constantin, and F. Della Sala. *Generalized gradient approximation bridging the rapidly and slowly varying density regimes: A PBE-like functional for hybrid interfaces*. Physical Review B **82**, 113104 (2010).

[Fed11] I. A. Fedorov, Y. N. Zhuravlev, and V. P. Berveno. *Electronic structure and chemical bond in naphthalene and anthracene.* Physical Chemistry Chemical Physics **13**, 5679 (2011).

[Fin79] C. R. Fincher, M. Ozaki, M. Tanaka, D. Peebles, L. Lauchlan, A. J. Heeger, and A. G. MacDiarmid. *Electronic structure of polyacetylene: Optical and infrared studies of undoped semiconducting $(CH)_x$ and heavily doped metallic $(CH)_x$*. Physical Review B **20**, 1589 (1979).

[Fin82] C. R. Fincher, C.-E. Chen, A. J. Heeger, A. G. MacDiarmid, and J. B. Hastings. *Structural Determination of the Symmetry-Breaking Parameter in trans-$(CH)_x$*. Physical Review Letters **48**, 100 (1982).

[Foc95] P. Focher and G. L. Chiarotti. *Ab-Initio Molecular Dynamics Simulation of Structural Phase Transitions*, in *Progress in Computational Physics of Matter* (edited by L. Reatto and F. Manghi), chap. 1, pp. 1–42. World Scientific (1995).

[For04] S. R. Forrest. *The path to ubiquitous and low-cost organic electronic appliances on plastic.* Nature **428**, 911 (2004).

[Fre14] M. French and T. R. Mattsson. *Thermoelectric transport properties of molybdenum from abinitio simulations*. Physical Review B **90**, 165113 (2014).

[Geh09] R. Gehrke. *First-Principles Basin-Hopping for the Structure Determination of Atomic Clusters*. Ph.D. thesis, Freie Universität Berlin (2009).

[Gha86] J. Ghanbaja, J. F. Marêché, E. Mc Rae, and D. Billaud. *Conductivity of heavy alkali metal doped polyacetylene*. Solid State Communications **60**, 87 (1986).

[Gir11] G. Giri, E. Verploegen, S. C. B. Mannsfeld, S. Atahan-Evrenk, D. H. Kim, S. Y. Lee, H. A. Becerril, A. Aspuru-Guzik, M. F. Toney, and Z. Bao. *Tuning charge transport in solution-sheared organic semiconductors using lattice strain*. Nature **480**, 504 (2011).

[Gol13] R. Golesorkhtabar, P. Pavone, J. Spitaler, P. Puschnig, and C. Draxl. *ElaStic: A tool for calculating second-order elastic constants from first principles*. Computer Physics Communications **184**, 1861 (2013).

[Gri04] S. Grimme. *Accurate Description of van der Waals Complexes by Density Functional Theory Including Empirical Corrections*. Journal of Computational Chemistry **25**, 1463 (2004).

[Ham99] B. Hammer, L. B. Hansen, and J. K. Nørskov. *Improved adsorption energetics within density-functional theory using revised Perdew-Burke-Ernzerhof functionals*. Physical Review B **59**, 7413 (1999).

[Har84] J. Harris. *Adiabatic-connection approach to Kohn-Sham theory*. Physical Review A **29**, 1648 (1984).

[Hee01] A. J. Heeger. *Nobel Lecture: Semiconducting and metallic polymers: The fourth generation of polymeric materials*. Reviews of Modern Physics **73**, 681 (2001).

[Hei11] G. Heimel, I. Salzmann, S. Duhm, and N. Koch. *Design of Organic Semiconductors from Molecular Electrostatics*. Chemistry of Materials **23**, 359 (2011).

[Hey03] J. Heyd, G. E. Scuseria, and M. Ernzerhof. *Hybrid functionals based on a screened Coulomb potential*. The Journal of Chemical Physics **118**, 8207 (2003).

[Hey06] J. Heyd, G. E. Scuseria, and M. Ernzerhof. *Erratum: "Hybrid functionals based on a screened Coulomb potential" [J. Chem. Phys. 118, 8207 (2003)]*. The Journal of Chemical Physics **124**, 219906 (2006).

[Hir77] F. L. Hirshfeld. *Bonded-atom fragments for describing molecular charge densities*. Theoretica Chimica Acta **44**, 129 (1977).

[Hir98] S. Hirata, H. Torii, and M. Tasumi. *Density-functional crystal orbital study on the structures and energetics of polyacetylene isomers*. Physical Review B **57**, 11994 (1998).

[Hoh64] P. Hohenberg and W. Kohn. *Inhomogeneous Electron Gas*. Physical Review **136**, B864 (1964).

[Hol11] B. Holst, M. French, and R. Redmer. *Electronic transport coefficients from ab initio simulations and application to dense liquid hydrogen*. Physical Review B **83**, 235120 (2011).

[Hum03] K. Hummer, P. Puschnig, and C. Ambrosch-Draxl. *Ab initio study of anthracene under high pressure*. Physical Review B **67**, 184105 (2003).

[Ihr15] A. C. Ihrig, J. Wieferink, I. Y. Zhang, M. Ropo, X. Ren, P. Rinke, M. Scheffler, and V. Blum. *Accurate localized resolution of identity approach for linear-scaling hybrid density functionals and for many-body perturbation theory*. New Journal of Physics **17**, 093020 (2015).

[Joh05] E. R. Johnson and A. D. Becke. *A post-Hartree-Fock model of intermolecular interactions.* The Journal of Chemical Physics **123**, 24101 (2005).

[Jur06] P. Jurečka, J. Šponer, J. Černý, and P. Hobza. *Benchmark database of accurate (MP2 and CCSD(T) complete basis set limit) interaction energies of small model complexes, DNA base pairs, and amino acid pairs.* Physical Chemistry Chemical Physics **8**, 1985 (2006).

[Kah87] H. Kahlert, O. Leitner, and G. Leising. *Structural properties of trans- and cis-$(CH)_x$*. Synthetic Metals **17**, 467 (1987).

[Kaj67] T. Kajiwara, H. Inokuchi, and S. Minomura. *Charge Mobility of Organic Semiconductors under High Pressure. Anthracene*. Bulletin of the Chemical Society of Japan **40**, 1055 (1967).

[Kal58] H. Kallmann and M. Pope. *Preparation of Thin Anthracene Single Crystals*. Review of Scientific Instruments **29**, 993 (1958).

[Kar89] N. Karl. *Studies of Organic Semiconductors for 40 Years–III*. Molecular Crystals and Liquid Crystals Incorporating Nonlinear Optics **171**, 31 (1989).

[Kar01a] N. Karl. *Introduction*, in *Organic Electronic Materials: Conjugated Polymers and Low Molecular Weight Organic Solids* (edited by R. Farchioni and G. Grosso), Springer Series in Materials Science, chap. 6, pp. 215—-239. Springer (2001).

[Kar01b] N. Karl and J. Marktanner. *Electron and Hole Mobilities in High Purity Anthracene Single Crystals*. Molecular Crystals and Liquid Crystals Science and Technology. Section A. Molecular Crystals and Liquid Crystals **355**, 149 (2001).

[Kar03] N. Karl. *Charge carrier transport in organic semiconductors*. in *Synthetic Metals*, vol. 133-134, pp. 649–657 (2003).

[Kim07] J. H. Kim, S.-m. Seo, and H. H. Lee. *Nanovoid nature and compression effects in organic light emitting diode*. Applied Physics Letters **90**, 143521 (2007).

[Knu15] F. Knuth, C. Carbogno, V. Atalla, V. Blum, and M. Scheffler. *All-electron formalism for total energy strain derivatives and stress tensor components for numeric atom-centered orbitals*. Computer Physics Communications **190**, 33 (2015).

[Koh65] W. Kohn and L. J. Sham. *Self-Consistent Equations Including Exchange and Correlation Effects*. Physical Review **140**, A1133 (1965).

[Koh96] W. Kohn, A. D. Becke, and R. G. Parr. *Density Functional Theory of Electronic Structure*. The Journal of Physical Chemistry **100**, 12974 (1996).

[Koh99] W. Kohn. *Nobel Lecture: Electronic structure of matter–wave functions and density functionals*. Reviews of Modern Physics **71**, 1253 (1999).

[Koh06] J. Kohanoff. *Electronic Structure Calculations for Solids and Molecules: Theory and Computational Methods*. Cambridge University Press (2006).

[Kön90] G. König and G. Stollhoff. *Why Polyacetylene Dimerizes: Results of Ab Initio Computations*. Physical Review Letters **65**, 1239 (1990).

[Kör12] T. Körzdörfer, R. M. Parrish, J. S. Sears, C. D. Sherrill, and J.-L. Brédas. *On the relationship between bond-length alternation and many-electron self-interaction error.* The Journal of Chemical Physics **137**, 124305 (2012).

[Kre99] G. Kresse and D. Joubert. *From ultrasoft pseudopotentials to the projector augmented-wave method*. Physical Review B **59**, 1758 (1999).

[Kru06] A. V. Krukau, O. A. Vydrov, A. F. Izmaylov, and G. E. Scuseria. *Influence of the exchange screening parameter on the performance of screened hybrid functionals.* The Journal of Chemical Physics **125**, 224106 (2006).

[Kud00] K. N. Kudin and G. E. Scuseria. *Linear-scaling density-functional theory with Gaussian orbitals and periodic boundary conditions: Efficient evaluation of energy and forces via the fast multipole method*. Physical Review B **61**, 16440 (2000).

[Kuz80] H. Kuzmany. *Resonance Raman Scattering from Neutral and Doped Polyacetylene*. physica status solidi (b) **97**, 521 (1980).

[Kwa79] J. F. Kwak, T. C. Clarke, R. L. Greene, and G. B. Street. *Transport properties of heavily AsF5 doped polyacetylene*. Solid State Communications **31**, 355 (1979).

[Lee88] C. Lee, W. Yang, and R. G. Parr. *Development of the Colle-Salvetti correlation-energy formula into a functional of the electron density*. Physical Review B **37**, 785 (1988).

[Lee10] K. Lee, É. D. Murray, L. Kong, B. I. Lundqvist, and D. C. Langreth. *Higher-accuracy van der Waals density functional*. Physical Review B **82**, 081101 (2010).

[Lei84] G. Leising. *Fully Oriented Non-Fibrous Crystalline Polyacetylene*. Polymer Bulletin **11**, 401 (1984).

[Lei88] G. Leising. *Anisotropy of the optical constants of pure and metallic polyacetylene*. Physical Review B **38**, 10313 (1988).

[Mac01] A. G. MacDiarmid. *Nobel Lecture: "Synthetic metals": A novel role for organic polymers*. Reviews of Modern Physics **73**, 701 (2001).

[Mad06] G. K. H. Madsen and D. J. Singh. *BoltzTraP. A code for calculating band-structure dependent quantities*. Computer Physics Communications **175**, 67 (2006).

[Mah96] G. D. Mahan and J. O. Sofo. *The best thermoelectric*. Proceedings of the National Academy of Sciences of the United States of America **93**, 7436 (1996).

[Mar04] R. M. Martin. *Electronic Structure: Basic Theory and Practical Methods*. Cambridge University Press (2004).

[Mar11] M. A. L. Marques, J. Vidal, M. J. T. Oliveira, L. Reining, and S. Botti. *Density-based mixing parameter for hybrid functionals*. Physical Review B **83**, 035119 (2011).

[Mas64] R. Mason. *The Crystallography of Anthracene at 95°K and 290°K*. Acta Crystallographica **17**, 547 (1964).

[Min87] J. Mintmire and C. White. *Local-density-functional results for the dimerization of trans-polyacetylene: Relationship to the band-gap problem*. Physical Review B **35**, 4180 (1987).

[Mon76] H. J. Monkhorst and J. D. Pack. *Special points for Brillouin zone integrations*. Physical Review B **13**, 5188 (1976).

[Moo87] Y. B. Moon, M. Winokur, A. J. Heeger, J. Barker, and D. C. Bott. *X-ray scattering from oriented Durham polyacetylene: structural changes after electrochemical doping*. Macromolecules **20**, 2457 (1987).

[Mos82] D. Moses, A. Feldblum, E. Ehrenfreund, A. J. Heeger, T.-C. Chung, and A. G. MacDiarmid. *Pressure dependence of the photoabsorption of polyacetylene*. Physical Review B **26**, 3361 (1982).

[Mur44] F. D. Murnaghan. *The Compressibility of Media under Extreme Pressures*. Proceedings of the National Academy of Sciences of the United States of America **30**, 244 (1944).

[Nag11] N. Nagasako and T. Oguchi. *Stress Formulation in the All-Electron Full-Potential Linearized Augmented Plane Wave Method*. Journal of the Physical Society of Japan **80**, 024701 (2011).

[Nak64] I. Nakada and Y. Ishihara. *The Effects of Temperature and Electric Field for the Photo-Generation of Free Carriers in Anthracene*. Journal of the Physical Society of Japan **19**, 695 (1964).

[Nie83] O. H. Nielsen and R. M. Martin. *First-Principles Calculation of Stress*. Physical Review Letters **50**, 697 (1983).

[Nie85] O. H. Nielsen and R. M. Martin. *Stresses in semiconductors: Ab initio calculations on Si, Ge, and GaAs*. Physical Review B **32**, 3792 (1985).

[Nob98] *The Nobel Prize in Chemistry 1998*. http://www.nobelprize.org/nobel_prizes/chemistry/laureates/1998/.

[Nob00] *The Nobel Prize in Chemistry 2000*. http://www.nobelprize.org/nobel_prizes/chemistry/laureates/2000/.

[Noc06] J. Nocedal and S. Wright. *Numerical Optimization*. Springer, edn. 2 (2006).

[Nye85] J. F. Nye. *Physical Properties of Crystals: Their Representation by Tensors and Matrices*. Oxford University Press (1985).

[Oeh02] M. Oehzelt, R. Resel, and A. Nakayama. *High-pressure structural properties of anthracene up to 10 GPa*. Physical Review B **66**, 174104 (2002).

[Oni02] G. Onida, L. Reining, and A. Rubio. *Electronic excitations: density-functional versus many-body Green's-function approaches*. Reviews of Modern Physics **74**, 601 (2002).

[Ono77] T. Ono, M. Kimura, and T. Miyamoto. *Selective epitaxial growth of single-crystal anthracene*. Journal of Applied Physics **48**, 2102 (1977).

[Par89] R. G. Parr and W. Yang. *Density-Functional Theory of Atoms and Molecules*. International Series of Monographs on Chemistry. Oxford University Press (1989).

[Per81] J. P. Perdew and A. Zunger. *Self-interaction correction to density-functional approximations for many-electron systems*. Physical Review B **23**, 5048 (1981).

[Per83] J. P. Perdew and M. Levy. *Physical Content of the Exact Kohn-Sham Orbital Energies: Band Gaps and Derivative Discontinuities*. Physical Review Letters **51**, 1884 (1983).

[Per92] J. P. Perdew and Y. Wang. *Accurate and simple analytic representation of the electron-gas correlation energy*. Physical Review B **45**, 13244 (1992).

[Pér95] J. M. Pérez-Jordá and A. D. Becke. *A density-functional study of van der Waals forces: rare gas diatomics*. Chemical Physics Letters **233**, 134 (1995).

[Per96a] J. P. Perdew, K. Burke, and M. Ernzerhof. *Generalized Gradient Approximation Made Simple*. Physical Review Letters **77**, 3865 (1996).

[Per96b] J. P. Perdew, M. Ernzerhof, and K. Burke. *Rationale for mixing exact exchange with density functional approximations*. The Journal of Chemical Physics **105**, 9982 (1996).

[Per99] J. P. Perdew, S. Kurth, A. Zupan, and P. Blaha. *Accurate Density Functional with Correct Formal Properties: A Step Beyond the Generalized Gradient Approximation*. Physical Review Letters **82**, 5179 (1999).

[Per03] J. P. Perdew and S. Kurth. *Density Functionals for Non-relativistic Coulomb Systems in the New Century*, in *A Primer in Density Functional Theory* (edited by C. Fiolhais, F. Nogueira, and M. A. L. Marques), vol. 620 of *Lecture Notes in Physics*, chap. 1, pp. 1–55. Springer (2003).

[Per08] J. P. Perdew, A. Ruzsinszky, G. I. Csonka, O. A. Vydrov, G. E. Scuseria, L. A. Constantin, X. Zhou, and K. Burke. *Restoring the Density-Gradient Expansion for Exchange in Solids and Surfaces*. Physical Review Letters **100**, 136406 (2008).

[Pod13] V. Podzorov. *Organic single crystals: Addressing the fundamentals of organic electronics*. MRS Bulletin **38**, 15 (2013).

[Poh62] H. A. Pohl, A. Rembaum, and A. Henry. *Effects of High Pressure on Some Organic Semiconducting Polymers*. Journal of the American Chemical Society **84**, 2699 (1962).

[Pop62] M. Pope, H. P. Kallmann, A. Chen, and P. Gordon. *Charge Injection into Organic Crystals: Influence of Electrodes on Dark- and Photoconductivity*. The Journal of Chemical Physics **36**, 2486 (1962).

[Pop99] J. A. Pople. *Nobel Lecture: Quantum chemical models*. Reviews of Modern Physics **71**, 1267 (1999).

[Pot69] G. T. Pott and D. F. Williams. *Low-Temperature Electron Injection and Space-Charge-Limited Transients in Anthracene Crystals*. The Journal of Chemical Physics **51**, 1901 (1969).

[Pro75] K. H. Probst and N. Karl. *Energy Levels of Electron and Hole Traps in the Band Gap of Doped Anthracene Crystals*. physica status solidi (a) **27**, 499 (1975).

[Pul69] P. Pulay. *Ab initio calculation of force constants and equilibrium geometries in polyatomic molecules*. Molecular Physics **17**, 197 (1969).

[Pul80] P. Pulay. *Convergence acceleration of iterative sequences. the case of scf iteration*. Chemical Physics Letters **73**, 393 (1980).

[Pus02] P. Puschnig and C. Ambrosch-Draxl. *Suppression of Electron-Hole Correlations in 3D Polymer Materials*. Physical Review Letters **89**, 056405 (2002).

[Qiu12] S. L. Qiu and P. M. Marcus. *Equilibrium lines and barriers to phase transitions: the cubic diamond to beta-tin transition in Si from first principles.* Journal of Physics: Condensed Matter **24**, 225501 (2012).

[Rei98] L. E. Reichl. *A Modern Course in Statistical Physics*. Wiley-VCH, edn. 2 (1998).

[Ren12a] X. Ren, P. Rinke, V. Blum, J. Wieferink, A. Tkatchenko, A. Sanfilippo, K. Reuter, and M. Scheffler. *Resolution-of-identity approach to Hartree–Fock, hybrid density functionals, RPA, MP2 and GW with numeric atom-centered orbital basis functions*. New Journal of Physics **14**, 053020 (2012).

[Ren12b] X. Ren, P. Rinke, C. Joas, and M. Scheffler. *Random-phase approximation and its applications in computational chemistry and materials science*. Journal of Materials Science **47**, 7447 (2012).

[Ric13] N. A. Richter, S. Sicolo, S. V. Levchenko, J. Sauer, and M. Scheffler. *Concentration of Vacancies at Metal-Oxide Surfaces: Case Study of MgO(100)*. Physical Review Letters **111**, 045502 (2013).

[Rin05] P. Rinke, A. Qteish, J. Neugebauer, C. Freysoldt, and M. Scheffler. *Combining GW calculations with exact-exchange density-functional theory: an analysis of valence-band photoemission for compound semiconductors*. New Journal of Physics **7**, 126 (2005).

[Sch78] L. B. Schein, C. B. Duke, and A. R. McGhie. *Observation of the Band-Hopping Transition for Electrons in Naphthalene*. Physical Review Letters **40**, 197 (1978).

[Seb83] L. Sebastian, G. Weiser, G. Peter, and H. Bässler. *Charge-transfer transitions in crystalline anthracene and their role in photoconductivity*. Chemical Physics **75**, 103 (1983).

[Sei96] A. Seidl, A. Görling, P. Vogl, J. A. Majewski, and M. Levy. *Generalized Kohn-Sham schemes and the band-gap problem*. Physical Review B **53**, 3764 (1996).

[Shi67] K. Shimamura, M. Hatano, S. Kanbara, and I. Nakada. *Electrical Conduction of Poly-Acetylene under High Pressure*. Journal of the Physical Society of Japan **23**, 578 (1967).

[Shi77] H. Shirakawa, E. J. Louis, A. G. MacDiarmid, C. K. Chiang, and A. J. Heeger. *Synthesis of Electrically Conducting Organic Polymers: Halogen Derivatives of Polyacetylene, $(CH)_x$*. Journal of the Chemical Society, Chemical Communications p. 578 (1977).

[Shi01] H. Shirakawa. *Nobel Lecture: The discovery of polyacetylene film-the dawning of an era of conducting polymers*. Reviews of Modern Physics **73**, 713 (2001).

[Sol02] J. M. Soler, E. Artacho, J. D. Gale, A. García, J. Junquera, P. Ordejón, and D. Sánchez-Portal. *The SIESTA method for ab initio order-N materials simulation*. Journal of Physics: Condensed Matter **14**, 2745 (2002).

[Ste94] P. J. Stephens, F. J. Devlin, C. F. Chabalowski, and M. J. Frisch. *Ab Initio Calculation of Vibrational Absorption and Circular Dichroism Spectra Using Density Functional Force Fields*. The Journal of Physical Chemistry **98**, 11623 (1994).

[Ste10] T. Stein, H. Eisenberg, L. Kronik, and R. Baer. *Fundamental Gaps in Finite Systems from Eigenvalues of a Generalized Kohn-Sham Method*. Physical Review Letters **105**, 266802 (2010).

[Str96] R. E. Stratmann, G. E. Scuseria, and M. J. Frisch. *Achieving linear scaling in exchange-correlation density functional quadratures*. Chemical Physics Letters **257**, 213 (1996).

[Su79] W. P. Su, J. R. Schrieffer, and A. J. Heeger. *Solitons in polyacetylene*. Physical Review Letters **42**, 1698 (1979).

[Suh95] S. Suhai. *Electron correlation and dimerization in trans-polyacetylene: Many-body perturbation theory versus density-functional methods*. Physical Review B **51**, 16553 (1995).

[Sun02] G. Sun, J. Kürti, M. Kertesz, and R. H. Baughman. *Dimensional changes as a function of charge injection for trans-polyacetylene: A density functional theory study*. The Journal of Chemical Physics **117**, 7691 (2002).

[Sun15] J. Sun, A. Ruzsinszky, and J. P. Perdew. *Strongly Constrained and Appropriately Normed Semilocal Density Functional*. Physical Review Letters **115**, 036402 (2015).

[Tan80] T. Tani, P. M. Grant, W. D. Gill, G. B. Street, and T. C. Clarke. *Phototransport effects in polyacetylene, $(CH)_x$*. Solid State Communications **33**, 499 (1980).

[Tan87] C. W. Tang and S. A. VanSlyke. *Organic electroluminescent diodes*. Applied Physics Letters **51**, 913 (1987).

[Tho02] T. Thonhauser, C. Ambrosch-Draxl, and D. J. Singh. *Stress and pressure within the linearized-augmented plane-wave method*. Solid State Communications **124**, 275 (2002).

[Tia04] M. Tiago, M. Rohlfing, and S. Louie. *Bound excitons and optical properties of bulk trans-polyacetylene*. Physical Review B **70**, 193204 (2004).

[Tip08] P. A. Tipler and G. Mosca. *Physics for Scientists and Engineers*. W. H. Freeman, edn. 6 (2008).

[Tka09] A. Tkatchenko and M. Scheffler. *Accurate Molecular Van Der Waals Interactions from Ground-State Electron Density and Free-Atom Reference Data*. Physical Review Letters **102**, 073005 (2009).

[Tka12] A. Tkatchenko, R. A. DiStasio, R. Car, and M. Scheffler. *Accurate and Efficient Method for Many-Body van der Waals Interactions*. Physical Review Letters **108**, 236402 (2012).

[Tor08] M. Torrent, F. Jollet, F. Bottin, G. Zérah, and X. Gonze. *Implementation of the projector augmented-wave method in the ABINIT code: Application to the study of iron under pressure*. Computational Materials Science **42**, 337 (2008).

[Tot03] G. E. Totten and D. S. MacKenzie. *Handbook of Aluminum: Volume 1: Physical Metallurgy and Processes*. Marcel Dekker (2003).

[Tsu92] J. Tsukamoto. *Recent advances in highly conductive polyacetylene*. Advances in Physics **41**, 509 (1992).

[Vah93] O. Vahtras, J. Almlöf, and M. W. Feyereisen. *Integral approximations for LCAO-SCF calculations*. Chemical Physics Letters **213**, 514 (1993).

[Väk93] K. Väkiparta, M. Reghu, M. R. Andersson, Y. Cao, D. Moses, and A. J. Heeger. *Temperature dependence of the electrical conductivity of potassium-doped polyacetylene as a function of pressure and magnetic field*. Physical Review B **47**, 9977 (1993).

[VAl88] C. Van Alsenoy. *Ab initio calculations on large molecules: The multiplicative integral approximation*. Journal of Computational Chemistry **9**, 620 (1988).

[vLe94] E. van Lenthe, E. J. Baerends, and J. G. Snijders. *Relativistic total energy using regular approximations*. The Journal of Chemical Physics **101**, 9783 (1994).

[Vog89] P. Vogl and D. K. Campbell. *Three-dimensional structure and intrinsic defects in trans-polyacetylene*. Physical Review Letters **62**, 2012 (1989).

[Vog90] P. Vogl and D. K. Campbell. *First-principles calculations of the three-dimensional structure and intrinsic defects in trans-polyacetylene*. Physical Review B **41**, 12797 (1990).

[Vos80] S. H. Vosko, L. Wilk, and M. Nusair. *Accurate spin-dependent electron liquid correlation energies for local spin density calculations: a critical analysis*. Canadian Journal of Physics **58**, 1200 (1980).

[Vyd08] O. A. Vydrov, Q. Wu, and T. Van Voorhis. *Self-consistent implementation of a nonlocal van der Waals density functional with a Gaussian basis set.* The Journal of Chemical Physics **129**, 014106 (2008).

[War85] W. Warta and N. Karl. *Hot holes in naphthalene: High, electric-field-dependent mobilities*. Physical Review B **32**, 1172 (1985).

[Wei79] B. R. Weinberger, J. Kaufer, A. J. Heeger, A. Pron, and A. G. MacDiarmid. *Magnetic susceptibility of doped polyacetylene*. Physical Review B **20**, 223 (1979).

[Wil70] D. F. Williams. *dc and Pulsed Electroluminescence in Anthracene and Doped Anthracene Crystals*. The Journal of Chemical Physics **53**, 3480 (1970).

[Wil72] W. G. Williams, P. L. Spong, and D. J. Gibbons. *Double injection electroluminescence in anthracene and carrier injection properties of carbon fibres*. Journal of Physics and Chemistry of Solids **33**, 1879 (1972).

[Wu87] C.-q. Wu, X. Sun, and K. Nasu. *Electron Correlation and Bond Alternation in Polymers*. Physical Review Letters **59**, 831 (1987).

[Wu02] Q. Wu and W. Yang. *Empirical correction to density functional theory for van der Waals interactions*. The Journal of Chemical Physics **116**, 515 (2002).

[Xu14] B. Xu and M. J. Verstraete. *First Principles Explanation of the Positive Seebeck Coefficient of Lithium*. Physical Review Letters **112**, 196603 (2014).

[Yan83] C. S. Yannoni and T. C. Clarke. *Molecular Geometry of cis- and trans-Polyacetylene by Nutation NMR Spectroscopy*. Physical Review Letters **51**, 1191 (1983).

[Yan14] Q. Yan, P. Rinke, A. Janotti, M. Scheffler, and C. G. Van de Walle. *Effects of strain on the band structure of group-III nitrides*. Physical Review B **90**, 125118 (2014).

[Yin82] M. T. Yin and M. L. Cohen. *Theory of static structural properties, crystal stability, and phase transformations: Application to Si and Ge*. Physical Review B **26**, 5668 (1982).

[Zha98] Y. Zhang and W. Yang. *Comment on "Generalized Gradient Approximation Made Simple"*. Physical Review Letters **80**, 890 (1998).

[Zhu92] Q. Zhu, J. E. Fischer, R. Zusok, and S. Roth. *Crystal structure of polyacetylene revisited: An x-ray study*. Solid State Communications **83**, 179 (1992).